Manufacturing Metrology Team

Centre for Additive Manufacturing

Faculty of Engineering

Surface texture measurement of metal additively manufactured parts by X-ray computed tomography

by

Adam Thompson

September 2018

Thesis submitted to the University of Nottingham for the degree of

Doctor of Philosophy

Supervisors: Prof. Richard Leach, Dr Ian Maskery

Abstract

Additive manufacturing (AM) is beginning to come of age. With the freedom of design that is offered by AM, new functionality is now available that has not previously been possible because of tool access limits in machining processes. However, as with any emerging technology, a long list of unsolved problems exist. Particularly, in order for AM to become an established method of high value part manufacture, rigorous verification protocols must be followed, and the processes that produce these parts must be well understood in order for them to be well controlled. In verification, surface characterisation is a well-accepted tool in ensuring that a surface has a set of desired functional properties. Surface characterisation is also commonly used in process development, where it is used to improve process understanding. However, verification of AM parts represents a great challenge, as the tools and processes that exist in current standards fall down when the demands of ultra-complex AM components are considered, and the processes themselves are also not yet well understood. In this Thesis, I present the use of X-ray computed tomography (XCT) for surface measurement, for the purpose of verification and process improvement in an AM context. In particular, I focus on the surfaces of metal powder bed fusion parts. In the first portion of this Thesis, I examine metal AM surfaces in detail, using established methods of surface measurement and visualisation to build up a deep understanding of the features present on these surfaces. Particularly, I find that when compared, discrepancies between measurements of surface features made on data acquired using different measurement instruments can be of similar magnitudes to the sizes of the features in question. Following this work, I detail new methods for the measurement of surfaces using XCT, describing a pipeline for extracting and characterising surface information from raw XCT data. Later, I examine some of the factors that affect XCT surface measurements, particularly investigating how varying scan magnification and volumetric reconstruction grid resolution affects measurements. In this work, I find that increasing geometric magnification in the range of $5\times$ to $50\times$ improves precision, while accuracy and bias do not always improve. Altering resolution, I find that decreasing sampling resolution to 50 % worsens metrological

performance, while increasing it to 150 % may lead to slight improvements. Finally, I bring together the various aspect of the Thesis by applying the techniques developed throughout to an industrial case involving the measurement of internal channel surfaces. In this study, I discuss the outcomes of the Thesis as a whole, showing that XCT is capable of surface measurement in cases where the surfaces of interest are relatively rough (i.e. with an arithmetic mean height of the scale limited surface, $Sa > 1$ μm) and are located on or inside parts that are generally penetrable by X-rays produced using state-of-the-art systems (e.g. a cube of Ti6Al4V < 20 mm × 20 mm × 20 mm in size). In the future work, further characterisation of the factors influencing the measurement, overcoming issues relating to 'black-box' commercial systems and the development of existing methods of data comparison are identified as core research avenues, and a need for developing metrological traceability in XCT measurement is noted.

"It's got nothing to do with clouds."

– Anon. metrologist

Table of contents

List of figures

List of tables

Declaration of authorship

I, Adam Thompson, declare that this Thesis entitled "Surface texture measurement of metal additively manufactured parts by X-ray computed tomography" and the work presented in it are my own and has been generated by me as the result of my own original research. I confirm that:

1. This work was done wholly while in candidature for a research degree at this University;
2. Where I have consulted the published work of others, this is always clearly attributed;
3. Where I have quoted from the work of others, the source is always given. With the exception of such quotations, this Thesis is my own work;
4. I have acknowledged all main sources of help; most notably that of my supervisors, Richard Leach and Ian Maskery, and my colleague Nicola Senin. I received guidance throughout the project from Richard, Ian and Nicola, and other contributors to different Chapters are acknowledged in the publications associated with each Chapter, as referenced at the beginning of each Chapter.
5. Where the Thesis is based on work done by myself jointly with others, I have made clear exactly what was done by others and what I have contributed myself. Particularly, Nicola Senin was responsible for the production of MATLAB code used in comparative assessment of topographies (See Chapter 5), as were specific comparison metrics, while the comparisons themselves were performed by myself. Hence, Nicola is credited as primary author on the latter of the two publications that comprise Chapter 5;
6. Parts of this work have been published as works presented in the list of publications.

List of publications

Work performed during my PhD has been published in a variety of journal papers, conference papers and posters, and presented as non-paper conference presentations. These publications are listed here. As this Thesis is based on a number of the journal papers presented in this list, my contribution to the production of each journal paper is also presented following each listing.

Journal papers

Townsend A, Racasan R, Bills P, Leach R K, Senin N, Thompson A, Ramsey A, Bate D, Woolliams P, Brown S and Blunt L 2018 An interlaboratory comparison of X-ray computed tomography measurement for texture and dimensional characterisation of additively manufactured parts *Additive Manufacturing* **23** 422-432

- Contribution: Performed comparative experiments in line with guidelines set out by Townsend, reviewed manuscript.

Thompson A, Senin N, Maskery I and Leach R K 2018 Effects of magnification and sampling resolution in X-ray computed tomography for the measurement of additively manufactured metal surfaces *Precision Engineering* **53** 54-64

- Contribution: Planned and performed experiments and analysis, drafted manuscript.

Thompson A, Senin N, Maskery I Körner L, Lawes S, and Leach R K 2018 Internal surface measurement of metal powder bed fusion parts *Additive Manufacturing* **20** 126-133

- Contribution: Planned and performed experiments and analysis, drafted manuscript.

Senin N, Thompson A, and Leach R K 2017 Feature-based characterisation of signature topography in laser powder bed fusion of metals *Measurement Science and Technology* **29** 045009

- Contribution: Performed experiments and analysis, reviewed manuscript.

Xu Z, Hyde CJ, Thompson A, Leach R K, Ravi GA, Maskery I, Tuck C and Clare A 2017 Staged thermomechanical testing of Nickel superalloys produced by selective laser melting *Materials and Design* **133** 520-527

- Contribution: Performed X-ray computed tomography experiments, reviewed manuscript.

Gomez C, Su R, Thompson A, DiSciacca J, Lawes S and Leach R K 2017 Optimisation of surface measurement for metal additive manufacturing using coherence scanning interferometry *Optical Engineering* **56** 111714

- Contribution: Performed data analysis, reviewed manuscript.

Senin N, Thompson A, and Leach R K 2017 Characterisation of the topography of metal additive surface features with different measurement technologies *Measurement Science and Technology* **28** 095003

- Contribution: Planned and performed experiments and analysis, co-drafted manuscript.

Thompson A, Maskery I and Leach R K 2017 X-ray computed tomography for additive manufacturing in medicine: a review *International Journal of Metrology and Quality Engineering* **8** 17

- Contribution: Planned and performed literature review, drafted manuscript.

Thompson A, Senin N, Giusca C and Leach R K 2017 Topography of selectively laser melted surfaces: a comparison of different measurement methods *CIRP Annals – Manufacturing Technology* **66** 543–546

- Contribution: Planned and performed experiments and analysis, drafted manuscript.

Thompson A, Maskery I and Leach R K 2016 X-ray computed tomography for additive manufacturing: a review *Measurement Science and Technology* **27** 072001

- Contribution: Planned and performed literature review, drafted manuscript.

Conference papers

Thompson A, Tammas-Williams S, Senin N, Leach R K and Todd I 2018 Correlating volume and surface features in additively manufactured metal parts *ASPE/euspen conference: advancing precision in additive manufacturing* (Berkeley, USA)

Rivas Santos V M, Maskery I, Sims-Waterhouse D, Thompson A, Leach R K, Ellis A, Wooliams P 2018 Benchmarking of an additive manufacturing process *ASPE/euspen conference: advancing precision in additive manufacturing* (Berkeley, USA)

DiSciacca J, Gomez C, Su R, Thompson A, Lawes S, Leach R K, Colonna de Lega X and de Groot P 2017 True-color 3D surface metrology for additive manufacturing using interference microscopy *euspen/ASPE conference: dimensional accuracy and surface finish in additive manufacturing* (Leuven, Belgium) pp 145-148

Senin N, Thompson A, and Leach R K 2017 Feature-based characterisation of laser powder-bed fusion surfaces *euspen/ASPE conference: dimensional accuracy and surface finish in additive manufacturing* (Leuven, Belgium) pp 121-123

Hyde CJ, Xu Z, Thompson A, Leach R K, Maskery I, Tuck C and Clare A 2017 On the use of X-ray computed tomography for monitoring the failure of a Two-Bar small specimen manufactured by Selective Laser Melting *Solid freeform fabrification symposium* (Austin, USA)

Leach R K, Thompson A, and Senin N 2017 A metrology horror story: the additive surface *ASPEN/ASPE conference: manufacture and metrology of structured and freeform surfaces for functional applications* (Hong Kong, China)

Thompson A, Körner L, Senin N, Lawes S, Maskery I and Leach R K 2017 Measurement of the internal surface texture of additively manufactured parts by X-ray computed tomography *Conference on industrial computed tomography (iCT)* (Leuven, Belgium)

Thompson A, Senin N and Leach R K 2016 Towards an additive surface atlas *ASPE/euspen conference: dimensional accuracy and surface finish in additive manufacturing* (Raleigh, USA)

Non-paper conference presentations

Thompson A, Senin N, Newton Land Leach R K 2018 Additive manufacturing surfaces and mapping their evolution *FLEXIFINISH - automated post processing for additive manufacturing* (Coventry, UK)

Senin N, Thompson A, Newton L and Leach R K 2018 Towards a quantitative understanding of surface topography in additive manufacturing *MAPP 1st international conference* (Sheffield, UK)

Thompson A, Senin N, Maskery I and Leach R K 2017 A sensitivity analysis for the measurement of internal additively manufactured surfaces by X-ray computed tomography *Dimensional X-ray computed tomography* (Coventry, UK)

Thompson A, Körner L, Senin N, Lawes S, Maskery I and Leach R K 2017 X-ray computed tomography of additively manufactured metal parts: the effect of magnification and reconstruction sampling on surface topography measurement *16th international conference on metrology and properties of engineering surfaces* (Gothenburg, Sweden)

Thompson A, Körner L, Senin N, Lawes S, Maskery I and Leach R K 2017 X-ray computed tomography for the measurement of internal surface texture of additively manufactured hollow parts *CIRP winter meeting* (Paris, France)

Leach R K, Thompson A, and Senin N 2016 Trials and tribulations in measuring additive surfaces *66th CIRP general assembly* (Guimaraes, Portugal)

Posters

Thompson A, Maskery I and Leach R K 2018 Internal surface measurement by X-ray computed tomography: an additive manufacturing case study *Dimensional X-ray computed tomography* (Nottingham, UK)

Gomez C, Su R, Thompson A, DiSciacca J, Lawes S and Leach R K 2017 Optimisation of surface topography measurement and characterisation for metal additive manufacturing using coherence scanning interferometry *euspen/ASPE conference: dimensional accuracy and surface finish in additive manufacturing* (Leuven, Belgium) pp 162-166

Xu Z, Hyde CJ, Thompson A, Leach R K, Maskery I, Tuck C and Clare A 2017 Defect evolution in laser powder bed fusion additive manufactured components during thermo-mechanical testing *euspen/ASPE conference: dimensional accuracy and surface finish in additive manufacturing* (Leuven, Belgium) pp 113-115

Gomez C, Thompson A, DiSciacca J, Lawes S and Leach R K 2017 Coherence scanning interferometry for additive manufacture *16th international conference on metrology and properties of engineering surfaces* (Gothenburg, Sweden)

Townsend A, Racasan R, Bills P, Thompson A, Senin N, Leach R K and Blunt L 2017 Results from an interlaboratory comparison of areal surface texture parameter extraction from X-ray computed tomography of additively

manufactured parts *euspen's 17th international conference & exhibition* (Hannover, Germany)

Book chapters

Thompson A and Leach R K 2017 Introduction to industrial X-ray computed tomography In: *Industrial computed tomography* (New York, USA: Springer) pp 1-23

Acknowledgements

Over the course of my PhD, I have been incredibly lucky in both my professional and personal interactions, and have had the pleasure of working and living alongside individuals who have made me a better scientist and a better person. I won't pretend I enjoyed every minute of my PhD (who does?), but I was lucky enough to have enjoyed the vast majority of it. There are too many individuals to name everyone, but I would like to thank certain people for their input into my PhD here.

Firstly, the continued support of my supervisors, Richard Leach and Ian Maskery, has been instrumental in my success. Between them, Richard and Ian have provided support both scientific and pastoral, and have pushed me to achieve in every aspect of this doctorate. They were permanently available and quick to respond, and always provided what I consider to be exemplary supervision. I'd also like to thank Nicola Senin, who constantly pushed me towards better science as my enduring co-author, but generally via the most painful route.

I would next like to thank all of my various colleagues from the Centre for Additive Manufacturing and the Manufacturing Metrology Team, and in particular the colleagues who became close friends: Alex Gasper, Andrew Dickins, Carlo Campanelli, Duncan Hickman, Hatim Cader, Lewis Newton, Luke Todhunter, Patrick Bointon and Vicente Rivas Santos. Particularly, I'd like to thank my colleague, Katie Blake, who helped me through the hardest part of my PhD, when other aspects of my life were not going so well. Thanks for being a best friend when I needed one.

I would also like to thank my family and friends for their continuing support throughout my PhD, and I'd like to thank the love of my life, Emma Plummer, from the bottom of my heart for every day of our 7 years together. Emma, you are my rock and my partner, and you do more for me than you will ever know.

For Shack, who taught me the two

best rules for science I know:

"Be more specific"

"Never have too many variables"

1. Introduction

In this Chapter, I present an introduction to the subjects examined throughout this Thesis, and explain the motivations for each. Some material from this Chapter has been published in a review paper in 2016 [1], as well as in a book in 2017 [2].

1.1 Additive manufacturing overview

Figure 1.1. An example product produced using metal powder bed fusion, containing non-machinable internal features. Part courtesy of 3TRPD.

Additive manufacturing (AM) is defined as the "process of joining materials to make parts from 3D model data, usually layer upon layer, as opposed to subtractive manufacturing and formative manufacturing methodologies" [3]. AM technologies have gained traction in the manufacturing community recently, for their ability to produce parts containing complex geometries that were previously impossible to manufacture by conventional means [4]. Their perceived physical beauty aside (see figure 1.1), these geometries are capable of enabling all kinds of functionality for a myriad of different applications: lightweighting, osseointegration, vibration isolation, impact protection; the list

goes on. Also, because of the reduction of existing design constraints that AM technologies facilitate, the production of single-piece parts that would previously have been constructed as complex assemblies is possible [4]. Additionally, as AM technologies rarely require part-specific tooling, there is little to no setup cost associated with changing the part being built, essentially allowing for low volume production of parts in a way that is not possible for mass production parts [5]. Low volume production has the further advantage of allowing for mass-customisation of parts, meaning that manufacturers will be able to produce bespoke products at greater volume than previously possible.

The generic AM process involves eight key stages, beginning with a computer aided design (CAD) model, and resulting in a finished part. The generic flow progresses as shown in figure 1.2, and is divided into the following stages[4]:

- CAD: a digital design is created in line with the specifications laid down by the designer (usually a solid parametric model).

- Conversion to triangulated model: The CAD design is converted into a triangulated model, which describes the external surfaces of the CAD as a set of connected triangles (often .STL format).

- File transfer to the AM machine: The triangulated model is loaded onto the AM machine, and the file is set up at some position within the build volume. The triangulated model is generally sliced into layers, and machine-readable code generated to manufacture the layers.

- Machine setup: Process parameters are set up for the build process on the machine, and the machine-readable code is loaded.

- Build: the part is built by the machine.

- Removal: Many AM machines work at high temperature, so the build volume is cooled if required. The part is removed from the build volume.

- Post-processing: The part is cleaned, and any support structures are removed.

- Application: The finished part is ready to be used.
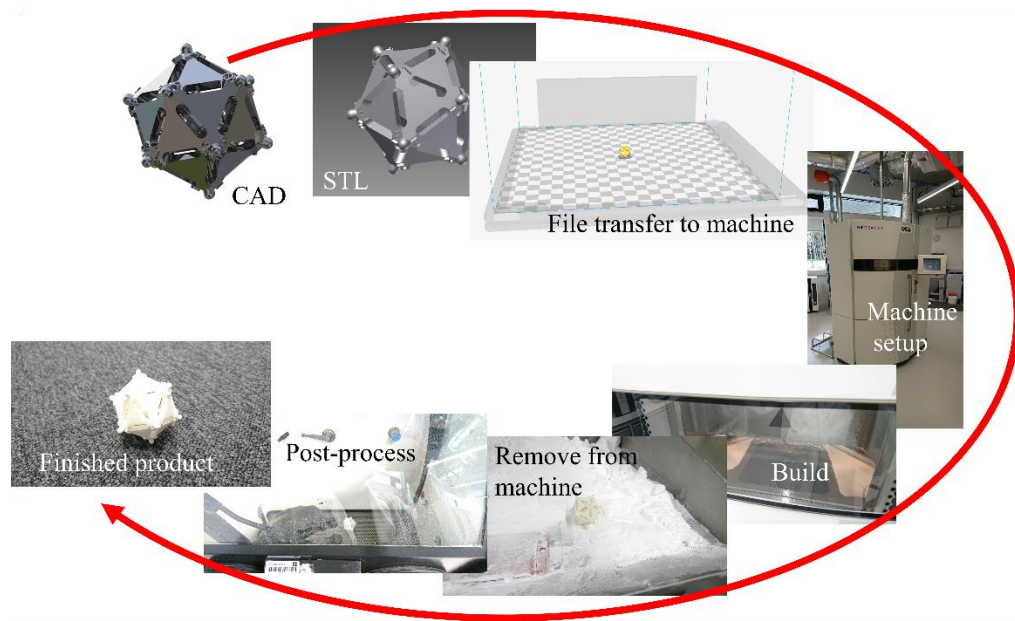
Figure 1.2. Generic AM process, showing the eight steps from CAD design to the finished product.

1.1.1 Summary of AM process families

The International Organisation for Standardisation (ISO) is an independent organisation that publishes physical and specification standards to ensure that products, services and systems meet desired levels of quality, safety and efficiency. Standards for AM have been under development for a number of years within the ISO community, with the first being published in 2014. These standards are based on earlier standards published by the USA based standards organisation, ASTM, but these have not been withdrawn and superseded by their ISO counterparts [6]. ISO identifies seven process categories under the broad banner of additive manufacturing. These process categories are defined by ISO as follows [3]:

- Binder jetting: an additive manufacturing process in which a liquid bonding agent is selectively deposited to join powder materials.
- Directed energy deposition: an additive manufacturing process in which focused thermal energy is used to fuse materials by melting as they are being deposited.

- Material extrusion: an additive manufacturing process in which material is selectively dispensed through a nozzle or orifice.

- Material jetting: an additive manufacturing process in which droplets of build material are selectively deposited.

- Powder bed fusion: an additive manufacturing process in which thermal energy selectively fuses regions of a powder bed.

- Sheet lamination: an additive manufacturing process in which sheets of material are bonded to form a part.

- Vat photopolymerisation: an additive manufacturing process in which liquid photopolymer in a vat is selectively cured by light-activated polymerisation.

AM techniques offer a range of benefits when compared to conventional manufacturing processes. The primary benefit presented by AM is the huge freedom of design offered by the various additive processes. This benefit means that geometries that were previously impossible to produce using existing machining techniques are now possible using additive techniques. Such parts are made possible because AM does not have the requirement for tool access that hinders most machining techniques [4]. For example, the tool access requirement has previously been a problem when creating tooling for injection moulding applications, as the construction of cooling channels was restricted by the straight line limitations of drilling operations [7] (see figure 1.3). Given the nature of additive processes, AM also allows for small production runs when compared to technologies such as injection moulding, as there is no tooling cost associated with producing new parts [4].
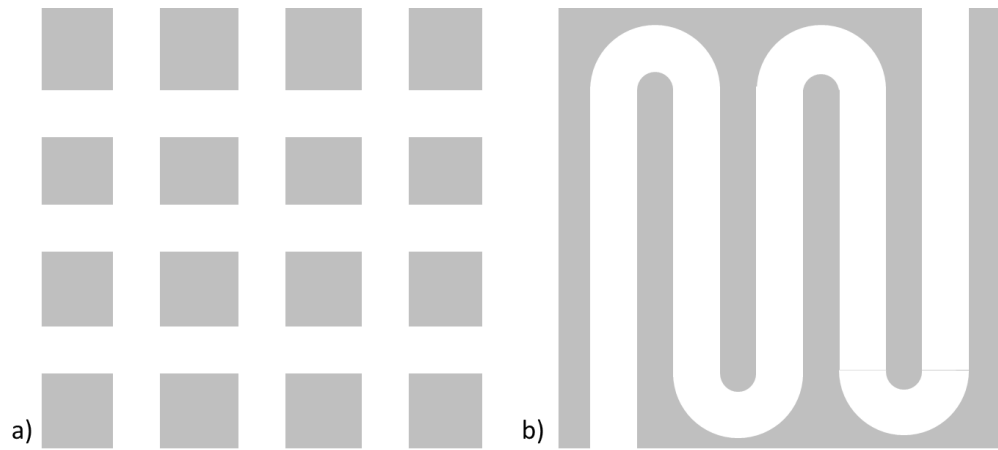
Figure 1.3. Cross-section of example parts containing a) conventional; and b) conformal cooling channels

As with any manufacturing technology, however, there are issues that limit AM processes, and much work is currently being undertaken to address these. For example, when compared to mature manufacturing processes, such as injection moulding or computer numeric control (CNC) machining, AM processes are universally slower by orders of magnitude. While AM is rarely used to make parts that can be used by these methods, manufacturers are constantly striving to improve manufacturing speeds, and AM processes are broadly considered to be slow compared to many mature processes [4]. There are also limitations in regards to available materials, as only a relatively small library of suitable materials for the fabrication of AM parts exists. Many AM processes also still require significant post-processing, due to the requirement for support structures in the manufacturing process [4], the residual stresses that result from thermal effects [8] and the rough surfaces that result from many these processes [9]. In addition, dimensional accuracy is a significant problem in AM technologies, as for example, typical accuracies for industrial metal powder bed fusion processes are in the range of a few tens of micrometres [4], far poorer than the nanometre accuracy now possible using ultra-precision machining [10]. It should be noted that some micro-additive processes are capable of accuracy in the range of a few micrometres, but these processes are only currently capable of producing relatively small parts and, therefore, are restricted in their application (e.g. two-photon polymerisation, often used for biomedical applications) [11].

In terms of industrial applications, the processes used most commonly in today's manufacturing sector include vat photopolymerisation and material extrusion processes (primarily used for prototyping), as well as various powder bed fusion processes (now used to produce polymer and metal parts for end use) [4]. Inkjetting for the fabrication of 3D parts has also begun to be considered a credible industrial method, due to its scalability and multi-material part production [12]. Figure 1.4 explains diagrammatically how parts are produced using example powder bed fusion, vat photopolymerisation and inkjetting methods. Powder bed fusion and vat photopolymerisation involve using an energy source (a laser in the examples provided) to create each layer, and then moving the part down to begin manufacturing the next layer. In the inkjetting example, the printheads are moved up after each layer in order to build the next layer.
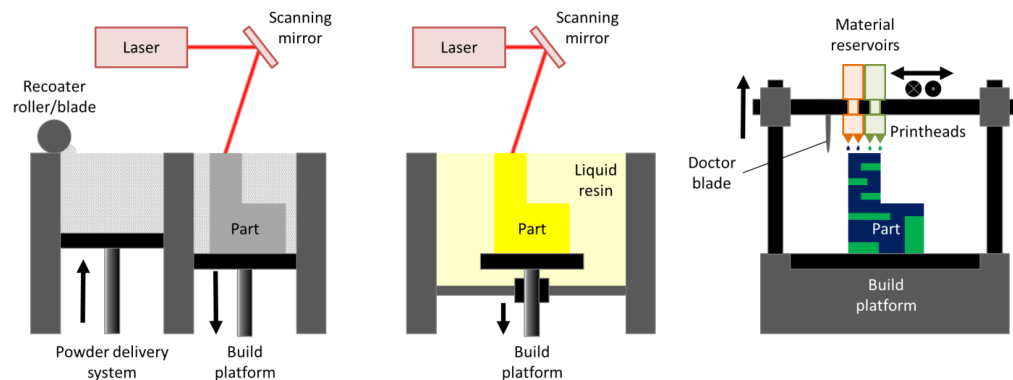
Figure 1.4. Schematic diagrams depicting example processes from the families of powder bed fusion, vat photopolymerisation and material jetting, respectively [4]. Figure published in [1].

Although AM has recently become more viable for part production, following improvements in part quality and process reliability, a number of barriers to increased adoption of AM parts exist, relating to the difficulties in applying quality assurance principles, such as dimensional and geometric inspection and verification [13]. In particular, when inspecting AM surfaces, optical and contact surface measurement solutions are often incapable of measuring the inaccessible and internal surfaces. Such conditions are common with typical AM geometries, such as hollow parts and lattice structures [9,14,15]. The work performed during my PhD explores these challenges, and I will go into

6

significant depth regarding aspects of verification of and metrology for AM parts later in this Chapter and throughout this Thesis.

1.1.2 Metal powder bed fusion

With recent developments, AM has increasingly become a viable manufacturing solution in a number of industries, and large volumes of polymer parts are now in production for a range of applications (e.g. aerospace, medical) [16]. On a research front, however, metal AM processes are amongst the most interesting of the more industrially mature applications of AM technology, as high value applications (e.g. parts for high temperature aerospace engines) demand extremely high quality and rigorous quality control, which are not yet possible using AM [17]. As such, I decided to focus on metal AM processes during my research, and particularly metal powder bed fusion (MPBF) processes.

While liquid-phase sintering, indirect processing, and pattern methods are used to create metal parts, the most common MPBF processes employ full-melting of a powder source [17,18]. As such, these methods represented the most logical focus for the purposes of the work performed during my PhD, and hence I focus on these methods here. Of those that melt parts fully, there are two main streams of MPBF processes, categorised by the energy source used to fuse particles in the powder bed. These two process types use a laser and an electron beam respectively. In both cases, the energy source is used to heat particles in the powder bed to the point where they are fully molten, flowing into and thereby fusing with their neighbours [18].

Full-melting MPBF processes generally flow as follows [18]:

- An appropriate atmosphere is generated for manufacture. The energy sources are either laser of electron beam, and each source type broadly requires a different atmosphere. Generally, laser systems operate under an inert gas atmosphere, while electron beam systems operate under

vacuum. For both system types, the build chamber is generally heated to reduce thermal gradients and cooling effects during processing.

- A layer of powder is moved from some storage receptacle to the build area, where it is deposited in a layer of some defined thickness. The raw powder can be produced via a variety of methods, but generally comprises a powder with a normal distribution of sizes between some limits specific to the application.

- The energy source then scans across select areas of the powder layer, melting the powder where it passes. The melted powder then solidifies, forming a single layer in the space where the energy source has passed. Scanning strategies can take many forms, but often employ some kind contour pattern of layer edges with a rastered infill. Electron beam systems also often undergo a pre-heating step using a low-power scan prior to actual particle fusion.

- Following layer production, the build platform moves down by a step defined by the chosen layer thickness.

- Another layer of powder is deposited and the fusion process repeats until the whole object has been fabricated. The build chamber is finally cooled slowly to reduce the risk of thermal cracking.

Reading this Thesis, it will become clear that in the work performed throughout my PhD, I focussed on laser MPBF as opposed to electron beam MPBF parts. This choice resulted from the fact that laser MPBF is the more common of the two types of process seen in industry [17], but similar work shows that while electron beam MPBF surfaces tend to be rougher than the laser MPBF equivalents, the set of challenges present in both cases are similar [9,18], and so results emanating from this work can be seen as broadly applicable for both cases.

1.2 Metrology overview

The Vocabulaire International de Métrologie (VIM) formally defines metrology as "the science of measurement and its application" [19], noting that "metrology

includes all theoretical and practical aspects of measurement, whatever the measurement uncertainty and field of application". Metrology broadly encompasses the various fields of research that seek to develop the science and technology of measurement, be that measurement of any of the seven base quantities from the International System of Units (SI) [20], or any of the units derived from these base quantities. These base quantities are: length, mass, time, electric current, thermodynamic temperature, amount of substance and luminous intensity [19].

The great physicist, Lord Kelvin, once expressed, "To measure is to know," and also, "If you cannot measure it, you cannot improve it." These sentiments are rarely more applicable than in the manufacturing industry, where we are interested both in ensuring that a manufactured component meets the dimensional specification laid out by the designer, and in constantly improving upon existing products. In pursuit of these goals, we are often most concerned with the first of the SI base units; the metre. The metre is defined as the distance travelled by light in a vacuum in a time of $1/c$ seconds, where c is the speed of light; 299 792 458 ms^{-1}. The metre is currently realised practically through the use of a 'femtosecond comb', which allows the coupling of the frequency standard (from an atomic clock) to the optical frequencies emitted by stabilised lasers [21]. Specifically, the metre is realised through the wavelength of radiation from an iodine-stabilised helium-neon laser (emitting at 633 nm), and has an uncertainty of 2 parts in 10^{11}.

Dimensional measurements are routinely made of components after (or during) a manufacturing process, in order to compare measured dimensions to a specification. The designer will generally specify a dimension and a tolerance on the dimension, and provided the measured quantity lies within the defined tolerance, the component will pass that part of the inspection process.

However, ensuring parts meet their specification is not quite so simple, as each measurement (dimensional or otherwise) has an associated measurement uncertainty (i.e. a "non-negative parameter characterizing the dispersion of the

quantity values being attributed to a measurand, based on the information used" [19]). Estimation of measurement uncertainty is a complex procedure, and is usually performed in line with the Guide to the Expression of Uncertainty in Measurement (GUM) [22]. Uncertainty estimation is generally performed by making measurements that are 'traceable' to the definition of the SI metre. The VIM defines traceability as a "property of a measurement result whereby the result can be related to a reference through a documented unbroken chain of calibrations, each contributing to the measurement uncertainty" [19]. Traceable measurements allow for the successful estimation of uncertainty, and are generally a base requirement for the verification of manufactured goods. Traceability is considered by the international community as the only means by which evidence can be provided towards a given product fulfilling the requirements set out by its designer.

To provide an example, let us consider a length measurement made between two faces on an AM part, on the shop floor of an AM production facility. This length may be measured using a calliper, which is calibrated using an artefact; most commonly a gauge block. This gauge block is in turn calibrated by a more accurate instrument, which is itself calibrated using a more accurate gauge block. This more accurate gauge block will be calibrated in reference to an optical interferometer with a laser source. The laser source is calibrated against the iodine-stabilised laser that is used to realise the definition of the metre, and so traceability is established from the shop floor length measurement, all the way to the definition of the metre. Each stage of the traceability chain has some discernible uncertainty, which generally increases as we move down the chain (as instrument accuracy decreases). Estimation of the uncertainty at each link in the chain is essential; it is impossible to have a traceable measurement without the inclusion of an uncertainty with that measurement. The traceability chain is described diagrammatically in figure 1.5 [21,23].
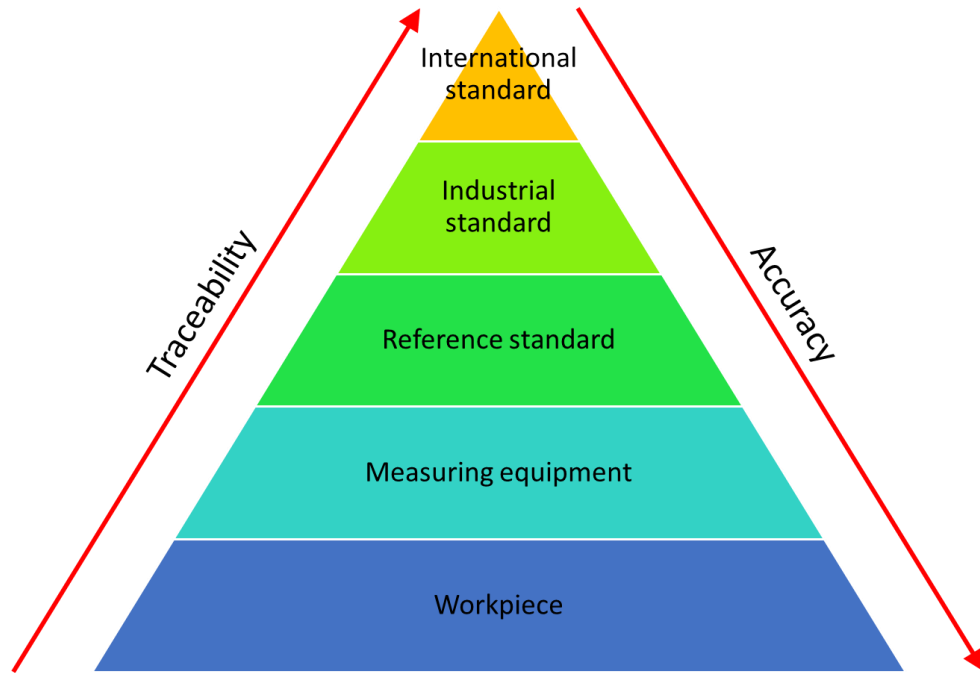
Figure 1.5. The traceability pyramid. Traceability is transferred between each level by calibration, which includes an evaluation of uncertainty in the realised length.

The scientific field of dimensional metrology can be separated into a number of sub-fields, particularly regarding the measurement of length (i.e. the distance between two fixed points), displacement (i.e. the change in position of an object or feature with respect to a reference), form (i.e. the deviation of an object from the definition of the corresponding geometrical primitive) and texture (i.e. the surface topography of an object) [24]. Two of these themes (form and texture) have been identified in the literature as requiring significant research specifically in an AM context [9,15]. As such, I will elaborate briefly on these two research themes, as well as separately on the measurement of volume, which blurs the boundary between form and texture measurement. Another note must be made at this point, in that the science of metrology in a manufacturing context also involves the development of techniques for monitoring manufacturing processes themselves, as well as the parts that are produced by those processes. This is a huge field of research in and of itself, but in this Thesis I focus on off-line measurements of AM parts. As such, I will not cover in-process and in-situ metrology here, but refer the reader to two recent reviews covering these aspects of metrology for AM in detail [25,26].

1.2.1   Form metrology basics

In their recent book chapter [24], Ferrucci et al. defined form metrology as "the deviation of the measured surface or path from the fundamental definition of the corresponding geometrical primitive, also known as the reference geometry feature". Generally speaking, form measurement entails the measurement of deviations from a reference in the following areas: peak-to-reference (i.e. maximum deviation from a reference in the positive direction), reference-to-valley (i.e. maximum deviation from a reference in the negative direction), peak-to-valley (i.e. maximum variation in measured points) and root-mean square (i.e. the distribution of measured points) [24]. Measurement of form allows for the characterisation and quantification of shape deviation in part production, relating to various aspects of a manufacturing process. Form measurement comprises the following types of measurement: straightness (i.e. the deviation of a geometry from a line), roundness and cylindricity (i.e. the deviation of a geometry from a circle or cylinder); and flatness and parallelism (i.e. the deviation of a geometry from a plane and the degree to which two geometries are parallel to one another) [24].

Form measurement is generally performed using some kind of co-ordinate measurement system (CMS) [24,27]. There are many different types of CMS, (e.g. contact, optical, X-ray computed tomography) and performance verification of such systems is standardised as part of the ISO 10360-X series [28]. The 10360-X series is constantly updated and added to as new technologies are created for the measurement of physical geometries. The most common type of CMS is the conventional coordinate measuring machine (CMM), which is a contact-based measurement system that typically use spherical probes to acquire data from measured objects [21,24]. The CMM is a staple of industrial production, with machines coming in many different configurations, designed to fit specific tasks. The range of tasks that CMMs are applied to is highly diverse: CMMs exist to measure sub-millimetre watch movements, and CMMs exist to measure double decker buses.

Recent developments in form metrology involve the use of optical technology as CMSs, generally split into five families: interferometry and confocal, conoscopic holography, triangulation, time of flight (phase-based) and time of flight (pulse-based) [15]. Of these technology families, triangulation-based techniques are the most common in the manufacturing industry, particularly laser triangulation and structured light systems. In their recent review [15], Stavroulakis and Leach examined the applicability of optical CMSs to AM, and found these two technologies to be broadly the most applicable to AM.

While form measurement represents a broad field of open research, this PhD project did not involve measurement of form to a significant degree, so I will not elaborate on the measurement of form beyond this brief overview. For further information regarding the measurement of form in an AM context, the recent book by Leach and Smith [23] provides an extensive discussion of form metrology, and the recent review by Stavroulakis and Leach [15] examines the state of the art in form metrology for AM.

1.2.2   Surface metrology basics

Surface metrology is primarily concerned with the physical technologies and algorithmic techniques used to characterise surface topography [29,30]. Numerous technologies and comparison methodologies exist, and are outlined below. For the purposes of this work, there are some definitions that must be stated that will remain relevant throughout this Thesis. In their recent book chapter, Ferrucci et al. [24] defined the following terms:

- Surface topography: local deviations of a surface from a perfectly flat plane of all the surface features treated as a continuum of spatial wavelengths.
- Surface texture: the geometrical irregularities present at a surface. Surface texture does not include those geometrical irregularities contributing to the form or shape of the surface

1.2.2.1 Surface metrology instrumentation

The most common data acquisition technology by far is the contact stylus system [29,31] (see figure 1.6). These instruments employ mechanical contact between a probe and the surface being measured, and use a transducer to convert the vertical movement of the stylus across the surface into an electrical signal that is subsequently recorded by a computer. Stylus systems involve dragging a spherical probe (generally made of diamond and with radii as small as 2 μm) along the surface at a constant speed, and recording the height position of the sphere at regular intervals. Such systems have existed since the 1930's, and can be found on the shop floors of many manufacturing companies, being used to verify components at all points of the manufacturing industry value spectrum. Such systems employ relatively simple principles, meaning that acquiring an understanding of a system's limitations (e.g. minimum resolution and maximum slope height) is relatively straightforward. These limitations are defined by the stylus probe tip geometry, in that the stylus cannot acquire topographic detail smaller than $2\pi\sqrt{ar}$ (where a is the amplitude of the surface and r is the tip radius) [21], nor can it successfully measure slopes that contact parts of the probe other than the tip (probes often have conical geometries, see figure 1.6). Stylus systems are also limited by the intrinsic nature of physical contact systems, in that there is a danger that damage is incurred by the measurement process (though this damage is generally considered to be minimal in most cases). Damage can be reduced using low force probes, but lowering the contact force increases the chance of the stylus leaving the sample surface when passing over peaks ('stylus flight'), so measurement speed must then be reduced to compensate [21,24].
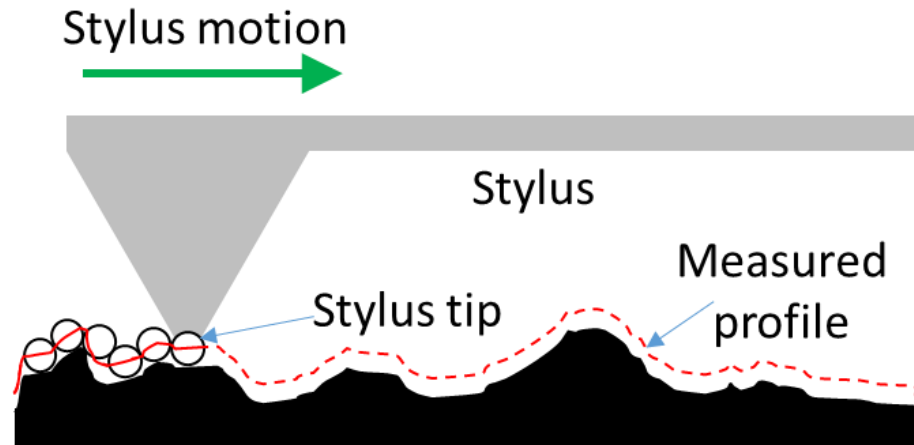
Figure 1.6. Schematic representation of a contact stylus measurement system. The stylus moves a spherical probe across the surface, capturing the topography of the surface.

However, by comparison to modern areal measurement systems, stylus systems are slow, and are generally only capable of acquiring profile data; while it is possible to scan a probe across the sample surface in a raster pattern, this process essentially involves the acquisition of a series of adjacent profiles, as opposed to data that can be considered to be truly 'areal' [29]. Because of the intrinsic nature of the contact measurement paradigm, while a single profile can be acquired quickly (a few seconds), acquiring the thousands of densely packed profiles required to generate information about an area of a surface quickly becomes a very lengthy task. As manufacturing processes have evolved over time, the need for improvement of these processes based upon an intimate knowledge of the underlying physics has grown, and so a need has developed in manufacturing for new technologies that are capable of quickly capturing much greater amounts of information about surfaces than possible using contact systems.

To fulfil this need, a series of optical methods of surface data acquisition have been developed, capable of generating data in a fraction of the time required by a stylus system [29]. These new methods come with their own disadvantages, often relating to the more complex measurement principles that accompany optical probing systems when compared to contact methods. Particularly, two significant limitations present themselves. Firstly, because of the microscope optics commonly employed by these systems, there is a fundamental restriction

regarding measurable slope angles resulting from the numerical aperture (NA) of any such optic. Referring to figure 1.7, the NA of an objective is given by

$$A_N = n \sin \alpha,$$ 1.1

where n is the refractive index of the surrounding medium (approximately 1 in air), and α is the acceptance angle [24]. This equation applies to the case where reflection is specular [32]. Secondly, each objective lens has an intrinsic optical resolution that defines the minimum distance between two lateral features on a surface. The resolution is given by

$$r = \frac{k\lambda}{A_N},$$ 1.2

where k is a constant depending on the definition of 'resolvable' and λ is the wavelength of light used to make the measurement [24]. A number of criteria (i.e. different values for k) exist to define this minimum distance, based on varying definitions of what is 'resolvable', but the most commonly used in optical metrology are the Rayleigh [33] and Sparrow [34] limits. For incoherent illumination, the Rayleigh limit is given by $0.61\lambda/A_N$, while the Sparrow limit is given by $0.47\lambda/A_N$. In general, the Sparrow limit is used most often by microscope objective manufacturers, as it gives the lower value.
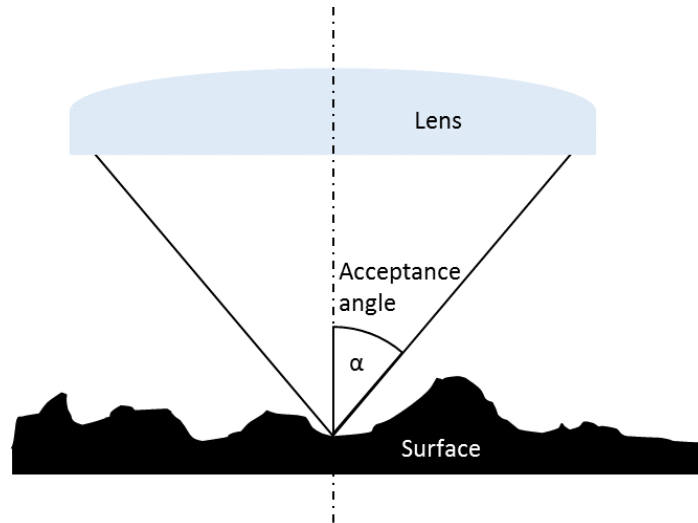
Figure 1.7. Schematic representation of the numerical aperture of a microscope objective lens.

To note, throughout this Thesis, I often refer to 'optical' systems. While X-ray computed tomography systems (see Section 1.2.3) technically use optics in their operation (in that X-rays are a form of light), this terminology is used to refer to optical systems using visible light, particularly those described here.

Limitations aside, these optical systems serve to overcome the speed issues that plague contact systems, and are, therefore, becoming increasingly used in both industrial and research contexts [29]. The most common types of systems can be split into two sub-categories: raster scanning and areal optical methods. Raster scanning methods are slower than areal (though not generally as slow as stylus methods as they are not limited in probe movement speed by stylus flight issues), and include confocal instruments (imaging [35,36] and chromatic [37,38]) and point autofocus instruments [39,40]. Areal methods describe those capable of acquiring truly areal datasets, building up large volumes of height map (i.e. a 2.5 D grid of z points on an xy plane) in a short space of time, and include coherence scanning interferometers [41,42], phase-shifting interferometers [43,44] and focus variation microscopes [45,46]. Many other types of optical measurement technologies exist (e.g. triangulation instruments, digital holographic microscopes, and area integrating scattering instruments) but these are collectively less used in industrial measurement contexts and are not yet standardised, so I will not discuss these in any more depth here [29].

Of the optical systems that have so far undergone standardisation efforts as part of the ISO 25178 [47] series, the most commonly used for AM surfaces are confocal, coherence scanning interferometry and focus variation instruments [9]. As these are the systems that were eventually used most commonly throughout my PhD, I will briefly describe their operating concepts here.

Confocal microscopy

Confocal microscopy (CM) involves the production of optical section images by restricting the illumination of the sample and observing the reflected light

[36]. Strictly, what is described here is laser-scanning confocal microscopy, as opposed to 'chromatic' confocal microscopy, which are similar instruments that alternatively use incoherent broadband light (i.e. 'white light') for illumination. While chromatic systems are occasionally used for surface measurement, they are less common than laser-scanning systems as the achievable accuracy is lower, so I will focus here on laser-scanning confocal systems [36]. Figure 1.8 shows the general setup of a laser-scanning CM system.
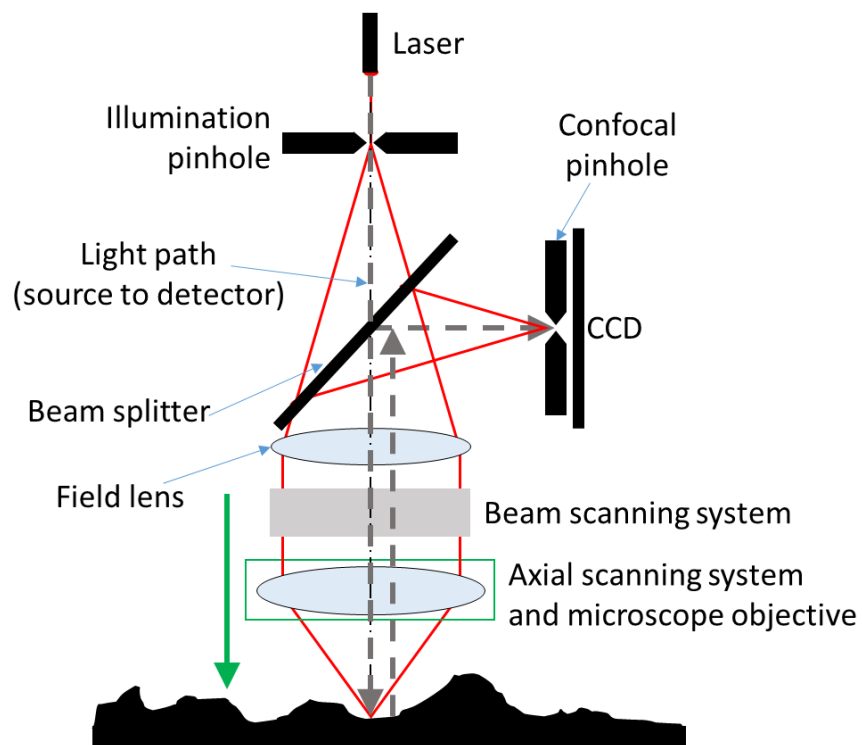
Figure 1.8. Schematic representation of a confocal microscope [36]

The method by which CMs operate is as follows. In laser-illuminated systems, the CM scans a laser across a surface in a raster pattern, using a galvanometer system. Disk scanning systems also exist, but are less common. The laser illuminates a pinhole, which is imaged onto the sample via the system's optics. The light is reflected from the surface back through the system's optics, and imaged onto a second pinhole, placed in a conjugate position to the first pinhole (the confocal pinhole in figure 1.10). A charged-coupled device (CCD) detector placed behind this pinhole then records the signal reflected from the surface. Out of focus light is prevented from reaching the detector by this pinhole, so only the parts of the surface lying the in the confocal plane are recorded. The

whole objective lens is then moved by a step along the z axis, and the process repeated. By iterating this process for each step, a measured surface can be built up, providing a complete height map of the surface.

In general for current commercial systems, CM is capable of achieving the greatest lateral resolution of any surface measurement technology, because of the use of the pinhole in the instrument setup [36]. However, CM systems tend to be slower than other systems because of their scanning nature, which generally takes longer than acquiring a 2D. Additionally, CM systems tend to have higher noise than CSI systems.

Coherence scanning interferometry

Coherence scanning interferometry (CSI) involves the evaluation of changes in an interference signal to determine the position of the surface [42]. In concept, these systems use optical interference to determine the position of a surface, based upon the position in an image where the constructive interference effect is strongest, scanning through a height range to acquire data for a measured surface. Light sources for CSI are incoherent with a broadband spectrum (i.e. white light), as the short coherence length offered by white light avoids ambiguity in determining the fringe order. Figure 1.8 shows the general setup of a CSI system. CSI systems use various interference objectives (e.g. mirau, Michelson, Linnik), though Mirau is the most common [42].

The method by which CSI systems works is as follows. The light is first split using a beam splitter (labelled as the 'interferometer beam splitter' in figure 1.8). One beam is directed towards a reference mirror, while the other is directed at the sample. Both beams are reflected back to the beam splitter, where the two beams recombine to be sent to a CCD detector. As the light has low coherence, interference is only observed where the two optical path lengths (sample and reference) are almost identical. The detector acquires an image, and the positions on the detector of maximum interference can be found. Using this information, the position of the surface is then determined for the acquired

image. After acquiring an image, the objective lens is moved by a step along the *z* axis (depicted by the green arrow in figure 1.8), and the process repeated. By iterating this process through the full depth of the sample surface, a height map is generated.
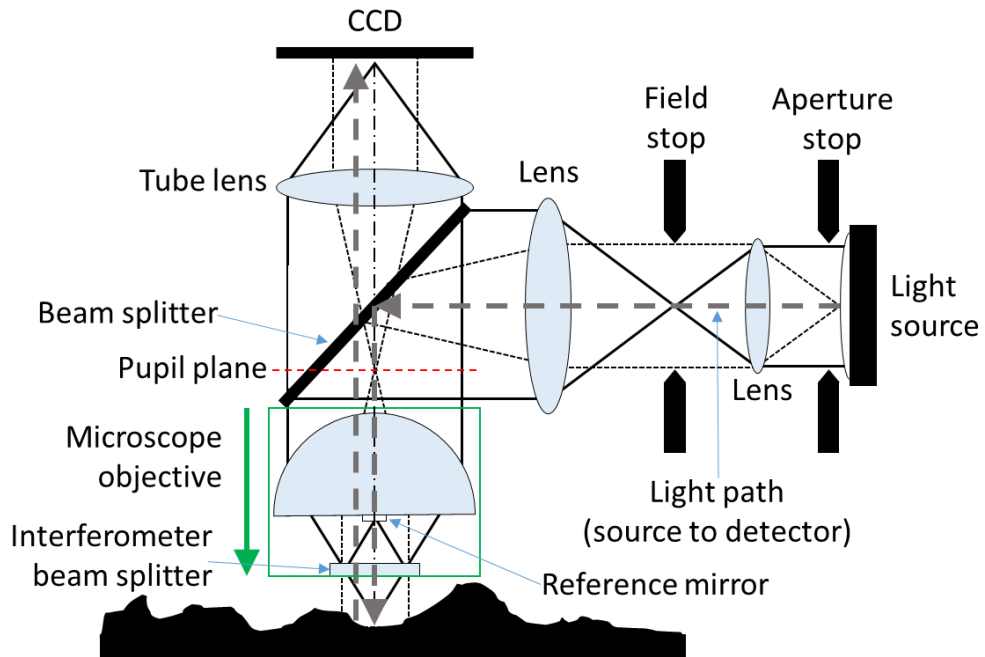
Figure 1.9. Schematic representation of a coherence scanning interferometer, using a Mirau interference objective lens [42].

In general for current commercial systems, CSI is capable of achieving better lateral resolution than other surface measurement systems, except for confocal microscopes. CSI is particularly useful for measuring smooth surfaces (i.e. surface with maximum peak-to-valley distance is < 50 nm [48]), though has historically not been as successful when measuring rough surfaces. However, recent developments have shown that with advanced functions, CSI systems are now also capable of measuring rough surfaces [49]. CSI systems tend to have the lowest noise of any system type. CSI systems, however, tend to be slower than focus variation systems, so measurement of large areas takes much longer periods of time.

Focus variation microscopy

In concept, focus variation (FV) microscopy uses limited depth of field optics to scan vertically through a measurement depth, acquiring images at regular steps through a scanning process [46]. Figure 1.10 shows the general setup of an FV system.

The method by which FV systems operate is as follows. A light source is directed at the sample, and the light is reflected from the surface. Reflected light passes through optics that provide a limited depth of field, so that much of the image will be out of focus. This image is captured using a CCD detector. The image is then passed into a computer, which computes the local contrast for each pixel in the image. As the depth of field is shallow, the surface is determined by the positions in the image where the local contrast is at a maximum. The whole FV instrument is then moved by a step along the z axis, and the process repeated. By repeating this process for each image acquired, a measured surface can be built up, providing a complete height map of the surface.
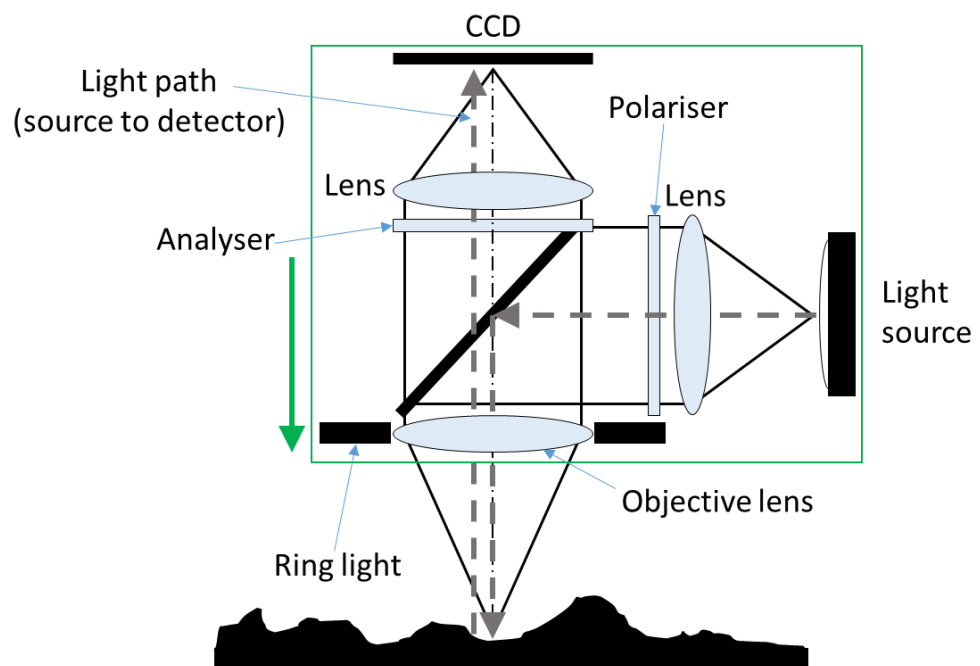
Figure 1.10. Schematic representation of a focus variation microscope [46].

As with CSI, FV systems employ white light illumination, but as FV systems can use both specular and diffuse reflections from the surface, they can also employ a number of different lighting setups, depending on the specific measurement case. This is possible in FV systems because of the reliance on contrast in the data; the user is provided with many measurement setup options to maximise this contrast. Particularly, light can be delivered to the surface via two methods of illumination: coaxial (i.e. via the microscope optics), and from a ring light (i.e. from the area surrounding the objective lens). A polariser is also available for the coaxial illumination, which is generally used when measuring more reflective samples [46].

In general for current commercial systems, FV is particularly useful for the measurement of rough surfaces and surfaces with high slope angles, as the system is capable of using diffuse reflection to avoid the limitation of the numerical aperture of the objective lens (see equation 1.1). Focus variation systems also intrinsically provide colour information, which allows for additional features to be characterised that may not be identifiable in height map data (e.g. surface oxidation). FV systems are not capable of measuring smooth surfaces (e.g. optical lenses and mirrors), as the local contrast required for these systems to determine the position of the surface is not present in such cases. At present, FV systems require surfaces to have an Sa of at least 15 nm at $\lambda c = 2 \ \mu m$ (see Section 1.2.2.2) in order for measurement to be possible [46]. FV systems are also not capable of measuring transparent and translucent materials (again as local contrast is not detectable), but successful measurements of both smooth and non-opaque materials are possible using surface replicates [46].

1.2.2.2 Surface characterisation

Surfaces can be characterised in numerous different ways using data acquired using surface measuring instruments [30]. Data are generally reduced to some scalar parameter or set of scalar parameters, and specifications are applied to parts based on conformation of a surface to a single parameter. Generally

speaking, raw data of sufficient sample size (as defined in ISO 4287 [50] for profile and ISO 25178-2 [51] for areal) have the underlying form removed and are filtered to create conditions that allow for the generation of parameters in such a way that the generated parameters are comparable to those generated for some other surface.
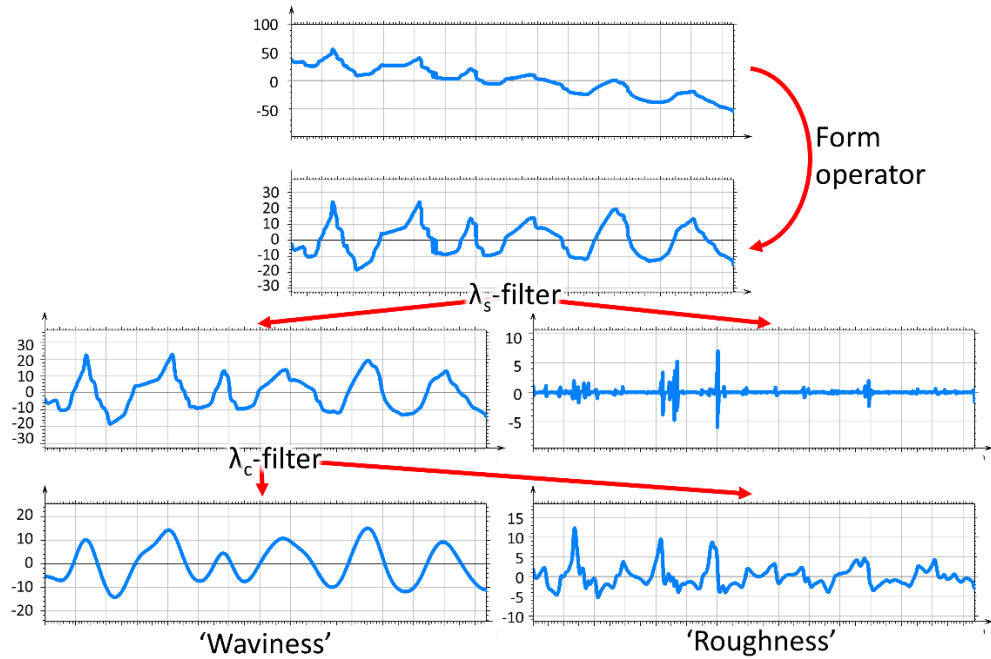
Figure 1.11. Schematic representation of the form removal and filtering process, commonly employed during surface measurement.

The form removal and filtering process is described diagrammatically in figure 1.11, and essentially involves three (or sometimes four) key steps [52]. The first step involves a form removal operation, employed to account for the fact that it is not possible to make a sample perfectly level prior to measurement. Second, a spatial frequency filter is applied to remove noise and high frequency information, known as a 'λs filter' for profiles or an 'S-filter' for surfaces. Thirdly, a second spatial frequency filter is applied, known as a 'λc filter' for profiles or an 'L-filter for' surfaces. The purpose of the λc/L-filter is to separate features on the surface from one another by scale. Broadly, features are separated into 'roughness' features (i.e. features with spatial wavelengths smaller than the λc/L-filter cut-off length), and 'waviness' features (i.e. features with spatial wavelengths larger than this cut-off length). Where these larger

features are of interest, an additional step is performed: a third filter is applied to differentiate between these mid-scale components and features relating to the underlying form. This filter is known as the 'λf filter' for profiles, or the F-operator for surfaces. In both cases, this operation is performed following the form removal operation. Filters, as described here, are most commonly Gaussian convolution filters, using 50 % cut-offs at the specified spatial frequency values (i.e. 50 % of the spatial frequencies are removed at the value). The way that surface features are separated into roughness and waviness components by the spatial frequency filtration process is shown in figure 1.12.
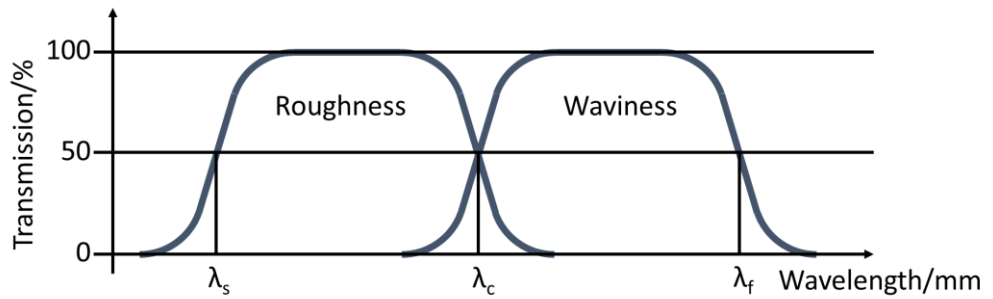
Figure 1.12. Separation of surface features using spatial frequency filters [52].

Once filtering has been performed, summative parameters representative of the surface can be generated. There are many parameters described by ISO 4287 [50] (profile) and ISO 25178-2 [51] (areal), designed for as many different scenarios. A number of these parameters are in more common usage than others. The leader of these common parameters by far, across all fields of manufacturing, is *Ra* [9], the arithmetical mean deviation of the assessed profile is given by

$$Ra = \frac{1}{l}\int_0^l |z(x)|dx,\qquad\qquad 1.3$$

where *z(x)* is the height of the assessed profile at any position *x* and *l* is the sampling length (i.e. the length in the direction of the *x* axis used for identifying the irregularities that characterise the profile under evaluation [53]) [50]. When a profile is measured across a manufacturing process tool mark (i.e. the 'lay')

using the default evaluation length (i.e. the total length in the *x* axis used for the assessment of the profile under evaluation [53], generally equivalent to five sampling lengths) and then filtered using the default settings (both as defined by ISO 4287 [50]), the resulting *Ra* value has been used to compare surfaces in a plethora of scenarios for many different manufacturing processes. However, *Ra*, and its areal surface allegory, *Sa*, represent one aspect of the surface and are often not useful in isolation [30]. It is for this purpose that many other methods of surface characterisation have been developed. For example, there are many more field parameters beyond a simple *Ra*/*Sa* that provide other information, such as the proportion of material above or below the mean line/plane (skewness), or the 'spikiness' of a profile/areal surface (kurtosis) [52]. Beyond these amplitude parameters, field parameters have been developed to characterise spatial information (i.e. parameters defined from all the points on a scale-limited surface [51]), functional information, and feature parameters have been designed to algorithmically segment out and characterise features on a surface (i.e. parameters defined from a subset of predefined topographic features from the scale-limited surface [51,52]).

Common parameters

Throughout my PhD I performed various comparisons of surface data acquired using different measuring instruments (see Chapters 5 to 8). As part of these comparisons, I generally began by examining a set of common ISO 25178-2 [51] areal parameters. In each case, parameters were chosen specifically because they are commonly used for analysing surfaces, based on the review published by Townsend et al. [9] near the beginning of my PhD. Generally, I use these parameters to demonstrate how instruments can provide statistically different results for the same measured surface, and to illustrate how discrepancies between instruments can be studied by using other surface characterisation methods. However, it is important to discuss the specific parameters used in these Chapters, so I will define the parameters used through this Thesis here. All definitions are taken from ISO 24178-2 [51], and explanations made in reference to [48].

Sa, the arithmetic mean height of the scale limited surface, i.e. the arithmetical mean of the absolute of the ordinate values within a definition area (*A*). Where *z(x,y)* is the height of the assessed profile at any position *x,y*, *Sa* is given by

$$Sa = \frac{1}{A} \iint_A |z(x,y)| \, dx \, dy. \qquad 1.4$$

Sq, the root mean square height of the scale-limited surface, i.e the root mean square value of the ordinate values within a definition area (*A*) is given by

$$Sq = \sqrt{\frac{1}{A} \iint_A |z^2(x,y)| \, dx \, dy}. \qquad 1.5$$

Ssk, the skewness of the scale-limited surface, i.e. the quotient of the mean cube value of the ordinate values and the cube of *Sq* within a definition area (*A*). *Ssk* describes the shape of the topography height distribution and measures profile symmetry about the mean plane, so is negative when the bulk of material is above the mean plane and positive when the bulk is below the mean plane. *Ssk* is given by

$$Ssk = \frac{1}{Sq^3} \left[\frac{1}{A} \iint_A |z^3(x,y)| \, dx \, dy \right]. \qquad 1.6$$

Sku, the kurtosis of the scale-limited surface, i.e. the quotient of the mean quartic value of the ordinate values and the fourth power of *Sq* within a definition area (*A*). *Ssk* is a measure of the sharpness, or 'spikiness' of the surface height distribution, and is given by

$$Sku = \frac{1}{Sq^4} \left[\frac{1}{A} \iint_A |z^4(x,y)| \, dx \, dy \right]. \qquad 1.7$$

Sdr, developed interfacial area ratio of the scale-limited surface, i.e. the ratio of the increment of the interfacial area of the scale-limited surface within the definition area (A) over the definition area. This is essentially the ratio between the actual area of the surface and the projected area on the *xy* plane. *Sdr* is given by

$$Sdr = \frac{1}{A}\left[\iint_A \left(\sqrt{\left[1 + \left(\frac{\partial z(x,y)}{\partial x}\right)^2 + \left(\frac{\partial z(x,y)}{\partial y}\right)^2\right]} - 1\right) dx\, dy\right]. \qquad 1.8$$

Sal, the autocorrelation length, i.e. the horizontal distance of the autocorrelation function, $f_{ACF}(t_x, t_x)$, which has the fastest decay to a specified value s, with $0 \leq s < 1$. By default, $s = 0.2$ in this Thesis and in all practical applications. When *Sal* is large, a surface is dominated by low spatial frequency components, and the converse is true when *Sal* is small. The autocorrelation function is given by

$$f_{ACF}(t_x, t_y) = \frac{\iint_A z(x,y)z(x - t_x, y - t_y)\, dx\, dy}{\iint_A z(x,y)z(x,y)\, dx\, dy}, \qquad 1.9$$

where *z(x-t$_x$,y-t$_y$)* is the height of the assessed profile at the translated position *x-t$_x$,y-t$_y$*. *Sal* is then given by

$$Sal = \min_{t_x, t_y \in R} \sqrt{t_x^2 + t_y^2}, \text{ where } R = \{(t_x, t_y): f_{ACF}(t_x, t_y) \leq s\}. \quad 1.10$$

Sdq, the root mean square gradient of the scale-limited surface, i.e. the root mean square of the surface gradient within the definition area (*A*) of a scale-limited surface. *Sdq* is given by

$$Sdq = \sqrt{\frac{1}{A}\iint_A \left[\left(\frac{\partial z(x,y)}{\partial x}\right)^2 + \left(\frac{\partial z(x,y)}{\partial y}\right)^2\right] dx\, dy}. \qquad 1.11$$

Std, the texture direction of the scale-limited surface, i.e. the angle, with respect to a specified direction, θ, of the absolute maximum value of the angular spectrum. The angular spectrum is given by

$$f_{APS}(s) = \int\int_{R_1}^{R_2} r|F[r\sin(s-\theta)\,r\cos(s-\theta)]|^2\,dr, \qquad 1.12$$

where R_1 to R_2 is the range of integration in the radial direction and s is the specified direction. *Std* represents the lay of the surface texture. For surface data presented in this Thesis, $Std = 0°$ when the texture direction is parallel the x axis.

Str, the texture aspect ratio, i.e. the ratio of the horizontal distance of the $f_{ACF}(t_x, t_x)$ which has the fastest decay to a specified value s to the horizontal distance of the $f_{ACF}(t_x, t_x)$ which has the slowest decay to s, with $0 \le s < 1$. *Str* is given by

$$Str = \frac{\min\limits_{t_x,t_y \in R} \sqrt{t_x^2 + t_y^2}}{\max\limits_{t_x,t_y \in Q} \sqrt{t_x^2 + t_y^2}}, \text{ where } \begin{array}{l} R = \{(t_x, t_y): f_{ACF}(t_x, t_y) \le s\} \\ Q = \{(t_x, t_y): f_{ACF}(t_x, t_y) \ge s \,\&\, *\} \end{array} \qquad 1.13$$

where * is the property that the $f_{ACF} \ge s$ on the straight line connecting the point (t_x, t_y) to the origin.

The list of surface characterisation methods is the subject of many journal papers and books (with an overview provided in [52]), so I will not continue further than what has been discussed in this Section. However, characterisation methods form a significant aspect of this Thesis, and will be discussed at length in Chapters 4 to 9.

1.2.3   Volumetric metrology basics

For the purposes of this Thesis, I define 'volumetric metrology' as the measurement of a part holistically, measuring an entire part in a single step. At present, a number of techniques are used for non-destructive testing that are capable of measuring a volume (e.g. eddy currents, ultrasonic arrays; see reviews of these technique in [54,55]). However, at present the only method of volume measurement that is capable of providing accuracy is by using X-ray rays, specifically using an X-ray computed tomography CMS [56]. X-ray computed tomography (XCT) is a method of forming three-dimensional (3D) representations of an object by taking many X-ray images around an axis of rotation and using these images to reconstruct a 3D model [57,58]. XCT is well established in medicine, but its use in the industry is more recent.

In an industrial setting, the primary aim of performing XCT scans differs greatly from the requirements of the medical field. In most of the cases, industrial XCT scanning is not so concerned with X-ray dosage to the sample as it would be in medicine, and while fast scans are certainly an advantage, the requirement for ultra-fast scan times (to account for patient movement) is not yet present in an industrial setting. Work is currently being performed to apply fast XCT to industry (i.e. for use in process) using shorter scans (a few seconds to minutes) and faster reconstruction algorithms (e.g. iterative approaches), but this research is at an earlier stage of technological readiness because of the image quality loss that comes with increased speed [59]. Industrial XCT is, therefore, capable of using higher intensity X-ray sources, and of increasing scan times to long periods when useful to achieve high precision in scans. Industrial XCT is mostly used for materials characterization, non-destructive testing and metrology applications and so the focus is generally geared more towards achieving the maximum possible scan resolution, accuracy and precision [57,58]. Further industrial XCT applications also exist in areas such as in the examination of fibre reinforced composites [60].

As opposed to common XCT systems seen in medical applications, where the

scanning apparatus is rotated around the patient, in most industrial systems the scanning apparatus is fixed and the sample rotated. This design allows for the construction of XCT systems with higher accuracy and stability than used in medicine, features that are crucial to the applications for which they are produced [57]. Another major difference between the clinical and industrial type scanners is the input parameters. Parameters differ significantly because the material being scanned (human tissue in medicine, mainly metals and polymers in industry), as well as the desired output and the size of the object being scanned, differ greatly between applications [58]. Most industrial XCT scanners are based on the 'third generation' XCT scanner design (see [2]). These systems are then split into two categories, each using a fan or cone beam of X-rays respectively; dependent on the specific application of the scanner (see Sections 1.2.3.1 and 1.2.3.2).

Compared to medical systems, a number of other additions and modifications are made particularly in the case of metrology XCT systems, designed in reference to touch-probe CMSs. For example, metrological XCT systems commonly have high precision mechanical setups for modifying the relative positions of sample, detector and source, as well as thermally stable structures in their construction [58]. These systems also commonly contain high precision temperature stabilising cooling devices, and are kept in temperature-controlled laboratories.

1.2.3.1 Industrial fan beam CT scanners

In terms of their setup, fan beam CT scanners are essentially the same as third generation scanners [2], except for the previously-stated difference of rotating the sample as opposed to the scanning gantry. Figure 1.13 shows a fan beam setup schematically. As with conventional third generation scanners, the X-ray source outputs a pseudo-2D fan of X-rays, which pass through the object being scanned and onto a detector. The detectors used in industrial XCT commonly utilise scintillators with modern CCDs, and may be curved or straight, line or flat panel in construction [61]. Fan beam systems can acquire slice data in either

a helical or step-wise manner, and are, therefore, much slower than the cone beam scanner type, when used to produce a full 3D reconstruction of the object being measured. Fan beam scanning, however, does not suffer from some of the imaging artefacts that cone beam XCT experiences, and so is capable of producing scan data of higher accuracy than the cone beam counterpart, especially in case of high-energy sources [61]. This makes fan beam scanning a useful option in dimensional metrology, where dimensional accuracy is important. Fan beam scanners are occasionally used in material analysis applications, when higher X-ray energies and precision are required.
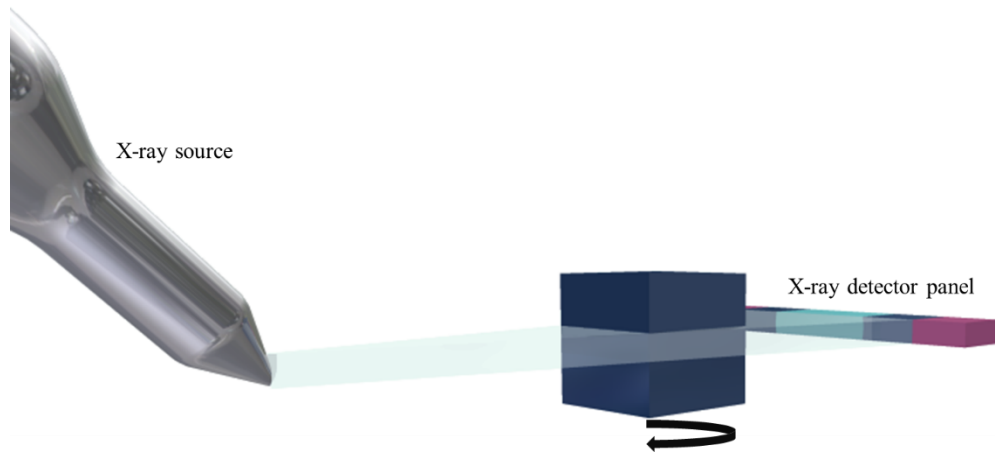
Figure 1.13. Schematic diagram of a fan beam scanning setup, operating similarly to a conventional third generation scanner. Note how the sample rotates while the scanning gantry remains stationary. Figure published in [56].

1.2.3.2 Industrial cone beam CT scanners

Unlike in the fan beam setup, cone beam XCT scanners are capable of acquiring 3D volumetric data in a single rotation. Cone beam scanners utilise a 3D cone of X-rays to scan an entire object in one go, and so represent a very fast acquisition compared to fan beam systems. Similarly to the fan beam scanners, these systems operate by rotating the object being scanned between a stationary source and detector. For applications where the object being scanned is larger than the field of view, it is possible to move the object through the X-ray beam in either a step-wise or helical cone beam manner [58]. Figure 1.14 shows the cone beam scanner geometry schematically.

Compared to fan beam, cone beam XCT is subject to a number of additional Feldkamp imaging artefacts due to unavoidable flaws in the design of cone beam systems [56]. As such, cone beam scans will typically be of lower quality than scans taken by fan beam systems. Cone beam XCT is, therefore, less commonly used when large parts and/or difficult-to-penetrate materials are scanned using high-energy X-rays. In such cases, the use of cone beam CT would result in substantial imaging artefacts and, therefore, inaccurate results [57]. In these situations, fan beam scans are preferred, though in general, for relatively small parts that have low X-ray absorption, a majority of applications today use cone-beam scanning for the speed advantages offered by the technology.
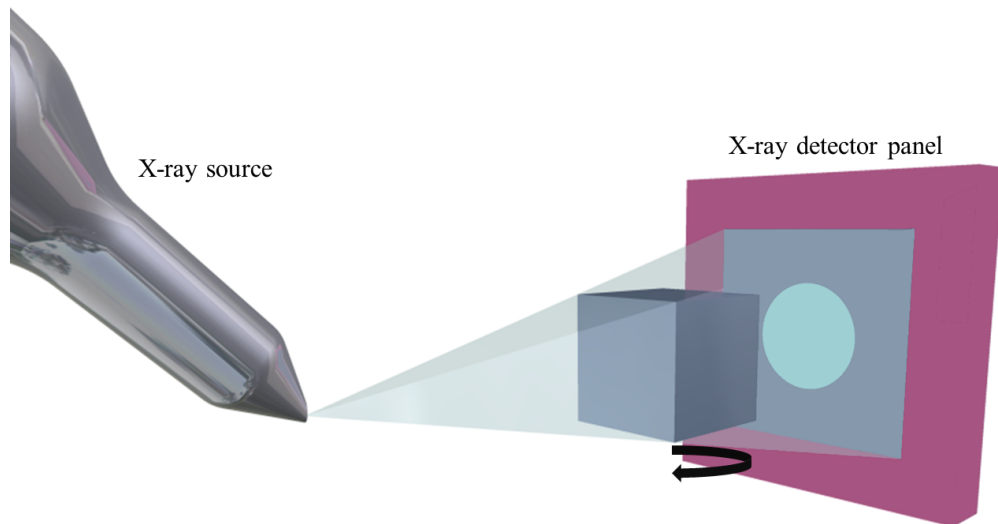
Figure 1.14. Schematic diagram of a cone beam scan setup, showing how these systems acquire 3D volumetric data in a single rotation. Figure published in [56].

1.2.3.3 The XCT measurement pipeline

Throughout this Thesis, I refer to the XCT measurement 'pipeline'. What is meant by this is the general series of processes required to generate a 3D model on which measurements can be performed. For clarity, I will outline the steps of the pipeline here, and then elaborate on some of the individual stages of the pipeline. The first step is to perform a scan using a system, producing a series of raw X-ray projections. These data are then reconstructed into a 3D image that

a surface determination algorithm can be performed upon, to create a 3D model on which measurements can be made. The pipeline is represented in figure 1.15.
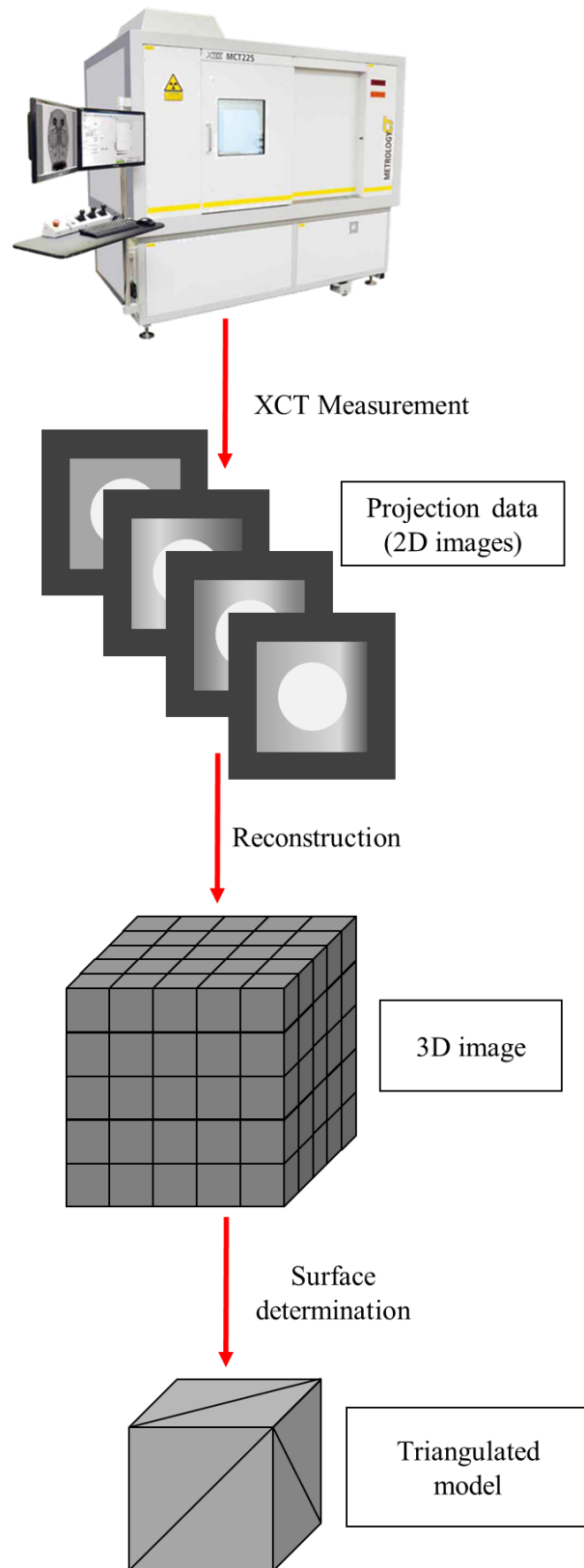
Figure 1.15. The XCT measurement pipeline

XCT Measurement

Early X-ray detection utilised scintillation detectors with photomultiplier tubes, while more recent technological advances allow the use of element-based CCDs for detection [62]. It should also be noted that when performing XCT measurements, the quality of the image (i.e. the resolution and contrast of the image) is the primary concern. In relation to the image quality, there are always trade-offs that should be considered when performing XCT measurements. Because of the nature of XCT and the reliance on X-ray penetration of the scanned object (or field of view), an increase in the size of the object being measured has the associated effect of decreasing the resolution of the image by reducing the maximum possible magnification of the scan. Reducing the magnification therefore increases the size of the scan voxels and so decreases the image quality. High density materials are also more difficult to measure than low density materials due to higher X-ray absorption, and so object size is also limited by the material density as in order to achieve a reliable contrast, longer exposure times must be used. It is therefore often the case that in XCT scanning, in order to improve the image quality, a small piece of the scanned object, or a reference coupon with similar properties to the object, is measured in place of the whole object. It is possible to improve scan quality in this manner, but this method carries the disadvantage that the actual object of interest is not the object that is scanned, and so results can be skewed.

XCT scans require the setup of a number of parameters. In practice, there are hundreds of minor parameters that can be tuned to alter the result, but those logged in this Thesis are those that can be considered to have the greatest effect on the outputted data, based on previous findings presented by the community [57,58]. These parameters presented in Table 1.1, alongside descriptions of broadly what that parameter pertains to, and how it affects the measurement [56]. In general in this Thesis, all measurements were set up in such a way that image resolution was limited by detector pixel size as opposed to the focal spot, in order to neglect the influence of the focal spot size on measurement data [63].

Table 1.1. Relevant XCT measurement setup parameters

Setup Parameter	Description
Geometric magnification	The ratio between the X-ray source-to-detector distance and the X-ray source-to-object distance. Determines voxel size (generally, voxel size is pixel size in millimetres divided by the magnification).
Projection settings	Includes number of projections, the number of frames used to create a single projection and the amount of time per frame. Determines scan time and affects image brightness and contrast.
X-ray voltage	Peak voltage of electrons used to generate X-rays. Affects image contrast and brightness.
X-ray current	Average current of electrons used to generate X-rays. Affects image brightness, and to a lesser extent, contrast.
X-ray pre-filter	Hardware filter made from a highly X-ray attenuating material, used to remove low energy X-rays from the outputted spectrum, with the aim of creating a pseudo-monochromatic X-ray spectrum. Affects image brightness and contrast, reduces beam-hardening artefacts [64] in reconstructed data.
Shading correction settings	Includes the number of light and dark frames used to create the shading correction. Compensates for irregularities in the X-ray detector – longer corrections compensate better but heavily impact measurement setup time.
Flux normalisation	Toggled on/off to automatically homogenise background brightness in XCT images. Affects image brightness and can reduce reconstruction artefacts [65].

XCT reconstruction

Once data has been collected using one of the methods outlined above, the data are processed by a computer system that performs a reconstruction using the acquired X-ray intensity readings for each of the detector elements. These intensity readings result from the summation of individual linear attenuation coefficients along a vector through the measured object from the X-ray source to the detector element. Using these values, the computer builds up individual slice images, which can then be stacked into a 3D reconstruction [62].

In this work, the Feldkamp-Davis-Kress practical cone beam algorithm [66] was used for reconstruction, broadly accepted by the XCT community as the most robust algorithm for performing metrology [57,58]. This algorithm is an implementation of the filtered backprojection algorithm [67]. Filtered backprojection is, in turn, based upon Fourier slice theorem, which is well covered elsewhere [67]. I will provide a brief description of both Fourier slice theorem and filtered backprojection here.

In Fourier slice theorem, an object's cross-section is considered as a 2D function $f(x,y)$ and the measured X-ray attenuation at the detector is considered to be a line integral dependant on the object function, denoted as $P(\theta,t)$. For the function $P(\theta,t)$, θ is the projection angle and t is the position on the detector. This function is specifically termed the Radon transform of $f(x,y)$, owing to its mathematical discovery by Johann Radon in 1917 [68]. $S(\omega)$ is the 1D Fourier transform of the projection function, equivalent to a radial line of the Fourier transform of the object, in turn denoted as $F(u,v)$. This concept is illustrated in figure 1.16 [67,69].

Fourier slice theorem allows the reconstruction of a 2D slice from a series of projections acquired at angles around the object. However, two issues present in the Fourier slice theorem become apparent when the theorem is implemented practically. The first issue relates to practical implementation of the theorem, in that such an implementation requires finite sampling of the function $f(x,y)$ along

radial lines. In order to use the result, an interpolation of the points onto a square grid is necessary. However, the interpolation process causes image degradation when implemented, because of the decreasing sampling frequency that occurs as we move radially outward from the origin in the Fourier domain. As such, interpolation errors affect high spatial frequency components more than low frequency components. This problem is solved by summing over projections in the spatial (as opposed to Fourier) domain, as spatial domain interpolation provides better results than Fourier domain interpolation [67,69]. Performing this summation in the spatial domain is termed 'backprojection'.
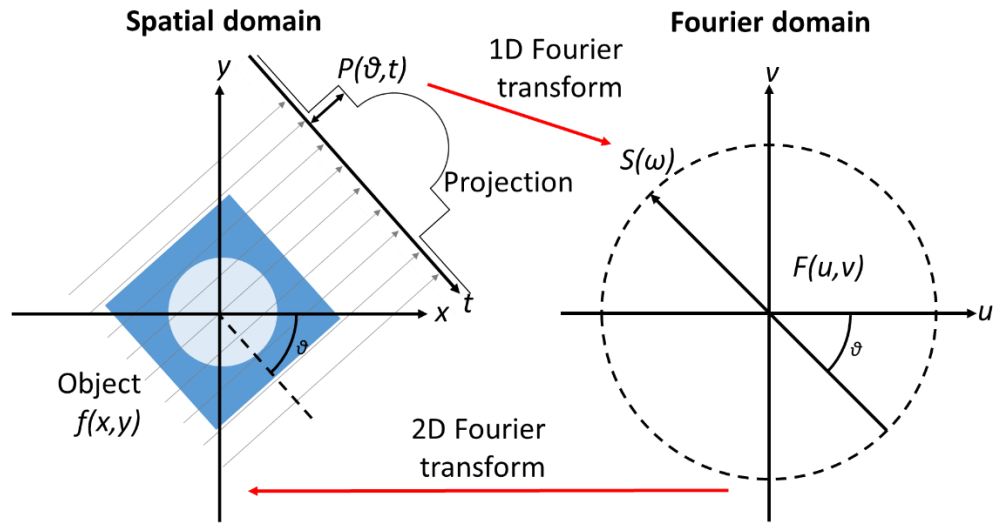
Figure 1.16. The illustrated Fourier slice theorem for a parallel projection

The second problem with the practical implementation of the Fourier slice theorem is that if a simple summation of terms is performed over the interpolated square grid, components towards the centre of the image are artificially enhanced, while components near the edge of the image are supressed. This problem is overcome through the use of a weighting function (or 'filter'), that multiplies higher spatial frequencies by a relatively low value and lower spatial frequencies by a relatively high value [67,69]. This filter usually takes the form of a simple 'ramp' function, but other filters are used that have other functions (e.g. Hanning filters for noise reduction) [70].

As with XCT measurement, a great many parameters affect the reconstruction process, through the application of a plethora of corrections and filters. For this work, however, such correction and filtering was kept to a minimum, and improvement of data quality was performed through optimisation of the scan settings as opposed to by applying corrections at a later stage. The settings applied during reconstructions performed as part of this work are summarised in Table 1.2

Table 1.2. Relevant XCT reconstruction setup parameters.

Setup Parameter	Description
Rotation centre calculation	Applied to all reconstructions to compensate for inaccuracies in the physical setup of the scanner, to determine the true centre of rotation for the individual scan.
Beam hardening correction	Applied to correct for any residual beam hardening artefacts [64] not removed by application of a hardware filter.
Reconstruction resolution	The resolution of the volumetric reconstruction grid. Determines sampling in the reconstruction volume (see Chapter 8).

XCT surface determination

In order to perform measurements on a reconstructed XCT volume, the data must first be converted from a 3D image to 3D model (point cloud or triangulated). To perform this conversion, a surface determination algorithm is applied to the data, and a surface is created using the information present in the image. The most basic surface determination is a simple thresholding, in which a 'grey value' (i.e. the integer value taken by each voxel on a scale of 'black' to 'white') is determined to represent the surface, so any value greater than this value it considered 'material', while any value lower than this value is considered to be 'background' [71]. In modern systems, these grey values are 16 bit integers, so take values from 0 to 65535. The choice made for what this

value takes can be manual (i.e. arbitary) or automatic. The most common automatic method involves examining the histogram of grey values for the whole dataset, and automatically finding the peaks for the material and background, and then defining the threshold value as the grey value at the midpoint between the grey values for these two peaks. This is referred to as the ISO-50 method [57] of surface determination (see figure 1.17).
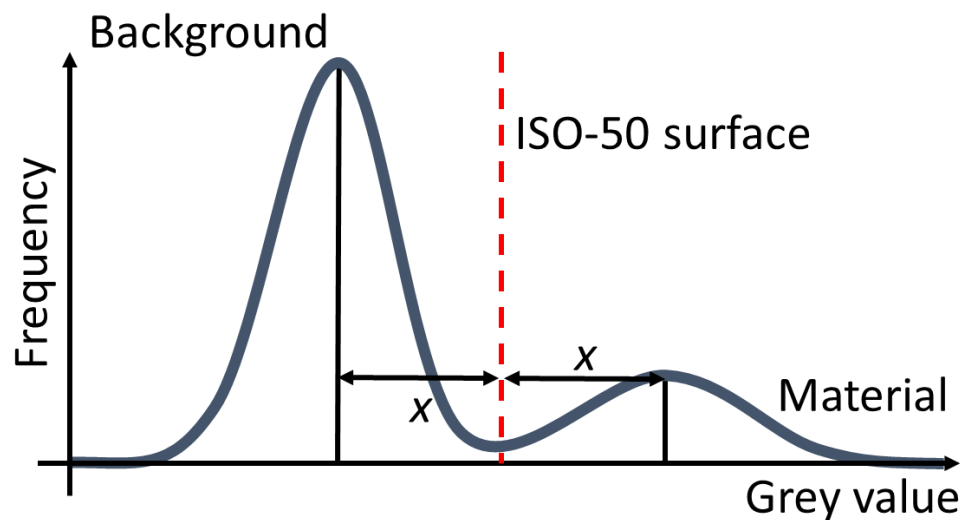
Figure 1.17. ISO-50 surface determination

While this simple method allows a surface to be defined automatically, comparative studies have found that errors can be induced by the ISO-50 method, in that the determined surface is often shifted with respect to the real surface [57]. As such, a number of advanced surface determination algorithms exist, the most common of which involves a gradient-based method initially described by Canny [72]. In this method, a starter surface is used (e.g. the ISO-50 surface), and the grey values either side of the surface are measured along a line normal to the surface, extending a defined number of voxels from the surface (i.e. the 'search distance'). By the convention established in the community, this is most commonly four voxels [57]. These values are plotted and interpolated to form an intensity profile, and the intensity profile is differentiated. The position of the peak of the derivative is then logged as the position of the surface along that line [69]. This process is generally performed at a resolution higher than the voxel size, providing sub-voxel precision for the

determined surface. Figure 1.18 explains this process visually for a 2D example. The most common implementation of this algorithm is that employed by VGStudio MAX [73], which is the algorithm used most often by the XCT community for metrological purposes [57]. However, the exact algorithm employed in VGStudio Max is proprietary, and so surface determination represents an open area of research. The VGStudio MAX algorithm also optionally adds an iterative function, which (presumably) iteratively repeats the gradient search using different search distances and/or start points if the search over the initially defined number of voxels fails to meet some (unknown) acceptance criteria. Throughout this Thesis, the gradient-based method has been used, but the advantages and disadvantages of doing so are also discussed (see Chapters 6 to 9).
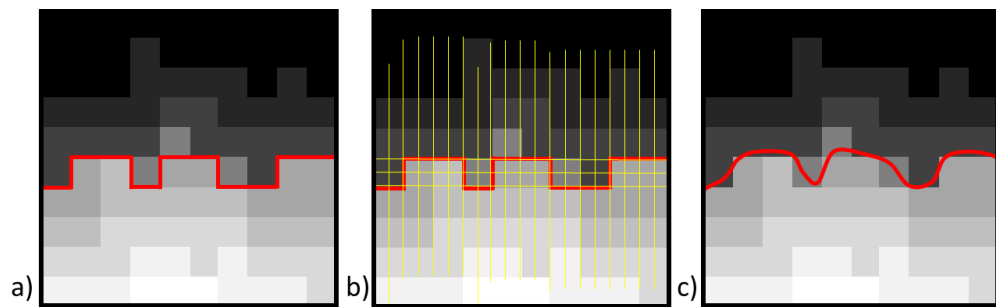
Figure 1.18. Schematic representation of the gradient based surface determination algorithm: a) the ISO-50 surface; b) ISO-50 surface with 'search lines' extending for four voxels in the directions normal to the surface at a frequency 3× that of the pixel size; c) the gradient-based determined surface.

1.3 Metrology for AM

Due to the increased freedom of design offered by AM processes, complex and intricate geometries can be manufactured in a near net-shape fashion. Whereas previously, a series of simpler shapes manufactured conventionally by machining, forming, or casting would have had to have been assembled, the freedom of design afforded by AM allows the designer to simultaneously engineer both shape and structure at the part level. Historically, however, AM technologies have not been capable of achieving the design requirements of many function-critical parts, often failing in their ability to attain the desired

structural integrity, mechanical properties or geometric accuracy required by the designer, in comparison to the properties expected from a conventionally manufactured counterpart [17,74–76].

Although industrial adoption of AM is increasing (particularly regarding the production of polymer parts), in order for AM to be further adopted as a method of advanced manufacture, capable of producing high-value goods, the future of the technology must lie in the manufacture of metallic and ceramic components. Owing to the unique advantages offered by AM (in particular, achieving geometric complexity without assembly), the aerospace, medical and other industries are now becoming aware of the potentially tremendous impact of AM in these fields. An economic and technological race has begun worldwide, in order to bridge the remaining technological gaps barring increased adoption of AM [77]. A number of major barriers to adoption exist, particularly including the need for improvement of geometric accuracy and precision (dimensional, form and surface) [14], the need for improvement of structural and mechanical properties, the need for broadening the range of available materials and the need for a broadening of the range of scales of manufacturable goods (i.e. a reduction in the current limitations relating to production of very small and very large parts).

During the design of manufactured components, it is important to define tolerances for each feature in order to ensure that the part conforms to specifications (e.g. using the geometrical product specification defined by the ISO [78]). In manufacturing, a tolerance is defined as the "difference between the upper and lower tolerance limits", where tolerance limits are "specified values of the characteristic giving upper and/or lower bounds of the permissible value" [79]. In order to verify that a feature on a manufactured component is within the defined tolerance, some form of measurement is needed. As discussed, AM provides freedom of design that is generally infeasible by other manufacturing methods, particularly regarding the creation of complex internal features that are inaccessible to well-established measurement tools. AM parts require verification as do those produced by any other manufacturing process,

and as such X-ray computed tomography (XCT) is currently the best method of measurement for these internal features, due to the volumetric nature of the XCT process. XCT is, however, not yet as firmly established as a measurement tool compared to other methods of dimensional metrology, and so research regarding various aspects of the technology is still required to enable XCT to become an industrially relevant technology [80]. However, as AM and XCT have recently become more viable as methods of production and measurement, and partner so well because of their respective advantages, I will document instances over time of their combined use here.

1.3.1   Volumetric metrology for AM

XCT and AM were first jointly used in a medical context, to reverse engineer a model of a skull in 1990 [81]. Since this first use, there have been many developments in medicine using XCT and AM to produce increasingly complex models as well as implants for animal and human patients. In this Section I will focus on the industrial use of XCT and AM and so details of medical use will not be examined. A review of XCT and AM in medical modelling can be found in reference [82].

1.3.1.1 History pre-1995

The very early use of AM and XCT was in a medical modelling context, and as such, although an increasing array of studies involving the reverse engineering of organs were published, very little AM and XCT was performed in a non-medical engineering context. Ashley's editorial in the popular *Mechanical Engineering* magazine [83] allows insight into the use of XCT in AM at the time; outlining processes and discussing the then recent papers. The editorial mentioned the potential use of AM parts as implants and prostheses, as well as in surgical planning, indicating the direction that technologies were moving at the time.

1.3.1.2 History 1995 to 2005

Throughout the early 1990s, the use of AM and XCT increased rapidly, resulting in a plethora of published research featuring an increasing array of AM and XCT technologies. Whilst remaining primarily a method of reverse engineering for medical modelling, the technologies began to expand during these years as XCT measurement and AM resolutions improved. As such, studies involving the use of XCT as an inspection tool for manufactured parts began to be published. The first example of a quantitative measurement of an XCT/AM part was performed in 1997, in a paper by Berry et al. [84] that compared measurements performed on SLS models to measurements performed on the source XCT data. The authors concluded that models were in good dimensional agreement (±0.5 mm) with the XCT source data. It should be noted, however, that initial builds showed a part much larger than expected due to an error in communication that the authors did not explain, which was accounted for by scaling of the measured values; a method which cannot be seen as an accurate comparison of measurements. It was clear from this study that the selective laser sintering (SLS) technology (see [18]) represented a viable method of production of accurate orthopaedic models. During the latter half of the 1990s, the first industrially-focussed papers were published, improving AM technology and examining case studies of the first industrial end-use parts. For example, in 1995 Jamieson and Hacker [85] investigated sliced contours as an input to AM machines in comparison to STL files, noting that production of these files is possible directly from XCT data. The authors concluded that direct sliced CAD models are often preferable for additive use in manufacture over the STL standard. The first industrial case study [86] used SLS to form sand casts for production of an engine cylinder head. XCT was then used on the cast part to examine porosities produced using the casting process, concluding that this method of porosity examination was useful for rudimentary detection of pores (see figure 1.19).
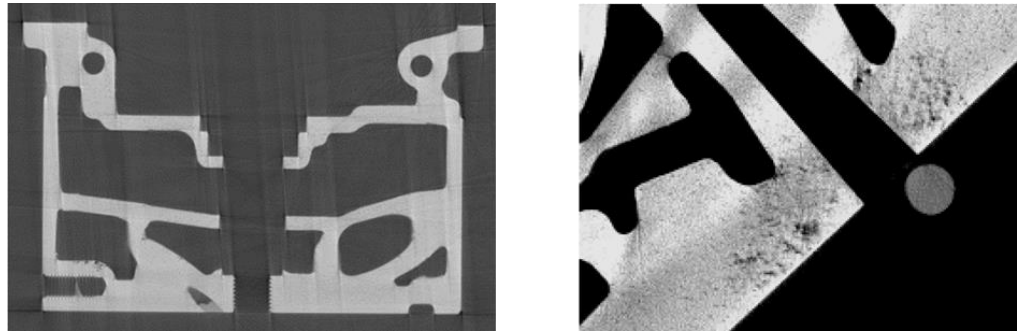
Figure 1.19. Examples of an XCT slice of an aluminium sand cast engine cylinder head and of porosities found when producing parts by this method. The authors note the sharp definition of internal cavities as a result of the relatively high SLS accuracy. Images reproduced from reference [86]. Figure published in [1].

1.3.1.3 History 2005 to 2010

The 2005 to 2010 period showed an increase in the use of XCT for measurement of AM parts, specifically using XCT as a pore measurement tool. During this time, authors began to measure overall porosity through calculation of the ratio of the number of voxels representing pores to the number voxels representing solid material in an XCT scan [87], as well as performing dimensional measurements of individual pores using the method presented by Hildebrand and Rüsegger in 1997 [88]. Hildebrand and Rüsegger detailed a method of depicting complex spatial structures (i.e. pores) through distance transformations, using XCT data. Regarding overall porosity measurement, examples of this use can be found elsewhere [89–97] for a variety of AM purposes, such as: assessment of osseointegration potential, AM process comparisons, CAD/as-built comparisons, and general characterisation of tissue scaffolds and similar porous structures. The authors of references [89–97] also commonly performed more established characterisation methods such as scanning electron microscope (SEM) imaging and mechanical testing in conjunction with XCT porosity measurements, adding the XCT as a complementary technique. The 2008 paper by Heinl [90] also represents an example of the use of the aforementioned Hildebrand and Rüsegger method of pore diameter measurement [88]. In the 2010 paper by Kerckhofs et al. [97], the authors provide further novel use of XCT data alongside mechanical

performance data to map strain at different loads in porous Ti-6Al-4V structures, in order to correlate structural and mechanical characteristics.

The current state of the art in XCT metrology for AM (i.e. based upon works produced since 2010) contains a broad volume of published work, and the associated set of current challenges is equally broad. A significant analysis of both the state of the art and the current challenges forms the basis of the review presented in Chapter 2. As such, I will not discuss current challenges in XCT for AM here, but will refer the reader to the following Chapter to gain such an insight.

1.3.2 Surface metrology for AM

Metal AM represents a relatively new tool in the field of advanced manufacturing, beneficial to an array of potential applications, but numerous barriers exist to the technology's increased industrial adoption. Particularly, in relation to the verification of parts produced by metal AM processes, a requirement for further research in accurate, 3D topography measurement has been identified [77,98].

There are currently a number of substantial barriers to increased adoption of AM technologies [32,99]. If a manufacturer wishes to place a part into a commercial aircraft, for example, rigorous verification standards must be met in order to ensure that part's quality. However, when compared to parts produced by conventional means, additive manufacturers encounter issues relating to poor mechanical performance (e.g. fatigue [100], creep [101]), limitations in the pool of available materials, and difficulty in verification of parts [77,98].

Existing part inspection and verification practices are well developed, and work well for conventionally manufactured parts, but AM parts commonly cause additional issues. Conventional verification methods involving co-ordinate measuring systems are often not possible [15], as the geometries commonly

produced by AM processes contain features inaccessible to conventional measurement technologies. In particular, AM parts commonly contain function-critical surfaces that are inaccessible to both contact and optical measurement technologies [102].

As discussed in Section 1.2.2.1, an array of technologies are now available for capturing the three-dimensional (3D) topographic formations on surfaces at micrometric and sub-micrometric scales [21]. Optical technologies, particularly including confocal microscopy [35,36], coherence scanning interferometry [41,42] and focus variation microscopy [45,46], are capable of returning dense point-based samplings of a surface in relatively short measurement times.

Conversely to the historical use of XCT for AM over the past 30 years, at least at the beginning of this PhD there was a very small amount of in-depth research focussing on the application of surface metrology to AM [9].

In order to provide solutions to the aforementioned barriers to adoption of AM technologies, a fundamental issue must first be addressed: the need for a more thorough understanding of each AM process technology (see [76] for a recent review of these issues). Simulation and in-process monitoring of AM processes is non-trivial, as the basic physical interactions of interest are often both very complex and highly numerous. Experiments examining these issues are, however, ongoing in a number of research institutions [25,103]. An improvement in understanding is a necessary condition for optimisation of the manufacturing process, for control of the process during execution, and ultimately for achieving higher quality manufactured goods.

Surface topography investigation is widely recognised as a fundamental tool for improvement of manufacturing processes [104]. Topographic formations, such as localised protrusions, recesses or widespread waviness, are the result of the manufacturing process, that is, they carry the process signature or fingerprint. Qualitative and quantitative assessment of such topographic formations can, therefore, help to shed light on the fabrication process, thus facilitating the

identification of how process and material parameters influence the structural, mechanical and geometrical properties of the manufactured part.

Surface topographies produced by MPBF are highly complex [9,105–108], featuring relevant topographic detail at multiple scales, with a mixture of high and low aspect-ratio formations, high slopes, undercuts and deep recesses. Surfaces also often feature non-uniform optical properties due to local oxidisation effects and the presence of complex micro-scale topographic patterns. MPBF surfaces are typically highly challenging for any type of areal measurement technology, optical or non-optical [32]. Examination of the features present on MPBF surfaces formed a significant part of my PhD research and is presented in this Thesis in Chapters 2 and 4.

1.4 Aims and Objectives

In order to verify manufactured parts, currently available measurement techniques require either direct contact with a measurement instrument, or in the case of optical systems, line-of-sight between the measurement instrument and the measured object. For traditionally manufactured objects, tool access is commonly similarly required, and so many machined features are relatively easily accessible to measuring instruments. However, due to the nature of the layer-by-layer construction methods used in additive manufacture (AM), AM processes are capable of producing parts with complex internal features which were not feasible prior to the advent of AM technology. When the part is fabricated, these internal features often do not have the tool access that more established manufacturing methods require, and so are frequently similarly unmeasurable by traditional measuring instruments.

The internal feature problem was not an issue until recently, as AM was previously used mainly in rapid prototyping applications, where an approximate representation of a design is commonly all that is required from a prototype. However, as AM is now becoming a viable method of end-use part manufacture, internal features produced in AM parts are increasingly subject to stringent

tolerancing principles, and so new metrology must be developed to verify parts that can now feasibly be produced. For example, defects on the surface of a load-bearing component can lead to premature failure of the component, regardless of whether the surfaces of that component are easily accessible or internal. In such a case, a tolerance is likely to be applied to the internal features to ensure the part cannot fail prematurely.

In line with the requirement for new metrology, the overall aim of this PhD project is to develop a new approach to the measurement of the surface texture of internal features using XCT, specifically for the inspection of additively manufactured metal parts. The aim of this project is separated into a number of subordinate objectives, each representing novel contributions to the field:

- Contribution 1: state-of-the-art review of literature regarding the combined use of XCT and AM in industry.
- Contribution 2: production of an 'atlas' of powder bed fusion surfaces, designed to provide a deeper understanding of the types of surfaces that metal AM produces.
- Contribution 3: application of novel methods of directly comparing surface topography data acquired using different measurement technologies.
- Contribution 4: determination of a bespoke pipeline for the measurement of surface texture using XCT, using new methods of extracting surfaces from raw XCT data, which are comparable to surface datasets acquired using established technologies.
- Contribution 5: understanding the sensitivity of XCT systems to surface topography measurement, investigating certain key measurement and data processing parameters that affect topographies extracted from XCT data.
- Contribution 6: application of the newly developed XCT surface measurement procedure to an industrial test case.

1.5 Structure of the Thesis

The remainder of this Thesis is structured so as to reflect the objectives set out in Section 1.4. As such, the Chapters presented here will flow as follows.

The first objective of the project was to determine an appropriate focus within the wide topic of 'Validation of X-ray computed tomography for use in additive manufacture', provided as an initial briefing for this PhD project. As such, an extensive review of the available literature was conducted, examining the use of XCT with AM, identifying the requirement for volumetric dimensional measurements in industrial verification of AM parts. This state-of-the-art review of the use of XCT with AM is presented in Chapter 2.

Following the review process, an appropriate project was determined; examining internal surface texture of additively manufactured parts. A method of measuring internal surface texture by XCT (or indeed, otherwise) had not yet been described, and so new research was required in order to develop such a method. Before attempting to develop a new method of internal surface texture characterisation using XCT however, it was necessary to understand the nature or additive surfaces, which, due to a number of difficulties relating to high slope angles and undercuts, resulting in multiple reflections and shadowing, cannot easily be described by established methods [1]. As such, the first experimental task of this project was to produce an 'atlas' of AM surfaces, by acquiring a comprehensive measurement and analysis library using contact, optical and scanning electron microscopy measurement techniques; as well as initial measurements performed using XCT. The reason for producing this atlas was to gain a deep understanding of the nature of AM surfaces, in order to provide a reference for later evaluation of the surfaces using XCT. As AM surfaces vary greatly between process families, I decided that the atlas should focus initially on the metal laser powder bed fusion process. This work is presented in Chapter 4.

In Chapter 5, I present the direct comparison of topographies acquired using different instruments, as well as of the features contained with those topographies, in addition to the comparison of ISO 25178-2 surface texture parameters. In this study, I compared existing technologies and examined the discrepancies between technologies, including XCT as a method of surface texture measurement.

In Chapter 6, I specifically examine XCT surface measurement in greater depth than in earlier Chapters. In this work, I formalised methods of surface topography extraction from XCT data. Here, I present a comparison of established surface topography characterisation methods between data acquired using two XCT systems, to two of the optical methods was used as a means to establishing this method, and I also present a number of specific issues relating to XCT surface measurement.

Following on from the methods established in Chapter 6, I present an analysis of some of the measurement setup parameters that influence an XCT measurement. I present this work in Chapter 7, where I show how the geometric magnification used, as well as the resolution of the grid used in tomographic reconstruction were varied and the measurement results analysed using developed versions of the direct topography comparison methods presented in Chapter 5.

In Chapter 8, I present the application of the methods developed during my PhD to an industrially representative case study, developed in collaboration with my sponsor company, 3TRPD, who are a major UK-based additive manufacturer. The case study involved the measurement of the surfaces of internal channels in a test part, which was then sectioned to allow comparison of XCT data to data acquired using optical methods.

A summary of the final conclusions of this work, as well as the avenues for future work that stem from these conclusions, is presented in Chapter 9.

2. State-of the-art review

In this Chapter, I present the state-of-the-art review of literature performed throughout this PhD, designed to inform the research conducted through analysis of the state of the art in the field. With the broad initial briefing provided at the beginning of the PhD ('Validation of X-ray computed tomography for use in additive manufacture'), I examined the use of X-ray computed tomography (XCT) in all aspects of AM, and determined key areas where a research niche existed. A summary of the findings presented during this initial phase is presented in Section 2.1; much of this work formed the majority of a review paper published in 2016 [1], though the material presented here has been updated to include work created since the review paper was published. A specific area of research was identified during this period which contained both a niche and a personal interest, and I decided that this would form the primary focus of the PhD. This focus was in the area of XCT for measurement of surfaces in metal additive manufacture (AM), for the purpose of measuring internal and hard-to-access surfaces. As the chosen niche involved surface texture measurement, a review of the state of the art in AM surface texture measurement (in itself, a complex and fledgling research field) has also been included, and this work is presented in Section 2.2.

2.1 X-ray computed tomography for additive manufacture

In Chapter 1, the fundaments of XCT technology were discussed, and historical uses of XCT and AM were outlined from their initial published combined use in 1990 to 2010. Since approximately 2010, both AM and XCT have experienced significant growth commercially and in research, and as such, the volume of publications involving their combined use has greatly increased. In this Section, I present an overview of both the relatively recent historical publications (2010 to 2014) and what can be considered the state of the art in XCT measurement of AM parts (works published since the beginning of this PhD in 2014).

2.1.1 Recent historical uses of XCT with AM (2010 to 2014)

During the 2010 to 2014 period, research regarding uses of XCT and AM shifted focus. While earlier publications predominantly involved manufacturing AM prototypes based on XCT scan data for the purposes of medical modelling [109], more recent publications increasingly focussed on the use of XCT for metrological applications. Particularly, XCT has been used for porosity quantification and measurement of individual pores, as well as direct dimensional measurement of part geometry. As a now well-established technique for measurement of porosity (or conversely density) through comparison of empty to filled voxels [87], XCT was used between 2010 and 2014 by authors covering a wide range of research areas [110,111,120–124,112–119]. Furthermore, some of these authors [111,112,117] compared XCT porosity data to values gained using other methods, most notably the Archimedes method (outlined in reference [112]). These studies generally found that, for metals, the Archimedes method is capable of producing substantially more accurate and precise porosity values than through the use of XCT alone, and that porosity values gained via the Archimedes method were systematically larger than via XCT. Spierings et al. [112] specifically addressed this discrepancy and attributed it to the loss of data from small pores due to the relatively poor resolution of XCT data, noting the effect to be particularly prevalent in highly dense parts. Spierings et al. also compared their findings to scanning electron microscopy (SEM) micrographs, which gave porosity values similar to those gained using the Archimedes method for highly dense parts, but displayed substantially more variation. As a result of these findings, a number of subsequent studies used the Archimedes method as the sole porosity measurement [125,126]. In these papers, the authors concluded that the Archimedes method currently remains the most appropriate method for porosity evaluation of metals, as XCT data is not yet comparably accurate. Although the Archimedes method technically measures density, it is usually possible for metals to translate the obtained density into a porosity value, as the bulk density of the metal is usually well known. It should be noted, however, that in the case of polymer parts, the part density commonly varies depending on the polymer microstructure (i.e. amorphous versus crystalline phases) and so the bulk

density of AM polymers is often not well known as the microstructure depends upon the processing of the part [127,128].

A number of authors during this period also examined the porosity of polymer laser metal powder bed fusion (MPBF) parts using XCT [111,115,122,123]. The results of these studies differed in their findings compared to those examining metal parts, in that the Archimedes measurements used by some of these authors were not found to be as similarly accurate as found in the papers discussed above. For example, Rüsenberg et al. [111] compared Archimedes, XCT and gas pycnometer (i.e. measuring displaced gas) porosity measurements, reporting lower porosities with larger uncertainties from the Archimedes measurements that from the pycnometer measurements. Compared to the Archimedes measurements, XCT measurements reported lower porosities again, but this was attributed to the fact that the XCT samples were taken from the centre of the sample bulk, while more pores were concentrated near the edges of the part. Dupin et al. [115] similarly measured the density of laser polymer powder bed fusion (PPBF) processed polyamide 12 using the same three methods, again reporting higher closed porosities using the Archimedes method when compared to XCT. In this study, however, the authors attributed this difference to an overestimation of the closed porosity by Archimedes measurements because of the degree of crystallinity of the processed polymer having a higher density than the density of the powder measured by pycnometry.

The aforementioned studies ([110,112,117]) note that the Archimedes method is incapable of providing any information about the internal part geometry beyond an overall porosity, and so XCT has continued to be used for dimensional pore measurement and internal defect detection [112,113,117,118,120,124,125]. In addition to the measurement of pore morphology, XCT also allows visualisation of pore distribution within parts. In the paper by Léonard et al. [129] for example, the authors studied the formation of elongated pores in electron-beam powder bed fusion parts, correlating to intentionally misaligned overlap regions between contour and hatched sections within parts. Similarly, Attar et al. [126] examined crack formation due to pores and unsintered powder in laser MPBF titanium parts, using XCT.

This period saw a rise in the use of XCT as an inspection tool for part and process verification [130,131], and as a dimensional measurement tool. As examples of dimensional measurements, the authors of a number of the aforementioned studies used XCT for the measurement of lattice structure feature sizes in addition to porosity. The authors of these papers also increasingly presented measurement uncertainties and the related influence factors alongside measurement data; not a practice often seen in previous medically focussed references [113,116]. A further example of XCT use for dimensional measurement can be found in the paper by Fukuda et al. [132], where the authors investigated the ideal scaffold pore size for generating bone ingrowth by simulating pores with varying size channels and subsequently measuring the channel dimensions by XCT. Similarly, Van der Stok et al. [133] used XCT following the implantation of bone scaffolds into mice, to periodically measure the volume of integrated bone, as well as to initially verify implant placement.

During this period, a series of publications by Pyka et al. [116,121,134–136] pioneered the use of XCT data as a method of analysing surface texture, through extraction of surface texture parameters from XCT data. In a 2010 paper by Pyka et al. [134], the authors highlighted the difficulties in the measurement of surfaces in porous 3D structures by traditional methods, and so defined a protocol for XCT topography measurement by generating profiles from 2D XCT slices. The authors measured laser MPBF Ti-6Al-4V struts using XCT and validated the method by comparison with interferometric measurements. Texture parameters generated using both methods were shown to be similar and differences in topography between the tops and bottoms of struts were identified by the authors. It should be noted, however, that Pyka et al. presented preliminary results; texture parameters were quoted generally without filtration (see Chapter 1 and [53]) or uncertainties (i.e. by using repeat measurements and constructing statistical models in line with the guide to the expression of uncertainty in measurement [22]), which is not in line with good practice for the generation of surface texture parameters. Kerckhofs et al. [135] rigorously compared the surface parameters *Pa*, *Pq* and *Pt* of porous Ti-6Al-4V samples, measured using optical, contact and XCT methods. The data showed XCT

measurements to be accurate and robust for micro-scale roughness, whilst sub-micrometre measurement was stated to be currently impossible. *Pa* values for rough surfaces (5 μm to 30 μm) were statistically similar for each technique, although optical measurements gave higher values on rougher samples due to data dropout from the presence of steep slopes (i.e. lower accuracy compared to the XCT technique). *Pa* values for low roughness surfaces (<1 μm) were overestimated using the XCT technique and the data were highly affected by noise. Measurements of porous structures showed no differences between internal and external struts when top and bottom values were averaged, implying successful topography measurement throughout the volume. The authors clearly discussed caveats of the technique regarding poor lateral and vertical resolution, although did not perform any filtering of the extracted profiles (to gain texture parameters, as is common practice) and did not explain why this was not performed. Figure 2.1 illustrates the method of profile extraction from XCT data (from reference [135]). This method of parameter extraction was then applied in further papers by Pyka et al. [116,136] and Van Bael et al. [121]. In the papers by Pyka et al., the authors used the profile extraction technique to compare scaffold strut surface primary profiles after various surface finishing processes, while Van Bael et al. used the same technique to study strut surfaces for in vitro applications. It should be stressed, however, that whilst the development of this technique holds promise for future surface measurements, the data gained are of poor lateral and vertical resolution in comparison to established surface measurement methods, and the parameters obtained for surface texture measurement are now in the process of being supplanted by other methods of surface metrology [106]. Development of the Pyka et al. method, therefore, represents a stimulating research challenge for future work.
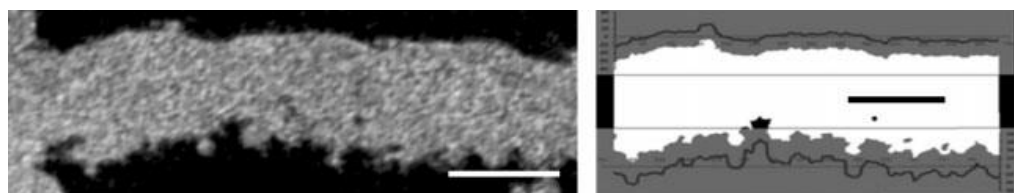
Figure 2.1. An XCT image used to generate surface texture parameters, with a binarised version of the slice and the extracted profiles. Scale bar = 200 μm. Figure published in [1].

As XCT technology by 2010 represented a viable metrological tool, this period also saw the publication of a review article summarising the industrial use of the technology up until this point. In this review, Kruth et al. [57] studied the use of XCT for dimensional quality control, including traceable dimensional measurements and tolerance verification. The review outlined the principles of XCT metrology, highlighting various data acquisition strategies as well as problems associated with scatter, beam hardening and edge detection (see reference [62]). The authors studied test cases and explained the use of XCT in internal feature metrology, as well as in combining dimensional quality control with material quality control. Kruth et al. finally highlighted the remaining work on enlarging the applicability of XCT metrology in the areas discussed. This review also noted the lack of reference objects for the purpose of XCT verification and calibration, and presented a number of reference objects proposed for this purpose. In the subsequent presentation by Carmignato et al. [137] and in the related paper by Carmignato [138], the authors elaborated upon the Kruth et al. review, summarising methods of accuracy evaluation of XCT dimensional measurements. Carmignato also discussed performance verification and traceability establishment methods, noting the importance of XCT for measurement of AM parts. The authors further discussed the results from the first international XCT comparison of four proposed reference objects (see figure 2.2). In his paper, Carmignato concluded that there is a need for physical and specification standards regarding performance verification and traceability, in order for XCT to be accepted as a metrological tool.
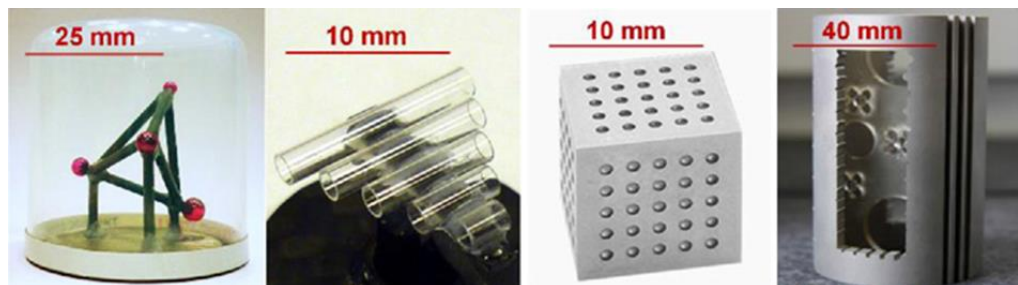
Figure 2.2. Reference objects used in the international XCT comparison, from left to right: CT tetrahedron, pan flute gauge, calotte cube and QFM cylinder. Figure published in [1].

The 2011 paper by Kiekens et al. [139] similarly presented initial work into using XCT for metrological purposes, investigating the influence of workpiece orientation, magnification, edge detection and calibration on measurement accuracy and repeatability using a test artefact (see figure 2.3). The artefact illustrated the use of co-ordinate measuring machines (CMMs) for the purpose of XCT calibration by comparing various calibration strategies. The authors specifically noted the requirement for the measurement of complex internal features in AM and outlined a measurement strategy. The authors concluded that the artefact was uniquely useful in the measurement of scale and offset errors, allowing scaling and thresholding calibration with a single artefact, and explained the ability of the artefact to allow internal and external measurements. Further to these general XCT artefacts, in 2012 Moylan et al. [140] of the National Institute of Standards and Technology (NIST) presented the initial development of an AM general test artefact, noting the lack of standardised AM parts and reviewing existing test parts. The authors used existing test parts to form a set of rules to design an artefact for standardisation by the standards organisation ASTM International. The authors then specified design intent and presented the part, detailing each feature and the measurement strategy using CMM, surface texture measurement, ultrasonic testing and XCT. Moylan et al. finally presented preliminary results (successful manufacture by several AM techniques) and outlined future work (see figure 2.3 and Section 2.1.4.4). It should be noted that this artefact was not designed for XCT dimensional metrology; Moylan et al.'s suggestion in this case was to examine a small section of the sample using XCT to characterise internal defects. The artefact as a whole is not particularly suitable for XCT due to the large differences in X-ray penetration length with orientation.
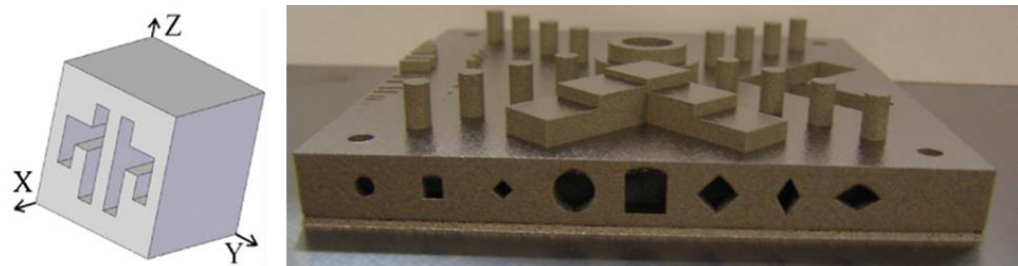
Figure 2.3. Left to right: the 'cactus' XCT artefact of size (45 × 45 × 45) mm, reproduced from [139] and the NIST AM artefact of size (240 × 240 × 19) mm. Figure published in [1].

2.1.2   State-of-the-art in XCT in AM reverse engineering

While medicine represents the most common application of XCT and AM reverse engineering [82], the technology has spread into other research areas, often for the examination and reproduction of cultural artefacts or archaeological remains. As examples of this, Laycock et al. [141] reproduced 19th century chess pieces through digital modification of incomplete XCT data from broken and incomplete artefacts, while Howe et al. [142] used XCT data to reverse engineer historical wind instruments with a view to producing working copies of antique models (see figure 2.4). Laycock et al. concluded that reconstruction using XCT with AM was possible; particularly noting that XCT data provided previously unknown information about construction methods of the original chess pieces. Howe et al. drew similar conclusions, noting that the method used showed promise for the production of historical instruments. The authors did, however, cite drawbacks relating to machine cost, as well as pore formation and rough surface texture as barriers to adoption of the technology due to the resulting effects on musical tone.

As an example of archaeological use, Ishida and Kishimoto [143] used XCT to perform dimensional measurements of height and width of a radiolarian fossil on the order of 100 μm, as well as to inspect the form and the arrangement of pores in the fossil skeleton. These data agreed with conventional measurements performed by other authors and also revealed a previously unexamined structure in the skeleton. The authors binder-jetted a model of this skeleton to provide a detailed observational analogue and concluded that XCT and binder-jetting are effective tools for radiolarian studies. Similarly, Henson [144] reproduced biological remains from XCT and optical scanner data using binder-jetting, where comparison of the reproductions showed that XCT gave higher accuracy models compared to 3D scanner data. Henson concluded in this instance that the models produced were not sufficiently accurate for extensive skeletal research, but noted that the models allowed for population and basic morphological studies, and that they were applicable to outreach and teaching as well as for use in exhibitions. Appleby et al. [145] similarly used laser PPBF

to replicate the skeleton of Richard III from XCT data of remains famously found in a Leicester car park. The resulting model has since been exhibited, as well as used to provide new information about the king's life and his spinal defect.

Figure 2.4. Left: XCT data of a saxophone mouthpiece, right: AM reproduced saxophone mouthpieces with original wooden mouthpiece (second from left). All the AM mouthpieces were produced by scaling of the original scan data and the rightmost mouthpiece was stated to be sufficiently dense as to operate successfully. Figure published in [1].

2.1.3   State-of-the-art in XCT in AM pore measurements

The use of XCT for the non-destructive measurement of density and porosity, as well as the study of pore morphology and distribution, is now a well-established practice which applies particularly to the measurement of AM parts. As one of the primary techniques currently available to evaluate pore morphology and distribution non-destructively (the other being ultrasonic non-destructive testing [NDT]), XCT is increasingly being used in AM for a variety of applications and recent publications reflect this use [146,147,156–165,148–155]. A number of these publications represent novel uses of XCT in porosity measurement and will be described here in more detail. Before discussing these uses, however, it is at this point appropriate to highlight studies involving measurements of small features which are examined in essentially the same manner as pores. For example, in the paper by Slotwinski et al. [166] and the review by Slotwinski and Garboczi [167], the authors discuss using XCT to analyse the morphology of particles used in powder bed fusion. Similarly,

Chlebus et al. [161] used XCT not only to measure porosity but also to quantify the amount of rhenium dissolved in molten titanium, through measurement of remnant rhenium particles in final parts. In another example of small feature measurement, Tammas-Williams et al. [164] used XCT to examine pores within a powder feedstock, as well as pores present in final parts.

2.1.3.1 Recent novel XCT porosity measurements

In the paper by Cox et al. [146], the authors produced binder-jetted hydroxyapatite (HA) and poly(vinyl)alcohol tissue scaffolds, using XCT to measure the percentage by mass of HA in the scaffolds, whilst also quantifying the undesigned porosity of the structure in green and post-sintered parts. To note for the purposes of this discussion, designed porosity is generally defined as the macroscopic voids between solid features in lattice structures, while undesigned porosity is defined as the porosity naturally arising as a by-product of AM processes. Designed porosity is present only in lattice structures while undesigned porosity is found commonly in all AM parts. Another example was presented in the recent paper by Carlton et al. [156], in which the authors performed tensile tests of laser MPBF as-built and annealed 316L stainless steel in-situ during white light synchrotron XCT. This experiment showed that the role of the porosity distribution is larger than the role of bulk density in affecting fracture mechanisms.

Using XCT alongside SEM fractography, Carlton et al. showed that in samples with large inhomogeneous void distributions, failure was dominated by individual flaws as opposed to bulk density, with cracks consistently initiating at pre-existing voids. Carlton et al. particularly noted the capability of laser MPBF in creating parts with a wide range of porosities, porosity distributions and morphologies, as well as that final mechanical properties are dependent on all of these factors. Figure 2.5 shows results of the in-situ testing.
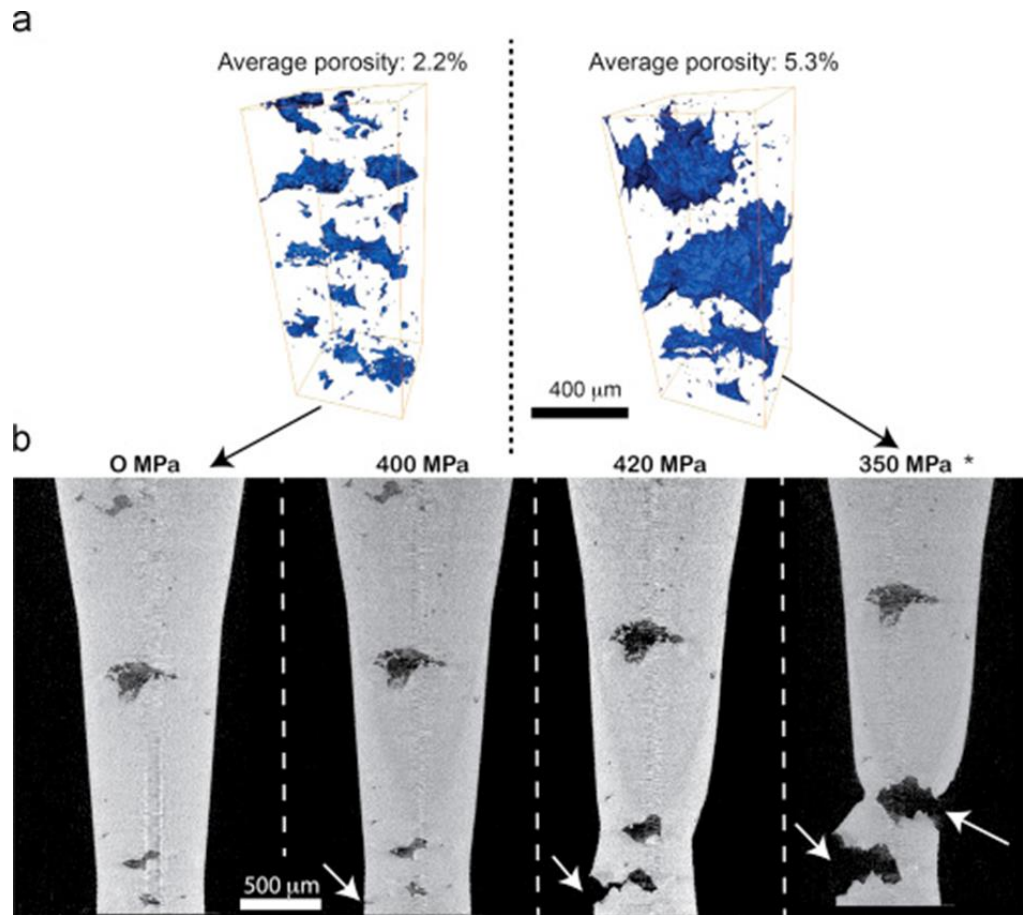
Figure 2.5. (a) Volume renderings of voids in a high porosity stainless steel sample prior to mechanical testing (left) and immediately before catastrophic failure (right). (b) XCT images at different load and displacements during in-situ tensile loading. Figure published in [1].

Similarly to Carlton et al.'s [156] examination of porosity in relation to mechanical performance, Siddique et al. [155] and Leuders et al. [157] respectively used XCT to relate part porosity to stress concentration in laser MPBF processed Al-12Si and to fatigue performance in laser MPBF processed Ti-6Al-4V, examining as-built and hot isostatically pressed (HIP) samples. Siddique et al. concluded that XCT was effective in detection of fatigue-critical pores, while Leuders et al. showed poor accuracy in failure prediction which they attributed to the high defect density of laser MPBF parts. Leuders et al. did, however, identify methods of optimising prediction accuracy through SEM examination of crack surfaces and initiation sites. Leuders et al. also noted a strong correlation between defect location and fatigue damage, broadly agreeing with Carlton et al.'s findings. Tammas-Williams et al. [164] evaluated the use of XCT in the measurement of the effect of porosity distribution on fatigue

performance in Ti-6Al-4V electron beam MPBF samples, noting that while XCT cannot capture small pore data, it is capable of capturing fatigue-critical larger pores which other methods (such as SEM metallographic sectioning) may miss due to sampling issues. The authors concluded that coarser scans (of resolution ~25 μm/pixel) are sufficient in capturing all fatigue-critical flaws and so XCT represents a viable detection method for this purpose, agreeing with the conclusions of Siddique et al. [155]. Attar et al. [159] used XCT in the study of compressive failure, this time in scaffolds of varying porosity produced from titanium and Ti-TiB by laser MPBF. XCT was used to verify designed porosities and identify additional undesigned porosities, as well as to show that cracks resulting from low strut ductility in porous areas cause early-stage compressive failure. In their study of laser MPBF processed AlSi10Mg, Maskery et al. [160] examined the effect of post-process heat treatments on pore size, position and morphology, noting no changes after annealing and precipitation hardening of samples. The authors specifically noted the usefulness of XCT in quantitative defect analysis when compared to conventional SEM cross-sectioning, as the number of micrographs required to provide a pore sample size of equivalent statistical quality would be prohibitively large. The authors in this case also identified a requirement for development of robust image analysis procedures, in particular thresholding or segmentation, in order to ensure reliable pore morphology measurements in the future.

2.1.3.2 Hybrid porosity measurements

The authors of the studies discussed in Section 2.1.2 commonly used XCT as part of a larger sphere of characterisation methods to relate porosity to other part features. In continuation of this theme, several instances where XCT has been used in pore measurement with other techniques are of note; either to verify experimental measurement procedures through twin data acquisition, or as a hybrid measurement tool. In the paper by Tammas-Williams et al. [159], the authors compared XCT data to SEM metallographic cross-section data to further examine pore morphologies and showed that XCT data generally agreed with 2D cross-sectional measurements down to a lower pore size limit of ~5 μm. Maskery et al. [160] stated their agreement with the pore size data presented by

Tammas-Williams et al., noting very similar pore sizes in their study. Castilho et al. [162] similarly studied the dimensional accuracy, porosity and mechanical properties of binder-jetted parts as a function of binder saturation. Using the Archimedes method, SEM, XCT and high resolution photo-scanning, the authors measured physical properties, while compression tests were performed to examine mechanical properties following post-processing of parts. XCT was used to visualise pore distribution in part interiors, while the Archimedes method was used to evaluate overall porosity. The photo-scanner was used in this case to evaluate dimensional accuracy by measuring the scanned images.

XCT was used by Grünberger and Domröse [148] in development of a method for in-situ monitoring of laser MPBF through the measurement of light emissions during the manufacturing process. This monitoring aimed to provide an in-situ pass/fail status for parts, defined by tolerancing of the resultant part porosity as measured post-process by XCT. Slotwinski et al. [149] developed a method of in-situ porosity monitoring by ultrasonic sensing, correlating ultrasonic porosity data to porosity data gained using three other methods; mass/volume, the Archimedes method and XCT. The authors in this instance noted that porosity values varied significantly between measurement procedures and so further destructive testing would be required to ascertain the 'true' porosity value. They concluded that there was a linear correlation between ultrasonic measurements and porosity despite a lack of morphological or distributional homogeneity. This paper is also noteworthy for the detail in which XCT porosity measurements are described, as the authors very clearly outlined the method and related uncertainty calculations. A third method of in-situ monitoring was proposed by Mireles et al. [154] using infra-red thermography, again comparing results to post-process XCT scans. They showed that thermography was capable of reliably detecting large pores (<600 μm) in-situ. In terms of hybrid measurements, Nassar et al. [150] and Siddique et al. [155] both presented defect location and pore size data measured using XCT with optical cross-sectional metallography. Nassar et al. compared their data to another method of in-situ defect detection, this time using optical emission spectroscopy, while Siddique et al. critiqued the two methods. Siddique et al. noted that due to the lack of significant difference between the techniques, they

favoured the XCT data due to its non-destructive nature, despite a discrepancy between data sets and the substantially more expensive acquisition process compared to cross-sectional optical microscopy. Kasperovitch and Hausmann [158] similarly analysed porosity using XCT and metallographic cross-sectioning, although they used SEM micrographs as opposed to the optical microscopy used in the aforementioned papers.

The current state of XCT porosity measurement in AM is very clear from the studies discussed here. XCT is now very commonly used for the measurement of pores and similar small features, and XCT has been deemed sufficient in the detection of fatigue-critical flaws. The technique has its limitations compared to other methods of porosity quantification (such as the Archimedes method), mostly pertaining to poor resolution in comparison to the size of the smallest pores. The resolution of XCT scans is related to the size of the sample and maximum achievable magnification afforded by the XCT apparatus. The result of this is that larger samples provide lower accuracy porosity measurements because the shapes and sizes of internal pores are misrepresented. The limitations discussed here will likely only be overcome with the advancement of XCT technology. These conclusions will be discussed in more detail in Section 2.1.5.1.

2.1.4   State-of-the-art in XCT in dimensional metrology of AM parts

In addition to porosity measurements, XCT is now commonly used in general dimensional metrology as a substitute for other co-ordinate measurement techniques, in cases where traditional methods of measurement (such as CMM) are impractical. This is most notably the case with AM parts due to the aforementioned complex geometries and surface textures that are now commonly present. For example, in their recent work, Rivas Santos et al. [168] showed that due to the presence of very rough surfaces, CMM measurements of AM parts often provide poor results in terms of uncertainty estimation. Further to older studies discussed earlier in this Chapter, there have recently been many publications exploring the use of XCT for direct measurements of part features

and a number of these will be discussed in the following Section [58,162,177–186,169,187,188,170–176].

2.1.4.1 Validation against CAD models

One of the common foci of current work involving metrological XCT is as a method of accuracy assessment through validation against CAD models, and consideration of related measurement uncertainties and tolerancing is becoming an increasingly significant feature of these studies. Cooper et al. [183], for example, investigated the potential benefits of AM in improvement of fuel efficiency through lightweighting of engine valves, using XCT to reverse engineer finite element simulations in order to redesign the valves. Following production of the re-engineered part, the authors used XCT to validate the part against the CAD model and to detect defects. The part geometry was in good agreement with the CAD model under a tolerance of ± 0.15 mm, with no significant defects detected. The authors noted difficulties in edge detection using XCT during this process and detailed steps were taken to overcome the problem by manually segmenting internal geometries. Cooper et al. concluded that XCT was used successfully as a reverse engineering tool for CAD generation and that production of a functional, lightweight part was possible using AM. Villarraga et al. [181] similarly used XCT to compare parts made by material extrusion and vat photopolymerisation, as well as to assess their inkjetted nanopositioning flexure stage for air voids and morphological accuracy. The authors performed morphological deviation and defect analyses in comparison to nominal CAD designs. In the paper that followed, Lee and Tarbutton [182] described the final results of their work and concluded through testing of the flexure stage that their method was capable of producing a cost-effective alternative to other similar stages, achieving 25 nm positional precision over a 500 μm range.

2.1.4.2 Medical measurements

Aside from the use of XCT in medical reverse engineering, medically focussed studies have also increasingly used XCT as a metrological tool. Wüst et al.

[169], for example, used XCT to examine the geometry of bioprinted channels through comparison of cross-sectional area measurements to theoretical values. In another application, Huang et al. [173] used XCT to plan appropriate plate and screw trajectories for complex bone surgery, and then used an AM surgical guide to achieve these trajectories. The authors performed post-operative XCT to assess screw placement deviations with respect to the entry point, screw length and screw direction. Li et al. [174] used XCT to measure integrated bone volume at four and twelve weeks following implantation of tissue scaffolds in rabbit femurs, while Mroz et al. [175] evaluated post-operative integrated bone volume using XCT. These authors all particularly show development in the use of metrology in medicine due to their consideration of measurement uncertainties; representing good practice not commonly observed previously in medical studies. This consideration implies that the medical field is beginning to adopt a more rigorous approach to implant production, in appreciation of modern manufacturing technology. It should also be noted that the use of XCT and AM in medicine is highly extensive, though a review of medically focussed publications has been omitted from this Chapter as the relevance of such a review to this Thesis is low. However, during the early review stages of my PhD I produced an additional review paper focussing on such publications, which can be found elsewhere [109]. This review work presented in this publication goes into far greater depth than the brief outline of XCT and AM use in medicine presented here.

2.1.4.3 Measurements of lattice structures

Lattice structures that were impossible prior to the inception of AM due to tool access constraints have been identified as a useful output of AM, as when compared to fully dense parts, components utilising lattices in the place of bulk material have been shown to retain strength whilst reducing total mass [180]. The use of lattices in tissue engineering represents a stimulating field of research, but these structures are also of interest to engineers for a wide array of applications; from support structures, to heat dissipation and energy absorption [189]. As such, the past year has seen a series of studies into lattice materials and the recent review on microlattices by Xiong et al. [180] discusses the use of

XCT in measurement of AM lattices at length. Van Grunsven et al. [172], Sercombe et al. [185] and Abele et al. [187] all produced metallic lattice structures via a variety of additive processing methods, and used XCT to compare built parts to CAD models. The latter paper by Abele et al. is of particular significance in that the authors critically analysed the comparison, noting that their findings were based on a specific geometry and material, and that further research is required to generalise findings. Sercombe et al. used XCT in their study to examine the deformation and failure of scaffolds through generation of FEA mesh models, which were then shown to agree with experimental data. This study indicates the capability of XCT for the purpose of FEA model generation; agreeing with the conclusions made in 2005 by Williams et al. [190].

2.1.4.4 AM and XCT artefact development

Further to the work discussed earlier in this Chapter, development has occurred over the past year in the creation of test artefacts for both XCT and AM. Most notably, the AM general test artefact as proposed by Moylan et al. of NIST [140] (discussed in Section 2.1.1) has been further developed towards standardisation. Moylan et al. [171] recently proposed the a new version of the NIST test artefact for the evaluation of AM machines, comparing and contrasting previously proposed artefacts and summarising the features of each artefact. These features were then funnelled into specific design criteria for the standardised artefact. Based on this specification, the authors proposed the final artefact for measurement primarily by CMM and surface measuring instruments, but also utilising ultrasonic NDT and XCT for examination of internal defects. Primary studies of the artefact were based on DMLS, binder jetting and material jetting builds, and demonstrated how metrology can be used to characterise and improve specific AM systems. The artefact was also successfully manufactured using vat photopolymerisation, laser MPBF, electron beam MPBF and laser PPBF. As a parallel, Möhring et al. [179] recently presented a general test artefact for analysis of various manufacturing processes, simulation methods, machining techniques and measurement strategies (see figure 2.6). The authors presented results of a round robin test of the artefact as manufactured by several

parties using micro-milling (various manufacturers and machines) and AM (various material extrusion and laser MPBF machines). A measurement strategy was defined and artefacts were measured using two XCT systems to compare with nominal CAD data, investigating global and individual feature alignment in order to analyse machine performance. Möhring et al. stated that the proposed test artefact intentionally included features that were challenging to produce and that additive processes were limited by the achieved process resolution. The authors concluded that through simulation, machine analysis and appropriate measurement, the separation and identification of the influencing factors on deviation from the nominal was possible, further stating that XCT was sufficient in part evaluation.

Teeter et al. [186] recently produced a test artefact specifically dedicated to dimensional verification in AM for biomedical applications. The authors designed the artefact in reference to the biomedical focus to contain holes, cylinders, gaps and lattices; studying how positioning on the build plate affected manufacture. Results showed that in this study location on the build plate had no effect on dimensional accuracy. The minimum feature size for this material and process (laser MPBF of stainless steel) was found to be of 0.3 mm as features designed under this size were overbuilt to at least 0.3 mm, while the average deviation between as-built parts and the nominal was shown to be uniformly less than 0.1 mm. The authors concluded that the test artefact was effective for system and material verification, as well as for determination of build plate positional effects and minimum feature size. Measurements were made generally using a measurement microscope, while lattice components were measured using XCT.

Rivas Santos et al. [168,191] et al. recently sought to address another issue in AM manufacture, namely the fact that with the near-infinite design freedom offered by AM, there is an underused opportunity to allow for improving the ease of verification in design. As such, Rivas Santos et al. present artefacts exhibiting the concept of 'design for metrology', for the purpose of benchmarking a polymer powder bed fusion system. The authors suggesting that such artefacts can facilitate such benchmarking exercises in the future,

allowing assessment of common benchmarking artefacts using a variety of measurement systems.
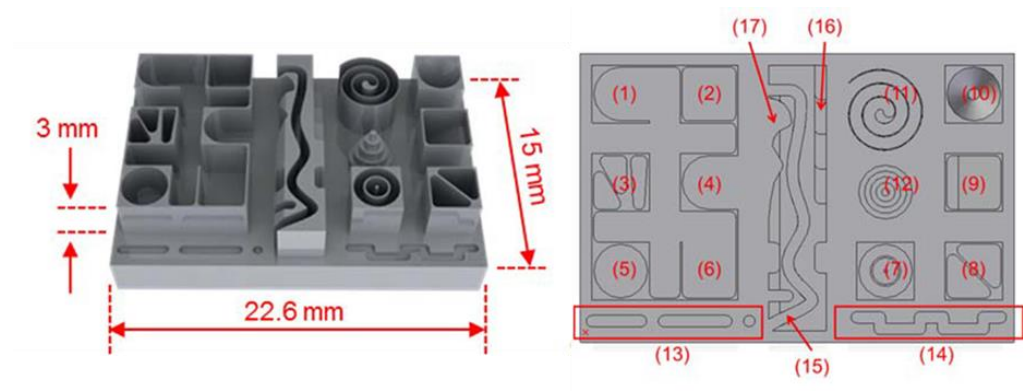
Figure 2.6. CAD model and top view of the Möhring et al. general test part with numbered features. Each feature has defined purposes, generally designed to be difficult to manufacture and requiring an array of machining methods. Figure published in [1].

In addition to the artefacts discussed here, Rebaioli and Fassi [192] recently published a review of existing benchmarking artefacts, summarising the plethora of artefacts discussed in the literature. In this review, Rebaioli and Fassi categorised artefacts by the aspects of the AM process they were designed to characterise, particularly noting the use of artefacts in both performance evaluation and parameter optimisation, and suggested guidelines for artefact design in the future.

2.1.4.5 Hybrid dimensional measurements

As discussed in Section 2.1.3.2 in regards to porosity measurements, XCT is now often used in collaboration with other measurement techniques to characterise parts, and this trend is similarly present in general dimensional measurements as well as porosity measurements. In illustration of this trend, Narra et al. [176] recently presented a method validating the mechanical behaviour of biodegradable vat photopolymerisation scaffolds using XCT with in-situ deformation, in which XCT measurements were made before and after compression loading using a mechanical compression device. The authors concluded in this case that the method was appropriate for validation of printed

scaffolds and claimed that the related deformation fields could be used to corroborate simulated designs with as-built parts.

2.1.4.6 Surface texture measurements

Around the same time that I published the review based on this work [1], another review was published by Townsend et al. [9] examining surface texture measurement in AM. While the findings of Townsend et al.'s review will be detailed in Section 2.2.1, it is important to note at this point that Townsend et al. also found a research niche in the area of surface measurement using XCT, citing the same papers as those discussed previously in Section 2.1.1 ([116,121,134–136]). Townsend and his colleagues have since produced a number of publications examining the use of XCT for surface measurement in AM [99,193–197], which I shall outline here. In a conference paper and later a journal paper, Townsend et al. [99,193] successfully extracted surface data from an XCT measurement of both a reference sample and an AM sample, and compared ISO 25178-2 [51] parameters computed on the XCT surface to those computed for a focus variation (FV) [45,46] measurement. Townsend et al. aligned measurements using an iterative closest point algorithm and used a reference artefact to ensure correct scaling of voxels in the XCT volume. With these considerations, Townsend et al. reported small discrepancies (~2.5 %) between parameters generated using XCT and FV measurements. In their second spate of investigations, Townsend et al. [194,195] developed an interlaboratory comparison of surface measurements of an AM sample using XCT systems located in different laboratories. Particularly, similar XCT systems at the Universities of Huddersfield and Nottingham, the National Physical Laboratory and Nikon Metrology were used. This study was performed in collaboration with myself, and a journal paper was recently published [198]. In this work, Townsend et al. compared ISO 25168-2 parameters generated from data acquired at each lab to FV data and found similar results from all labs (see figure 2.7).

In their 2017 paper [196], Townsend et al. commented on a number of influence factors that may affect XCT measurements (again by comparing ISO 25179-2

parameters generated from XCT data to those generated from FV data); finding the following for each examined influence factor. Firstly, when considering different surface detection methods, the commercial local iterative surface determination algorithm in VolumeGraphics VGStudioMAX 3.0 [73] was found to consistently produce results most similar to FV data. Secondly, significant changes in results were found to be induced by XCT filament change, and finally there was no observed significant effect of an 'internal' versus 'external' surface measurement.
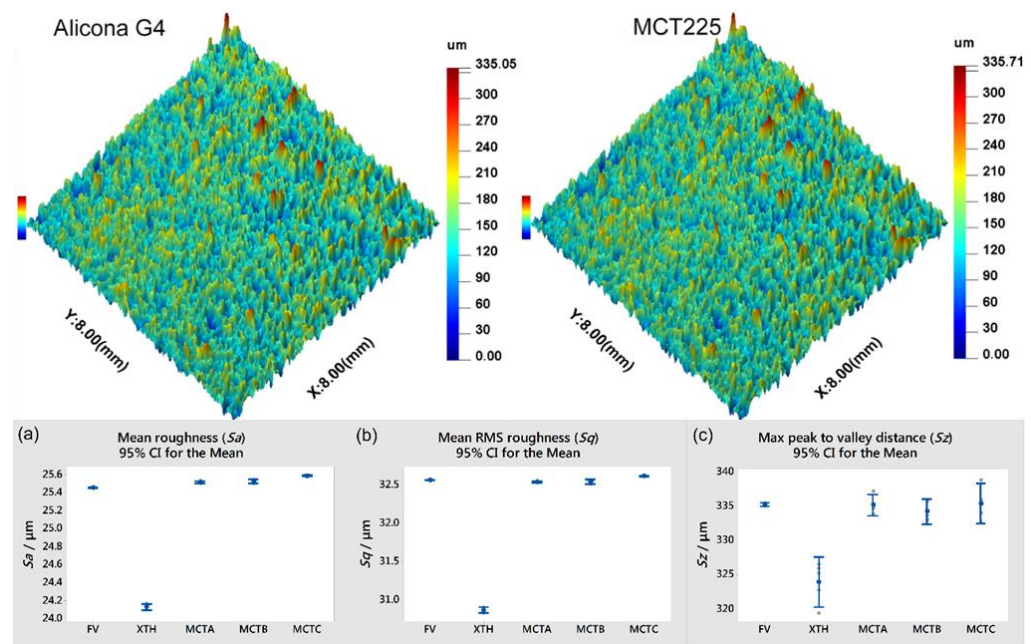
Figure 2.7. False colour height maps from focus variation and XCT systems, and surface parameter results: a) *Sa*, b) *Sq* and c) *Sz*, reproduced from [179].

In their most recent conference paper [197], Townsend et al. examine measurement and characterisation of re-entrant surfaces using XCT for AM samples, introducing a modified version of the ISO 25178-2 *Sdr* parameter (defined as "the percentage of additional surface (including re-entrant surfaces) contributed by the texture as compared to a plane the size of the measurement area" [197]). The authors compare the actual surface area and volume of XCT surfaces to those in which re-entrant features have been projected onto a height-map grid and find substantial discrepancies between instances. Townsend et al. suggest that the new parameter, '*Sdr*$_{prime}$', could be correlated to functional performance in applications where surface area is critical.

Aside from the work by Townsend et al., there has been some work by other authors examining the use of XCT for surface measurement presented and published during the course of my PhD. In their recent conference paper [199], Fox et al. presented their findings in comparing optical and XCT surface measurements. In this work, the authors extracted surfaces from Inconel and stainless steel samples and then manually aligned and compared them to surfaces acquired using confocal microscopy [35,36]. Scanning electron microscopy was also used for visual comparison to the XCT and confocal surfaces. The authors noted that the resolution used in this case for XCT scans (10.9 μm voxel size) was not sufficient to allow quantifiable comparison to confocal data, owing to the surface determination methods used, and pointed to a requirement for higher resolution measurements in their future work. Additional comparison work was recently performed by Stimpson et al. [200], and Maszybrocka et al. [201], who similarly performed measurements of AM surfaces with XCT. Zanini et al. [202] also recently presented a comparison of XCT with confocal data, in addition to a concept for the generation of a reference sample to evaluate the accuracy of XCT surface topography measurement. However, the proposed method hinges upon referencing XCT data to a profile, so is currently hindered by a heavy dependence on highly accurate alignment of three-dimensional volumetric XCT data to a two-dimensional profile; in turn likely highly dependent upon the surface determination methods used on the XCT data. This issue has not yet been addressed, and, as stated in their conference presentation, represents an area of future work by Zanini et al.

2.1.4.7 Relevant review work

Finally of note in this Section, a number of reviews have been published recently regarding XCT and AM, and the findings of these reviews are worthy of discussion. In De Chiffre et al. [58], the authors examined all aspects of XCT in an industrial setting, highlighting that XCT is the only method currently able to perform non-destructive measurements of inner features as well as non-destructive porosity verification. De Chiffre et al. also discussed in detail the application of XCT to individual industries, including AM, as well as challenges

and barriers to the technology, noting the following as primary concerns: measurement accuracy, large and high density parts, signal-to-noise ratio, reconstruction algorithms, task-specific measurement setups, multi-material measurements, setup time, measurement uncertainty, in-line measurements and high costs. Todorov et al. [170] studied NDT methods of complex AM alloy components, discussing defect formation and mitigation, and qualitatively defining design complexity into five groups. Group one, for example, contained simple parts that could be inspected using conventional methods, whereas groups four and five comprised components producible exclusively by AM and requiring new NDT inspection techniques. The authors conducted a literature review into various NDT techniques and concluded that XCT is the most promising method for evaluation of complex geometries. The Manufacturing Technology Centre (MTC, UK) also recently produced two relevant reports reviewing the use of XCT for NDT and the use of simulation in enhancing inspection [177,178]. In the first of these reports [177], Turner discussed the now common use of XCT in NDT, material characterisation, dimensional measurement and digitisation; through the acquisition of volumetric scan data from measured objects. Turner particularly observed how XCT is useful in NDT of AM components, due to the ability to extract internal surface data. The author further reviewed the state of the art in XCT NDT and discussed several topics regarding his findings. The first of these points was in regards to the hardware trade-off during scans, discussing advantages and disadvantages of various systems. The second section addressed methods of compensation for the limitations of XCT, including: image artefacts and contrast, workpiece dimensions and penetration, and cycle time. Turner also highlighted the industrial applications of XCT, as well as the potential for future automation of the technology and the barriers to wider technological adoption. Turner noted the following as barriers to increased adoption: limited standardisation, large data volumes, system cost, a lack of understanding of system capability and personnel certification. Turner highlighted the use of XCT in AM and compared XCT to other NDT techniques (X-ray imaging, ultrasonic and acoustic resonance testing), concluding that XCT represents an attractive solution for NDT; particularly citing the lack of AM and XCT specification standards as the primary technological barrier. In the latter MTC report [178], Brierley and

Akhtar summarised the latest developments in radiography for high speed inspection of AM parts. The authors examined the various commercial machines and software available; noting that there is a wealth of technologies but that high speed XCT is not possible without constraints on part size and density. Everton et al. [25] recently reviewed the current state of in-situ metrology and process monitoring for AM, in order to address the lack of quality assurance in AM parts. The authors noted the development of many approaches to in-situ measurements, finding that XCT has not yet been used in-situ, despite having the potential for in-situ AM process inspection. The authors attributed the reason for XCT not having yet been investigated for in-situ inspection to the difficulty that would be experienced integrating the technology into AM systems, in comparison to simpler camera or thermal based monitoring techniques. The authors concluded that camera and thermal based systems likely represent the future of in-situ process monitoring and control, but noted that more complex methods utilising NDT techniques capable of sub-surface inspection (such as XCT) may also be integrated in the future.

2.1.5   *Section conclusions and future research*

The above discussion of current studies represents the state-of-the-art industrial use of XCT in AM. It is clear from the available literature that research utilising XCT and AM falls into two primary areas, although the number of unique applications is substantially in excess of this. These primary areas have been discussed in detail and it is possible to draw specific conclusions regarding each of the applications within each research area. It is of note that the majority of the literature examined in this review is in relation to AM of metal parts. While the discussion presented in this review reflects the available literature (which mainly focuses on metal AM), the conclusions made here should be assumed to be in reference primarily to metal parts unless otherwise stated. It may in some cases be possible to extrapolate the conclusions made here to cover polymer AM, but all conclusions are made in reference to the evaluated literature.

2.1.5.1 XCT for AM pore measurements

Through review of the aforementioned studies of porosity, it is clear that XCT is a well-suited tool in examination of designed and undesigned pores. As discussed, XCT porosity measurements of most metallic samples are not as accurate as measurements made by the Archimedes method, but represent the most reliable non-destructive method of evaluating pore distribution within parts. It should, however, be noted that unlike XCT where a small sample is preferable to increase the achievable magnification, Archimedes measurements suffer from increased errors associated with the surface effects (bubbles attached to sample surfaces) for small samples with high surface area. Uncertainties in measurements made by the Archimedes method are also dependent on the density contrast between the sample material and the measurement fluid [112], which is low for polymer parts. Coupled with the problems discussed previously in measuring density of polymer parts using the Archimedes method, XCT can, for some parts, potentially produce better results than using the Archimedes method [111,115]. XCT measurements can often be more accurate when compared to 2D, single layer, porosity measurements (via cross-sectioning) due to the nature of random sampling and relatively low numbers of pores. XCT is now commonly used alongside other measurements to correlate porosity and pore distribution with mechanical properties, and such studies have shown that pores routinely act as failure initiation sites. The main criticism of XCT porosity measurements is inaccuracy compared to Archimedes porosity measurements, which include information from pores of all sizes, while XCT is incapable of measuring pores smaller than the minimum voxel size. The solution to this problem is improvement of XCT resolution, which is a common focus area in XCT research.

The other main stream of future research will likely be the continued correlation of pore information with other information (e.g. mechanical) about parts, as discussed in Section 2.1.3.2. As XCT scans are relatively expensive in comparison to other measurement techniques, it follows that if other measurements can provide approximate information regarding the internal geometry of parts, then the cost of verification can conceivably be reduced

through the use of cheaper measurement techniques. By this, it may be possible to correlate the surface texture of an AM part with the part's near-surface porosity (a common feature in parts produced by powder bed fusion, relating to the interaction between border and hatch scans [129]). It is, therefore, conceivable that a relatively cheap measurement (e.g. using a contact stylus instrument) could potentially provide information about near-surface porosity.

2.1.5.2 XCT for AM in dimensional metrology

XCT is now clearly becoming a vital tool in the repertoire of many metrologists, and the large number of studies using XCT in the context of dimensional measurement reflects this. The use of XCT in direct comparison to CAD data allows for the rigorous tolerancing of freeform surfaces that were previously very difficult to measure by CMM due to the challenges faced in gaining a large number of points using a touch probe. XCT is also the sole industrially-viable method of gaining data relating to internal features of parts without destroying the part, as demonstrated throughout this review. As stated, XCT, therefore, works very well with AM; particularly in the measurement of lattice structures. As concluded in similar reviews regarding industrial metrology [57,58,80], future improvements of these measurements will focus on calibration and verification of XCT systems in regards to industrial metrology. Specific to the use of XCT in AM, there remains the potential for production of standardised artefacts, and those reviewed here represent likely candidates for standardisation. The artefact presented by NIST in particular [171] represents the capabilities of AM production and allows measurements using XCT systems, although it rests with the relevant committees as to whether further development is required. As stated previously, however, the XCT measurements discussed by Moylan et al. regarding this artefact were implied to be for defect characterisation of small portions of the artefact, as opposed to for dimensional metrology, as the artefact is not optimised for XCT measurement due to the large variation in penetration lengths with part orientation. This penetration length variation represents a difficult scenario for XCT dimensional metrology, as the high aspect ratio of the artefact causes difficulties in image acquisition relating to the achievable resolution and image

contrast. Imaging difficulties are present in XCT measurements of high aspect ratio objects because high energy X-rays are required for full penetration of the object's long side, while low energy X-rays are required to avoid scatter and overexposure of the object's short side [57]. The NIST artefact can, therefore, be considered non-ideal in terms of artefact design for XCT. It may also become apparent that an AM artefact more specific to XCT measurements should be developed, as the existing AM designs presented earlier do not necessarily represent objects that are easily measurable using XCT systems. Similarly, the artefacts currently used in XCT calibration and verification are not necessarily producible by additive methods, due to the resolution and material limits presented by many AM processes. For example, AM processes are not able to produce many features commonly found in reference artefacts, such as high precision spheres. As XCT will likely become a common tool for AM product verification, the development of an AM specific XCT artefact may be required. As the precision of AM improves, it will facilitate the production of a new class of metrological artefacts to be used throughout the manufacturing sector, such as those discussed in Section 2.1.4.4 as proposed by Rivas Santos [168,191].

An interesting area of XCT measurement that has not been widely covered is the use of XCT for the measurement of surfaces. Although resolution is generally poor compared to other surface measurement techniques, XCT scans are, as stated, the only method of measurement of internal surfaces. As shown, a number of studies have successfully extracted profiles from XCT data, so it follows that it should be possible to build up 3D surface maps of AM parts using similar techniques. It is clear that XCT represents an interesting potential method for the examination of internal AM surfaces. In terms of the potential limitations regarding XCT as an internal surface topography measurement method, the primary drawback of XCT in that the scan resolution strongly depends on the maximum achievable magnification and, therefore, the overall part dimensions. Internal texture will naturally, therefore, be harder to measure for larger parts than smaller parts. A substantial limitation also exists regarding the exact determination of surfaces from XCT data. It has been shown previously that, primarily due to the beam hardening artefact, the offsets of internal edges differ from those of external edges [64]. As surfaces are often

determined in reference to external surfaces, this may prove a substantial problem when examining internal surfaces.

Another factor worth considering as AM technology moves further into the realm of multi-material fabrication [77], is the need for XCT technology to co-develop to account for multi-material parts. Work has begun on using XCT for multi-material measurements, but it remains the case that when performing multi-material XCT on materials with differing attenuation coefficient materials, results tend to be unpredictable [203]. There clearly exists a broad open research topic in this area, though arguably represents a slightly lower level of technological readiness when compared to some of the slightly more mature AM processes (i.e. single material processes).

2.1.5.3 Summary of conclusions

The combined use of XCT and AM has become increasingly important in various fields of engineering. The use of both technologies is becoming more established in advanced manufacturing and metrology, respectively, and a great deal of research has been put into increasing the use of both technologies for a range of applications within these fields. This research should continue, as adoption is not yet widespread. The following are primary barriers to the increased adoption:

- In measurement of AM part porosity: two primary requirements, regarding increased resolution for the detection of small pores to allow for higher accuracy and precision in pore measurement, and correlating porosity and pore distribution measurements to more cost effective measurement techniques to potentially reduce verification costs.
- In dimensional metrology of AM parts: a continuation of work regarding XCT system calibration and verification to increase technology adoption, as well as the production of new research regarding XCT measurement of surface texture.

The fields of XCT and AM have both come a long way since the first combined use of XCT and AM in the reproduction of a model skull by Mankovich et al. [81] in 1990, and XCT has progressed far beyond its roots as a reverse engineering tool since this time. The now common use of metrological XCT in engineering increasingly works in symbiosis with AM to recreate, as well as to verify, parts in a wide range of fields, and through continued research will aid in the acceptance of AM as an industrially viable manufacturing method.

2.2 Surface texture measurement for additive manufacture

During the initial review work I performed, a niche in the field of XCT became clear to me, notably relating to the measurement of surfaces; particularly useful for AM surfaces because of the technology's ability to produce complex geometries, often inaccessible to existing state-of-the-art metrology solutions. It also became clear during the initial review phase that different measurement issues relate to different AM processes; most notably divided between polymer and metal parts. As such, I chose to focus on metal parts for this Thesis, based on what I perceived as the more pressing industrial need – in my opinion, metal AM processes (particularly metal powder bed fusion processes) are currently more industrially developed than their polymer counterparts. AM of ceramics is, of course, also a fledgling field of manufacturing and deserves a mention here, but AM ceramic processes exist at a much lower level of technological readiness than the polymer and metal processes [204]. As such, in order to compliment the review of the use of XCT in AM presented in Section 2.1, I include here a brief review of the state of the art in measurement of AM surfaces, but as a result of the above decision, focussing specifically on metal surfaces.

Although surface metrology is well established in research and industry in terms of both profile and areal measurement, measurement of metal AM surfaces remains very much a field of cutting-edge research; as alluded to previously in this Thesis. During the development of metal AM technologies, many researchers and industrialists have encountered difficulties in measuring the surfaces produced by these processes [9], owing to the highly complex nature of the features contained on them: features exist at a wide ranges of scales, with

surfaces often including high slopes, undercuts, step-like transitions and non-uniform surface properties.

The sheer complexity of these surfaces warrants an entire field of research in itself, and as such a number of recent additions to the literature have attempted to tackle the problem of understanding these surfaces. In this Section, I will discuss recent key publications in the field and describe trends in AM surface research.

2.2.1 Recent review work

As mentioned in Section 2.1.4.6, a recent review performed by Townsend et al. [9], includes a comprehensive examination of metal AM surface metrology. In the review, Townsend et al. report on a significant amount of published literature regarding the use of surface metrology for metal AM parts, noting that the most commonly examined process technology was laser MPBF. Townsend et al. also identified common challenges encountered in the AM community. Particularly, they alluded to difficulties faced by industrialists employing metal AM technologies, in complying with design requirements such as material properties, as well as dimensional and surface tolerances. Townsend et al. generally found that measurement of metal AM surfaces is complex, due to the presence of steep slopes and occlusions, as well as highly irregular and re-entrant features at a wide range of scales. The authors advise that great care must be taken in selection of appropriate instrumentation and characterisation methods.

Townsend et al. provide a summary of their findings in the review, which I will paraphrase here:

- Broadly, in the literature examined by Townsend et al., researchers have used surface metrology and associated characterisation methods in order to gain an improved understanding of their manufacturing processes, often employing task-specific custom-designed measurement artefacts. As surface measurement has been so-far used primarily to understand

manufacturing processes, there has been little to no investigation into correlation of surface properties with part function.

- The majority of surface metrology employed in the existing literature at the time of publication involved stylus-based profile measurement, and Townsend et al. note that much information about the surface is lost by performing such an approach. Similarly, the associated characterisation performed on these profile measurements usually involves primarily the computation of ISO 4287 [50] profile parameters, with the arithmetical mean deviation of assessed profile *Ra* being the most commonly used parameter.

- When areal measurements are employed, authors note the improvement in the amount of information contained within the outputted data compared to profile measurements. When such measurements are performed, similar analyses tend to be employed as on the equivalent profile measurements, in that ISO 25178-2 [51] parameters equivalent to their profile counterparts are the most commonly employed methods. This is exemplified in the use of the arithmetical mean height of the scale limited surface *Sa* as the most commonly employed areal parameter. As such, very little research effort has been employed in examining the use of feature parameters or other methods of surface characterisation in AM applications.

- Townsend et al. note significant failings in much of the literature, in that many of the publications do not quote essential details of the experiment (measurement conditions, levelling, void filling and filtering operations employed in the computation of parameters, etc.). Failure to quote these details means that results are not reproducible and so significantly limit the scientific value of the published work.

As a result of these findings, Townsend et al. note various applications of metal AM surface measurement in understanding metal AM processes, as well as in correlating process conditions to part functionality. The authors finally discuss that, as is clear from the literature and the associated failings, metal AM surface measurement is generally in its infancy, and represents a significant landscape for scientific research.

2.2.2 Work published since the 2016 review

Since the publication of Townsend et al.'s review in mid-2016, there have been numerous publications examining the measurement of metal AM surface texture. I detailed in Section 2.1.4.6 the use of XCT for surface measurement that has broadly developed since Townsend et al.'s work was published, but I will also discuss here some key relevant contributions published since 2016. I will exclude from this Section the majority of my own contributions to the field for the obvious reason that these will be detailed throughout this Thesis.

2.2.2.1 AM surface texture characterisation methods

As discussed above, significant issues inhibit successful measurement of metal AM surfaces, relating to the presence of complex features such as undercuts, high slopes and re-entrant features. While these features are difficult to measure, they also cause problems when employing traditional methods of surface characterisation, as commonly used ISO 4287 [50] (profile) and 25178-2 [51] (areal) parameters are, by definition, computed on height map data. Reflecting the majority of surface measurement technologies, height maps are essentially *z*-values on an *xy* grid, and so are not capable of accounting for undercut and re-entrant features, such as those present on metal AM surfaces. Work has begun on addressing this problem, with Pagani et al. [205] publishing a recent paper describing an extension to existing parameter calculation methods to account for the presence of re-entrant features. Pagani et al. utilised two representations of surfaces in their paper, including data computed for B-spline and triangulated model surface reconstructions, and noted that their algorithms approximated the ISO defined parameters on the examined test surfaces with small discrepancies. The authors also noted that, while the proof-of-concept was successful, significant future work exists in extending their method to encompass more than the basic few parameters examined in the work and in redefining the filtering methods used to produce an ISO-defined scale-limited surface [30]. Subsequent work by Pagani's colleagues (Lou et al. [206]) attempts to address this latter issue by beginning to redefine filtering methods using the diffusion equation in order to cope with fully 3D datasets. This work is, however, currently

unpublished beyond a conference proceedings and is limited in these proceedings to a simulated case, so still very much represents an interesting area of current and future investigation.

Efforts have also been made in other work by Lou et al. [207] in examining methods for feature-based characterisation of metal AM surfaces. In their conference paper, Lou et al. attempted to segment attached particles from a measured surface by watershed segmentation in order to characterise the underlying topography with 25178-2 [51] parameters. In work produced in part by myself during my PhD [208,209], we similarly sought to address the issue of metal AM surface characterisation. In this work, we presented a characterisation pipeline for feature-based measurement of metal AM surface features. Following on from work presented later in this Thesis (see Chapters 4 and 5), this method involves algorithmic segmentation of features present on AM surfaces, allowing repeatable dimensional metrology to be performed on micro-scale features.

In addition to the studies discussed above, a conference paper was recently published by DiSciacca et al. [210] (in collaboration with myself and a number of my colleagues), examining the novel use of colour imaging in coherence scanning interferometry (CSI) measurements of metal AM surfaces. DiSciacca et al. noted that the use of colour imaging in CSI measurement complements the existing height map outputs from CSI systems, allowing a user to detect surface contamination (e.g. oxidation), defects and discolouration that may not be otherwise recognised using height map data alone. The authors noted the prevalence of such features on metal AM surfaces, and so suggested the usefulness of the technology for investigation of such surfaces.

2.2.2.2 Good practice

During the early portions of my PhD, a clear need for good practice was uncovered in measurement of metal AM surfaces. The findings of Townsend et al.'s review informed this opinion greatly, in that the authors noted very clearly the presence of poor practice in presentation of data in much of the literature, in

turn often casting doubt on the quality of many analyses performed in the literature. As such, much of the work performed during my PhD has been in development of such measurement good practice, which I will cover in detail in the forthcoming Chapters. Additional work was recently published with my input by my colleague Carlos Gomez that is not covered in this Thesis, however, so I will describe this work briefly here. In Gomez et al. [49,211], we detailed good practice for acquiring measurement data for various metal AM surfaces, such that measurements are optimised for data coverage, measurement area and measurement time. We also examined the effects of complex measurement features (high dynamic range lighting, signal oversampling and spectral filtering) on such measurements, and suggested areas for future areas of research in understanding measurement noise when measuring complex surfaces.

Another of my colleagues, Lewis Newton, is involved in the development of a similar publication regarding the development of similar good practice for measurement of metal AM surfaces using focus variation systems [212]. In this work, Newton et al. present a study of a focus variation systems, examining various measurement influence factors (objective magnification, lighting, lateral resolution and vertical resolution) and their effect on the measurement of a number of test surfaces. In this work, Newton et al. note that while user-chosen settings have little influence on ISO 25178-2 [51] surface texture parameters, other measurement properties such as local repeatability error and the percentage of non-measured points are significantly affected.

2.2.2.3 Application work

In addition to the publication of work involving the development of novel methods of characterisation and good practice, there have been a number of notable publications demonstrating cases where surface measurement has been used to characterise metal AM surfaces in some way. Particularly, there have been numerous attempts to correlate surface topographies to process parameters [213–215]. In Koutiri et al. [213] and Cabanettes et al. [215], the authors examine laser MPBF surfaces and correlate various processing conditions to the

output surfaces. Both of these works involve the examination of surfaces built at different angles within the build volume, and the effects of varying this angle on various ISO 4287 [50] and 25178-2 [51] parameters. The former authors also correlate the *Sa* parameter to various laser processing conditions and examine the fatigue behaviour of samples, while the latter authors go into greater depth in the surface investigation and examine additional parameters with more direct correlation of parameters to features within the measured data. Sidambe [214] conducted similar experiments on electron beam MPBF surfaces, also analysing the effect of varying build angle on ISO 25178-2 parameters.

Examination of these studies shows an increase in good practice in some publications, since the publication of Townsend et al.'s review, in that the presentation of results appears to have improved (e.g. presentation of filter settings with parameters), but this practice is not yet uniform across all publications. Remaining failings, therefore, indicate there is still a significant way to go in establishing good practice across industry and research in metal AM surface measurement.

2.2.3   Section conclusions and future research

By examining Townsend et al.'s recent review, as well as work published more recently than the review, a number of conclusions can be drawn about the current state of the art in metal AM surface measurement. I have summarised these conclusions as follows:

- From the lack of available literature, and the references in recent work to the inadequacies of existing methods of surface characterisation to accommodate the highly complex surfaces present on metal AM parts, it is clear that significant work is required in developing new methods of characterisation for the purpose of understanding these surfaces and the manufacturing technologies used to produce them.
- Similarly, from the presence of poor data reporting practices in much of the literature, there is a clear need for development of good practice in

metal AM surface measurement. While efforts have begun in this area, there exist many avenues of future work where development would be not only of use to the manufacturing community, but can be considered an immediate need.

- With the development of new techniques for characterisation, it will be necessary to continue the publication of examples of these new techniques being applied to industrial case studies. Publication of such works aids the dissemination of good practice, and provides case studies for researchers using these new characterisation methods to better understand their manufacturing processes.

2.3 Chapter Summary

Through analysis of the available literature in both the use of XCT for AM and in measurement of AM surfaces, a number of available research avenues are made clear. As discussed in Section 2.1.5.3, the potential for using XCT as surface measurement tool is clear, and so I continued with an examination of the literature regarding AM surface measurement. From this latter review, it also became clear that there are some significant issues surrounding the use of surface measurement for understanding metal AM processes, which in turn hinder its more generalised use as a tool for gaining a thorough understanding of these processes. To summarise, the tool exists, but very few people, in manufacturing research or industry, are yet able to use it to its full potential.

There clearly exists much research to be performed in development of characterisation techniques and good practice, but, firstly, it is necessary to gain a deep understanding of the metal AM surface, so that these techniques and methods may be developed. I address this need in Chapter 4, through the presentation of an 'atlas' of metal AM surface measurements designed to provide an initial overview into how different measurement instruments react to the features present on a metal AM surface.

3. Experimental methods

In this Chapter, I will provide a short summary of the methods generally used during my PhD, documenting the production and preparation of samples used for the experiments described in Chapters 4 to 8. I will also describe the general setup conditions used for surface and X-ray computed tomography (XCT) measurements performed throughout the work.

3.1 Samples

A total of four samples were used throughout this PhD, each designed for the various experiments documented in Chapters 4 to 8. The words 'sample' and 'artefact' are used interchangeably throughout this Thesis to describe samples. Further details are provided throughout this thesis where relevant, but the list of samples used is as follows:

- Sample 1: A metal AM cube of size (20 × 20 × 20) mm. This sample was produced using a Renishaw AM 250 laser MPBF system based at the University of Nottingham and manufactured in Ti6Al4V. The CAD design used to produce the sample was a nominally flat cube, with deviations from the CAD representing the surface texture of the manufactured sample. Surfaces of the cube were labelled X+, Y+, Z+, X-, Y-, Z-, for reference and to relate built surfaces to the co-ordinate system of the Renishaw system. The sample was manufactured using the manufacturer's recommended processing parameters for Ti6Al4V, to be representative of common MPBF surfaces. This sample was used for the experiments presented in Chapter 4 and Section 5.2 and is shown in figure 3.1a.
- Sample 2: A clone of sample 1, produced via the same methods. This sample was again designed to be representative of common MPBF surfaces, but without using exactly the same surface as in other experiments. This sample was used for the experiment presented in Section 5.1 and is shown in figure 3.1a.

- Sample 3: A metal AM cube of (10 × 10 × 10) mm, produced in two parts, with a cube of (5 × 5 × 5) mm, removed from the centre, so that when assembled the sample is a metal cube containing a void. One part of the cube includes three pins, while the other contains three holes, to allow the cube to be assembled by press fit. This sample was produced using an EOSINT M 280 laser MPBF system based at the 3TRPD and manufactured in Ti6Al4V. The two separate CAD designs used to produce the sample were nominally flat, with deviations from the CAD representing the surface texture of the manufactured sample. The sample was manufactured using the manufacturer's recommended processing parameters for Ti6Al4V, to be representative of common MPBF surfaces. This sample was used for the experiments presented in Chapters 6 and 7 and is shown in figure 3.1b.

- Sample 4: A metal AM cube of size (20 × 20 × 20) mm, containing internal void channels. This sample was produced using an EOSINT M 280 laser MPBF system based at the 3TRPD and manufactured in Ti6Al4V. The CAD design used to produce the sample was nominally flat with nominally cylindrical channels, with deviations from the CAD representing the surface texture of the manufactured sample. The sample was manufactured using the manufacturer's recommended processing parameters for Ti6Al4V, to be representative of common MPBF surfaces. This sample was used for the experiments presented in Chapter 8 and is shown in figure 3.1c.
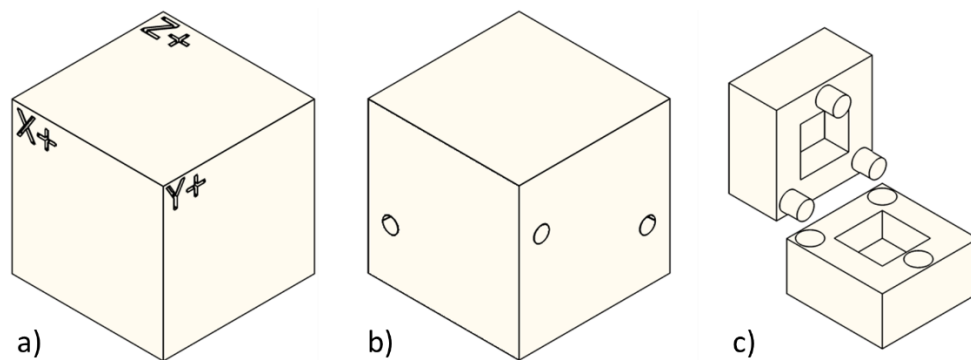
Figure 3.1. CAD designs of samples used during the production of this Thesis: a) samples 1 and 2; b) sample 3; c) sample 4.

Following production by either of the two AM systems used, samples were removed from build chambers, and separated from build plates. Support structures were removed. No heat treatment or finishing processes were performed, in order to maintain the as-built surfaces. Surfaces were cleaned using a compressed air gun prior to measurement to remove any loose powder particles and dust prior to measurements being made. Prior to and between measurements, samples were stored and transported in bubble wrap and a plastic case to protect the surfaces, and were handled with nitrile gloves when removal from the storage packaging was required. Prior to measurements, samples were 'soaked' in the measurement environment for no less than an hour, in order to ensure their temperature matched that of the measurement environment at the time of measurement.

3.2 General surface measurement conditions

A number of different optical and contact surface measurement technologies were used during the production of this Thesis. Although each instrument necessitated different measurement parameters, the measurement and sample setup was constant between these measurements. Particularly, the following conditions were employed:

- Measurements were made in various temperature-controlled laboratories, where temperature was set at (20 ± 1) ℃ in the poorest case.
- As samples were designed with flat bases and support structures required during manufacture were removed, no specific fixturing was required to hold samples. As such, samples were placed on the measurement base of each instrument. No clamping was required in any case.
- Multiple measurements of individual surfaces (i.e. repeats) were made in repeatability conditions, i.e. samples were not disturbed between measurements and measurements were made in immediate succession.
- Unless otherwise stated, optical measurements were performed before contact measurements, in order to prevent any effects of surface damage resulting from contact measurements.

Beyond these broad considerations, specific measurement parameters (e.g. objective magnification, illumination) are described in each measurement case in the relevant Chapters and Sections.

3.3 General XCT measurement conditions

Two different XCT systems were used during the production of this Thesis, one for the majority of measurements made, while another system was additionally used as part of the experiment documented in Chapter 6. Measurement settings are described in each case in the relevant Chapters and Sections, but as the with surface measurements, a number of XCT measurement conditions were kept constant for all measurements. These conditions are as follows:

- Measurements were made in temperature-controlled laboratories, where temperature was set at (20 ± 1) ℃. For the XCT system employed throughout the majority of the Thesis, additional temperature control was employed within the XCT cabinet itself, set at (20 ± 0.1) ℃.

- The XCT system used throughout the majority of my PhD was a system specifically designed for performing measurements; designated by the manufacturer as a 'metrology' system. The primary advantage of using a system setup for measurement is that the voxel size (i.e. the basis for measurements made on the XCT data) is provided by the system without the need for the inclusion of an artefact of known size in each scan, through the use of calibrated performance verification artefacts during the setup of the machine. For non-measurement systems, voxel scaling [198] operations are commonly performed using such artefacts to provide correct voxel sizes, though no such scaling operation was required for the system employed here. For the other system used during the production of Chapter 6, a scaling operation was considered but ultimately rejected as comparison of extracted topographies to data acquired using other systems did not yield any perceptible scaling error.

- The use of artefacts containing flat faces (such as cubes) for XCT measurements made using cone beam systems provides the potential for

unwanted imaging artefacts, if flat faces are placed orthogonal to the rotation axis (see Section 311.2.3.2 and [56]). To prevent such imaging artefacts, samples were fixtured so that all flat planes lay at an angle 45° to the rotation axis, through the use of a fixture containing a trihedral hole (see figure 3.2). This fixture was manufactured using a desktop material extrusion system.
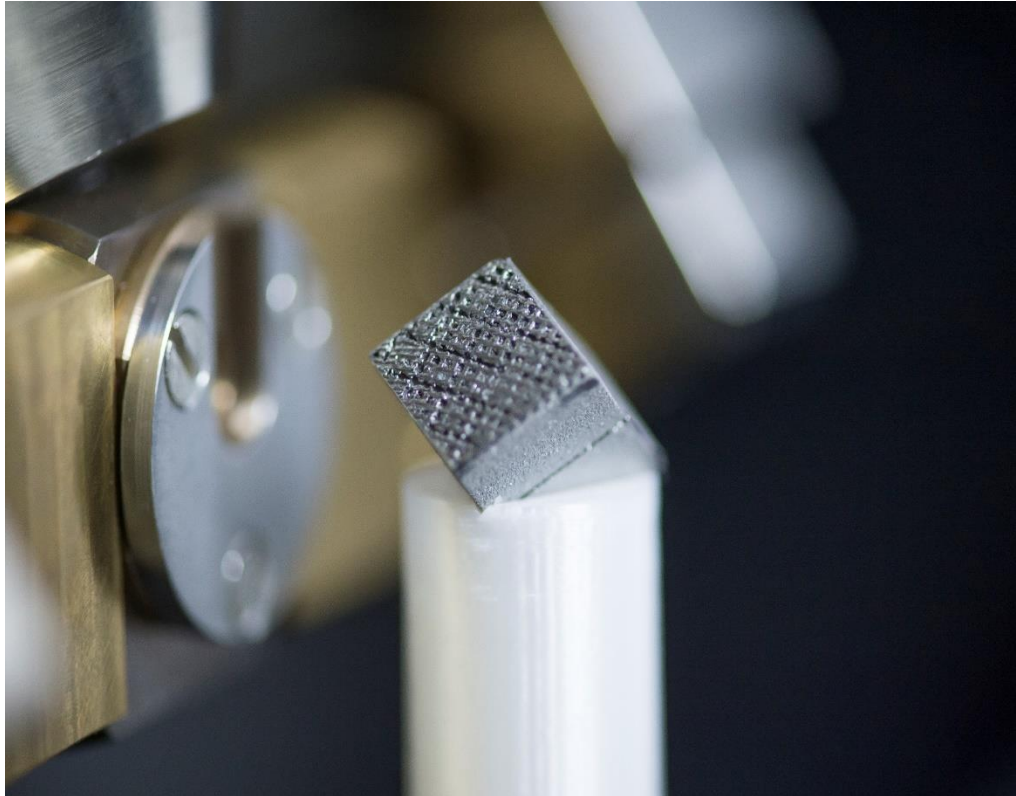
Figure 3.2. Sample 3 in the trihedral hole fixture, placed within the XCT system.

3.4 Summary of practical experiments

In this Section, I will briefly detail the practical experiments performed in pursuit of the general contributions to science described in Section 1.4. Excepting contribution 1, which involves no practical experiments (see Chapter 2), contributions are addressed with the following experiments:

- Contribution 2: production of an 'atlas' of powder bed fusion surfaces. This objective is addressed via a wide array of surface measurements of an area of sample 1, made using different systems in different setups.

The data are qualitatively assessed to determine instrument/surface interactions.

- Contribution 3: application of novel methods of directly comparing surface topography data acquired using different measurement technologies. This objective is addressed via repeat measurements of areas of samples 1 and 2 in 'good practice setups' (informed by the first experiment). The data are used to construct statistical models of topographies and to assess discrepancies between measurements.

- Contribution 4: determination of a bespoke pipeline for the measurement of surface texture using XCT. This objective is addressed by measurement of sample 3 using two different XCT setups and two different optical systems. The conversion of data from the raw XCT output to height map format is documented.

- Contribution 5: understanding the sensitivity of XCT systems to surface topography measurement. This objective is addressed by making repeat measurements of sample 3 using various XCT setups and assessing their similarity to a reference optical measurement.

- Contribution 6: application of the newly developed XCT surface measurement procedure to an industrial test case. This objective is addressed by measurement of sample 4, using two XCT and two optical methods.

3.5 Chapter summary

In this Chapter I detailed the samples and measurement conditions used throughout the Thesis. I have additionally described in brief the experiments performed in Chapters in reference to the novel contributions to science detailed in Section 1.4. Further information about the various experiments is provided throughout where relevant.

4. A metal additive surface measurement 'atlas'

In Chapter 2, a number of barriers to the increased adoption of AM technologies were identified, with the measurement of internal and hard-to-reach surfaces having been noted as an area where further research is needed. In order to develop methods for measurement of internal and hard-to-reach AM surfaces, a fundamental issue must first be addressed: the need for a more thorough understanding of the metal additive surface in general [9]. In this Chapter, initial investigations into the types of surfaces produced by metal AM as well as the various features present on a metal AM surface are documented, through qualitative comparison of surface measurements made using a variety of measurement technologies. This work forms the basis of the investigations that followed through my PhD, particularly providing the foundations for Chapter 5. The work in this Chapter was presented at the 2016 ASPE/euspen conference: Dimensional Accuracy and Surface Finish in Additive Manufacturing [216].

4.1 Towards an understanding of the metal additive surface

Metal AM topography is examined here at the micrometre scale (i.e. surface micro-scale topography), where many topographic features relevant to the metal AM signature exist [9,207]. As discussed in Chapter 1, a wide array of new and established measurement technologies are available for the investigation of surface features at such a scale [29]. For qualitative visual inspection, digital optical microscopy (DOM) and scanning electron microscopy (SEM) are the methods most commonly used for the production of colour or intensity images. Focus stacking (FS) technology [217] is frequently used in high magnification digital optical microscopy to compensate for the relatively shallow depth of field. Coarse dimensional assessment is sometimes possible using digital images produced by SEM or optical microscopy, provided the imaging technology allows pixels to be reliably assigned spatial coordinates. Even in such a case, quantitative measurements are typically limited to linear distances and areas in the image plane, and are subject to a series of further limitations

(e.g. due to shadowing or the orientation of the measurand features with respect to the imaging direction).

Where a quantitative measurement is required, contact stylus profilometry [29] is the most commonly used and often 'trusted' technology for the assessment of surface texture, due to the relatively simple and well-understand measurement process it employs. Profile data is encoded as a sequence of surface height values, arranged at regularly spaced points along a straight line. A quantitative assessment of profile properties is typically performed through the computation of profile texture parameters, according to ISO 4287 [50]. Areal topography information can be captured by having a contact stylus profilometer scan a series of (usually) parallel profiles, but the sequential and intrinsically slow nature of the process makes such a solution often untenable in a production environment [29]. The same speed issue is shared by atomic force microscopy (AFM) [218], which operates in a similar raster-scanning fashion. AFM is also further limited by small measurable ranges which are typically incompatible with rough surfaces and wide measurement areas, a common scenario experienced when measuring many metal AM surfaces [9].

A series of optical technologies have more recently been developed for areal surface topography measurement (see figure 4.1), combining both imaging and profilometry [29]. Optical technologies, such as confocal microscopy (CM) [35,36], coherence scanning interferometry (CSI) [41,42] and focus variation (FV) microscopy [45,46], allow for acquisition of topography information at much faster speeds than previously possible via stylus measurement (see Chapter 1). Instruments based on such technologies provide height maps, i.e. point height information arranged on a regular *xy* grid. Cross-sectional profiles can be extracted from the datasets for the computation of profile texture parameters, or, alternatively, the new set of areal surface texture parameters defined in ISO 25178-2 [30,51] can be computed directly from height maps, as a means of providing far more quantitative surface texture information than possible using a stylus system in the same time period. Also, it has been recently demonstrated that surface topography information can be extracted from volumetric data obtained via X-ray computed tomography (XCT) [193,216];

once the surface is extracted as a triangulated mesh, it is typically resampled into a height map from a chosen virtual observational viewpoint, and processed again to compute surface texture parameters.
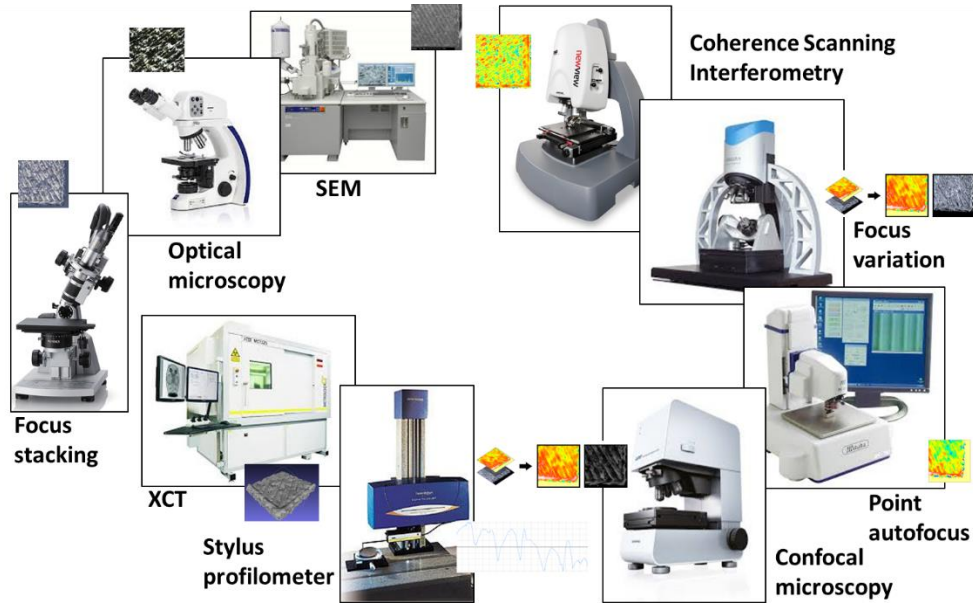
Figure 4.1. Examples of measurement technologies capable of measuring the metal AM surface and their returned types of datasets.

Regardless of the data source, when dealing with the understanding of a manufacturing process, examination of texture parameters is the solution typically adopted by industry and the scientific community. A recent review of surface metrology for metal AM [9] revealed that the ISO 4287 profile parameter *Ra* (see Chapter 1 for further information on this parameter), is still by far the most widely adopted indicator of surface texture. However, the computation of *Ra* and other simple amplitude parameters involves condensing all of the information present on a surface into a single scalar number, which is then often expected to represent all of surface's properties. In many cases, this process represents an over-simplification of the information, which may undermine the effectiveness of the surface data in the investigation of a manufacturing process signature: by treating all measured surface points the same, texture parameters are often incapable of capturing local topographic detail, which may carry valuable information related to the process signature

[219,220]. Moreover, significant topographic differences may result in the same values for several texture parameters [221].

Comparison of field texture parameters is typical in surface metrology practice, but it is often performed without consideration of whether or not the parameter (or indeed, the measurement technology itself) is actually capable of acquiring the required topography information. For example, the features that relate to the function of interest may be smaller than the resolution of the instrument, or completely obscured in parameter calculation by other dominant features. Alternative approaches to topographic assessment stem from the notion that the measured points should be first divided into subsets, each representative of a relevant topographic formation (i.e. feature-based segmentation of the field of view); then texture parameters can be computed by aggregating geometric properties of the individual features [51,221–225]. If feature-based approaches are to be further pursued as a viable means of investigating a manufacturing process 'fingerprint', especially when dealing with hard-to-measure surfaces, such as many of those produced by metal AM, a comprehensive evaluation of the capability of each measurement technology to return accurate local topography information is required. Topography measurement technologies vary as they cover different ranges of scales and resolutions, and may react differently even when operating at the same scales. Sensitivity to complex surface features varies across technologies and across instruments. These ideas are the subject of significant investigation and will be discussed throughout this Thesis, particularly in Chapter 5. Metal AM surfaces typically contain many complex features, such as high slopes, vertical walls, undercuts, deep recesses and changes in surface properties (such as local oxidation). Such features may escape skew results if the assessment is performed exclusively through the computation of texture parameters.

This work focuses on laser metal powder bed fusion (MPBF); a process which belongs to the powder bed fusion family of AM technologies [6]. In MPBF, source material in the form of fine particles (powder) is spread onto a metal plane and selectively fused by an energy source (laser or electron beam) traversing the surface, following a 2D toolpath. Once layer generation is

complete, a new powder layer is spread onto the previous layer, and the process is repeated in order to continue fabrication. During the process, a large number of physical interactions take place between the energy source, the surface of the powder bed and the layers underneath, and it is such interactions that must be fully investigated and understood, in order to improve the MPBF process. The typical surface features encountered on an MPBF layer, and representative of the manufacturing process fingerprint, are summarised in figure 4.2.
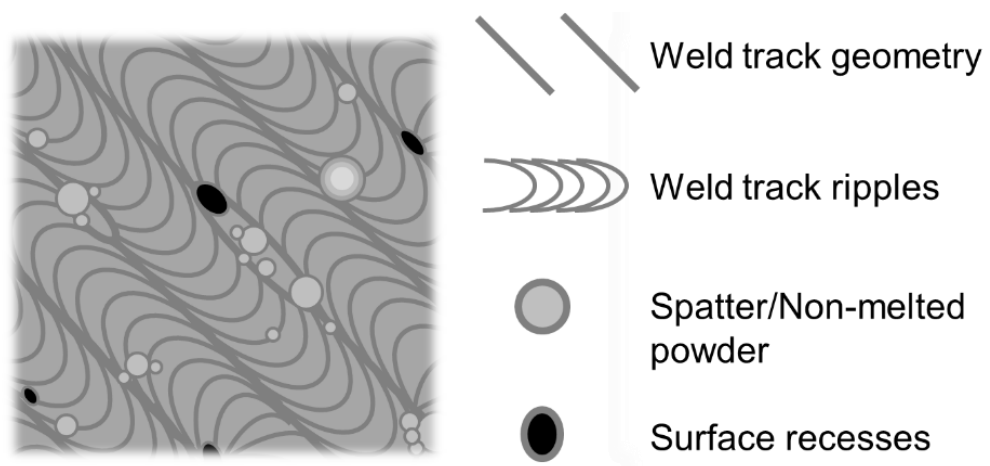
Figure 4.2. Topographic features relevant to investigation of the manufacturing process fingerprint, as they appear on a layer of an MPBF metallic part.

Laser MPBF surface topography is typically dominated by weld tracks, resulting from the fusion and subsequent solidification of consecutive melt pools [222], which impart a strong texture directionality indicative of the laser (or electron) beam path. At smaller scales, weld tracks are covered by chevron-shaped ripples, indicating the beam scanning direction, and may feature smaller-scale thermal cracks and areas of local oxidation. Throughout weld tracks, high aspect-ratio singularities are observable, typically consisting of deep recesses or sphere-like protrusions. Recesses may result from incomplete seams between weld tracks, balling phenomena (i.e. discontinuities of the track itself) or, at smaller scales, open micro-porosity [224–226]. Sphere-like protrusions are formed either from unmelted or partially-melted powder particles (appearing alone or in clusters), or spatter particles, i.e. molten material ejected from the melt pool during beam traversal, that impact the nearby surface during solidification [224]. As the MPBF surface is the result of multiple melting and

re-melting phenomena, involving the current layer as well as a number of layers underneath, multiple, larger-scale, wave-like components affect the final appearance of the top surface. This partially random, partially deterministic topography usually forms a recognisable pattern, i.e. the fingerprint of MPBF technology [103,227].

This Chapter represents a preliminary investigation into the metal additive surface, with the intention of understanding the features left behind by the MPBF process fingerprint, as opposed to analysing the finish of post-processed metal additive surfaces. It is appreciated that many AM parts are post-processed to modify their surface texture, but if the surface texture is to be used to control process parameters, then it is the unfinished surface that is of primary interest.

4.2 Chapter methodology

4.2.1   The MPBF specimen

For this work, a portion of the top surface of a MPBF artefact was selected as representative of the typical features encountered on a metallic surface produced by MPBF. The region of interest (ROI) used was a square of approximately (2×2) mm in size, taken from the top surface of a $(20 \times 20 \times 20)$ mm cube artefact, manufactured from Ti6Al4V using a Renishaw AM 250 laser MPBF machine from a CAD model of a cube. The ROI was deemed representative of the MPBF process, since it had not been post-processed other than cleaning and so still carried clear signs of the process fingerprint. The ROI was located at a corner of the artefact surface, so that the cube edges could be used as alignment references by which to compare topography measurements. The size of the ROI ensured that the field of view was adequately representative of the topographical formations expected to be found on the top surface, based on previous work by other authors [106]. It should be noted at this point that different AM machines will produce different surfaces, as does the use of different metals. Even for the same combination of machine and material, the actual geometry of the surface (flat, freeform, etc.), its orientation (orthogonal to the building direction, parallel, etc.) and position with respect to other part shape features (close or far

from the part edges) will all contribute to influencing the actual properties of local topography. However, the sample used in this work could be considered broadly representative of MPBF surfaces, as encountered during the review stages of my PhD (see Chapter 2). Further information about this sample is detailed in Section 3.1.

4.2.2   Measurement setups

A number of measurement technologies, types of returned datasets and measurement setups were considered at the qualitative stage of this research. Instrument names have been redacted to prevent direct comparison of commercial instruments. In the descriptions below, FOV is the field of view, LR is the lateral resolution and NA is numerical aperture. In each case, LR-pixel refers to the pixel spacing of the detector used by each instrument, LR-optical refers the calculated Sparrow optical limit [34] of each instrument and LR-contrast refers specifically to the distance from the centre of each pixel used by the FV instrument to compute local contrast; selected during the measurement. The Sparrow optical limit was calculated using a wavelength of 580 nm for white-light systems (CSI and FV) and 405 nm for the laser CM system. In each measurement setup for the optical systems, additional magnifications were considered but ultimately discarded; being either too low resolution to capture relevant topographic details, or too time consuming to achieve equivalent lateral coverage of the ROI and resulting in excessively large datasets. The measurement setups used and the outputted data types are outlined as follows:

- SEM: 2D intensity images, 61× magnification, in secondary electron mode;
- DOM: 2D colour maps, 100× to 1000× variable objective at 200× (FOV 3.05 mm × 2.28 mm) with FS.
- CM: height maps and 2D intensity maps (with FS) 20× objective lens (NA 0.6, FOV 0.64 mm × 0.64 mm, LR-pixel 0.63 μm, LR-optical 0.32 μm), stitching of multiple images performed using the manufacturer's software.
- CSI: height maps, 10× objective at 0.5× zoom (NA 0.30, FOV 1.68 mm × 1.68 mm, LR-pixel 1.64 μm, LR-optical 0.95 μm) , 10× objective at 1×

zoom (NA 0.30, FOV 0.83 mm × 0.83 mm, LR-pixel 0.82 μm, LR-optical 0.95 μm) and 20× at 1× zoom (NA 0.40, FOV 0.42 mm × 0.42 mm, LR-pixel 0.41 μm, LR-optical 0.68 μm), stitching of multiple images performed using the instrument manufacturer's software.

- FV: height maps and 2D colour maps (with FS), 5× (NA 0.15, FOV 2.82 mm × 2.82 mm, LR-pixel 1.76 μm, LR-optical 1.82 μm, LR-contrast 7 μm), 10× (NA 0.30, FOV 1.62 mm × 1.62 mm, LR-pixel 0.88 μm, LR-optical 0.91 μm, LR-contrast 4 μm), 20× (NA 0.40, FOV 0.81 mm × 0.81 mm, LR-pixel 0.44 μm, LR-optical 0.68 μm, LR-contrast 3 μm) and 50× (NA 0.60, FOV 0.32 mm × 0.32 mm, LR-pixel 0.18 μm, LR-optical 0.45 μm, LR-contrast 1.5 μm), multiple illumination settings, stitching of multiple images performed using the manufacturer's software.

- XCT: triangulated meshes, geometric magnification of 44.1×, leading to voxel size of 4.53 μm, 3142 X-ray projections formed by averaging two frames per projection, each lasting 2 s; X-ray tube voltage 145 kV and current 66 μA; a 0.25 mm copper X-ray pre-filter was used to attenuate lower energy X-rays and a warmup scan of approximately one hour was performed prior to the scan.

- Stylus profilometry: profiles, 2 μm spherical tip, sampling distance of 0.5 μm in the scan direction.

A note must be made here about the various types of data outputted by each of these systems, explaining what is meant by the terms used above. 'Colour maps' are images in which pixels are mapped to 2D xy coordinates. In contrast, 'height maps' consist of arrays of z points located on 2D xy grids. Although height maps serve to represent 3D surfaces, they are not considered to be truly 3D datasets. Height maps are limited, in that each xy point can take only one z value, so height map data cannot account for the presence of undercuts and overhanging features which are occasionally present on surfaces. As such, height maps are generally considered to be limited to '2.5D' data, and are referred to throughout this Thesis as such. 'Intensity maps' are similar to colour maps, in which each pixel in the intensity map provides a metric of the quality of the associated data point on the height map. For optical systems (as used here) points on these maps

generally pertain to the amount of light returned to the instrument's sensor that was used to create the related data point in the associated height map. In these intensity maps, a point high on the scale has received a relatively large amount of light and so is considered to be of relatively high quality, while a point lower on the scale has received relatively less light and so is considered to of relatively lower quality. These intensity maps are generally indicative of the point by point repeatability for the optical system [212]. 'Triangulated meshes' are fully 3D geometric models comprising a 3D set of triangles in a mesh, connected by their common corners and edges. These meshes are often created by drawing vertices between points on a 3D point cloud. As they are fully 3D, triangulated models do not have the same limits regarding undercuts as height maps and are able to capture this information fully. Currently, however, triangulated meshes must be resampled into height maps in order for texture parameters (such as those defined by ISO 25178-2 [51]) to be computed. Where possible, measurement solutions were also compared across different setups, including illumination (for optical technologies) and magnification. The investigation focused specifically on how topographic formations are processed by the various measurement solutions, analysing in particular the features discussed above that typically represent the MPBF manufacturing process fingerprint.

4.2.3   Data analysis

Raw data were analysed using the surface metrology software MountainsMap by DigitalSurf [228]. Areal topographies were levelled by least-squares mean plane subtraction using a reference region away from the sample edges. Dedicated functions in the software were used to align datasets, along with manual refinement via visual inspection of topographic formations. Stylus profile datasets were levelled by least-squares mean line subtraction. Profiles were coarsely aligned with respect to areal datasets through inspection of minor scratch marks produced by the stylus, visible in CM and CSI measurements acquired following stylus measurements. Fine alignment was performed by manually searching for the closest matches in the surroundings of each coarse alignment position.

XCT volumetric data were reconstructed using the manufacturer's software, using a second order beam hardening correction and a ramp filter. Surfaces (triangulated meshes) were determined in VGStudio MAX 2.2 by Volume Graphics [73], using the maximum gradient method over four voxels, with the ISO-50 isosurface as a starting point [139]. The surface was exported as a triangulated mesh and then automatically converted into a height map within the surface metrology software MountainsMap by DigitalSurf [228], at a spatial resolution automatically determined by MountainsMap (2.87 µm) to match the point density of the original triangulated mesh, approximately defined by the voxel size.

4.3 Chapter results

As discussed, data were acquired using a numerous different measurement technologies, so are presented here with respect to the different datasets outputted by each instrument.

4.3.1 Visual inspection of 2D colour or intensity images and maps
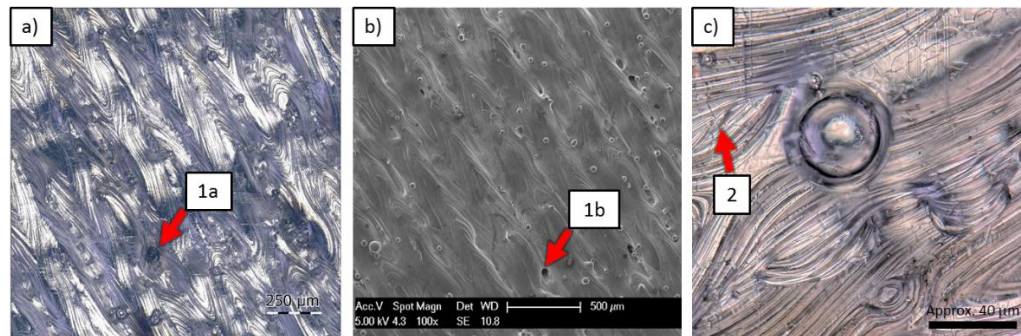
Figure 4.3. a) and c) Optical microscope and b) scanning electron microscope (SEM) images of topographic features typical of a Ti6Al4V MPBF surface, manufactured using a Renishaw AM 250. Arrows 1a and 1b point to the same example surface recess in optical and SEM images respectively, while arrow 2 indicates local cracking in a higher resolution image. Straight vertical and horizontal scratches also visible in the image were caused by contact stylus measurements performed during the experimental campaign. Figure published in [229].

In figure 4.3, the chosen ROI is shown as it appears in an SEM image, and in optical focus stacked colour maps generated by the DOM and FV. The

differences in colour between the optical images can be attributed to differing illumination conditions. Both the optical images highlight the role of reflected light, which reveals smaller-scale features, such as the weld track ripples, but leads to bright, highly saturated regions corresponding to the most exposed parts of the topography, strongly contrasted with the darker, deep recesses. This is a typical issue with optical imaging of MPBF surfaces: higher intensity incident light is needed to illuminate recesses, but increases the likelihood of saturation in more reflective regions, with the consequent loss of topographic detail [230]. This issue is in stark contrast to the output of SEM imaging, where it is generally easier to obtain clearer images overall. Differences in contrast between the SEM and optical images may also lead to different perceptions of depth (i.e. overall irregularity of the surface). Both optical and SEM images are characterised by artefacts specific to each measurement technology. Multiple reflections, projected shadows and optical chromatic/geometric aberrations are common for optical imaging [230]; while charging artefacts, smears and bright and dark halos are typical of SEM imaging [231]. For optical imaging, the same surface can look considerably different if imaged through coaxial or ring light, polarised or non-polarised light, monochromatic or polychromatic light, and if processed with different detector settings (saturation, contrast, etc. [212]). Analogously, SEM imaging is affected by multiple parameters, such as electron beam energy and detector sensitivity.

Both optical images of figure 4.3 have been produced by FS to compensate for small depth of field at high magnifications; this algorithmic processing operation influences the final quality of the obtained images. FS is not used in the SEM image. While there is no algorithmic processing in the SEM image, slight local discrepancies in focus may introduce bias in the visual interpretation of some topographic details. Finally, for optical measurement processes to cover a significant field of view at high magnification typically requires the use of stitching (i.e. collating multiple individual images, overlapped and aligned at their margins). Stitching produces results with uncertainties that are difficult to quantify and predict. While visual inspection of 2D images can be a powerful tool, the method is intrinsically subjective, and there is a tendency towards an over reliance on the technology, and a common assumption that visualisations

are representative of the 'truth'. Comparing colour or intensity images and maps obtained from multiple instruments is often helpful in avoiding such tendencies.

4.3.2   *Visual inspection of height maps*

4.3.2.1 Confocal microscopy
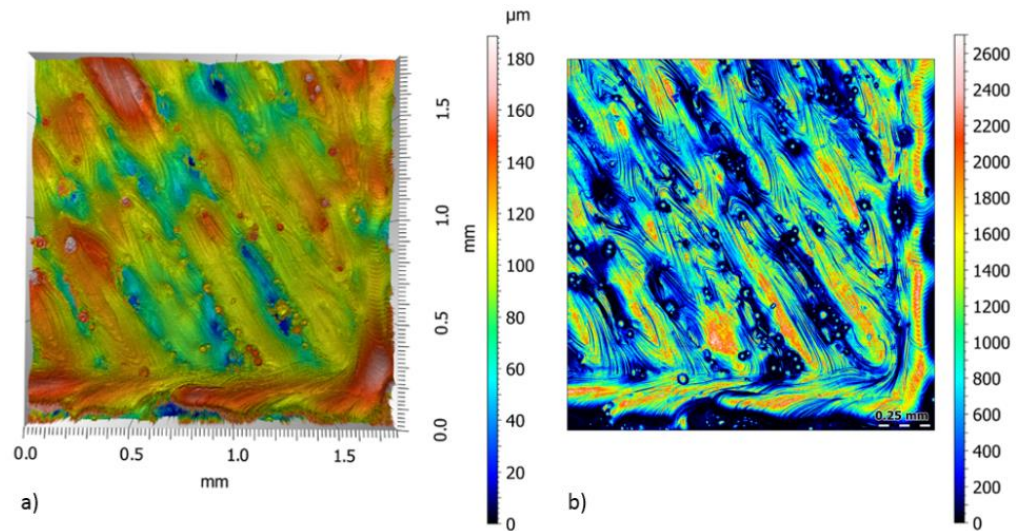
Figure 4.4. Datasets generated by the CM using a 20× objective lens and coaxial lighting: a) height map in false colours; b) intensity (quality) map in false colours.

A height map obtained with the CM is shown in figure 4.4a, rendered using false colours. Weld tracks, and longer-wavelength hills and recesses, are clearly visible. In addition, small-scale features, such as weld track ripples, are well resolved. Sphere-like protrusions (unmelted and spattered particles, depending on size) are not accurately reconstructed. This result is expected, since CM is well known to have issues when measuring spherical objects resulting from the presence of high slopes [232,233]. High spatial frequency noise artefacts scattered throughout the surface are easily detectable, generally corresponding to sharp height changes, located for example in the areas immediately surrounding unmelted and spattered particles. As an indication of the behaviour of CM over the MPBF surface, an additional intensity map produced by the instrument is reported together with the height map (figure 4.4b), also rendered using false colour. The intensity map provides an indication of the amount of light reflected back to the detector through the confocal pinhole in the best-focus

position for that pixel. Higher intensities indicate a stronger signal and, therefore, a higher probability that the instrument was able to obtain an accurate estimate of local height information. The intensity map clearly shows, as is understandable, that less light is reflected by recessed regions, making it more difficult for the instrument to correctly reconstruct recess topography. Similar low-intensity regions are observed around protruded singularities (i.e. unmelted and spattered particles) consistent with the poor quality reconstruction of such features in the height map.

4.3.2.2 Coherence scanning interferometry

Although older CSI technologies have shown difficulties in measurement of highly irregular surfaces [42], recent advances allow for the measurement of high slope angles (see Chapter 1 and [234,235]) and make CSI a viable option for measurement of AM surfaces [236]. The main advance allowing for high slope measurement is in CSI signal detection: by increasing camera acquisitions with oversampling, or through the use of increasingly sophisticated detection algorithms, CSI systems are now able to overcome previous limits on maximum measurable slopes. In figure 4.5, height maps obtained using the CSI are shown, highlighting the capability of CSI in the acquisition of small-scale topography (e.g. weld track ripples), showing performance similar to that seen using CM. The resolving power is proportionate to magnification: in the 5× data a visibly larger percentage of the topography than in higher magnification data falls below the measurement acceptability threshold and is encoded as missing values (voids) by the instrument. The amount of voids decreases as magnification increases, and the reconstruction of protruded singularities causes a reduced number of measurement artefacts than when using CM. Similarly to CM, however, and again because of the relatively low amount of light reflected back to the detector compared to the average for the measured area, the measurement of recessed features is where CSI technology has issues, where features identified as recesses using other technologies commonly result in a greater amount of non-measured points. Interestingly, aside from a reduced number of voids observed as magnification increases, the visible topographies reconstructed using CSI remain generally consistent at different magnifications.
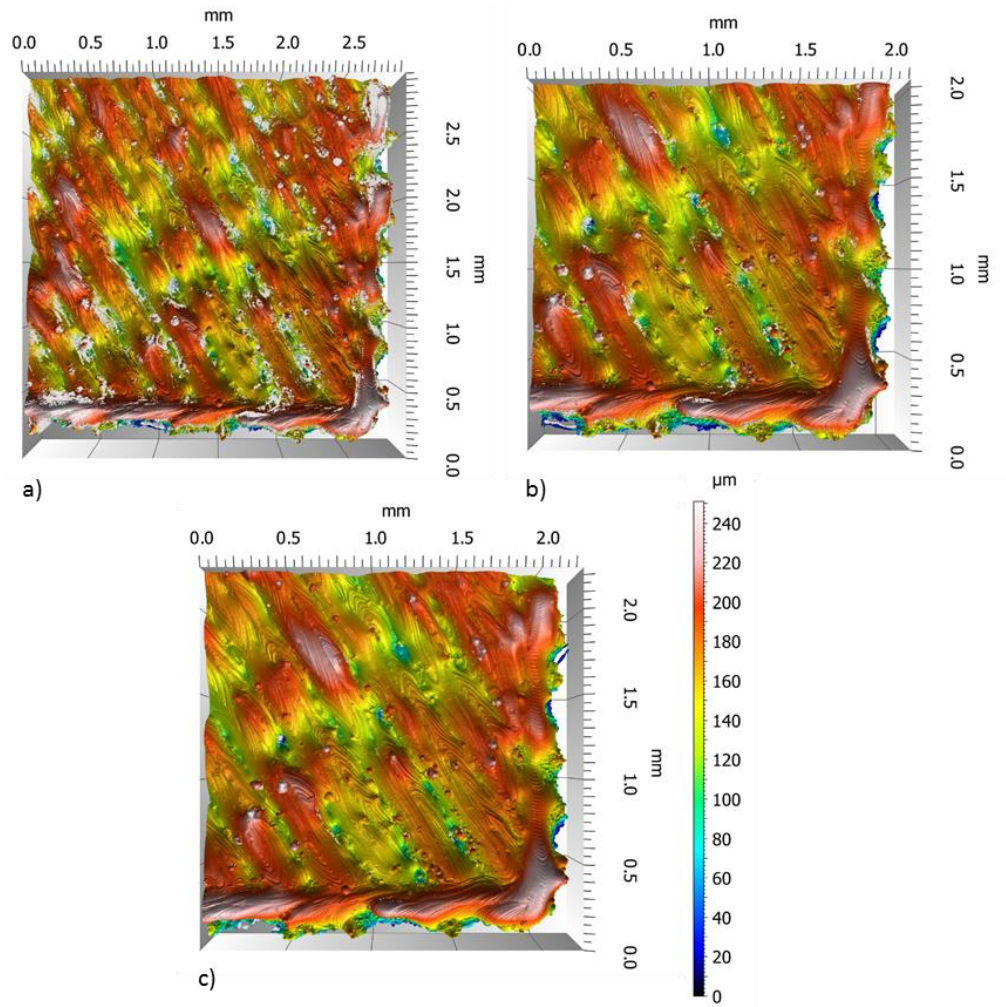
Figure 4.5. Height maps generated from CSI data: a) 5× magnification (10× objective lens, 0.5× optical zoom); b) 10× magnification (10× objective lens, 1× optical zoom); c) 20× magnification (20× objective lens, 1× optical zoom)

4.3.2.3 Focus variation microscopy

FV relies on an algorithmic assessment of local image contrast, through examination of pixel colour values on a series of vertically stacked images, to detect in-focus points, and thus determine a surface height corresponding to each pixel. As such, FV is also affected by how light is reflected back into the detector, i.e. the optical appearance of the surface (see [237] for a theoretical treatment of the imaging process in FV). For MPBF surfaces, the high number of surface irregularities provides ample information for the identification of patterns used to compute local contrast. However, the deep recesses present on MPBF surfaces return very little light, appearing dark and making detection of

106

contrast challenging. Similarly, protruded singularities may be highly reflective (and smooth at high magnifications) especially with the high intensity of incident light sometimes needed to illuminate the recesses; thus making it difficult to determine local contrast. Some topographies obtained with the FV at different illumination conditions are shown in figure 4.6.

To account for variations between lighting settings, the experimental campaign involved investigation of all possible combinations of coaxial and ring lighting; the presence or absence of polarisation; varying levels of emission intensities, and various exposure, contrast and gain setups at the detector; all examined at different magnifications. Some of the most relevant findings are reported in figure 4.6. Here, the use of ring light consistently produced results in better agreement with the other measurement technologies, independent of other setup variables. This result is in agreement with previous work on the FV theory [237], which indicates ring light illumination as the most appropriate for measurement of surfaces which feature a mixture of diffuse and specular reflections, as is the case for the MPBF surface. Figures 4.6a to 4.6c show the main differences between three optimal setups based on coaxial, coaxial polarised and ring light respectively. Figures 4.6d to 4.6f show how smaller-scale features, such as weld track ripples, become increasingly visible at higher magnifications, as is to be expected as a result of increasing the available lateral resolution. In comparison to CM and CSI measurements, FV results in the lowest amount of non-measured points, though it is difficult to assess whether this is due to generic use of FV technology, or the specific commercial implementation used in this example. The sphere-like appearance of unmelted and spattered particles is lost, as a result of unpredictable jumps in local focal height determination. Again, as the observed protruded singularities present as relatively smooth and reflective in data acquired using other systems, such behaviour is to be expected. Interestingly, some FV measurement artefacts are misleading and not easily detectable without comparison to other measurement technologies. For example, small-scale deep recesses are sometimes rendered as localised protrusions, because multiple specular reflections can cause the instrument to return a mirrored focal plane as the correct surface.
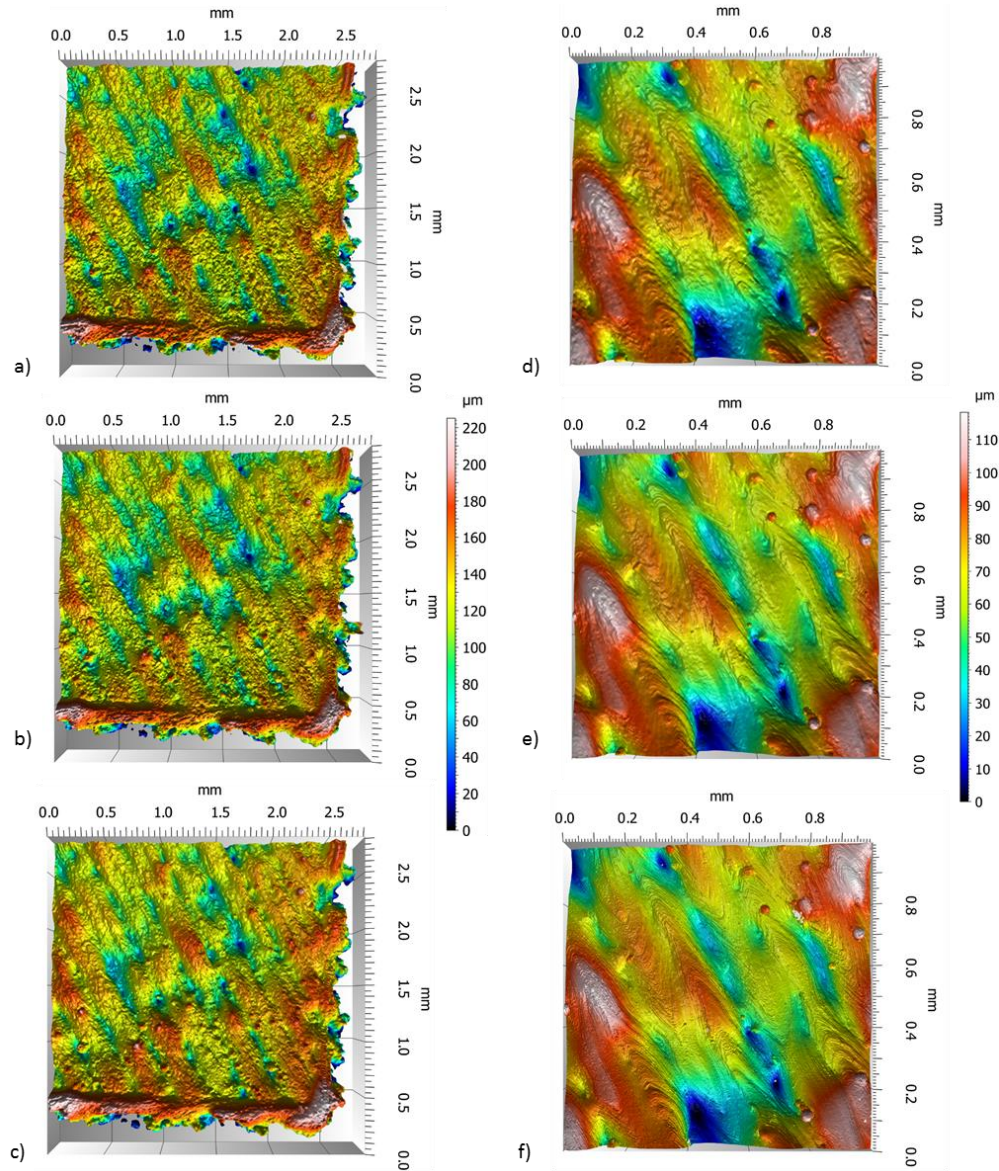
Figure 4.6. Height maps generated by FV: a) 5× magnification, coaxial light; b) 5× magnification, polarised coaxial light; c) 5× magnification, ring light; d) 10× magnification, ring light; e) 20× magnification, ring light; f) 50× magnification, ring light

4.3.2.4 X-ray computed tomography

In figure 4.7 a, a height map obtained from XCT measurement is shown. The height map has been obtained by conversion of a triangulated mesh (as shown in figure 4.7b and figure 4.7c); in turn extracted through a gradient-based boundary detection method from a volumetric XCT dataset [72]. Although the resolving power of XCT is not at a level achievable by some of the optical topography measurement setups discussed earlier, the gap is narrowing as XCT

technology improves. Triangulated meshes obtained from XCT have the advantage of capturing undercut topography, a feature which opens new possibilities for the development of novel topography exploration pathways. However, this advantage is generally not being exploited, as in order to compute conventional ISO surface texture parameters, data must be converted to height maps (though it should be noted that ongoing research seeks to address this issue [205]). In addition to the advantage of full 3D mesh production, XCT topography is unaffected by the discussed measurement issues relating to the use of objective lenses and visible light that affect the optical technologies (e.g. slope limits, multiple reflection), as it does not rely on the underlying physics that causes these problems. XCT does, of course, come with its own substantial set of challenges beyond the aforementioned resolution limits (which are dependent on both system and sample geometries), relating to difficulties in the determination of surfaces from volumetric data, traceability, instrument calibration, performance verification and reliability; high scanning costs and lengthy measurement times [57,58]. Also, the aforementioned conversion of XCT data from a triangulated mesh into a height map is of interest, as the outcome of this processing step is not understood. Particularly, in this case, MountainsMap performs the conversion operation as part of a 'black-box' (i.e. without explaining how the operation is performed), and it is probable that the height map topography is dependent in some way on how this operation is performed. I will expand on this point in the Chapter 5.
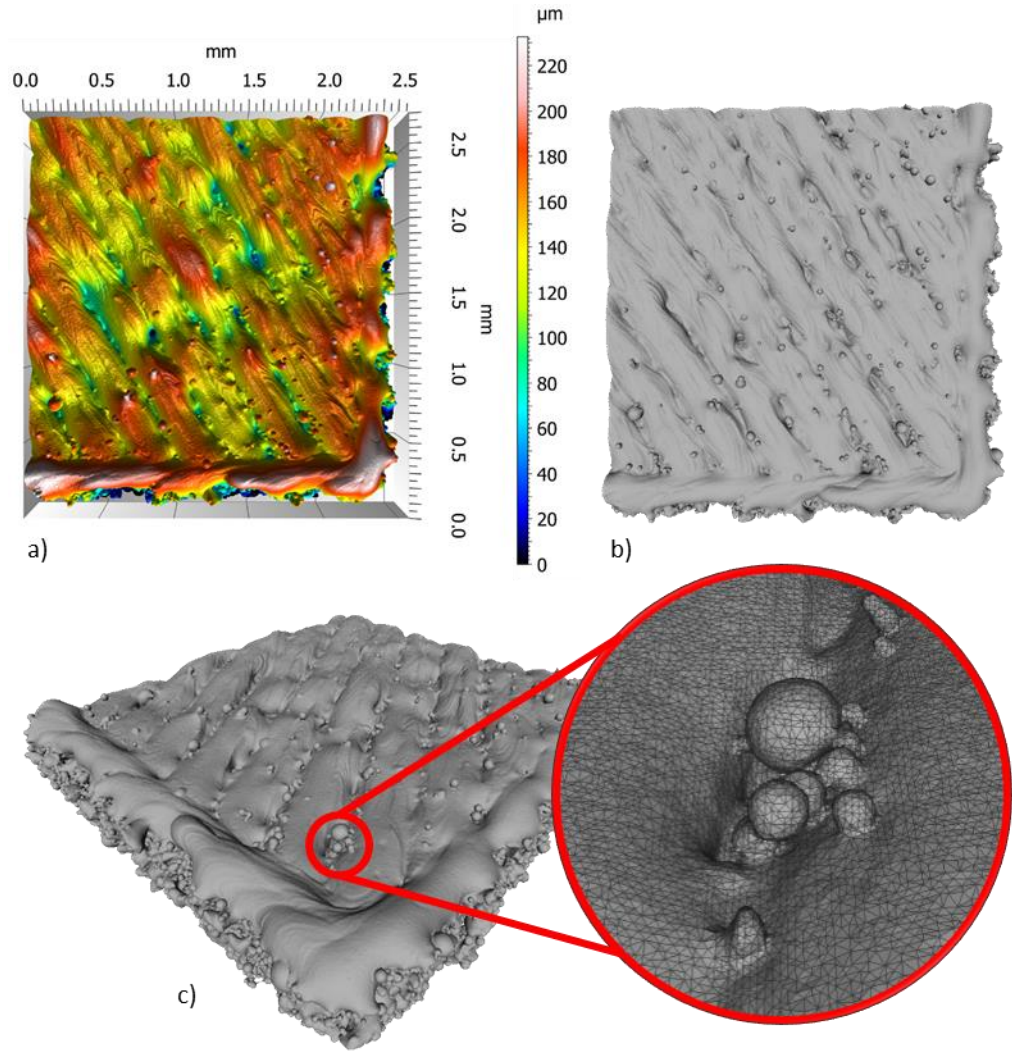
Figure 4.7. Datasets generated by the XCT at 44.1× magnification: a) height map; b) triangulated model (top view); c) triangulated model (isometric view) and magnified area showing individual triangles.

4.3.2.5 Visual inspection of localised features: additional considerations

Figure 4.8 shows close-up views of height maps and images obtained via different measurement solutions, in order to highlight some of the features which are most challenging to measure, as they appear upon application of each different measurement solution. The large recess in the bottom left quadrant is particularly interesting, as the returned information varies substantially between measurements. The protruded singularities are also of interest, as they result in a range of different measurement artefacts depending on the technology used to acquire the specific dataset. Finally, it is worthy of discussion that some

110

technologies are not truly non-destructive, which is a factor that should be considered in the comparison. For example, figure 4.8b and figure 4.8e highlight the presence of an exogenous particle later removed during stylus measurement (data shown in figures 4.8a, 4.8c, 4.8d and 4.8f were taken after the stylus). Accordingly, figure 4.8a highlights the presence of the scratch left by the stylus (stylus profilometry is discussed in the following Section), whilst the same scratch can be barely perceived in the CSI map (figure 4.8d).
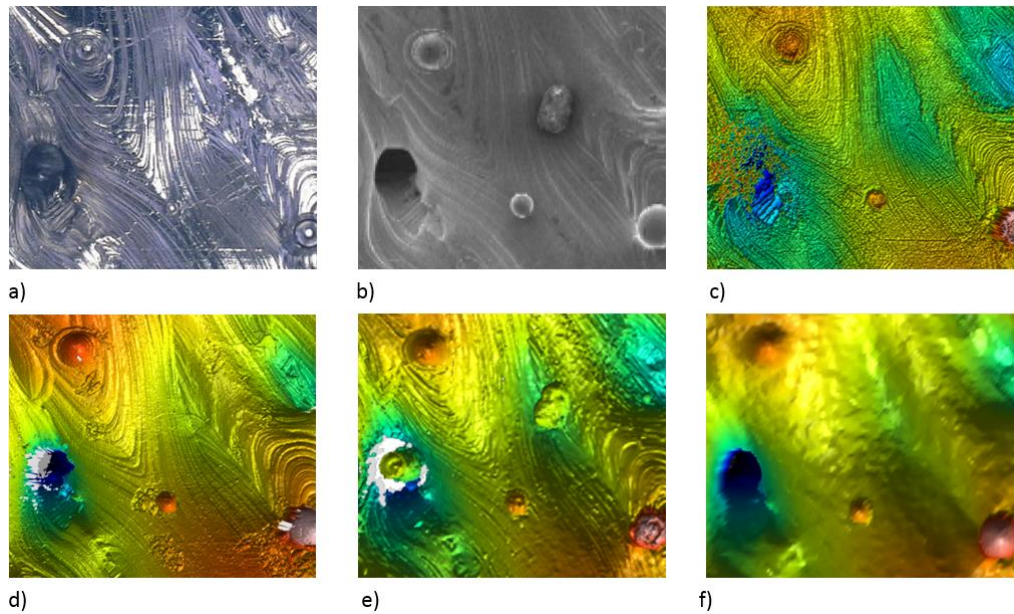
Figure 4.8. Topography details (field of view approximately 0.3 mm × 0.3 mm) captured with different measurement solutions; a) DOM at 500× magnification: coaxial light, FS; b) SEM at 61× magnification: intensity image from secondary electrons; c) CM with 20× objective lens: height map; d) CSI with 20× objective lens, 1× optical zoom: height map; e) FV with 50× objective lens and ring light: height map; f) XCT at 44.1× magnification: height map.

4.3.3   Profile comparison

While stylus profilometry is the only measurement technology examined here which natively returns profile information, cross-sectional profiles can be extracted from height maps in order to obtain a reliable source of comparison data [238]. Quantitative comparison implies the additional challenge of being able to register datasets (i.e. correctly co-localising them with respect to one-another in space), in order to ensure appropriate topography comparison. While several tools and algorithmic solutions are available to align entire height maps

[228,239], aligning a profile to a height map is more complicated, due to the lack of reliable local references. Scratch marks left by the contact stylus on the surface greatly simplify the problem, providing an initial, coarse localisation reference that can be used as a starting point for further refinement. In figure 4.9, the profile obtained by a stylus instrument is shown overlaid onto cross-sectional profiles extracted from the height maps obtained by different measuring instruments. Datasets in this case are not bandwidth-matched (i.e. resampled to similar point spacing and similarly filtered [238]), as they retain their original resolutions, but have been cropped to the same reference base length. Despite the inevitable presence of residual alignment errors, discrepancies amongst measurements are observed, owing to the sensitivity of each technology to each of the measured features. As expected, the most evident discrepancies occur surrounding surface recesses, which are more difficult to reconstruct for most measurement technologies. It should be noted that the aligned profile plot presented here represents a preliminary result based on a rudimentary alignment procedure. This type of surface analysis will be elaborated upon at length in Chapters 5 and 7, so I will not present further discussion of the plot here.
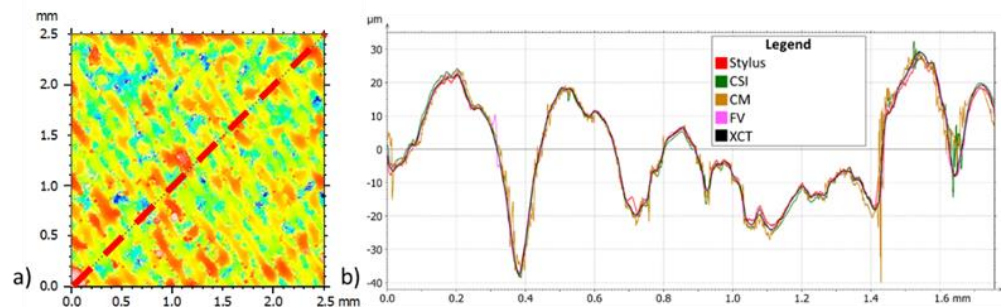
Figure 4.9. Topography profiles obtained with different measurement solutions: a) example 2D data with dashed line representing the extracted profile; b) extracted profiles.

4.4 Chapter discussion

Some considerations can be drawn from the available data acquired during this preliminary phase. Firstly, when an opinion needs to be reached about the topography of a MPBF surface, it is inadvisable to rely on any measurement

result obtained from a single instrument type. Experimental findings demonstrate that no single measurement technology or setup is optimal for the measurement of all notable features that need investigation. Secondly, no measurement technology or setup amongst those compared can be considered better than the others and thus act as reference. As such, the most appropriate point at which to begin establishing feature-specific references is a consistent output of multiple technologies and at multiple scales, i.e. agreement across technologies/setups in regards to a specific feature/topography detail. A quantitative assessment of topography measurement results involving different technologies and including the contribution of measurement uncertainties is therefore required as a result of these preliminary findings.

It should be noted that while the work presented in this Chapter describes measurements taken of a single portion of a single surface, the information acquired can be extrapolated to measurements of many other MPBF surfaces. This extrapolation is generally possible, as while the examined surface cannot represent all possible MPBF surfaces, MPBF surfaces are generally comprised of some or all of the features examined above (particularly: weld track geometry, weld track ripples, localised sphere-like protrusions and recesses), and so the findings discussed here are highly relevant for future investigations. For extension to measurement of surfaces produced by other AM methods, particularly those producing polymer surfaces, significant work remains to be performed, in order to address the wealth of challenges that relate not only to the presence of high slopes and undercuts, but also to the presence of potentially translucent and transparent surfaces. In addition, methods of quantifying the qualitative comparison performed here are being developed, and new algorithms and processing methods must be explored in order to effectively automate these assessments for the purposes of industrial inspection and process development.

4.5 Chapter summary

The preliminary work presented in this Chapter represents an introduction towards robust quantification of metal additive surfaces, through visual

comparison of measurements made using a variety of technologies, and involving the development of good practice in measurement of metal AM surface using different measurement technologies. Particularly, the results acquired during the production of this Chapter were used to inform later work performed throughout my PhD, particularly to form the basis of measurement setups used during production of the work presented in Chapters 4 to 8 of this Thesis. It is clear from the measurements made during this initial phase that the features present on these surfaces are represented in substantially different ways by each instrument, and, therefore, that individual measurements may not always be able to provide the information required to improve a metal AM process. However, the statistical significance of these qualitative differences is not clear from these preliminary results and a quantitative assessment of discrepancies is required to further understand the sensitivity of measuring instruments to these surfaces. Such a quantitative assessment of these differences is presented in Chapter 5.

While clearly possible, XCT surface measurement is in its infancy as a method, and significant work is required to validate the technique. I have addressed such a validation in Chapters 6 to 8.

5. Direct comparison of surface topographies

Following on from the conclusions presented in Chapter 4, a requirement for new methods of comparative assessment of data acquired using different surface measurement technologies was identified. In this Chapter, work is presented on the development of such methods and their application to metal AM surfaces, including the assessment of metal AM surfaces and their features. This Chapter is divided into two Sections, the first of which involves the presentation of a method used throughout this Thesis for the direct comparison of surface topographies, based on statistical assessment of discrepancies between technologies. This work was recently published [240]. In the latter half of this Chapter, an assessment of how individual features found on the metal AM surface are reconstructed from different measurement technologies is presented, particularly looking at four key features present on metal AM surfaces: attached particles, recesses, weld ripples and weld tracks. This work was also recently published in [229].

5.1 Developing methods of quantitative comparison

5.1.1   Quantifying discrepancies between AM surface measurements

Recent developments in areal topography measurement have enabled the fast acquisition of high-density surface datasets, allowing the reconstruction of detailed three-dimensional digital models of surface topography. There are a number of industrially recognised optical technologies for areal topography measurement; confocal microscopy (CM) [35,36], coherence scanning interferometry (CSI) [41,42] and focus variation (FV) microscopy [45,46] being the most prominent. Optical areal measurement technologies are becoming increasingly accepted alongside conventional profile measurement via contact stylus [241]. Recent work has also shown X-ray computed tomography (XCT) to be capable of capturing topographical information at scales approaching those captured by the optical methods [99].

Preliminary work (see Chapter 4 for further information) on the measurement of AM surfaces indicated that, for metal powder bed fusion (MPBF) surfaces, areal topography data obtained with different technologies show visible discrepancies. Thus far, however, the investigation has been conducted from a mostly qualitative standpoint. Differences between reconstructed topographic details sometimes appear to be of the same order of magnitude as the topographic features being investigated. In some instances, the overall shape of a topographic feature is reconstructed in an entirely different manner depending on the measurement technology: small recesses may become protrusions, while regular hemispheric shapes (e.g. spatter particles) may appear as completely irregular. The problem of assessing the metrological performance of the available optical, areal measurement technologies is as of yet unsolved. Little is currently known about how to quantify and correct bias in topographic reconstruction, or how to evaluate the associated uncertainty [242]. Research regarding the use of XCT for topographical measurement is even more in its infancy. Even for dimensional characterisation tasks, XCT measurement is generally hampered by numerous challenges [57].

A significant part of the problem of assessing the measurement error associated with the different technologies is the lack of a traceable reference measurement. For complex topography, the only technology that can be relatively easily employed as a reference is profile measurement via contact stylus [32]. However, the problem of how to reliably relocate profile data measured by a stylus onto areal topography data remains unsolved. Even in the case of successful relocation, the relocated profile only allows comparison with the cross-section of the areal topography dataset, and it is often not convenient to cover a large measured area with multiple stylus profiles due to the large amount of time required to scan multiple profiles at sufficient spatial resolution.

In the absence of a traceable reference to assess measurement error in areal topography data, it is still possible to compare surface measurements in terms of agreement and disagreement. This approach has been recently attempted for injection moulded replicas of nickel transfer standards, although comparison focused solely on the observation of texture parameters [243]. Texture

parameters are important, and represent the most dominant method currently used by the design and manufacturing communities to describe topographies. Efforts are, therefore, justified in providing measures of agreement and disagreement in terms of texture parameters. However, only comparative analysis of reconstructed topographies allows for acquisition of an understanding as to why calculated parameters differ.

In this Chapter, the surface of an MPBF sample is acquired with multiple topography measuring instruments. Topographies are relocated for the purpose of direct, quantitative comparison of reconstructed local features. Areal texture parameters are also computed and discrepancies discussed, starting from the differences observed in the reconstructed topographies.

5.1.2 Section methodology

5.1.2.1 The MPBF specimen

For this part of my PhD research, a region of interest (ROI) on a (20 × 20 × 20) mm Ti6Al4V cubic artefact, manufactured using laser MPBF with a Renishaw AM 250, was used as the test case. While similar, a different specific sample was used to that discussed in Chapter 4. A portion of the top surface (orthogonal to the building direction) was considered, located near the cube edges to facilitate relocation. The surface was not post-processed (other than light cleaning) so as to preserve the typical topographic features generated by MPBF. Further information about this sample is detailed in Section 3.1.

5.1.2.2 Measurement setups

Four commercial measuring instruments were used, each representative of a relevant measurement technology (CM, FV, CSI and XCT). Technologies were chosen for this investigation as a result of a distillation process applied following the preliminary work presented in Chapter 4. In this distillation, instruments were discarded according to their relevance to the investigation, considering only the instruments and setups found to be qualitatively suitable

for areal AM surface topography measurement. As such, imaging by digital optical and scanning electron microscopy was not performed due to the lack of outputted qualitative information. Stylus measurement was also not performed due to the associated constraints regarding unfeasibly slow measurement times. Specific measurement setups for the examined instruments were chosen to ensure that the generated data were representative of the sample surface, qualitatively comparable to one another and exhibited approximately similar measurement bandwidths [238]. Instrument names have again been redacted to prevent direct comparison of commercial instruments. The sample was measured three times consecutively with each instrument, with no re-fixturing between measurements, constant set-up parameters, and controlled temperature environments (CM: ±0.1 °C, CSI and FV: ±1 °C, XCT: ±0.2 °C). As in Chapter 4, FoV is the field of view, LR is lateral resolution and NA is numerical aperture. LR-pixel refers to the pixel spacing of the detector used by each instrument, LR-optical refers the calculated Sparrow optical limit [34] of each instrument and LR-contrast refers specifically to the distance from the centre of each pixel used by the FV instrument to compute local contrast; selected during the measurement. The Sparrow optical limit was calculated using a wavelength of 580 nm for white-light systems (CSI and FV) and 405 nm for the laser CM system. Based upon good practice acquired during preliminary findings, the following set-ups were adopted:

- CM: 20× objective lens (NA 0.6, FoV 0.64 mm × 0.64 mm, LR-pixel 0.63 μm, LR-optical 0.32 μm), measured area 2.9 mm × 2.9 mm, stitching of multiple images performed in the manufacturer's software.
- CSI: 20× objective at 1× zoom (NA 0.40, FoV 0.42 mm × 0.42 mm, LR-pixel 0.41 μm, LR-optical 0.68 μm), measured area 3.4 mm × 3.4 mm, stitching of multiple images performed in the manufacturer's software.
- FV: 20× objective lens (NA 0.40, FoV 0.81 mm × 0.81 mm, LR-pixel 0.44 μm, LR-optical 0.68 μm, LR-contrast 3 μm), ring light illumination, measured area 3.7 mm × 3.7 mm, stitching of multiple images performed in the manufacturer's software.
- XCT: geometric magnification of 42.6×, leading to a voxel size of 4.69 μm,

3142 X-ray projections formed from averaging of two exposures per projection, each lasting 2 s; X-ray tube voltage 150 kV and current 30 μA; a 1 mm copper X-ray pre-filter was used to attenuate lower energy X-rays. A warmup scan of approximately one hour was performed prior to the scan and data were reconstructed in the manufacturer's software, using no beam hardening correction and a ramp filter. Surfaces (triangulated meshes) were determined in VGStudio MAX 3.0 [73] from volumetric data, using the maximum gradient method over four voxels, with the ISO-50 isosurface as a starting point [139].

Despite efforts to maximise good practice in these measurements (as mentioned in Chapter 4), it should be noted that the results discussed below may vary as a function of measurement set-up.

5.1.2.3 Data processing

Data preparation

CM, CSI and FV measurements generated height maps useable in their native forms, while triangulated meshes extracted from XCT volumetric data were converted into height maps. This conversion was performed as described in Chapter 4, in that surfaces were first determined in VGStudio MAX 3.0 [73] by using the maximum gradient method over four voxels, with the ISO-50 isosurface as a starting point [139]. Determined surfaces were then exported as triangulated meshes in .STL format, and imported into Meshlab [244]. In Meshlab, surfaces were re-oriented by approximate manual alignment of the surface normal (determined visually) to the *z*-axis. The result was exported from Meshlab as an .STL, and imported into MountainsMap by DigitalSurf [228]. As performed previously in the work described in Chapter 4, MountainsMap automatically converted the triangulated mesh into a height map at an automatically determined spatial resolution automatically, to match the point density of the original triangulated mesh, approximately defined by the voxel size. This automatically determined point density was marginally different for each individual topography, but varied between 1.48 μm and 2.08 μm.

Relocation and extraction

As the method of alignment presented in Chapter 4 relied on visual inspection of scratches made in the sample surface, general applicability of the method is not possible. As such, a requirement for a robust methods of alignment of topographies was identified, in order for the topographies to be quantitatively compared. In this work, topography datasets acquired using the various systems were aligned using a two-stage method in MountainsMap. The alignment involved alignment of all data to a single 'master' dataset. The chosen master in this case was one of the CSI datasets. For the purposes of this explanation, datasets being aligned to the master will be referred to as 'moving' datasets.

The first stage of the alignment entailed a 'coarse' semi-manual alignment, performed using rigid transformations on the moving datasets with respect the master (only translations in x and y, no translation in z or rotation). This manual alignment involved the application of Procrustes method [245], which entailed applying a marker-based alignment system. During this stage, landmarks were visually identified in the data, using features present in both the master and moving datasets. In each case, four pairs of markers were then applied to landmarks in both the datasets, and the moving dataset was automatically translated to the position with respect to the master dataset that minimised the average distance between marker pairs (see figure 5.1).
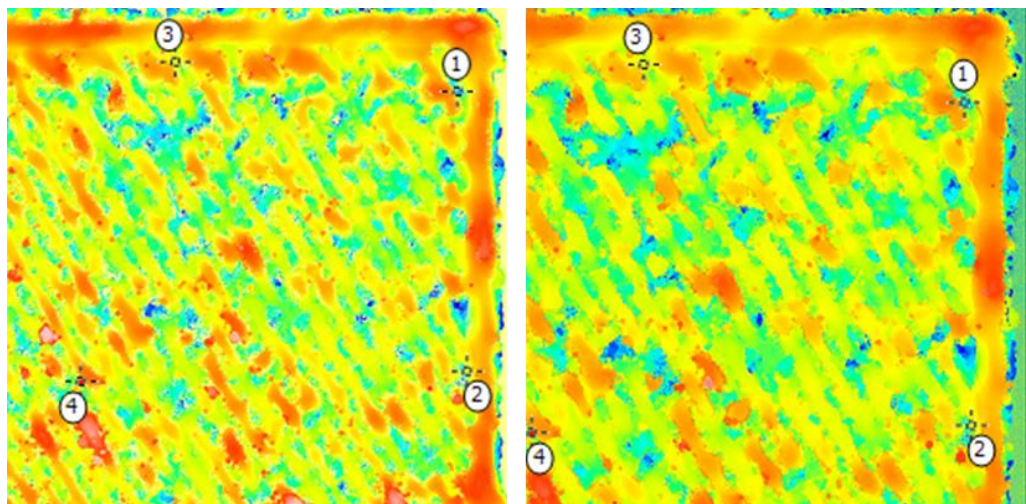
Figure 5.1. Example application of the Procrustes method [245] of marker-based alignment.

The second stage of this alignment process involved a 'fine' algorithmic alignment, performed by application of a cross correlation–based, global alignment [246]. This second stage alignment was performed in order to compensate for small misalignments caused by marker misplacement in the coarse alignment stage. The cross-correlation algorithm essentially entails a global comparison of the moving and master datasets, measuring the similarity of the two datasets as a function of their relative displacement. The algorithm minimises this value, thereby providing an optimum alignment. Although cross-correlation provides an optimum solution, the coarse alignment stage is required to prevent the cross correlation algorithm falling into a local minima. The cross correlation algorithm also only translates in the x and y directions, without translating the data in z or performing any rotation.

At this stage, a scaling error was recognised in the CM data. As such, a scaling correction factor was applied to all CM data, obtained by maximising the alignment of the CM data to the CSI master. Finally, aligned data were similarly cropped to a region of size (2.5 × 2.5) mm. The size of the region was chosen to ensure topographic significance of the sample, based on the suggestions made in previous work by Triantaphyllou et al. [106].

Detailed comparison of topographies

Cross-sectional profiles were extracted from the aligned regions at the same position in each dataset. This amounts to three profile replicates per instrument, for a total of twelve profiles. To compensate for the presence of void data points in the CSI, CM and FV data, a filling operation was performed on each profile, replacing any void points in the data using a weighted interpolation of valid nearest neighbours. For each cross-section, profiles were resampled along the horizontal axis (x) by linear interpolation, at the frequency corresponding to the highest lateral resolution in the original datasets, so as to allow comparison whilst retaining as much of the measured information as possible. The point spacing used in this case was 0.289 μm, from the resolution of the CSI data.

In order to compare topographies statistically, confidence intervals (CIs) were constructed for each profile at 95 % confidence. In order to generate these CIs, a mean profile was first computed for each instrument using the three measured profiles. To calculate these mean profiles, the z values of each profile were used to generate a mean z value for each x position, which were then combined to construct the full mean profiles. Following this step, upper and lower bound CI profiles were calculated for each mean profile. In order to construct these CI profiles, the local mean at 95 % confidence was calculated for each z point, using a t-distribution with two degrees of freedom, where DoF = sample size – 1 [247]. The equation used to calculate the position of each z point in the CI profiles is presented below as equation 4.1, where $\bar{z}$ is the mean z value, t is the t-value (i.e. the size of the difference relative to the variation in the sample data), s is the sample standard deviation and n is number of DoF). In the equation, the positive case represents the upper bound of the CI, while the negative case represents the lower bound. For this work, normality and an absence of spatial correlation are assumed. For 2 DoF at 95 % confidence for a distribution with two tails (as in this case), the t-value used is 4.303 [247].

$$CI\ z = \bar{z} \pm t\left(\frac{s}{\sqrt{n}}\right) \qquad\qquad 4.1$$

Using the mean and CI profiles for each instrument, overall discrepancy between instruments was then calculated. By overlaying the data acquired using each instrument and computing the number of x points where the CIs do and do not overlap, a measure of overall discrepancy between instruments was generated as the percentage of the profile length where CIs do not overlap.

Texture parameter computation

The following areal texture parameters were considered from ISO 25178-2 [51]: *Sa*, *Sq*, *Ssk*, *Sku* and *Sal* (see Chapter 1 for parameter definitions). These parameters were used as they were identified as common parameters for use in such evaluations in industry (see Chapter 2 and the recent review by Townsend at al. [9]). Parameters were computed on surfaces where only an F-operator was

applied (the F-set), and on scale-limited surfaces (the SL-set). The F-operator consisted of subtraction of a least-squares mean plane. To achieve bandwidth-matching [238] in the SL-set, an S-filter with a 6.29 µm cut-off (based on a grid of 4 × 4 pixels in the lowest resolution dataset) and an L-filter with a 0.8 mm cut-off (a common filter used to separate roughness and waviness [248]) were adopted. Parameter values computed for each dataset were aggregated by instrument type, and used to construct CIs of the mean at 95 % confidence, based on the same *t*-distribution model used to compute CI profiles in the direct topography comparison methodology.

5.1.3 Section results

5.1.3.1 Analysis of reconstructed topographies

Figure 5.2 provides a qualitative overview of how the different instruments render the same topography. Figure 5.3a shows twelve profiles obtained by cutting the aligned topographies in the same cross-sectioning plane. Figure 5.3b shows a portion of the same cross-section where means and CIs are calculated for each set of profiles. Table 5.1 shows the discrepancy between instrument pairs, (as a percentage of the profile length where CIs do not intersect) computed on the cross-section displayed in figure 5.3a.

Table 5.1. Profile discrepancy between instrument pairs

	CM/CSI	CM/FV	CM/XCT	CSI/FV	CSI/XCT	FV/XCT
Discrepancy %	51.7	61.9	48.5	57.4	42.9	48.8
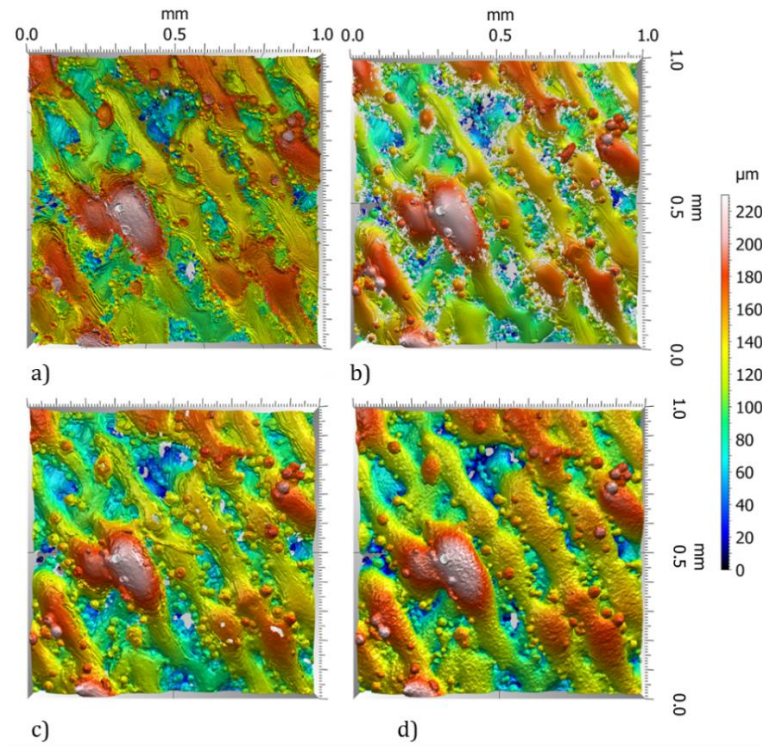
Figure 5.2. Reconstructed portions of aligned topographies (top views, height-based colouring): a) CM; b) CSI; c) FV; d) XCT. Figure published in [240].
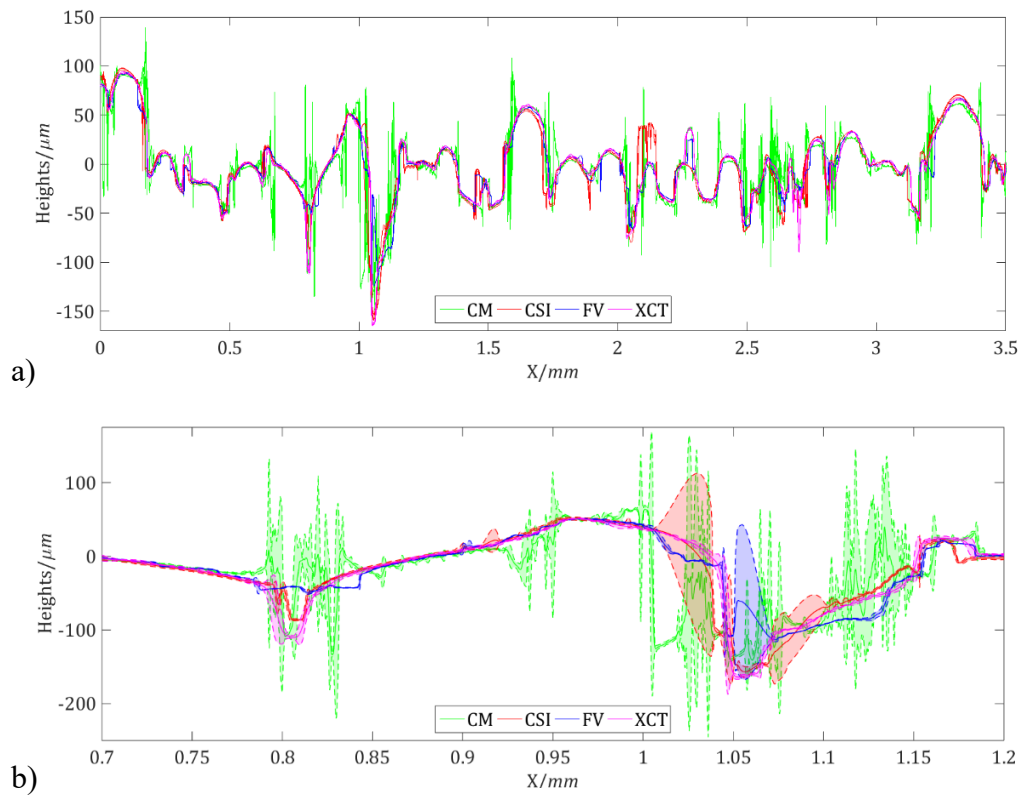
Figure 5.3. Profile comparison: a) twelve profiles (three for each instrument) obtained from cross-sectioning along the diagonal of the (2.5 × 2.5) mm aligned topographies; b) portion of the same cross-section: mean profiles and estimated CIs. Figure published in [240].

124

5.1.3.2 Comparison of texture parameters

Figure 5.4 shows the CI plots for the texture parameters computed on the F-set, and SL-set respectively.
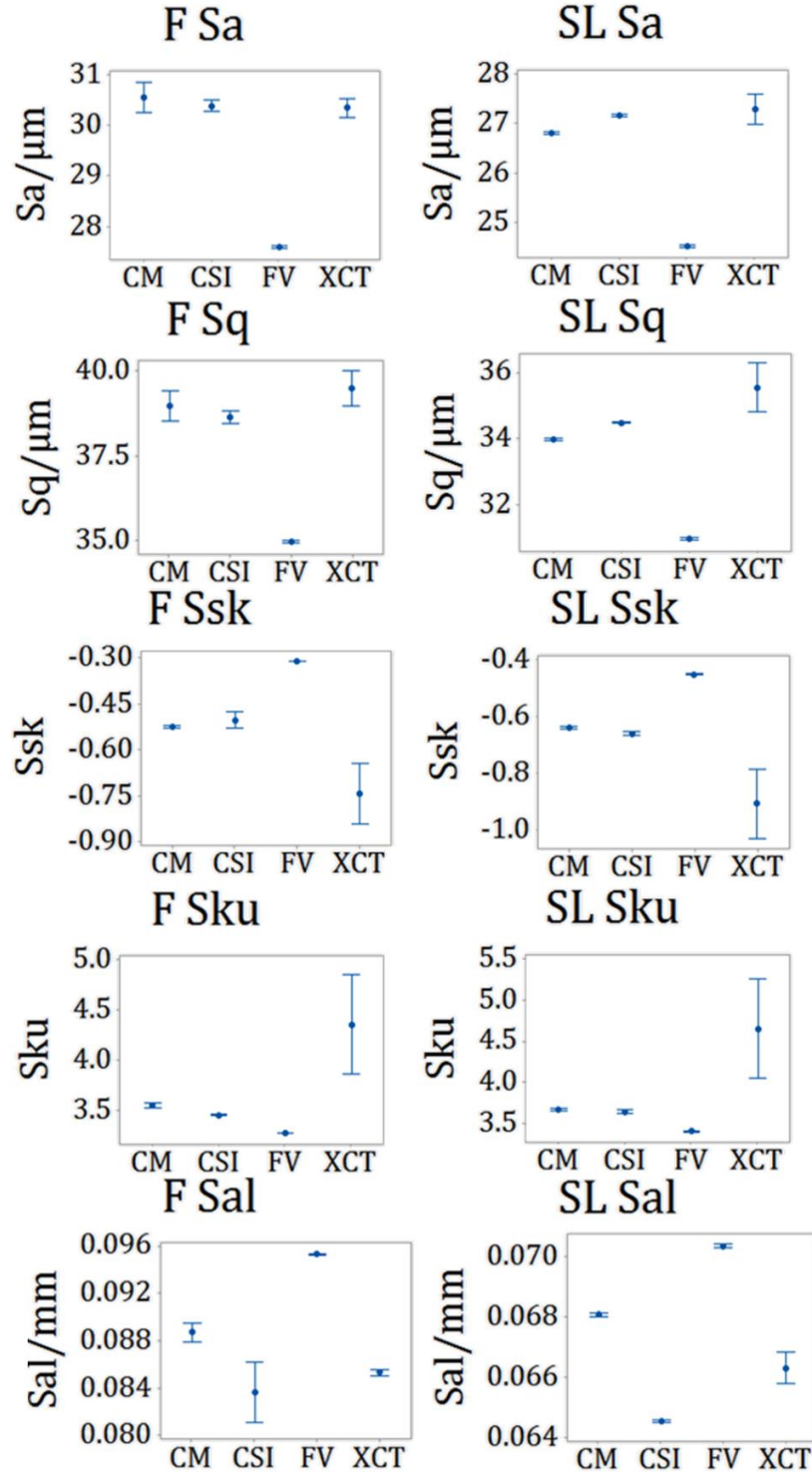
Figure 5.4. CIs for the texture parameters computed on the F and SL sets. Figure published in [240].

5.1.4   Section discussion

The overall discrepancy of local topographic reconstruction (table 5.1) is higher for those instruments with narrower CIs, i.e. better repeatability (figure 5.3b). Most local topographic differences are located in difficult-to-measure regions such as recesses and high slopes. While some spikes can be recognised through outlier detection, this is not possible for erroneously reconstructed, wider regions (e.g. a hill instead of a recess - see CSI and FV in figure 5.3b). Deep recesses are also more challenging for optical technologies, particularly FV, which requires sufficient reflected light to compute contrast. Most areas where topographic reconstructions are in disagreement are marked by a significant increase of the CIs, suggesting that CIs from replicates may become useful indicators of local measurement reliability. Stitching of multiple datasets in optical measurements was used to obtain suitable coverage width, whilst ensuring high lateral resolution. However, it should be noted that stitching may introduce uncharacterised effects in CI evaluation, due to stage repeatability and algorithmic stitching errors.

When examining texture parameters (figure 5.4), the same trends are observed in the F and SL sets, meaning that the removal of very high spatial frequencies (S-filter) does not significantly affect the performance differences between measurement technologies (although shifts in values are observed between the F and SL sets). Overall, XCT parameter results are most frequently the least repeatable (larger CIs), although FV data sometimes exhibit similarly poor repeatability. The scarce ability of FV to capture deep recesses is confirmed by the *Ssk* and *Sku* parameters combined, which also confirm the increased suitability of XCT for measurement of these features as observed on cross-section profiles. The most conventional type of 'roughness' assessment, i.e. via the *Sa* and *Sq* parameters (analogous to the *Ra* and *Rq* ISO 4287 [50] profile parameters), shows similar results for CM and CSI, with the XCT means coarsely located in the same region. Again, FV shows the largest discrepancy, potentially because of poorer capture of smaller scale peaks and pits. The *Sal* parameter confirms differences in the spatial frequencies captured by each instrument, even within the bandwidth-matched interval: FV generates the

highest *Sal* parameter confirming the dominance of larger wavelength topographic components. CSI and XCT are the technologies that appear the most capable of acquiring higher-frequency topographic content, although, as apparently indicated for the XCT case in figure 5.2, such content may be noise.

The results discussed up to this point illustrate a few interesting themes. Firstly, though texture parameters can be used to quantify differences between areal topography measuring instruments, when it comes to interpreting such results, the investigation of the aligned, reconstructed topographies is essential in order to provide information as to why specific results are obtained. The problem of accurate alignment and comparison of topographies becomes essential, with many currently unsolved challenges. Alignment is difficult in the presence of measurement error which can be as large as the topographic features of interest. Alignment results may be improved by replacing global alignment algorithms (such as cross-correlation) with selective alignment solutions based on maximising the overlap of those regions that have remained the most invariant across measurements. In turn, alignment error heavily affects statistical modelling, e.g. by unnaturally increasing the width of the CIs. Even with ideal alignment, a more statistically sound process for generating mean profiles and CIs would include spatial correlation effects, and some type of correction for simultaneous estimation of multiple CIs (e.g. Bonferroni [249]). Solutions are also required to align data in six degrees of freedom, as the two degrees of freedom used in this work (translation in *x* and *y*) are insufficient for providing rigorous comparison. Additionally, the alignment method used here (see Section 5.1.2.3) relies heavily on the use of commercial software, which, as is often the case with commercial software, employs a something of a 'black-box' methodology. While the software tells the user broadly what type of algorithm is employed, it does not clearly and fully explain the algorithms used. Such a closed system therefore presents another challenge, particularly when the end goal is ultra-precise rigorous alignment between partially dissimilar datasets. Both the alignment and statistical modelling problems are made more difficult by the need to handle areal data (i.e. $z = f(x, y)$ formulations), as opposed to profiles (i.e. $z = f(x)$ formulations). Methods developed as part of the work discussed in Chapter 7 describe an extension of the analysis presented in this

Section to areal topographies.

Additionally, in this work, MountainsMap was again used to convert XCT data from the outputted triangulated mesh format into a height map format, and, as discussed in Chapter 4, this conversion is performed without explanation. I will address this issue in Section 5.2.

5.2 Quantitative comparison of metal AM surface features

5.2.1   Quantifying discrepancies between AM surface feature measurements

As discussed in Chapters 1 and 4, in addition to providing the means to texture quantification of surfaces produced by the manufacturing process (e.g. roughness), areal topography measurement can capture detailed information about how topographic formations are generated and later evolve during processing, post-processing and the functional life of the part [9]. However, MPBF surfaces are often highly complex and irregular (as discussed in Section 5.1 and shown in figure 5.2), and, as shown earlier in this Chapter, measurements often exhibit significant discrepancies between measurement technologies [240].

As discussed, the MPBF topography is a challenge for areal topography measurement. High slopes, variable aspect-ratios, alternation between dark and overly bright regions (e.g. deep recesses and the tops of smoother regions of particles and weld tracks), as well as non-uniform optical properties as a result of local oxidisation and/or micro-roughness effects, cause the main issues faced by optical measurement technologies [30]. XCT measurement is subject to an equally complex series of non-optical challenges which affect the spatial resolution of the measurement, as well as the procedure used to determine a surface from XCT data [99]. Earlier in this Chapter, discrepancies between measurements made on MPBF surfaces using a number of areal topography instruments were quantified, and measurement error was found to be of the same order of magnitude as the size of localised topographic features captured by the measurement process. This comparison focused mainly on examination of how

changes in reconstructed topographies ultimately affected the results of the computation of texture parameters commonly used in industrial specifications (i.e. ISO 4287 [50] profile parameters and ISO 25178-2 [51] areal parameters). However, when the measurement concerned is performed with an interest in localised surface features, then the investigation of how local topography is reconstructed through different measurement technologies is of fundamental importance. In this case, particularly for MPBF surfaces, assessments of how different technologies reconstruct quasi-spherical shapes, deep recesses, abrupt height or slope variations and smaller-scale features, such as weld track ripples and/or thermal cracks, is of significant interest.

5.2.2 Methodology

In this work, a region of interest (ROI) on a Ti6Al4V MPBF surface was inspected using three optical areal topography instruments: a focus variation (FV) microscope, a confocal microscope (CM) and a coherence scanning interferometer (CSI). A fourth dataset was obtained by surface extraction from a volumetric reconstruction of data acquired using X-ray computed tomography (XCT). Multiple smaller regions were digitally extracted from the four topography datasets, representing examples of relevant MPBF surface features (particles, recesses, ripples and weld tracks). Individual feature topographies were aligned in the same coordinate system and cropped to the same field of view for comparison purposes, using a custom, dedicated geometric relocation procedure (see Section 5.2.2.3). For visual comparison, datasets were levelled to a consistent mean height and rendered with artificial colouring based on a shared colour palette, mapped to the same range of heights, in order to provide a visual indication of local similarities and differences. For quantitative comparison, local height discrepancies between pairs of aligned topographies were computed.

5.2.2.1 The MPBF specimen

The sample used during the work presented in this Chapter is detailed in Sections 3.1 and 4.2.1.

5.2.2.2 Measurement setups

Specific datasets were 'cherry-picked' from the data acquired during the preliminary work presented in Chapter 4, based on the results presented in that Chapter, ensuring that data were representative of the features present on the sample, qualitatively comparable to one another and exhibited similar measurement bandwidths [238]. In line with the good practice developed during this preliminary work, measurement setups used in this comparison were chosen so as to cover an area large enough to form a valid assessment of the MPBF surface, whilst considering total measurement time. In each optical measurement setup, additional magnifications were considered but ultimately discarded; being either too low resolution to capture relevant topographic details, or too time consuming to achieve equivalent lateral coverage of the ROI and resulting in excessively large datasets. The measurement setups used are outlined as follows:

- CM: 20× objective lens (NA 0.6, FoV 0.64 mm × 0.64 mm, LR-pixel 0.63 μm, LR-optical 0.32 μm), stitching of multiple images performed in the manufacturer's software.

- CSI: 20× at 1× zoom (NA 0.40, FoV 0.42 mm × 0.42 mm, LR-pixel 0.41 μm, LR-optical 0.68 μm), stitching of multiple images performed in the manufacturer's software.

- FV: 20× (NA 0.40, FoV 0.81 mm × 0.81 mm, LR-pixel 0.44 μm, LR-optical 0.68 μm, LR-contrast 3 μm) ring light, stitching of multiple images performed in the manufacturer's software.

- XCT: triangulated meshes, geometric magnification of 44.1×, leading to voxel size of 4.53 μm, 3142 X-ray projections formed by averaging two frames per projection, each lasting 2 s; X-ray tube voltage 145 kV and current 66 μA. A 0.25 mm copper X-ray pre-filter was used to attenuate lower energy X-rays. A warmup scan of approximately one hour was performed prior to the scan and data were reconstructed in the manufacturer's software, using a second order beam hardening correction and a ramp filter. Surfaces (triangulated meshes) were determined in

VGStudio MAX 2.2 [73] using the maximum gradient method over four voxels, with the ISO-50 isosurface as a starting point [139].

Here, as previously, LR-pixel refers to the pixel spacing of the detector used by each instrument, LR-optical refers the calculated Sparrow optical limit [34] of each instrument and LR-contrast refers specifically to the distance from the centre of each pixel used by the FV instrument to compute local contrast; selected during the measurement. The Sparrow optical limit was calculated using a wavelength of 580 nm for white-light systems (CSI and FV) and 405 nm for the laser CM system.

As in previous work, the XCT determined surface was exported as a triangulated mesh and then automatically converted into a height map within the surface metrology software MountainsMap by DigitalSurf [228], at a spatial resolution automatically determined by MountainsMap to match the point density of the original triangulated mesh (2.87 µm).

5.2.2.3 Data processing

To address alignment issues discussed earlier (see Section 5.1.4), an attempt at improvement of the method was made during this work, through the implementation of in-house code. This code was developed to particularly alleviate the issues related to the use of 'black-box' commercial software, and to maximise the overlap of regions of the data that have remained the most invariant between repeat measurements. The alignment methodology was implemented as described here.

Firstly, all data were converted to a common format by importing the raw data from the optical instruments into MountainsMap along with the XCT data, and then exporting all the data as a series of surface data files (.SDFs). These .SDF's were then imported into MATLAB as a custom height map file type; containing an array of z values arranged on an xy grid, as well as spacing information for the distance between each data point on the *xy* grid. Then, a filling operation was performed on each dataset, replacing any void points in the data using a

weighted interpolation of valid nearest neighbours. Void points were present in all datasets except for the XCT data, which is outputted from VGStudio MAX as a closed mesh.

In this instance (as previously), a master dataset was chosen. In this case, an arbitrary CSI dataset was chosen as the master. This time, however, a system of 'sub-masters' was set up, aligning a single (arbitrary) dataset from each instrument type to the overall master. All other datasets were then aligned to their respective sub-masters. While this method can potentially exacerbate systematic errors (as errors in alignment between the master and the sub-masters will translate to all datasets aligned to the sub-masters), this technique allowed for improved alignment between all datasets acquired using an individual instrument. Thus, by ensuring that sub-masters are well aligned to the overall master dataset, overall improved alignment was possible.

For the alignment process itself, all datasets were converted from the custom height map files into a custom triangulated mesh file type by Delaunay triangulation [250], in order to allow fully 3D alignment in six degrees of freedom. As in Section 5.1, alignment was performed as a two-stage process. The initial alignment step again involved a manual, marker-based coarse alignment, in which markers were manually placed by myself on both the master and moving datasets, and coarse alignment was obtained via resolution of the absolute orientation problem (i.e. finding the relationship between two coordinate systems using pairs of measurements) [251].

The second stage of the alignment process again entailed a fine alignment step. In this instance, however, fine alignment was performed via application of an iterative closest point algorithm [252] in six degrees of freedom. Essentially, this method involves the following process. Initially, the mean deviation between the moving and master datasets is assessed, and then the moving dataset is then rotated or translated with respect to the master (or respective sub-master) by some distance. Then, the mean deviation is reassessed, and a decision is made about whether the moving mesh is more or less well aligned with the master, depending on whether the mean deviation has increased or decreased.

If the alignment has improved, the mesh is then moved further in the same direction, whereas if the alignment has worsened, the mesh is moved back in the opposite direction by a smaller distance. The process is then iterated using ever-decreasing distance values, until such a point as the mean deviation between the datasets changes by less than an automatically pre-defined acceptance value.

After alignment, triangulated meshes were reconverted into height maps. In order to address the black-box issue noted in Chapter 4 regarding the use of MountainMap to perform this conversion, an in-house code was developed in order to perform this conversion in a controlled and well-defined manner. In order to convert from triangulated models to height maps, the *z*-axis is first extracted from the aligned data co-ordinate system. Then, beginning in a corner of the dataset, a '*z*-ray' is directed at the surface from above, in the direction antiparallel to the surface normal. The intersection between this *z*-ray and the surface is then recorded as the height value at point 0,0 on the *xy* grid. Using a pre-defined *xy* grid spacing (in this case, 0.5 μm), this process is then repeated across the surface in a raster scanning pattern (see figure 5.5). The 0.5 μm spacing was chosen here as a resolution slightly higher than the highest resolution of the original data, in order to avoid information loss while at the same time achieving resolution parity in the final datasets. Finally, the datasets are all cropped to the same lateral extents to homogenise the analysis area.
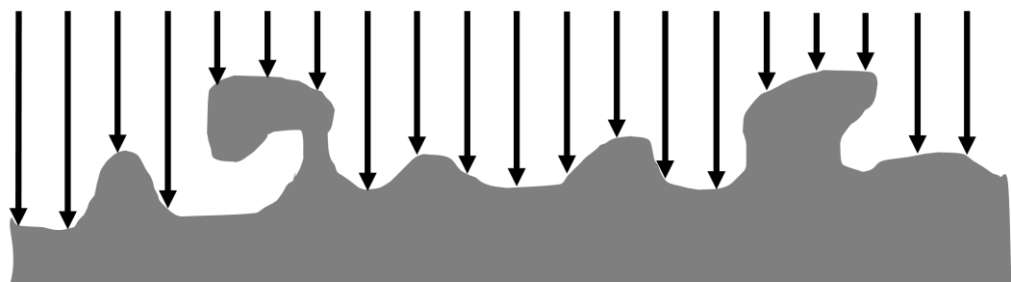
Figure 5.5. Visual depiction of the triangulated model to height map conversion process.

To compare data acquired using different systems, the computation of local height error was implemented between pairs of aligned height maps, where one

was always the CSI dataset, used as reference. Local height differences were computed at each *xy* position of the aligned height maps.

5.2.3   Section results

5.2.3.1 Full ROI

The complete ROIs are shown in figure 5.6. While the reconstructed topography appears relatively consistent between measurements, closer visual inspection yields topographic differences, in particular in relation to CSI and CM datasets featuring more content at high spatial frequencies, though this content is noisier in the CM case. Conversely, CSI contained more unmeasured points (voids), not shown in figure 5.6 because voids were filled during the alignment process by interpolation of valid neighbours.
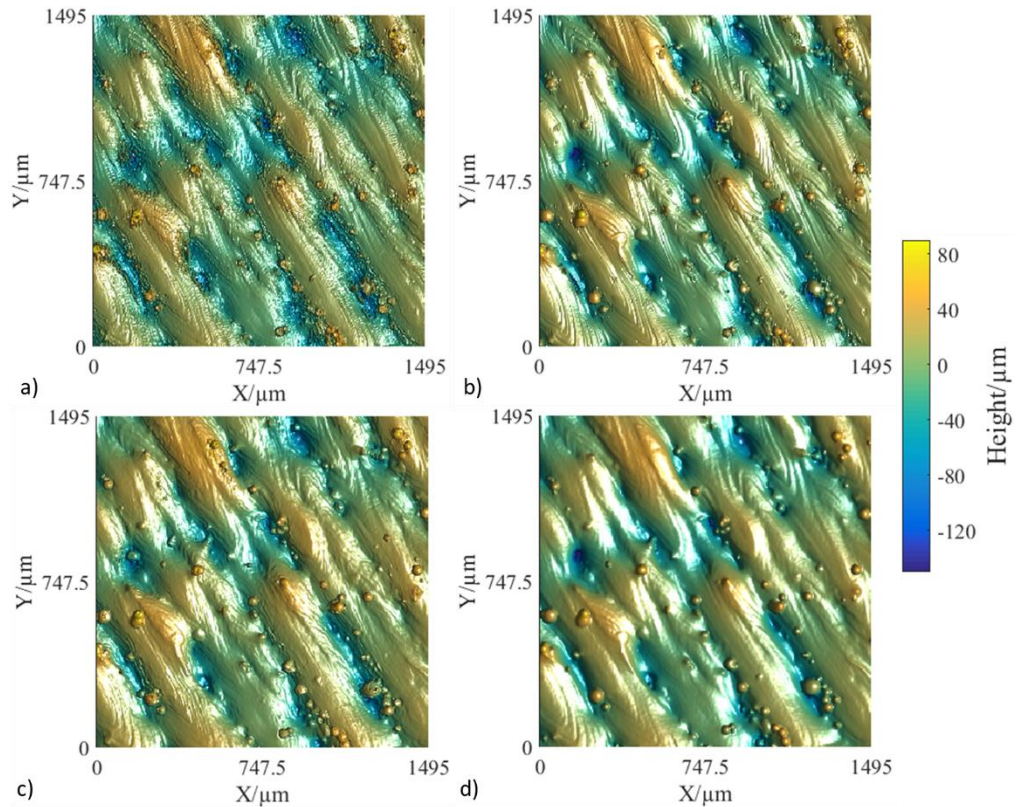
Figure 5.6. Complete topography datasets: a) CM; b) CSI; c) FV; d) XCT. Figure published in [229].

5.2.3.2 Attached particles

The topographies of two example attached particles are shown in figure 5.7. The process of aligning and computing local height differences, for the first particle shown in figure 5.7 is illustrated in figure 5.8, using the CSI and FV datasets as examples. In figure 5.9, local height error maps for the first particle shown in figure 5.7 are presented, using the CSI topography as a reference to better highlight the relationships between local error and topography.
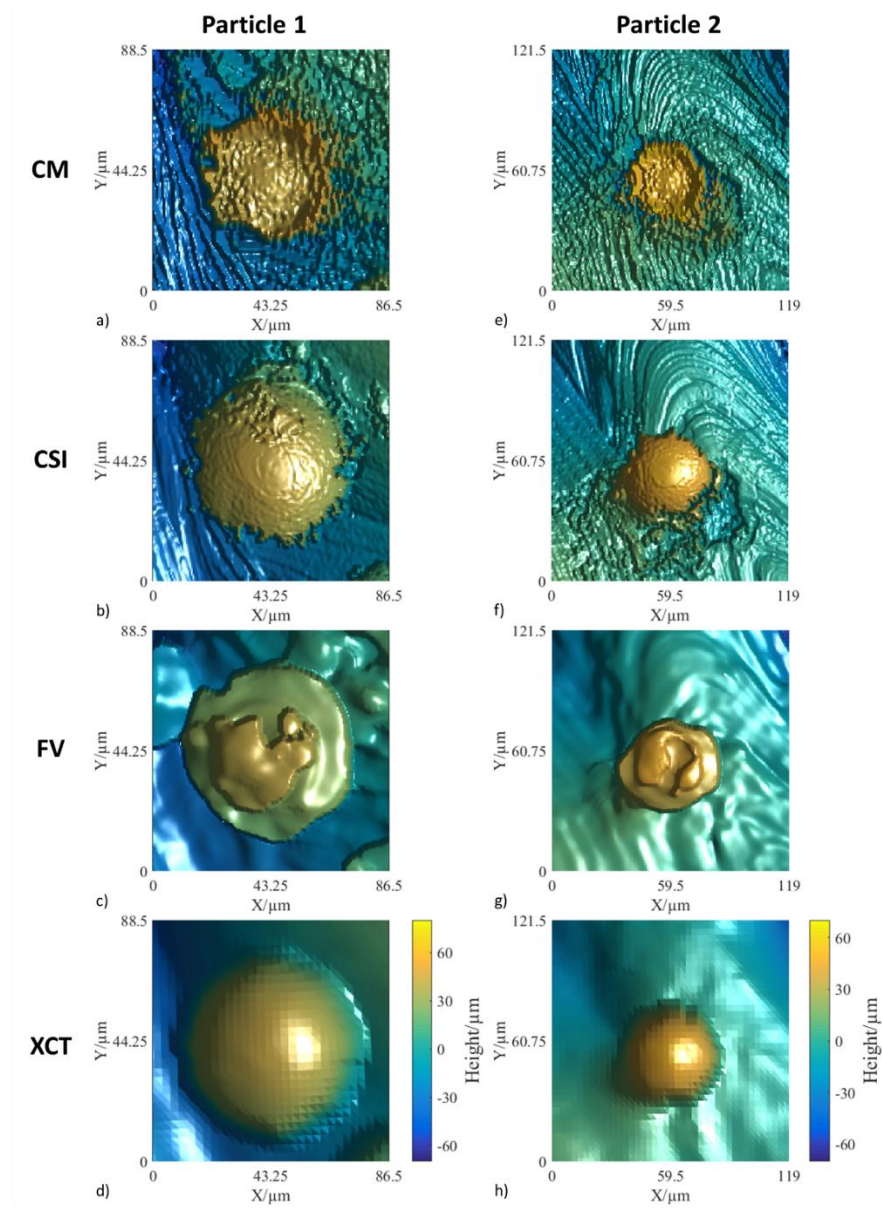
Figure 5.7. Topography of two attached particles. Two different window sizes were chosen, in the first case to highlight the particle, in the second case to additionally show a larger portion of the surrounding area. Figure published in [229].
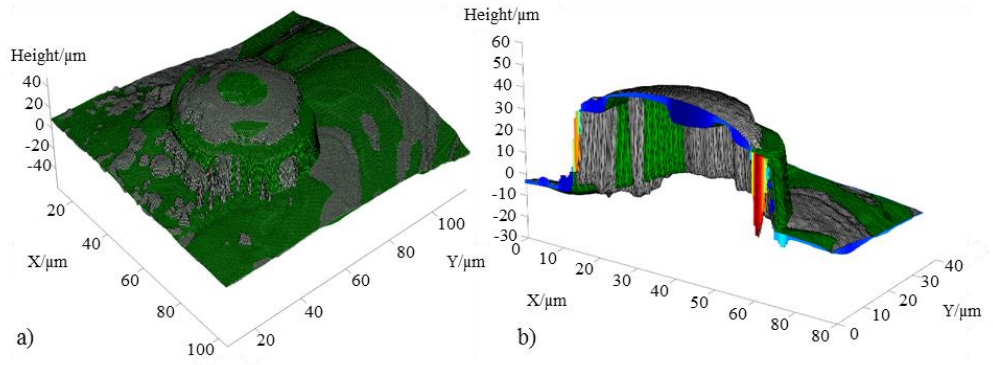
Figure 5.8. Computation of local height differences (error) between CSI (grey) and FV (green) datasets: a) aligned meshes; b) cross-section of the particle and local height error: blue and cyan indicate regions where the FV topography lies beneath the CSI topography, while orange and red represent where it lies above. Figure published in [229].
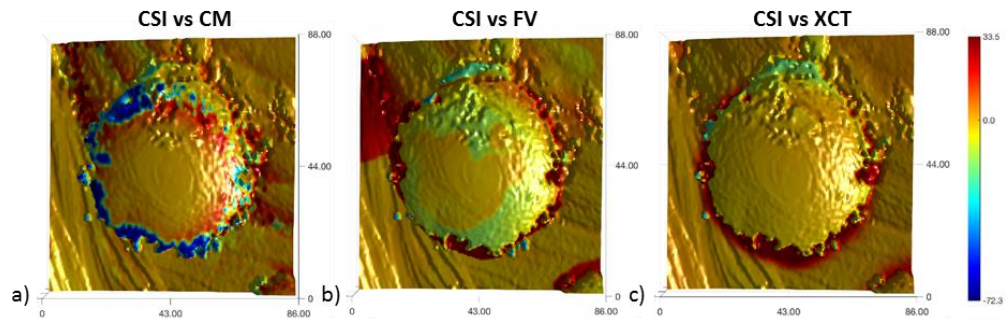
Figure 5.9. Local height error maps overlaid onto the CSI topography dataset. Colour is proportional to local (signed) height error. The range of local height error values is fixed for each feature instance, so that colours are comparable across images; the colour corresponding to zero error is highlighted in the colourbar (golden tint). Using CSI data as a reference, blue colouring indicates regions where the second measurement is lower, and red where it is higher. Figure published in [229].

Visual inspection of figure 5.7 to 4.9 reveals significant discrepancies between instruments. Although the technology is capable of recognising the presence of a protruding feature, CM is not in this instance able to correctly reconstruct the sphere-like nature of the particle (see also figure 4.3 as a reference). Nevertheless, feature boundaries are still clearly distinguishable, and make the particle distinguishable from the immediate surroundings. This behaviour can be partially attributed to the known effects on CM data when measuring spherical geometry [233], but more research is required to establish the exact cause. CSI better captures the sphere-like nature of the particle, albeit with local

136

irregularities that increase in frequency and amplitude with slope angle, as angles approach the measurable limit for the instrument [234]. FV operates by finding the probe-surface distance corresponding to maximum contrast within a region of observed image pixels, and thus experiences difficulty when a surface is locally very bright, very dark, or otherwise uniform because of its smoothness [46]. Sphere-like particles on MPBF surfaces are often very smooth and highly reflective [224], thus forcing the FV technology to locally approximate height information by interpolation of information acquired from better contrasted, neighbouring points; leading to the plateau-like formation observable in figure 5.7. In general, for optical instruments, most discrepancies occur in regions containing high local slopes (see figure 5.9) as would be expected [32]. XCT reconstructions (figures 5.7d and 5.7h), despite being characterised by lower spatial resolution, are those in which the sphere-like nature of the particle is best captured due to the lack of optical or directional effects. As an aside, it should also be noted that the actual surface information extracted from XCT data is encoded as a full 3D triangulated mesh, which additionally makes XCT the only technology currently capable of capturing the re-entrant nature of the features (in this case, the underside of the sphere) [197,253]. For the purposes of this comparative analysis, however, the outputted triangulated mesh was converted into a height map by raster scanning, in order to allow comparison to the optical datasets which natively return height maps. Because of raster scanning, the re-entrant parts of the feature are lost in this comparison.

5.2.3.3 Recesses

Surface recesses are another highly challenging family of features that result in substantially different reconstructions dependent on measurement technology, due to the presence of high slopes and high aspect ratios. Further challenges in recess measurement result from the presence of clusters of agglomerated powder particles, located inside or surrounding recesses. Reconstructions from two example recesses are illustrated in figure 5.10, which shows particularly that two technologies, CM and FV, can fail to recognise a recess entirely, returning either high-frequency noise (CM, figures 5.10a and 5.10e), or even a protruded measurement artefact (FV, mostly evident in figure 5.10c, and to a

lesser extent in figure 5.10g). The same result can be seen when examining the local height error maps overlaid onto the CSI dataset (figure 5.11) for the first recess shown in figure 5.10.
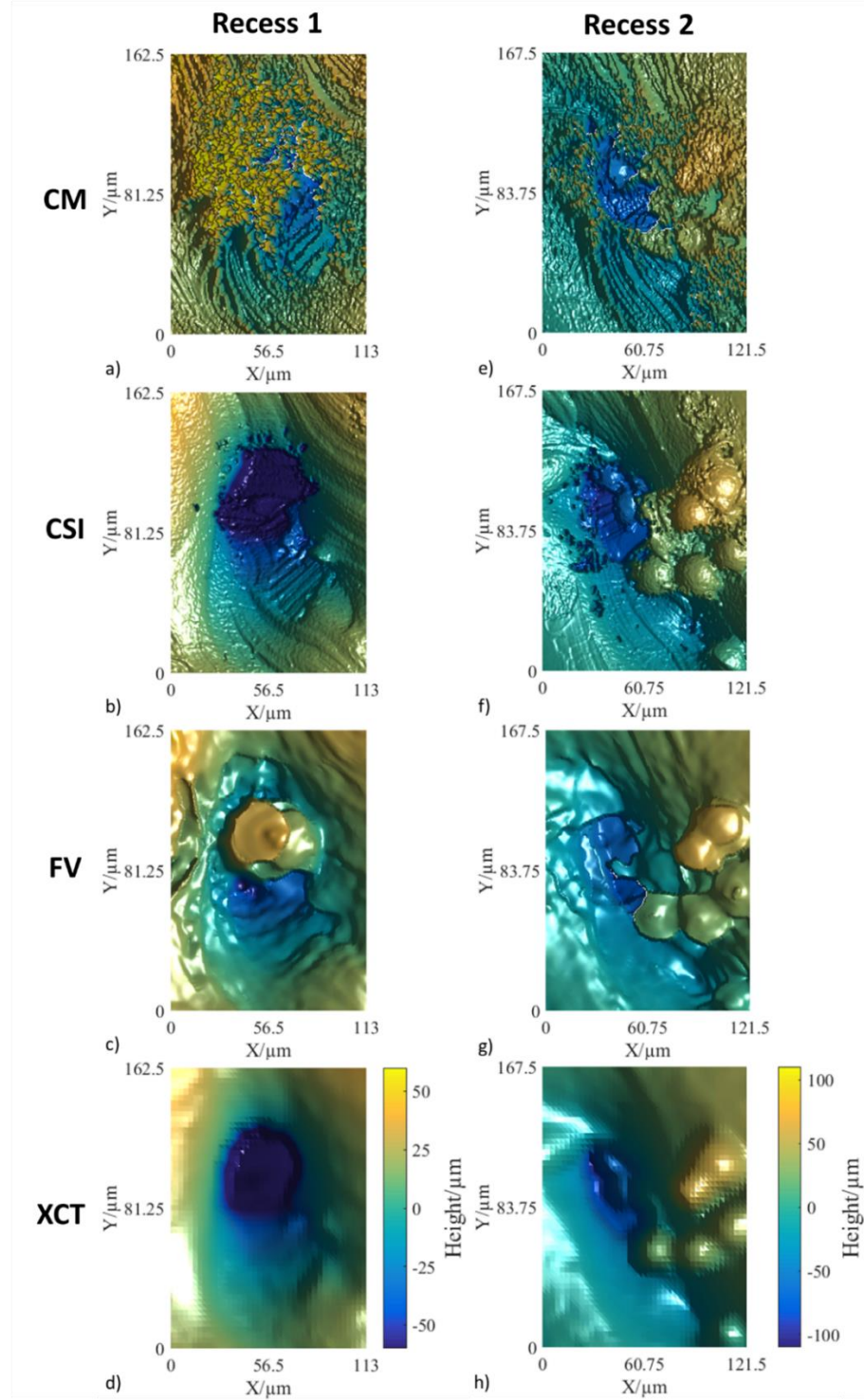
Figure 5.10. Reconstructions of two surface recesses. Two different window sizes were chosen in each case to highlight a single recess only, and a recess with surrounding particles. Figure published in [229].
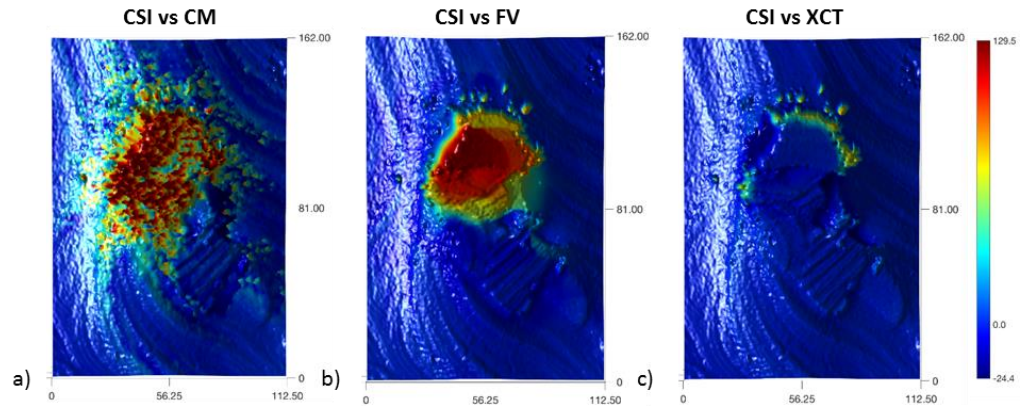
Figure 5.11. Local height error maps overlaid on the CSI topography dataset. Colour is proportional to local (signed) height error. The range of local height error values is fixed for each feature instance, so that colours are comparable across images; the colour corresponding to zero error is highlighted in the colourbar (blue tint). Using CSI as a reference, red colouring indicates regions where the second measurement is higher. Figure published in [229].

Difficulties encountered when measuring recesses result from a scarcity of reflected light and multiple reflections from within recesses as a result of the presence of high slopes and aspect ratios, which are challenging for optical technologies (such effects are discussed in the instrument-specific Chapters in [32]). It should be noted that despite the apparent superiority displayed in these results over CM and FV measurements, CSI measurements similarly suffer as a result of these issues; typically returning a greater number of non-measured points compared to other technologies (although, [49] suggests improvements to CSI technology that can mitigate some of these issues). This issue is not visible in figures 5.10 and 5.11 as non-measured points have been filled by interpolation of valid neighbours, for the purposes of accurate alignment. XCT measurements do not experience the difficulties faced by optical technologies, but the intrinsically lower resolution of the measurement can result in filtering of smaller recesses from the data. Similar to the case of particles, XCT is also the only technology capable of capturing re-entrant features in recesses, such as sub-surface pore networks. Again, similarly to the particle case, due to the height map conversion applied for comparison purposes in this work, such capability was not explored.

5.2.3.4 Weld ripples

When examining weld ripples (figure 5.12), significant differences between measurement technologies are apparent in regards to capture of high spatial frequency features.
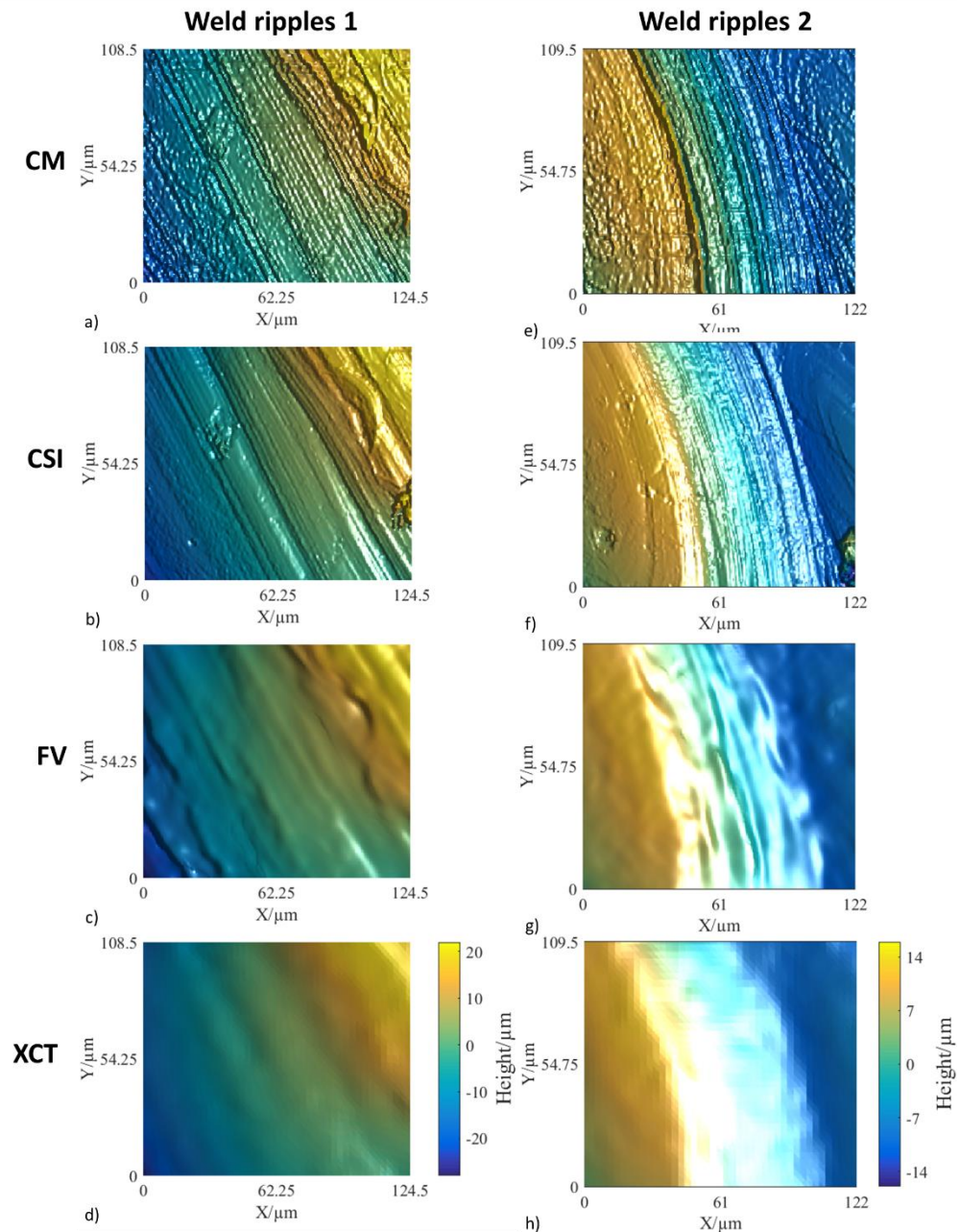
Figure 5.12. Reconstructed weld track ripples. Figure published in [229].

Both CM and CSI reconstructions of the same region return a high number of ripples, though the CM representation is more irregular. The presence of ripples

is reported in the FV datasets to a lesser extent, where, while most of the small-scale detail is lost, it is still possible to discern larger-scale ripples. The majority of ripple information is lost in the XCT dataset. Differences across technologies are mostly due to the different lateral resolving power achievable through each technology (see Section 5.2.4 for further details). When investigating weld ripples, very little information can be gained from examination of local height discrepancy maps (figure 5.13), as differences between measurements are spread across the entire FoV. Nevertheless, by comparing the numeric values of the discrepancies (colourbar in figure 5.13) with those observed for the particles (figure 5.9) and recesses (figure 5.11), it can be seen that the differences for the ripples are smaller, as a result of the lower aspect-ratios involved. Colour maps are not directly comparable across figures because they are scaled on feature-specific intervals.
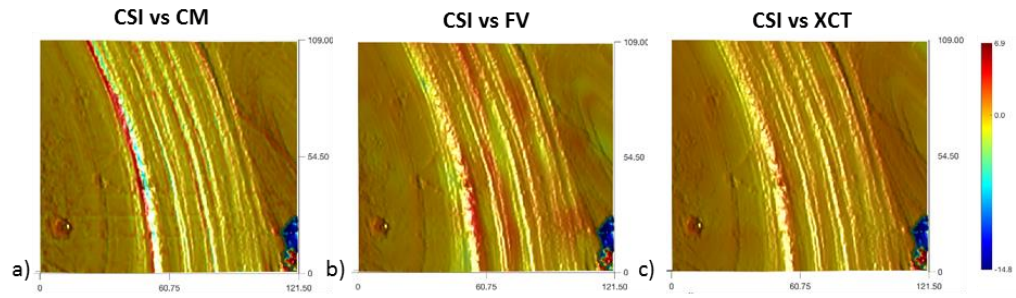
Figure 5.13. Local height error maps overlaid on the CSI topography dataset. Colour is proportional to local (signed) height error. The range of local height error values is fixed for each feature instance, so that colours are comparable across images; the colour corresponding to zero error is highlighted in the colourbar (golden tint). Using CSI as a reference, blue colouring indicates regions where the second measurement is lower, and red where it is higher. Figure published in [229].

5.2.3.5 Weld tracks

Weld tracks are complex, elongated protrusions, additionally comprising an assortment of ripples, particles, recesses, and other larger-scale wave-like components. Thus, when examining weld tracks, it is difficult to separate the underlying shape of the track from the smaller-scale features that cover its surface. Moreover, it is in itself often non-trivial to isolate an individual weld track, due to irregular boundaries and overlapping between multiple tracks [9]. One region approximately encompassing a pair of adjacent weld tracks is shown

141

in figure 5.14a – 4.14d. Local height error maps (displayed in figure 5.14e – 4.14g) show that the greatest discrepancies between measurements are concentrated around the smaller-scale features discussed previously (particularly particles and recesses), while the larger-scale components of the topography have a more consistent appearance across measurements.
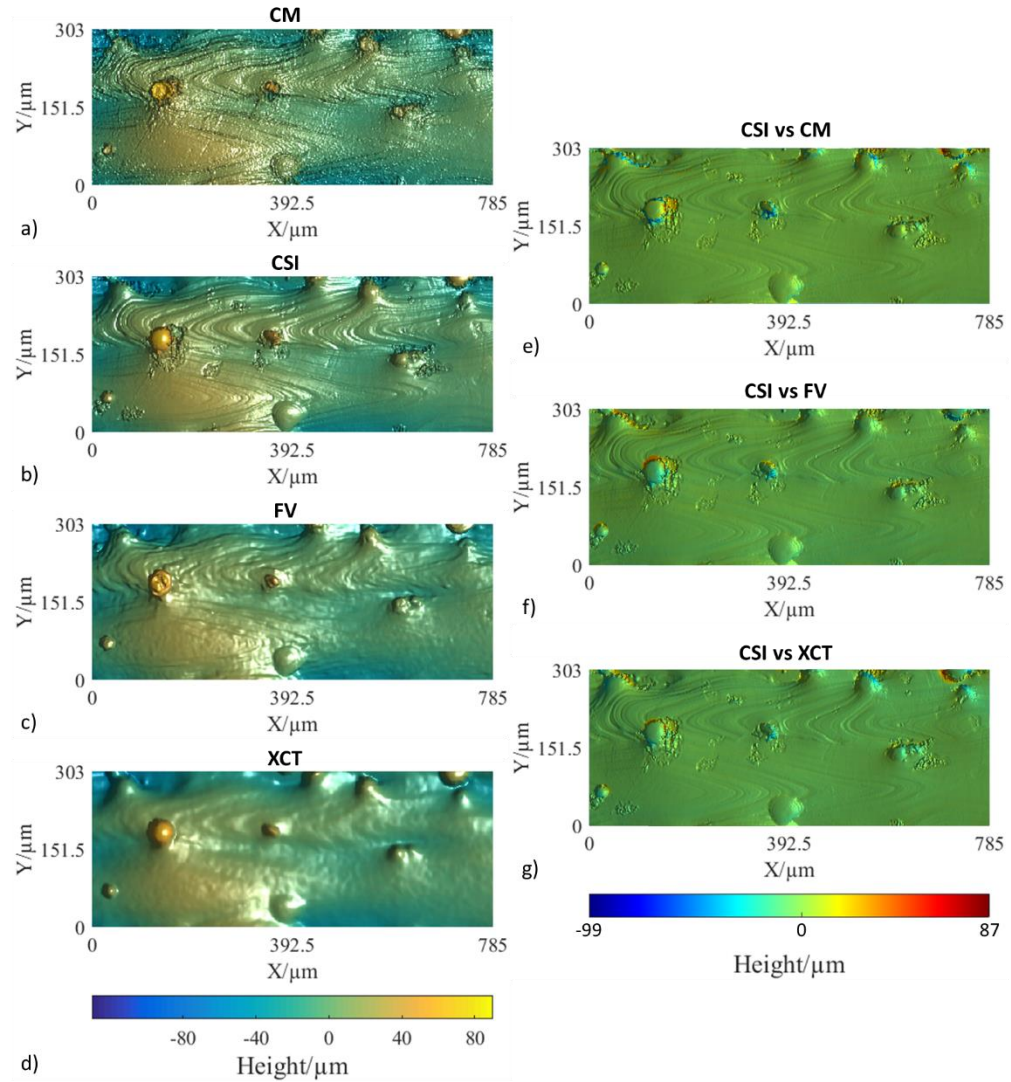
Figure 5.14. a) – d) Reconstructed weld tracks; e) – g) Local height error maps overlaid on the CSI dataset for the weld track region. The range of local height error values is fixed for each feature instance, so that colours are comparable across images; the colour corresponding to zero error is highlighted in the colourbar (green tint). Using CSI as a reference, blue colouring indicates regions where the second measurement is lower, and red where it is higher. Figure published in [229].

5.2.3.6 Distribution of local height error within the FoV

The distribution of local height error, again computed by using CSI as reference, can be investigated through the use of boxplots; those reported in figure 5.15 show the unsigned local height error (the absolute value of the signed error) for the features whose local height error maps have been shown in figures 5.9 (particle), 5.11 (recess), 5.13 (weld ripples) and 5.14 (weld track). The results show that the mean error is similar across measurement types, and most of the differences are in the tails of the distributions, classified as outliers.

From a statistical viewpoint, differences between measurements are generally small (the median error of each comparison is typically within the inter-quartile range of the others), and most of the significant differences appear as outliers. Provided the ROI is large enough to encompass a significant portion of the surface (e.g. multiple weld tracks), then the differences between measurements are less relevant as larger-scale topographic components are consistently captured across technologies. However, this scenario does not hold in the case where the FoV is occupied for the most part by difficult-to-measure topography. For example, a recess that occupies the majority of a FoV will lead to more significant non-outlier discrepancies, and so great care must be taken when assessing how much of the FoV is occupied by difficult-to-measure features, as the resulting consistency between instruments may be poor. For example, measurements made of the side surface of the same artefact used in this study as part of the wider experimental campaign yielded a dense array of attached particles (as reported elsewhere [9]), and by these results such a surface could represent the latter scenario discussed here.
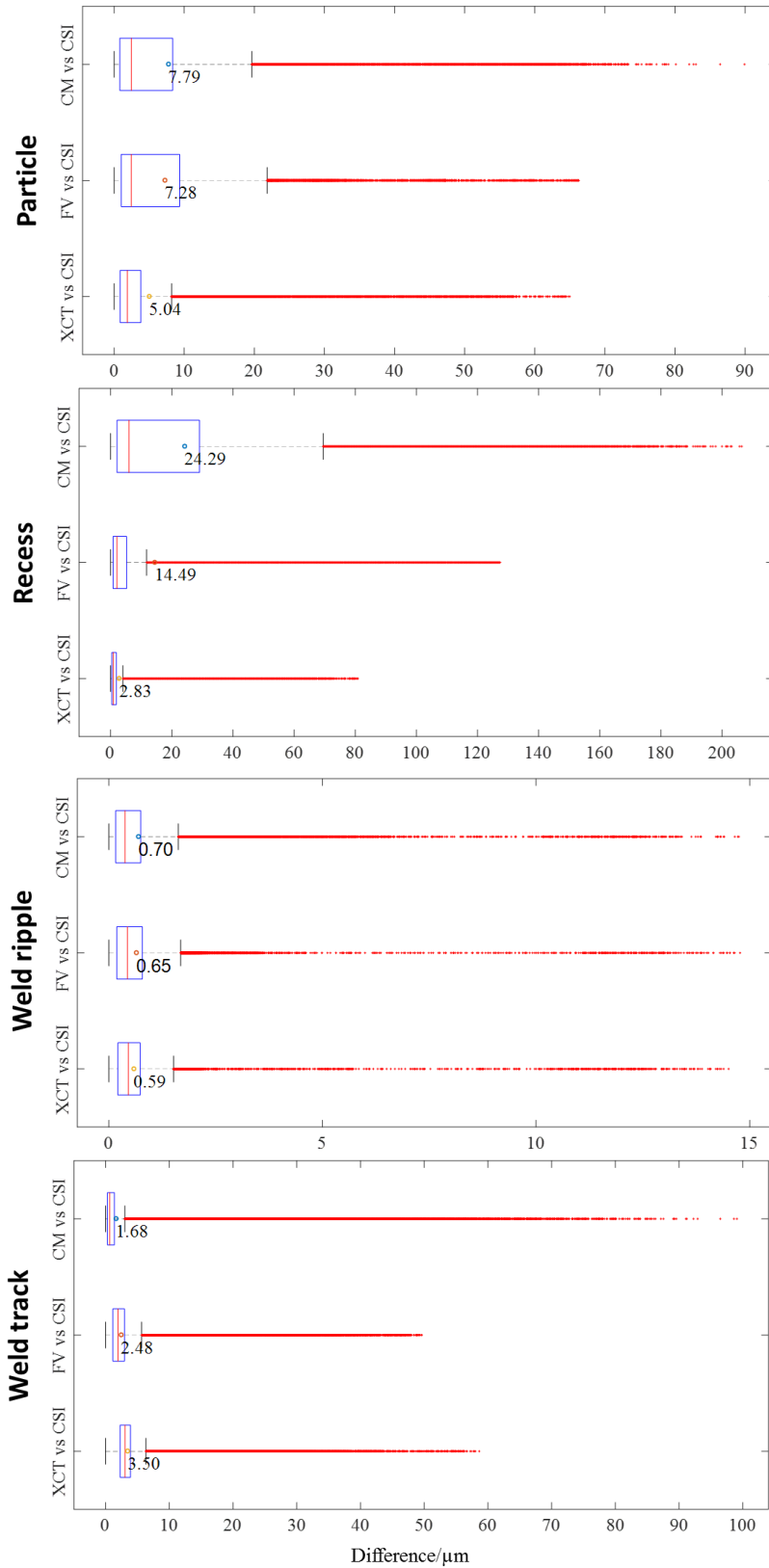
Figure 5.15. Boxplots illustrating the distribution of the unsigned local height error for the four features whose local height error map is reported in figures 5.9, 5.11, 5.13 and 5.14. Each box plot reports the median, interquartile range, whiskers and outliers (red dots). Labelled circles indicate arithmetic means. Figure published in [229].

5.2.4   Section discussion

Differences between measurement results obtained through the application of different measurement technologies to the same topography are evident. For MPBF, the most significant differences relate to smaller-scale, high aspect ratio localised features.

If the purpose of the investigation is surface characterisation of large ROIs through computation of texture field parameters, then the discrepancies across technologies may be considered to have limited effects on the characterisation results (see [240] for an in-depth discussion on the effects of measurement technologies on texture parameters for additive surfaces). However, if the investigation is targeted at localised, smaller-scale features, (often the case in off-line metrology for manufacturing process development and optimisation), then the discrepancies between technologies become more significant, and so great care must be taken in the analysis and interpretation of measured data.

The results presented in this Section point to high local slopes as a dominant factor in causing measurement error for optical technologies. More generally, high aspect-ratio features are the cause of many problems, as they often include a combination of high slopes and local variations in the amount of light returned to the detector (e.g. decreases in returned light relating to deep recesses, excesses in returned light from shiny, smooth protruded regions, such as attached particles). These problems do not affect XCT because there is no unidirectional probing involved. Other problems do affect XCT though; this is a subject of current debate and ongoing investigation (see Chapters 6 and 7, as well as [99,196]).

Moreover, as the majority of relevant differences observed in the work presented in this Chapter relate to the capability of instruments in reconstruction of small-scale topographic features, it is clear that measurement resolution factors in heavily. It is convenient to introduce the concept of lateral topographic resolution in measurement, as an indicator of a measurement technology's ability to resolve topographic detail at small scales on the surface plane. For the

optical techniques (CM, CSI and FV) a combination of optical resolution (related to wavelength and the NA of the objective), pixel spacing (related to detector characteristics), transfer characteristics (i.e. the instrument's response to different spatial frequencies) and the raw-data processing pipeline used to obtain height information, leads to the final resolving power achievable by each technology. Data processing plays a particularly large part in the determination of lateral resolution. For example, FV requires a window of adjacent pixels to compute contrast (and thus compute local height) for any given pixel, which means that the heights of two adjacent pixels are not entirely independent (i.e. they are not fully resolved). This dependency means that the actual lateral resolution of a FV instrument is significantly poorer than that calculated by considering only pixel spacing and the optical resolution limit. Similarly, the ability of CSI and CM to resolve heights at given spatial frequencies (a term referred to as the 'lateral period limit' in draft ISO specification standards) needs to be determined (see [254] for a proposed method). For XCT, overall resolving power results from the resolution of the raw projections (a function of X-ray spot size and pixel spacing at the detector), how the X-ray images are processed and recombined to create a volumetric dataset and how the surface mesh is computed and extracted from the volumetric dataset [137]. In the configurations adopted for this work, CM and CSI were able to achieve sub-micrometric resolutions, while FV and XCT were limited to a few micrometres. The exact determination of resolving power as a function of measurement technology, process parameters and surface properties needs further investigation, and is subject of ongoing research (e.g. see [254]).

A note should be made regarding the statistical significance of the observed results. Proper discrimination between measured topographies would imply a more thorough study of measurement-related error, in order to separate random and deterministic components. The problem of assessing the uncertainty associated with the topographic reconstruction, exists in this Section along with the need for obtaining a better quantitative assessment of the systematic error components. In the work presented in Section 5.1, this issue is preliminarily addressed through development of statistical models of measured topographies, but further effort is required   in order to attain comprehensive models, in

particular when modelling covariance (i.e. spatial correlation) between different points within the same field of view.

It is important to discuss how the results reported in this work can be generalised. The trends illustrated in this work have been consistently observed for multiple instances of particles, recesses, ripples and weld tracks. However, there remains a question regarding the portability of these results to different artefacts (different materials and/or different laser or electron beam MPBF processes, and to the surfaces after post-processing). So far, similar operating conditions have led to consistent results: e.g. the reconstructions of attached particles have consistently shown the same sets of issues, provided particles are nominally similar in size and shape. Other topographic features are more strongly dependent on set-up. For example, weld tracks may or may not be visible, depending on surface orientation, proximity to other features and the additive process used to fabricate the sample (e.g. laser against electron beam MPBF, but also layer scanning parameters). As such, measurement technologies may operate differently to how they are observed behaving here. Regardless, results consistent with the general conclusions illustrated earlier about the dependency on aspects such as slope or aspect-ratio should be obtained.

It is also worth considering the constant evolution of measurement technologies. As raw data processing within the instrument plays such a fundamental role in determining the final topographic reconstruction, it is expected that different results will be obtainable as new versions of measuring instruments enter the market. In such circumstances, the role of this work is to raise awareness about the fact that, at least currently, measurement error is far from negligible; in particular in the case where accurate rendition of small-scale, local topographic features is required.

5.3 Chapter summary

In this Chapter, a quantitative comparison of areal topography measurement by CM, CSI, FV and XCT technologies was firstly performed through analysis of agreement/discrepancy of aligned topographies (profiles) and the computation

of areal texture parameters. Illustrated results bring new insight into the behaviour of measurement technologies in inspection of MPBF surfaces, supporting a better-informed approach to topography inspection. The comparison method proposed in this Section is applicable to multiple scenarios where comparative topography assessment is required, and can also be considered a fundamental milestone towards improving our understanding of topography measurement artefacts and their effects on texture parameters. As the proposed method for computing CIs provides, amongst other things, an indirect indication of measurement repeatability, it would be interesting to see how the information compares to surface topography repeatability as defined in ISO 25178 (parts 603-607, [35,39,41,43,45]). It would also be interesting to see if the two results could be integrated to improve understanding of the behaviour and performance of complex surface topography measurement. Such work extends beyond the scope of this Thesis, but represents a stimulating avenue for future work. Issues were raised regarding data alignment procedures in Section 5.1.4, but issues were addressed in the latter half of this Chapter using a six degrees of freedom alignment process.

Secondly in this Chapter, it was shown through quantitative comparison of topography data obtained by using different measurement technologies (CM, CSI, FV and XCT), that disagreement between reconstructions can be significant. This finding is particularly true in the case of smaller-scale features, where local height differences are found to be on the same order of magnitude as the features being measured. The reasons for such discrepancies can be found in the phenomena taking place in the interactions between measuring instruments and the specimen surface (for optical measurement technologies) and in an equivalent series of phenomena taking place in XCT measurement that result from the different probing strategy employed by XCT (i.e. omni-directional, and based on the attenuation of transmitted rays as opposed to reflection). Some of these phenomena have been discussed in this Chapter, but significant research efforts are still needed and further work is in progress. At present, it can be stated that, for larger-scale topographic formations, all measurement technologies return relatively consistent results. However, no topography reconstruction should be assumed to be reliable, regardless of

measurement technology, particularly when the measured surface is as challenging as is often the case with MPBF surfaces. Even in the case where the final goal is not to obtain an accurate rendition of individual topographic features, but instead to simply compute texture parameters, a better understanding of how and why each instrument reacts in the way it does to specific topographic formations is a requirement for results to be accepted and processed.

Finally, for no reason should any one of the illustrated measurement technologies be considered inferior or superior when measuring MPBF surfaces. Results are heavily dependent on instrument make and model, current setup, and specific conditions related to the measured sample [49]. The primary message to be taken away from this work is that areal topography measurement of MPBF surfaces by any method is potentially affected by measurement errors comparable in size to the features being measured, and that this should be seriously considered in any measurement campaign with an intention of accuracy.

6. X-ray computed tomography surface measurement in depth

In Chapters 4 and 5, X-ray computed tomography (XCT) was demonstrated as a potential method of surface measurement, though a requirement for significant validation work was noted. In this Chapter, this need is addressed through comparison of data acquired, using two different XCT systems, to data acquired using coherence scanning interferometry and focus variation systems. Particularly, an artefact simulating an inaccessible surface is used to represent the case where XCT may be used in industry, where traditional contact or optical methods are not possible. The main output of this Chapter is the method, developed during this PhD, of surface extraction from raw XCT data, and this method is detailed towards the end of the Chapter. This work was recently published in [102] and was presented at two conferences during 2017 [255,256] on XCT and metrology and X-ray computed tomography, respectively.

6.1 Measurement of internal and difficult-to-access surfaces

As discussed throughout this Thesis, rigorous qualification of parts via the application of appropriate physical and specification standards is essential to ensure safety and quality in a manufacturing context. XCT has become established as a useful tool in holistic measurement of industrial parts, and is steadily being incorporated into the metrological toolbox [58]. Although much work remains in the standardisation of XCT for metrology (ISO 10360-11 [257] is still in the draft stages), XCT has begun to show promise for the verification of internal geometries present in AM parts. While the spatial resolutions typically achievable by XCT have not historically been at the level required to capture the smaller-scale formations of a surface, in addition to the overall shape, advanced systems are approaching these resolutions in their best-case measurement scenarios, and so XCT is becoming a viable option for surface topography measurement. When considering the fact that AM parts commonly feature complex, internal geometries, the prospect of using XCT for surface topography measurement appeals further, as a method of overcoming the access

requirement problems intrinsic to contact and optical measurements. The use of XCT for surface topography measurement is highlighted in a number of recent studies [99,134,135,194–196]. Pyka et al. [134,135] performed the first surface topography measurement using XCT, by extracting profiles from slice data obtained from XCT measurement of lattice struts. Townsend *et al.* [99,195,196] extended this work by initiating a more extensive examination of XCT topography measurement performance in comparison to optical surface measurements, with the most recent work by Townsend *et al.* [195] examining the output of a number of measurements performed across several laboratories. Much work exists in the validation of XCT for internal topography measurement. However, to date, no research effort has been specifically dedicated to investigating the challenges of measuring the topography of internal surfaces. To address this research need, an investigation comparing internal XCT surface measurements and measurements made using optical surface technologies is presented in this Chapter.

6.2 Chapter methodology

6.2.1   The MPBF specimen

A laser metal powder bed fusion (MPBF) hollow artefact was chosen as an appropriate artefact for this research. The artefact was measured using two commercial XCT systems (labelled 'XCT 1' and 'XCT 2' in this Chapter), as well as by two optical measurement systems. Measurements were performed using optimised parameters for each system based upon the manufacturer's recommendations, the experience of several trained operators and good practice acquired during the work presented in Chapters 4 and 5. All instrument names are once again redacted from this Chapter to prevent undue comparison of commercial instruments. The artefact used in this work was produced in two separable parts (see figure 6.1) from Ti6Al4V using an EOSINT M 280 metal MPBF machine. The manufacturer's process parameters for Ti6Al4V were used to produce the artefact. Ti6Al4V was chosen as the artefact material for its suitability to XCT measurement and general industrial relevance. When assembled, the artefact simulates the metrological challenge of internal

geometries as surfaces become inaccessible to optical surface measurement solutions. When separated, surfaces can be inspected using optical technologies. Further information about this sample is detailed in Section 3.1.
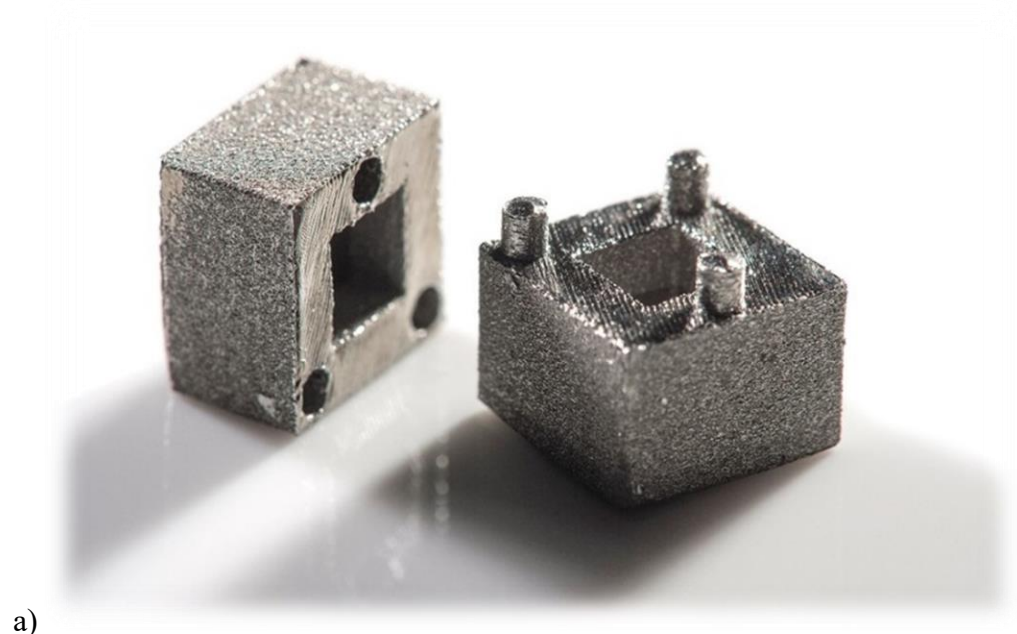
a)
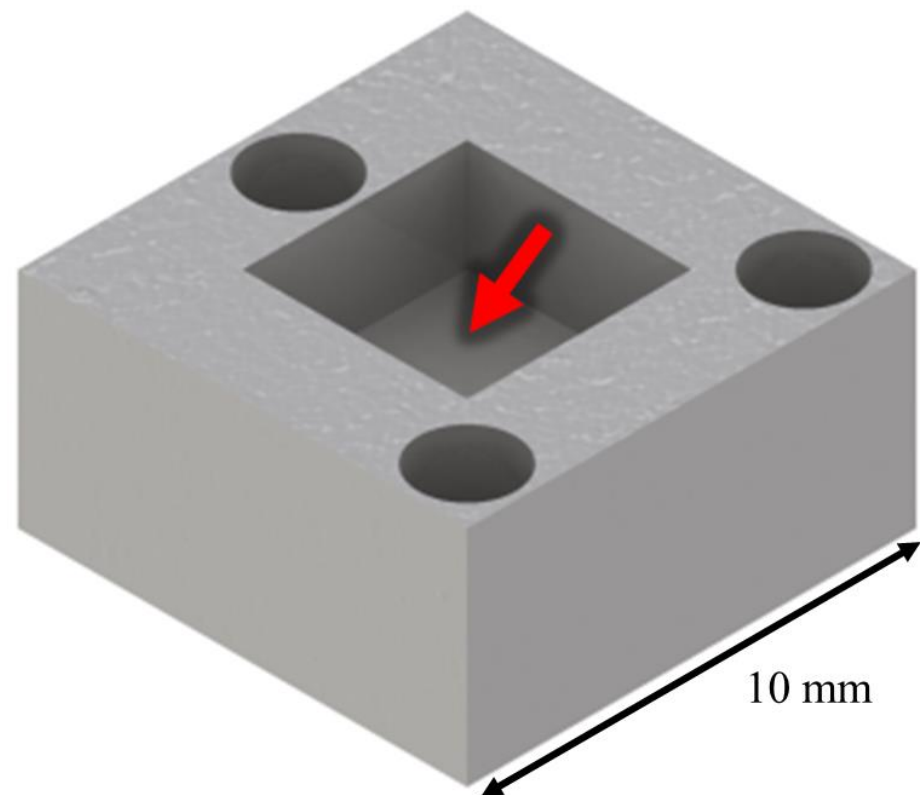
b)

Figure 6.1. a) Artefact for the measurement of internal surface texture. When assembled, cube dimensions are (10 × 10 × 10) mm; b) The surface of interest, indicated by the arrow on a CAD rendering of one half of the artefact. Figure published in [102].

6.2.2 XCT measurement setups

Measurements were made of the assembled artefact using two different (but broadly similar) commercial XCT systems, using measurement parameter sets suggested by experienced operators of each system. Parameters were selected to provide data that were qualitatively 'good' with respect to the experience of the operators. As the two commercial systems differed slightly in their characteristics (X-ray generation, detector response, etc.) the setup parameters were not consistent between the two systems, but both setups were expected to provide broadly similar results (based on the advice of the experienced operators). The following setups were used for the two systems:

- XCT 1: geometric magnification of 35×, leading to a voxel size of 5.7 μm, 3142 X-ray projections formed from averaging of two exposures per projection, each lasting 2.829 s; X-ray tube voltage 150 kV and current 36 μA; a 0.25 mm copper X-ray pre-filter was used to attenuate lower energy X-rays. Data were reconstructed in the manufacturer's software, using a beam hardening correction and a Hanning noise filter [70]. This filter was chosen to reduce image noise present when alternatively using an edge-preserving ramp filter, without substantially degrading the quality of the edges present in the data.

- XCT 2: geometric magnification of 5.75× and optical magnification of 0.4×, leading to a voxel size of 5 μm, 1600 X-ray projections formed from averaging of two exposures per projection, each lasting 6 s; X-ray tube voltage 160 kV and current 63 μA; a proprietary X-ray pre-filter was used according to the manufacturer's guidelines to attenuate lower energy X-rays. Data were reconstructed in the manufacturer's software, using a beam hardening correction and a Gaussian reconstruction filter in line with the manufacturer's guidance.

In both cases, reconstructed volumetric data were imported into VolumeGraphics VGStudioMAX 3.0 [73] and surfaces (triangulated meshes) were determined (as in previous Chapters) using the maximum gradient method

over four voxels, with the ISO-50 isosurface as a starting point (see figure 6.2a) [139].
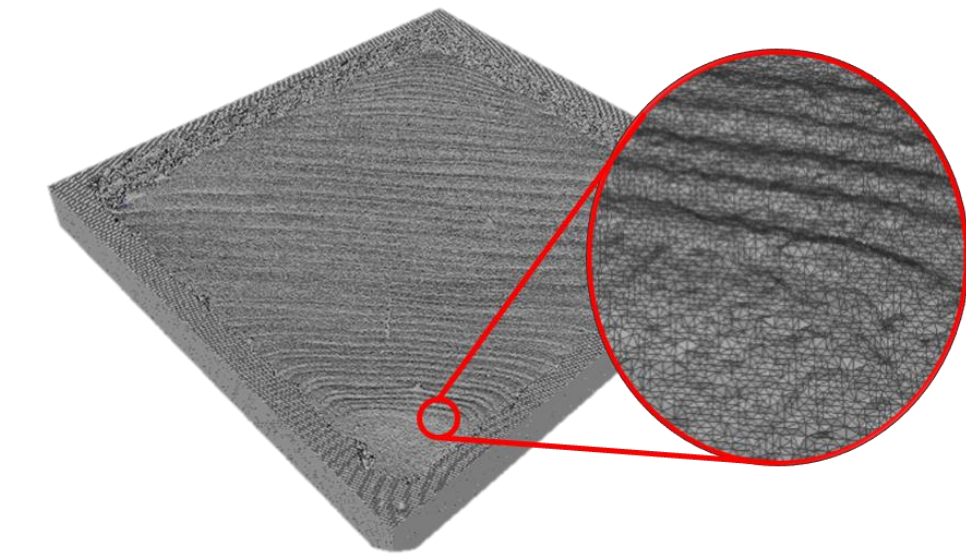
a)
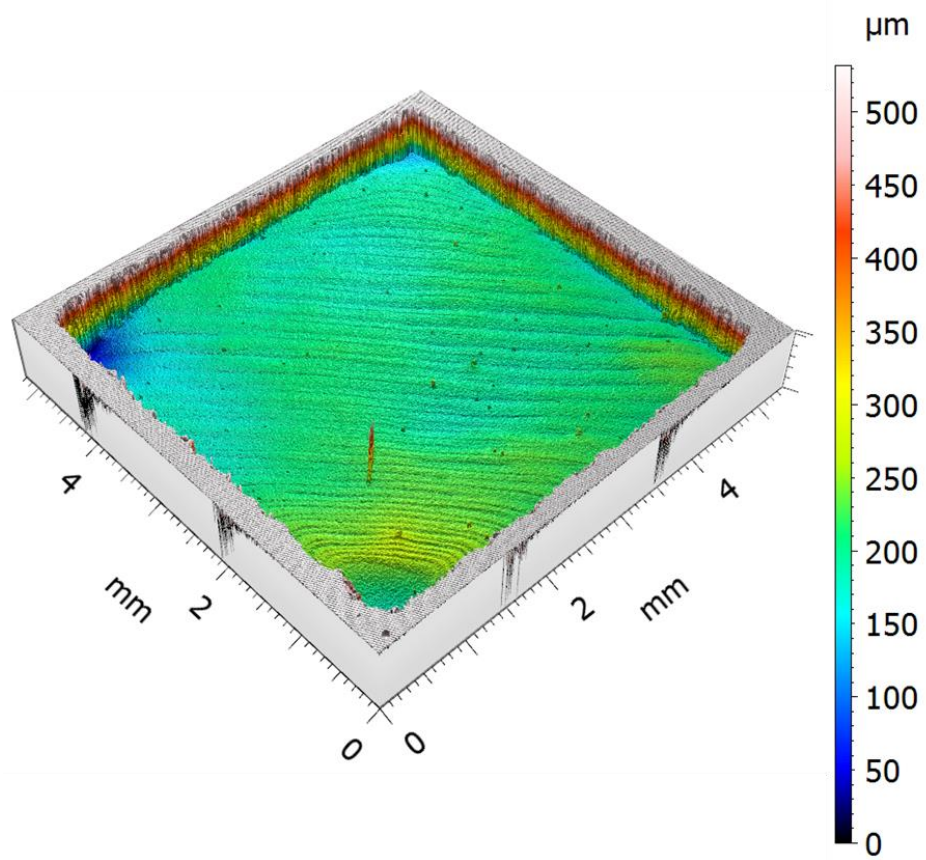
b)

Figure 6.2. Surface determined for XCT 1 data, and magnified area showing individual triangles: a) rendered in MeshLab [244]; b) resampled into a height map and rendered in MountainsMap. Figure published in [102].

6.2.3   Optical system measurement setups

The following setups were used for coherence scanning interferometry (CSI) and focus variation (FV) measurements, where FoV is the field of view, LR is lateral resolution and NA is numerical aperture. As in Chapters 4 and 5, LR-pixel refers to the pixel spacing of the detector used by each instrument, LR-optical refers the calculated Sparrow optical limit [34] of each instrument and LR-contrast refers specifically to the distance from the centre of each pixel used by the FV instrument to compute local contrast; selected during the measurement. The Sparrow optical limit was calculated using a wavelength of 580 nm for both systems.

- CSI: 20× objective lens at 1× zoom (NA 0.40, FoV 0.42 mm × 0.42 mm, LR-pixel 0.41 µm, LR-optical 0.68 µm), stitching of multiple images performed in the manufacturer's proprietary software. Vertical stitching was also applied, to merge two measurement z intervals (145 µm and 100 µm wide respectively, with 10 µm overlap).
- FV: 20× objective lens (NA 0.40, FoV 0.81 mm × 0.81 mm, LR-pixel 0.44 µm, LR-optical 0.68 µm, LR-contrast 3 µm), ring light illumination, measured area 3.7 mm × 3.7 mm, stitching of multiple images performed in the manufacturer's software.

6.2.4   Data processing

XCT surface data were cropped to extract the surface of interest in VGStudioMAX, and exported as triangulated meshes in .STL format. In Meshlab [244], surfaces were re-oriented by approximate manual alignment of the surface normal (determined visually) to the z-axis, and exported again as an .STL. The rotated mesh was then imported into the surface metrology software MountainsMap [228] and resampled into height maps at a resolution automatically determined by MountainsMap, to match the point density of the triangulated mesh, approximately defined by the voxel size (see figure 6.2b).

Height maps obtained by XCT and optical measurement were relocated in the same coordinate system using MountainsMap by application of a marker-based coarse alignment, followed by cross-correlation based global algorithmic alignment [246]. From the aligned height maps, regions of size (1.5 × 1.5) mm were extracted, and levelled by least-squares mean plane subtraction, allowing like-for-like comparison of surface data. This sample size was chosen as, at 20× magnification, measurement of a larger area by CSI was deemed unfeasible due to the prohibitive number of stitching operations and lengthy measurement times. Topography datasets were bandwidth-matched [238] (involving the application of filtering operations with identical cut-off wavelengths across datasets) to allow meaningful comparison of the resulting parameters. Extracted surfaces were initially filtered using a Gaussian convolution S-filter with a 13 μm cut-off to remove small-scale surface features; chosen as the minimum possible for the lowest lateral resolution height map (XCT 2), representative of a grid of 4 × 4 pixels. A Gaussian convolution F-operator with a 1.5 mm cut-off was then chosen as equal to the size of the region of interest. This operator was applied to remove tilt and waviness at scales larger than the FoV, therefore obtaining 'SF' surfaces (equivalent to a primary surface, as defined in [48,258]). A Gaussian convolution L-filter with a 0.5 mm cut-off was applied to remove smaller scale waviness; thus obtaining 'SL' surfaces (equivalent to a roughness surface, as defined in [48,258]). This cut-off was chosen based upon visual inspection of the surface in question, designed to remove underlying waviness features but to maintain weld tracks. SL surfaces were then manually truncated to remove attached particles detected in the measurement, by voiding height values above a set value. ISO 25178-2 [30,51] areal texture parameters were calculated for SF, SL and truncated SL surfaces. Additionally, analyses of texture direction and power spectral density were performed.

The bandwidth matching process applied to obtain the SL surfaces is designed to remove spatial wavelengths that are not captured by all the measurement technologies, thus homogenising the spatial measurement bandwidths of the examined data. This process allows for comparability between datasets regardless of differences between the resolutions of the raw data. However, the bandwidth matching process intrinsically involves the disposal of information

present in some of the datasets (those covering a wider range of scales), which is why the SF surfaces (i.e. the original datasets with no removed wavelengths) have also been considered in the analysis. The most notable difference between the investigated measurement technologies is observed at the shortest wavelengths (largest spatial frequencies) because of the intrinsically higher spatial resolution achievable using optical techniques as opposed to XCT. However, specifically regarding metal AM surfaces, in recent work by colleagues and myself (Senin *et al.* [229]), as well as in Chapters 4 and 5, it was demonstrated that many interesting MPBF surface topography features identified as part of the work presented in these Chapters are accurately represented within the bandwidths shared by all the compared technologies.

6.3 Chapter results

6.3.1   Comparison of surface topography features

Visual comparison was performed on reconstructed top views of the SF height maps (see figure 6.3). For visualisation, false colours proportional to heights were used in reconstructions. Colour scales were homogenised by truncating height points above and below a common reference vertical range. Truncation was applied in figure 6.3 to homogenise colour scales for visualisation purposes only, while the original datasets were maintained for quantitative comparison.

Investigation of the data presented in figure 6.3 revealed notable similarities between all datasets, in that all topographies feature a similar reconstruction of weld track features and of larger-scale waviness components. Reconstruction of smaller-scale features, however, varies greatly between datasets. Reconstructions from optical systems are similar, though FV data show high spatial frequency noise of greater magnitude and volume than CSI data. However, both XCT systems return noticeably larger amounts of high spatial frequency noise when compared to optical measurements.
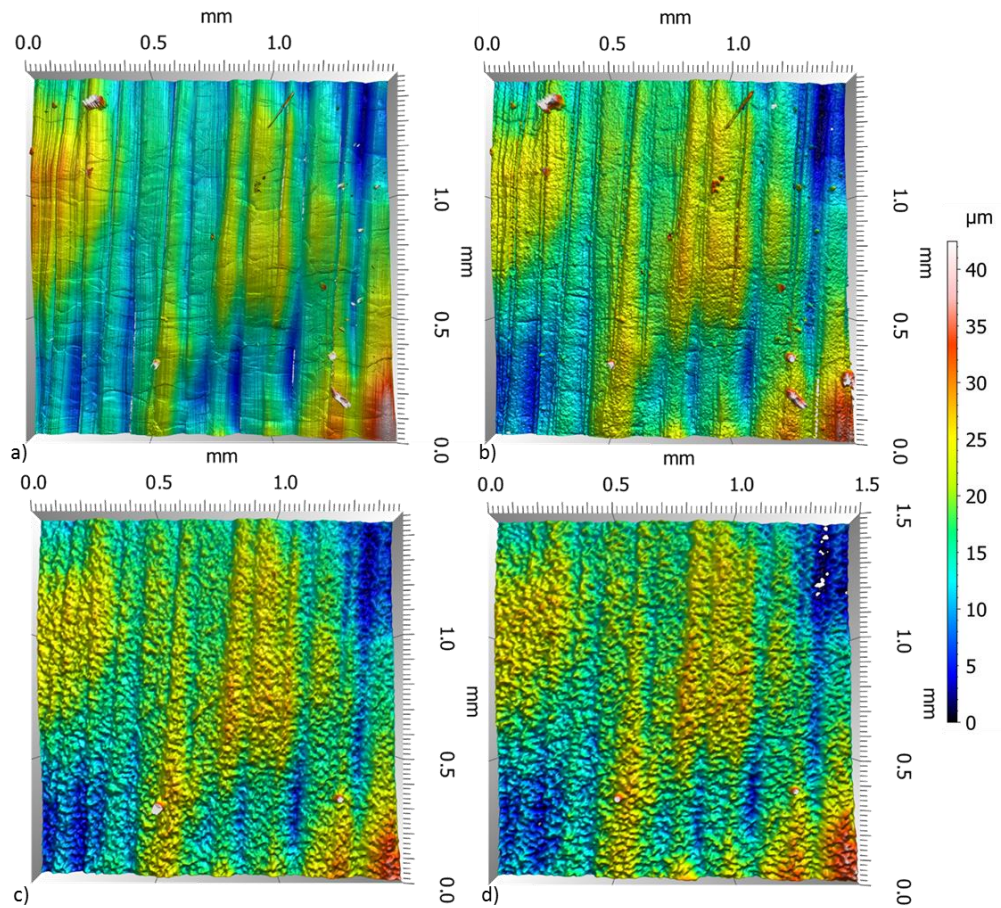
Figure 6.3. Levelled and truncated surface height maps: a) CSI; b) FV; c) XCT 1; d) XCT 2. Similarity is seen between datasets, though some smaller features present in data from optical systems are not all present in XCT data (e.g. particles). Figure published in [102].

6.3.2 Comparison of areal texture parameters

ISO 25178-2 [30,51] areal texture parameters calculated for the data displayed in figure 6.3 are presented respectively in table 6.1, table 6.2 and table 6.3, for SF, SL and truncated SL surfaces. As only one region was analysed, only one parameter value was generated per measuring instrument. The reported parameter values are, therefore, only indicative of the differences between the investigated datasets, and cannot be considered statistically significant indicators of overall performance of one measurement solution compared to another. Nevertheless, parameters can provide an indicator of the ability of different XCT systems to measure surface topography. Such a statistically significant comparison is performed elsewhere in this Thesis (see Chapters 5 and 8).

Six commonly used ISO 25178-2 [30,51] surface texture parameters are considered here: *Sa*, *Sq*, *Ssk*, *Sku*, *Std*, *Sal* (see Chapter 1 for parameter definitions). These parameters were used as they were identified as common parameters for use in such evaluations in industry (see Chapter 2 and the recent review by Townsend at al. [9]). First, parameters computed for SF surfaces are examined (see table 6.1). For the SF surfaces, the optical techniques return *Sa* and *Sq* parameters that are the most similar to one another, which is to be expected, as both technologies are well established topographical measurement solutions. XCT instruments also return similar *Sa* and *Sq* parameters, consistent with the results of visual observation of the reconstructed topographies (see figure 6.3). Large differences are seen between instruments for *Ssk* and *Sku* parameters, while similar values are returned for the *Sal* parameters. Consistency between *Std* parameters can be considered an indicator of the quality of the alignment of surfaces, as well aligned datasets will be similarly orientated.

Table 6.1. ISO 25178-2 [30,51] surface parameters for SF surfaces.

Parameter	CSI	FV	XCT 1	XCT 2
Sa/μm	3.33	3.33	3.30	3.47
Sq/μm	4.25	4.37	4.30	4.36
Ssk	0.88	0.94	1.25	0.15
Sku	7.31	8.45	18.7	3.31
Std/°	85.8	86.0	85.8	85.7
Sal/mm	0.108	0.104	0.113	0.116

Following assessment of SF surfaces, parameters computed from SL surfaces were examined. For SL surfaces, all instruments again returned similar *Sa* and *Sq* parameters, though the effect of the L-filter in this case appears to intensify differences between calculated *Sa* parameters, while slightly reducing differences between calculated *Sq* parameters. Differences between instruments for *Ssk* and *Sku* parameters are exacerbated by the L-filter, while reducing differences for *Sal* and *Std* parameters.

Table 6.2. ISO 25178-2 [30,51] surface parameters for SL surfaces.

Parameter	CSI	FV	XCT 1	XCT 2
Sa/µm	1.96	1.91	1.94	2.09
Sq/µm	2.67	2.72	2.67	2.68
Ssk	1.52	2.20	3.02	0.08
Sku	22.4	27.6	66.0	5.18
Std/°	85.8	85.8	85.8	85.7
Sal/mm	0.0415	0.0450	0.0390	0.0409

The most notable parameter differences in both of the aforementioned cases occur for *Ssk* and *Sku* parameters, with results varying by as much as a factor of 40 between instruments and filtering conditions. Calculations of *Ssk* and *Sku* parameters involve summation of higher order powers of surface height values than those for *Sa* and *Sq* [30] and as such are more heavily affected by the presence of outliers in the data. As part of preliminary investigations, a simple outlier removal operation was performed, but yielded no noticeable difference to the calculated parameters. However, further examination of raw and filtered surface data reveals that the instruments show different responses to attached particles, a common feature of parts produced by LBPF. Specifically, a number of attached particles within the region of interest appear clearly in data acquired by the optical systems, but do not appear at all in XCT data (see figure 6.3). These particles sit above the surface, and due to the outlier-sensitive natures of the *Ssk* and *Sku* parameters, could have a substantial effect on calculated parameters. This 'missing particles' phenomena is visualised in figure 6.4, where CSI data (figure 6.4a) contains three attached particles, while the algorithmically-determined XCT surfaces show only two particles (XCT1 data is shown as an example in figure 6.4b). While figure 6.4a was generated from CSI data, the missing particle is similarly present in FV data. While it is possible that such a particle could have been removed/deposited between measurements, and so could be missing in one dataset and present in another, further examination of XCT data in this case provides more information. If a surface is determined from XCT data through the use of thresholding, as opposed to by using the gradient based algorithm (as exemplified by figures 6.4c and 6.4d), the missing particle (bottom right of each image) can be seen, while the particle visible to the left of figures 6.4and 6.4b disappears. In the thresholding case,

however, the surface is greatly degraded by increased noise, and other particles may become indiscernible from noise for this surface (as is the case for the leftmost particle present in this data). The missing particle effect is due to differing material properties (i.e. X-ray attenuation) in the particle in question, resulting in errors in the algorithmically-determined surface.
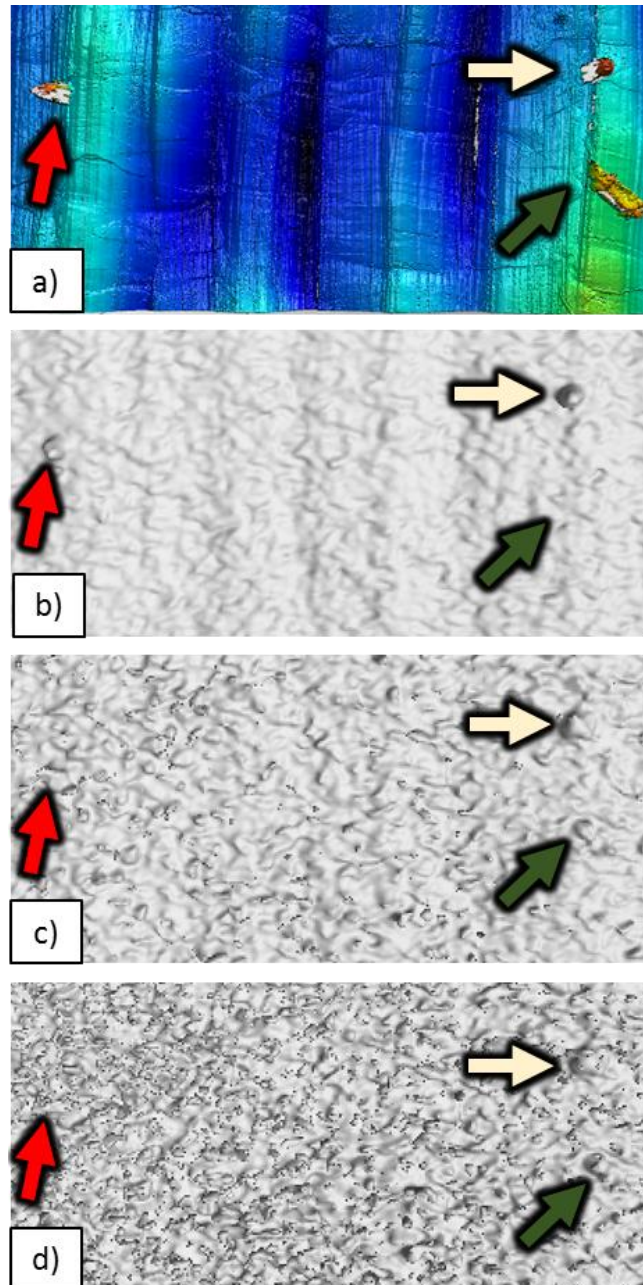
Figure 6.4. Comparison of particles present on a portion of the surface with differing surface determination: a) CSI reference (rendered in MountainsMap); b) XCT 1 using gradient based algorithmic surface determination; c) XCT 1 using ISO-50 grey value based surface; d) XCT 1 using manually chosen grey value based surface (XCT surfaces rendered in VGStudioMAX). Figure published in [102].

161

To account for the presence of attached particles on the measured surfaces and differences between datasets, data were truncated to remove particles from the measured data and parameters recalculated (reported in table 6.3). Following truncation, calculated *Ssk* and *Sku* parameters are much closer between instruments, and notably the sign of the *Ssk* parameter changes compared to the case where particles are not removed from the data, implying that the underlying surface has skewness properties that are not accurately represented before the removal of attached particles. It is clear that attached particles have a substantial effect on these higher-order parameters, and in good practice, care should be taken in the process of gaining a reliable XCT surface measurement as such particles can clearly be missed by the process. Lower order *Sa* and *Sq* parameters are changed by attached particle removal and discrepancies are slightly exacerbated, but the resultant parameters are less affected by the presence of attached particles. It is also of note that, in order to gain reliable *Ssk* and *Sku* parameters from MPBF surfaces, an attached particle removal operation is recommended.

Table 6.3. ISO 25178-2 [30,51] surface parameters for truncated SL surfaces.

Parameter	CSI	FV	XCT 1	XCT 2
Sa/μm	1.92	1.83	1.91	2.08
Sq/μm	2.42	2.32	2.41	2.64
Ssk	-0.330	-0.289	-0.301	-0.175
Sku	3.12	3.36	3.20	3.20
Std/°	85.8	85.8	85.7	85.7
Sal/mm	0.0422	0.0459	0.0406	0.0410

Although *Std* parameters are consistent between datasets in all cases, surface texture direction analysis (see figure 6.5) reveals more information than the parameters can alone, through further analysis of the directional attributes of features present in the XCT and optical datasets. Each plot represents the values of the angular power spectra for the SL surfaces as a function of surface direction. The angle corresponding to the maximum value is taken as *Std*. Direction analyses show that, while the position of the primary peak is consistent between spectra, the ratio between the size of the primary peak and the smaller peaks resulting from noise (i.e. the signal-to-noise ratio) varies. This

ratio is greatest in the CSI data and smallest in XCT 2 data, while the FV ratio is slightly greater than the CSI ratio, and the XCT 1 ratio is slightly lower than the XCT 2 ratio. As measurement noise is in this case random and, therefore, devoid of direction, this ratio is attributed to greater noise in XCT measurements than in optical datasets. It is clear that the values of the angular power spectrum are generally higher in multiple directions in the case of the noisier XCT datasets, making it more difficult to isolate the highest peak. Despite the increased noise, isolation of this peak is possible in both of these XCT cases, and improvement is likely possible with further optimisation of XCT acquisitions.
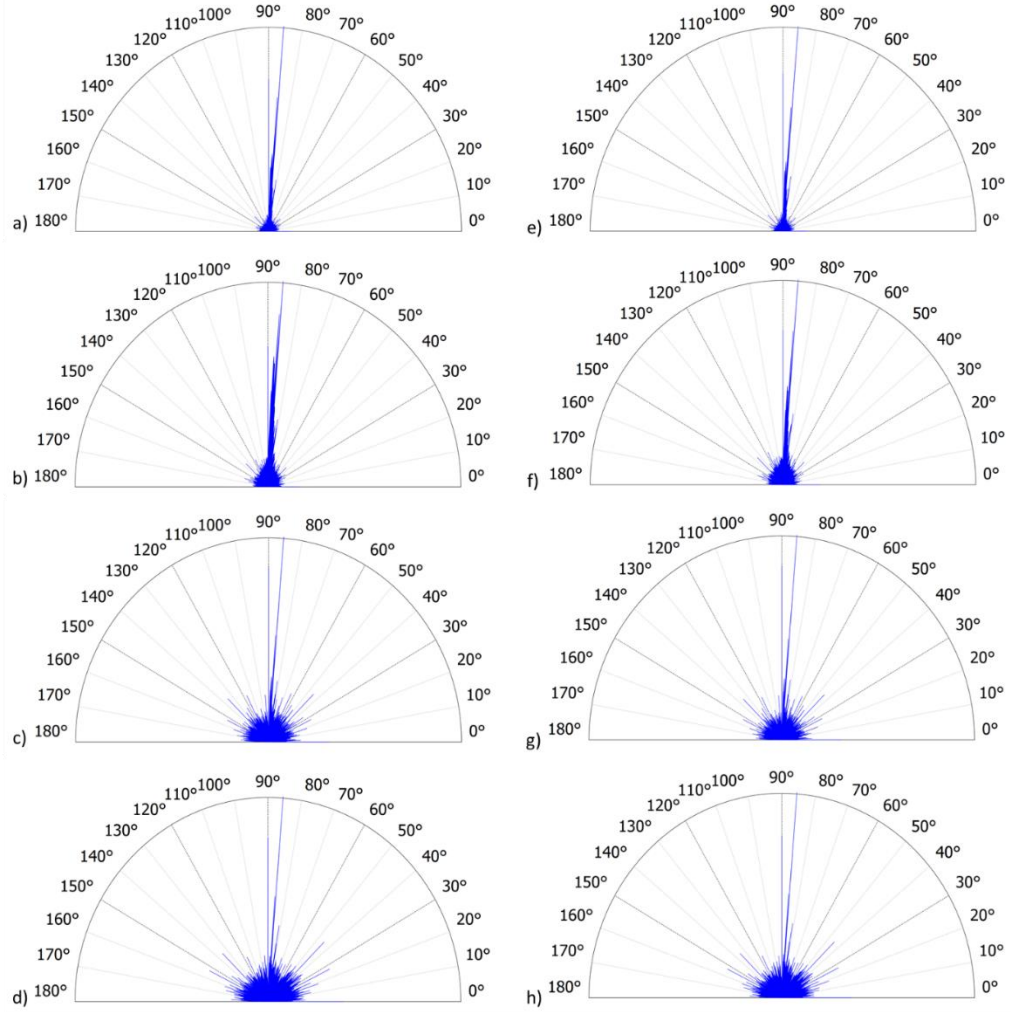
Figure 6.5. Surface texture direction: a) CSI SF-set; b) FV SF-set; c) XCT1 SF-set; d) XCT 2 SF-set; e) CSI SL-set; f) FV SL-set; g) XCT1 SL-set; h) XCT 2 SL-set. Figure published in [102].

Further information about the SF and SL surfaces can be provided by analysis of the averaged power spectral densities of the surfaces (APSDs, shown in figures 6.6 and 6.7). APSDs are used across surface measurement to identify the spatial frequencies present in a surface dataset [259], and are compared here to assess the ability of XCT to identify similar spatial frequencies to those present in optical data. In the plots, the ordinates have been truncated to 2.5 μm^2 to allow a better visualisation of the smaller peaks at longer wavelengths. Truncation results in a loss of visualisation of the largest peak between 0.00 mm and 0.10 mm, but these peaks are typically a combination of smaller scale features and high-spatial frequency noise, and of lesser interest than other visible peaks in this case. Generated APSDs are all similar; each demonstrating

164

a comparable representation of the relevant topography spatial frequencies. Peaks can be observed corresponding to the main periodic features to be expected in a MPBF surface (e.g. weld tracks, represented by the three peaks between 0.10 mm and 0.15 mm wavelengths). Minor discrepancies in peak heights are seen between measuring instruments, suggesting slightly different responses to the features on the surfaces, but all peaks can be seen in all datasets for both the SF and SL case, at similar magnitudes.

Examination of plots, such as the texture direction and APSD graphs, and more importantly, the similarities between those plots, further demonstrates the ability of XCT for surface assessment; beyond the generation of summative visual information and surface texture parameters.
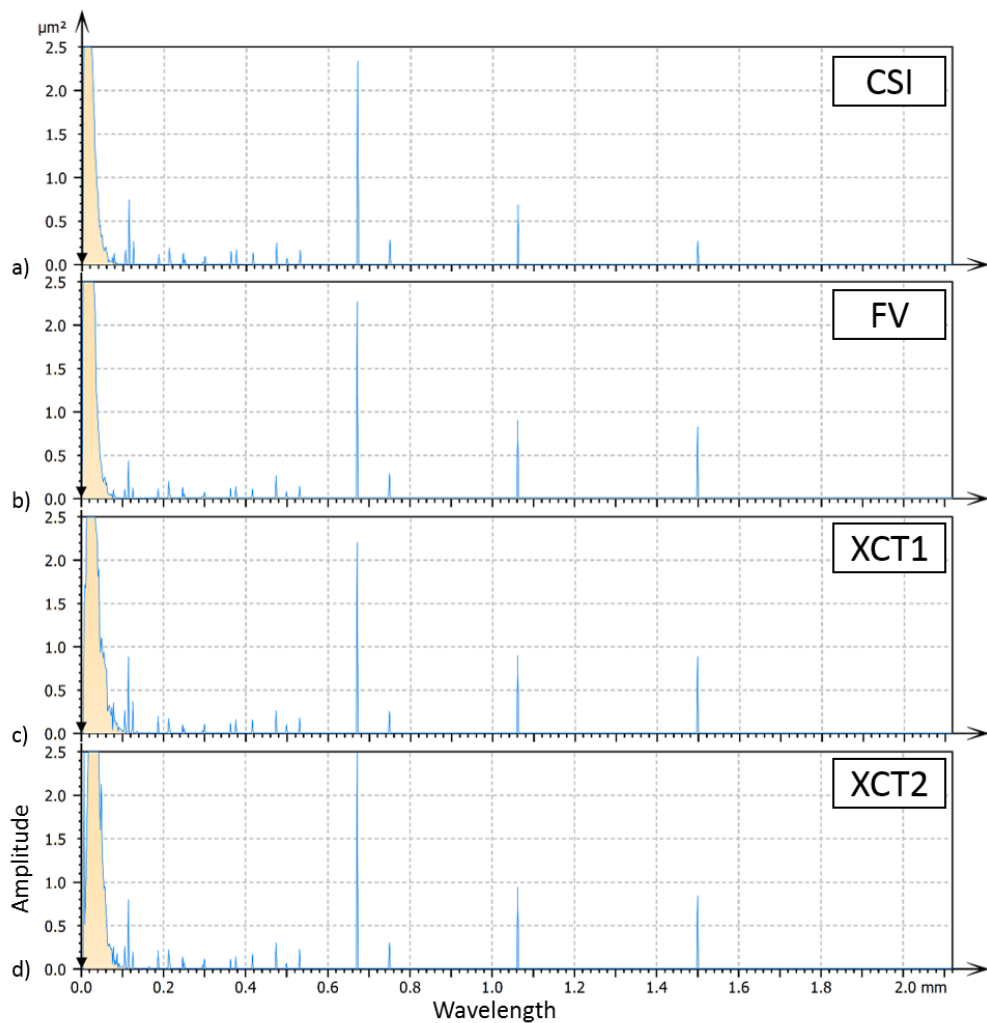
Figure 6.6. Averaged power spectral densities of SF-sets: a) CSI 2; b) FV; c) XCT 1; d) XCT 2. Figure published in [102].

165
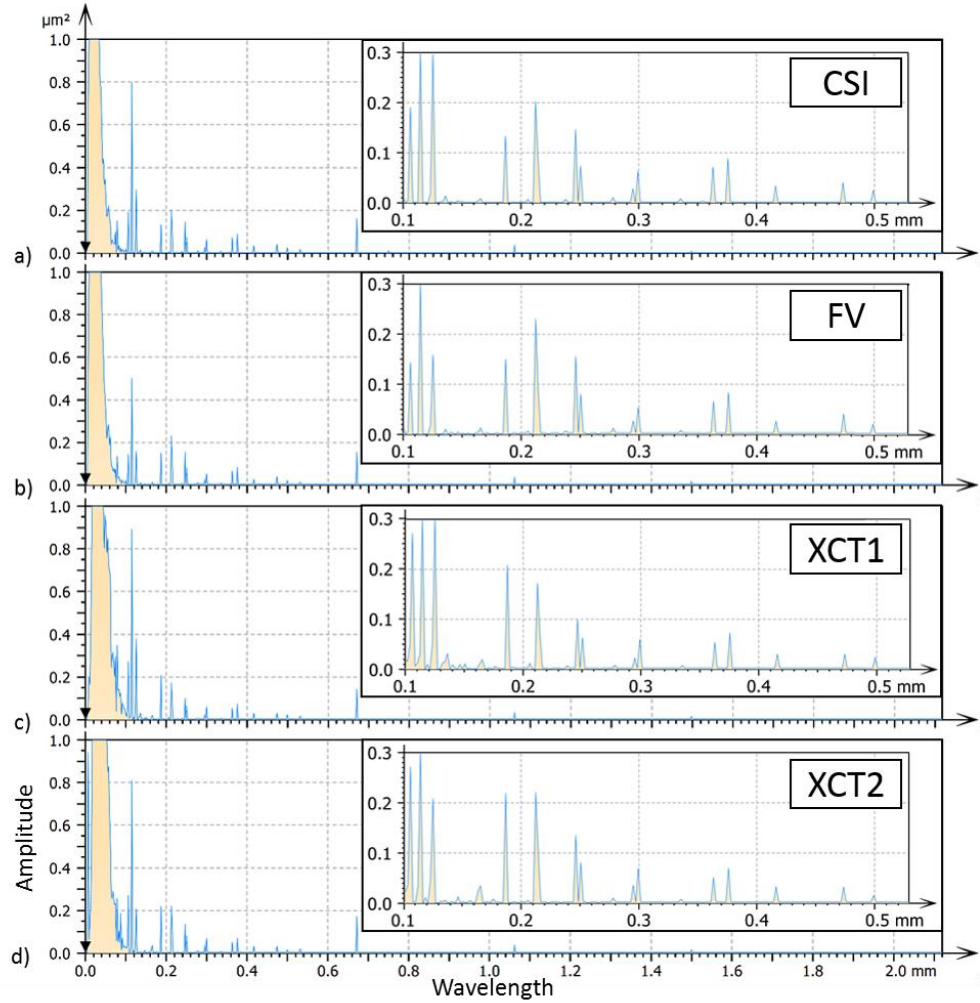
Figure 6.7. Averaged power spectral densities of SL-sets: a) CSI 2; b) FV; c) XCT 1; d) XCT 2. Insets are sections of the same data further truncated for clarity. Figure published in [102].

6.4 Chapter discussion

In this Chapter, comparison between data acquired using different surface topography measuring instruments has been facilitated by accurate alignment and similar cropping of surface datasets. Visual comparison of data acquired using different surface texture measuring instruments shows notable similarities between all datasets, with the two optical systems clearly showing the most visual similarity. Data acquired using the two XCT systems are also visibly similar to the data produced by the two optical systems, though discrepancies at the higher spatial frequencies are evident. Qualitative comparison of areal parameters calculated for aligned SF and SL surfaces showed similarity between values extracted from XCT and optical data. It is clear, therefore, that

166

XCT technology is capable of acquiring a range of information used in surface analysis, and is able to facilitate verification of parts featuring internal or otherwise difficult-to-access surfaces. This information is particularly applicable to the metal AM industry, because of the requirement for new validation techniques of complex parts, as well as for non-destructive assessment of metal AM parts during process development. These analyses build on work presented previously by Townsend *et al*. [99,196] and in Chapters 4 and 5, with further examination into the information that can be acquired using XCT instruments.

The work presented in this Chapter also involves demonstration of a method of extracting surfaces from XCT data, as described in Section 6.2.4. This method represents a notable contribution to the science of metrology, as such extraction had, to the best of my knowledge, not been performed prior to the work completed during the production of this Chapter (though has indeed been performed in numerous cases since [99,196]). The method, from raw data to surface characterisation result, generally flows as follows:

- Acquisition of raw projection data using an XCT system.
- Reconstruction of raw projections into a 3D volume.
- Determination of a surface on the XCT volume.
- Extraction of surface data by meshing of the determined surfaces into a triangulated model.
- Orientation of the 3D triangulated model to present the desired surface.
- Conversion of 3D triangulated model into a 2.5D height map.
- Characterisation of the 2.5D height map using, for example, ISO 25178-2 [51] texture parameters.

Additionally, key areas which may play important roles in future applications of XCT for AM surface measurement have been identified here. Primarily, the key caveat of this work is that it was based upon analyses of single measurements and, though it goes into further depth than presented in Chapters 4 and 5, still represents a relatively preliminary glance into the use of XCT for

surface texture. As such, significant work is required beyond what is presented in this Chapter in understanding XCT surface measurement (akin to those discussed during Chapter 5), in order to make statistically relevant comments about the results. In Chapter 7, I present the beginnings of such a further analysis.

Additionally, algorithmic processing used during the XCT measurement process (such as during surface determination), shows that errors are easily introduced into the characterisation process, despite following good practice, occasionally failing to capture features present on surfaces, such as attached particles on an MPBF surface. XCT measurement of topography should, therefore, be handled with great care, as results may be unreliable, and expert assessment and interpretation of results is still required. In terms of specific surface parameters, some clearly experience less variation than others between technologies, and the aforementioned measurement errors can greatly affect some texture parameters. It is clear that XCT has the potential to become a viable method of surface topography measurement, but performance may be strongly dependent on the specific measurement methodology, given the sheer number of variable choices required for an XCT measurement.

A note should also be added regarding the wider applicability of these findings to the general problem of using XCT to measure internal or otherwise difficult-to-access AM surfaces. In this work, a comparison has been made involving a flat surface, though it is often the case that internal AM surfaces take complex freeform geometries (e.g. lattice structures). Analysis of such surfaces should be feasible, provided suitable steps are taken to identify and remove the underlying local shape of the part (referred to as the form component in surface metrology), so that the analysis can be focussed on smaller-scale topography. Identification and removal of the underlying form of the surface when complex shapes are involved is a challenge which has been studied for a number of years [260], but there is little work specifically regarding AM and the intrinsic complexity of freeforms and lattice structures. Additionally, a lack of physical and specification standards makes the application of these techniques to industrial cases difficult, and the development of such standards will be a

requirement before XCT is accepted as a method of surface measurement in industry.

6.5 Chapter summary

The most notable outcome of the work presented in this Chapter is that in order to allow for the use of XCT for surface qualification in an industrial setting, a number of barriers remain. In regards to the metrology, methods of performing an appropriate uncertainty analysis for these measurements are not yet clear, and so great efforts must yet be made in order to attain traceable surface qualification. To address the latter issue, a rigorous sensitivity assessment of the minimum requirements of an XCT system used for surface topography applications is required. Variables that should be examined in this assessment will include at least geometric magnification, sampling strategies within the measurement, sample material, image contrast and many other control parameters currently affecting the XCT measurement process pipeline (as described in Chapter 1). The work presented in Chapter 7 begins this campaign of sensitivity analysis, addressing the effects of geometric magnification and sampling strategies in the XCT reconstruction volume.

7. X-ray computed tomography surface measurement sensitivity

In Chapter 6, I demonstrated that, while measurement of surface topography by XCT is possible, the resulting surface topographies can be highly variable (see figure 7.1), depending on the setup of the measurement parameters in the instrument. In this Chapter, I begin to assess the effects of setup parameters on the resulting XCT measurement using the artefact introduced in Chapter 6. While a broad plethora of measurement setup parameters exist, I cover the effects of two of the most important here. Particularly, I investigate varying geometric magnification in scanning and the resolution of the volumetric grid in reconstruction by comparison of XCT data to coherence scanning interferometry data here (see Section 7.1 for an explanation of these parameters and why they were selected over others). This work was recently published in [261] and was presented at two conferences during 2017 [262,263], winning an award for best presentation at the latter of these.

7.1 Beginning to understand XCT surface measurement

A comprehensive assessment of XCT performance and behaviour when measuring surface topography, as well as a thorough exploration of the effects of the numerous involved measurement process parameters, has not previously been performed. The challenge represented by this assessment is significant, because of the large number of variables involved in the initial acquisition of the X-ray projections, in their combination into a volumetric dataset, and in the final extraction of surface topography. In order for XCT surface measurement to be used in industry, there is a need for physical and specification standards, and in order for these to be developed, a rigorous understanding of the technology is required. This investigation represents the first steps towards gaining that understanding.

In this Chapter, I investigate the effects of changing two variables during the measurement process. When setting up an XCT measurement, there are dozens

of input parameters, all of which will have some effect on the outputted topography. To gain a deep understanding of the technology and how each parameter affects the resulting surface topography, a full investigation of all of these influencing parameters is required. In this Chapter I begin this investigation. For this work, two variables were chosen, based on the experience gained throughout my PhD (see Chapters 4 to 6) and in discussion with the manufacturer of the XCT system, as two of the parameters that were likely to have a large effect on the outputted topography. The first of which is one of the most important parameters set during X-ray image acquisition: the magnification of the X-ray projections. Referred to as *magnification* in the following, this is the ratio between the X-ray source-to-detector distance and the X-ray source-to-object distance [264] (see figure 7.2a). The latter variable is one of the most important variables set during volumetric reconstruction: the resolution of the volumetric reconstruction grid [67] (see figure 7.2b); referred to hereafter as *resolution*. Both magnification and resolution affect the capability of the instrument to resolve small topographic detail in the extracted surface. For this experiment, I use a cone beam XCT system, circular scanning and a planar detector. Volumetric reconstruction is performed using the manufacturer's implementation of the Feldkamp, Davis and Kress (FDK) algorithm [61].
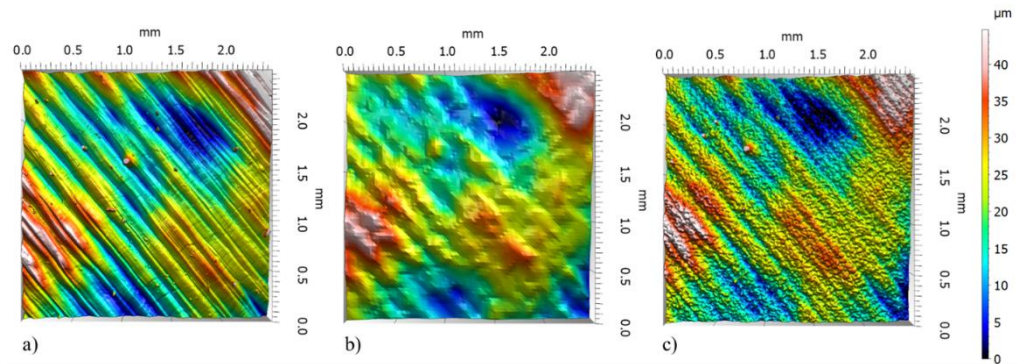
Figure 7.1. Example topographies obtained by varying XCT measurement setup: a) coherence scanning interferometry reference; b) XCT measurement using 5× magnification; c) XCT measurement using 20× magnification. Figure published in [261].
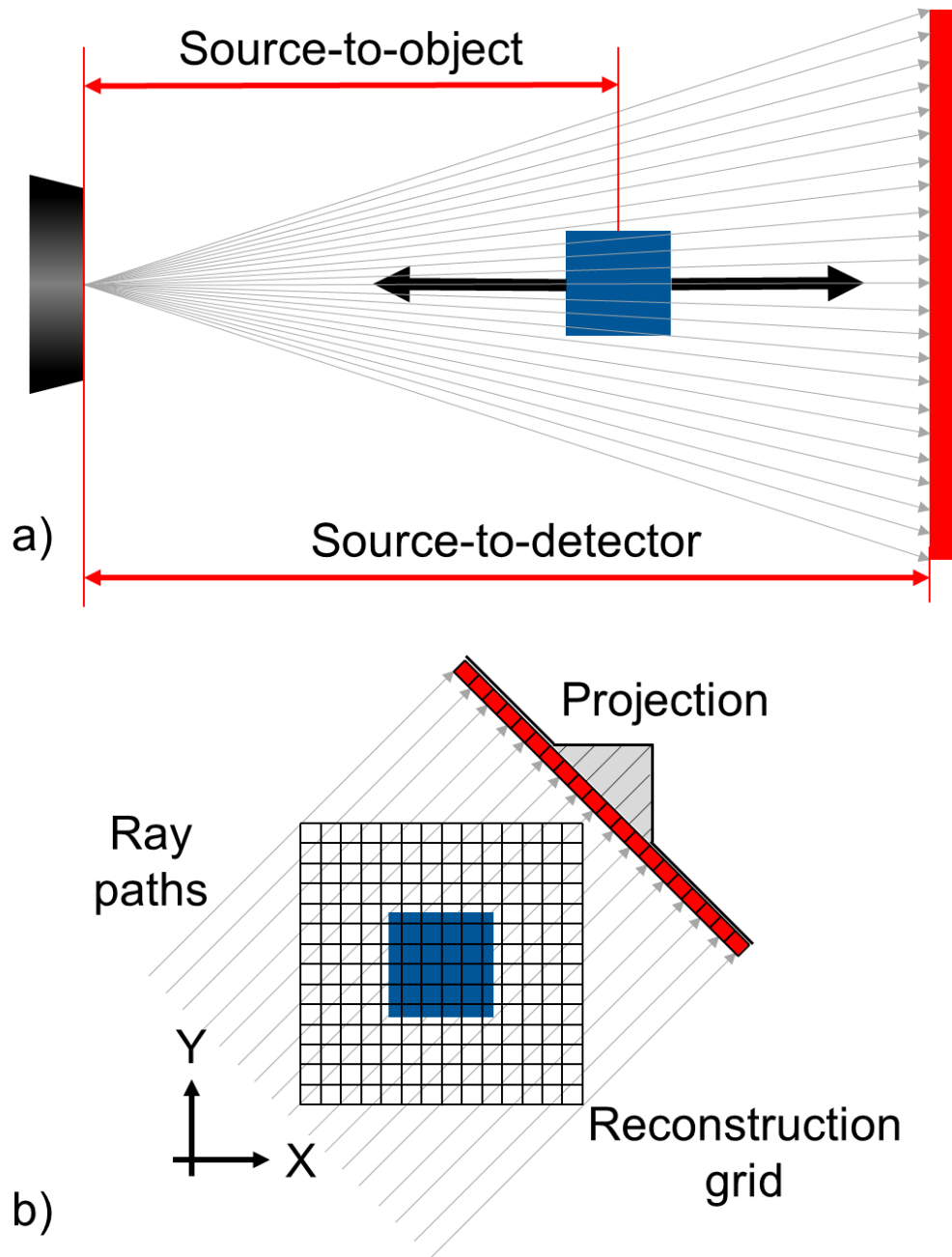
Figure 7.2. Investigated variables: a) geometric magnification in scanning; b) volumetric grid resolution in reconstruction by filtered back projection, representing the 100 % case [67]. Figure published in [261].

7.2 Chapter Methodology

7.2.1   The MPBF specimen

The test sample used in this part of my PhD was the same as that described in Chapter 6. To recap, this sample comprised two separable halves that could be combined to form a hollow cube of size $(10 \times 10 \times 10)$ mm. The sample was fabricated using an EOSINT M 280 laser metal powder bed fusion (MPBF) machine in Ti6Al4V. The test surface chosen was a nominally flat top surface, i.e. the final surface built in the MPBF machine, in the plane orthogonal to the build direction. X-ray images (i.e. projections) were taken at different magnifications ($5\times$, $10\times$, $20\times$ and $50\times$). Each set of projections was used for multiple volumetric reconstructions using resolutions: 50 %, 100 % and 150 %, where 100 % corresponds to the resolution of the detector. For example, in the $20\times$ magnification, 100 % resolution case, a detector containing a grid of 2000×2000 pixels of size (0.2×0.2) mm will yield a reconstructed volume containing $2000 \times 2000 \times 2000$ voxels, each of size $(10 \times 10 \times 10)$ µm. The 50 % and 150 % cases will then contain $1000 \times 1000 \times 1000$ voxels, each of size $(20 \times 20 \times 20)$ µm, and $3000 \times 3000 \times 3000$ voxels, each of size $(6.7 \times 6.7 \times 6.7)$ µm, respectively (see figure 7.2b). The 150 % and 50 % cases are examples of super-sampling (i.e. sampling at a frequency greater than that of the input data) and sub-sampling (i.e. sampling at a frequency lower than that of the input data) conditions, respectively. Further information about this sample is detailed in Section 3.1.

7.2.2   Measurement setups

The sample was measured using a number of XCT measurement setups, as well as by coherence scanning interferometry (CSI). In all measurement setups, five repeat measurements were taken in sequence, on the same instrument, with the same operator and without moving the sample between acquisitions. All instrument names are once again redacted to prevent undue comparison of commercial instruments.

XCT measurements were performed at geometric magnifications of 5×, 10×, 20× and 50×. The following parameters were used in all XCT measurement setups, based on good practice developed throughout my PhD and the manufacturer's guidelines: voltage 200 kV, current 49 µA, 3142 projections, exposure 2 s and gain 24 dB. A detector shading correction was applied by averaging 512 reference frames (256 bright and 256 dark) and a warmup scan of approximately one hour was performed prior to scans. A 0.5 mm copper pre-filter was used between the X-ray source and the specimen. X-ray imaging and volumetric reconstruction were performed using the manufacturer's software, using the FDK algorithm [61] with a second order beam hardening correction and a Hanning noise filter, with cut-off at the maximum spatial frequency. This filter was chosen to reduce image noise present when alternatively using an edge-preserving ramp filter, without substantially degrading the quality of the edges present in the data. Noise was an issue in certain measurement setups, in that these setups necessitated the application of an opening/closing operation on the determined surfaces to remove noise during the determination process (see Section 7.2.3). Modification of these measurement setups to alleviate this requirement was considered, but discarded because of the excessive time increases incurred by such changes. A filter with a greater effect on noise reduction was also considered to alleviate this requirement, but the literature suggests that the application of a stronger noise filter would have caused unacceptable degradation of edges, likely having significant effect on the outputted surfaces (see Bartscher et al. [70]). Super- and sub-sampling of the reconstruction grid was performed using CT Pro, creating twelve measurement setups in total. The voxel sizes resulting from each measurement setup are presented in table 7.1.

Table 7.1. Voxel size for each XCT setup/μm.

Magnification / Sampling resolution	5×	10×	20×	50×
50 %	80.0	40.0	20.0	8.0
100 %	40.0	20.0	10.0	4.0
150 %	26.7	13.3	6.7	2.7

CSI measurements were performed using in the following setup: 20× objective lens at 1× zoom (NA 0.40, FoV 0.42 mm × 0.42 mm, LR-pixel 0.41 μm, LR-optical 0.68 μm), stitching of multiple images performed in the manufacturer's software. As in Chapters 4 to 6, LR-pixel refers to the pixel spacing of the detector used by each instrument, LR-optical refers the calculated Sparrow optical limit [34] of each instrument and NA is numerical aperture. The Sparrow optical limit was calculated using a wavelength of 580 nm. During analysis, one CSI measurement was noted to have experienced unexpected data dropout across a portion of the measurement area, resulting in outliers in the calculation of ISO 25178-2 [51] texture parameters. This dataset was removed from the study and data comparison was performed using the remaining four repetitions (see Section 7.3.2). Regarding the uncertainty of the CSI system, the instrument manufacturer quotes surface topography repeatability of 0.12 nm, step height repeatability of 0.1 % and step height accuracy of 0.3 % [265]. When measuring rough surfaces, the absolute accuracy of surface topography measurement and topography repeatability are complex to evaluate, and the subject of current significant research efforts (e.g. see [266]). In Chapters 4 to 6, CSI systems were shown to be capable of measuring the various features present on metal AM surfaces with greater repeatability and fewer measurement artefacts than other optical systems (see Chapter 5 specifically) and so a CSI instrument is used here as a reference. Additionally, in the recent paper by Gomez et al. [49], we demonstrated how CSI can be optimised for use as a tool for metal AM surface measurement. Although establishing traceability [21] for data acquired using a CSI system has not yet been undertaken for such complex samples and likely represents a significant challenge, the CSI can in this case be considered as a sufficient reference when compared to XCT, which exhibits

substantially poorer accuracy and precision by comparison (see Chapter 5). Of course, other systems (e.g. focus variation, confocal microscopy) could have been incorporated into this comparison, but as a large number of XCT measurement setups were investigated, I used only one reference instrument in order to prevent over-complication of the results.

7.2.3 Data analysis

As previously, following reconstruction, XCT data were imported into Volume Graphics VGStudioMAX 3.0 [73] and surfaces were determined using the local maximum gradient algorithm over a search distance of four voxels, using the ISO 50 % isosurface [139] as the start point. For the three 50× datasets, an additional opening/closing [267] morphological operation was performed to remove noise artefacts from both above and below the determined surface. The opening operation involves eroding the determined surface by a set number of pixels, and then dilating the surface by the same number of pixels. The effect of this process is that small regions defined as material outside of the bulk are removed and no longer defined as material. The closing operation involves the opposite (dilation followed by erosion), and has the effect of removing pixels defined as background from within the bulk material, so that they are no longer defined as background. This process is explained diagrammatically for a 2D example in figure 7.3. As can be seen in the figure, the opening/closing operations inevitably also change the desired parts of the determined surface in some way, and so a second surface determination using the local maximum gradient algorithm was performed for the three 50× datasets after the opening/closing operation, using the post-operation surface as the start point.
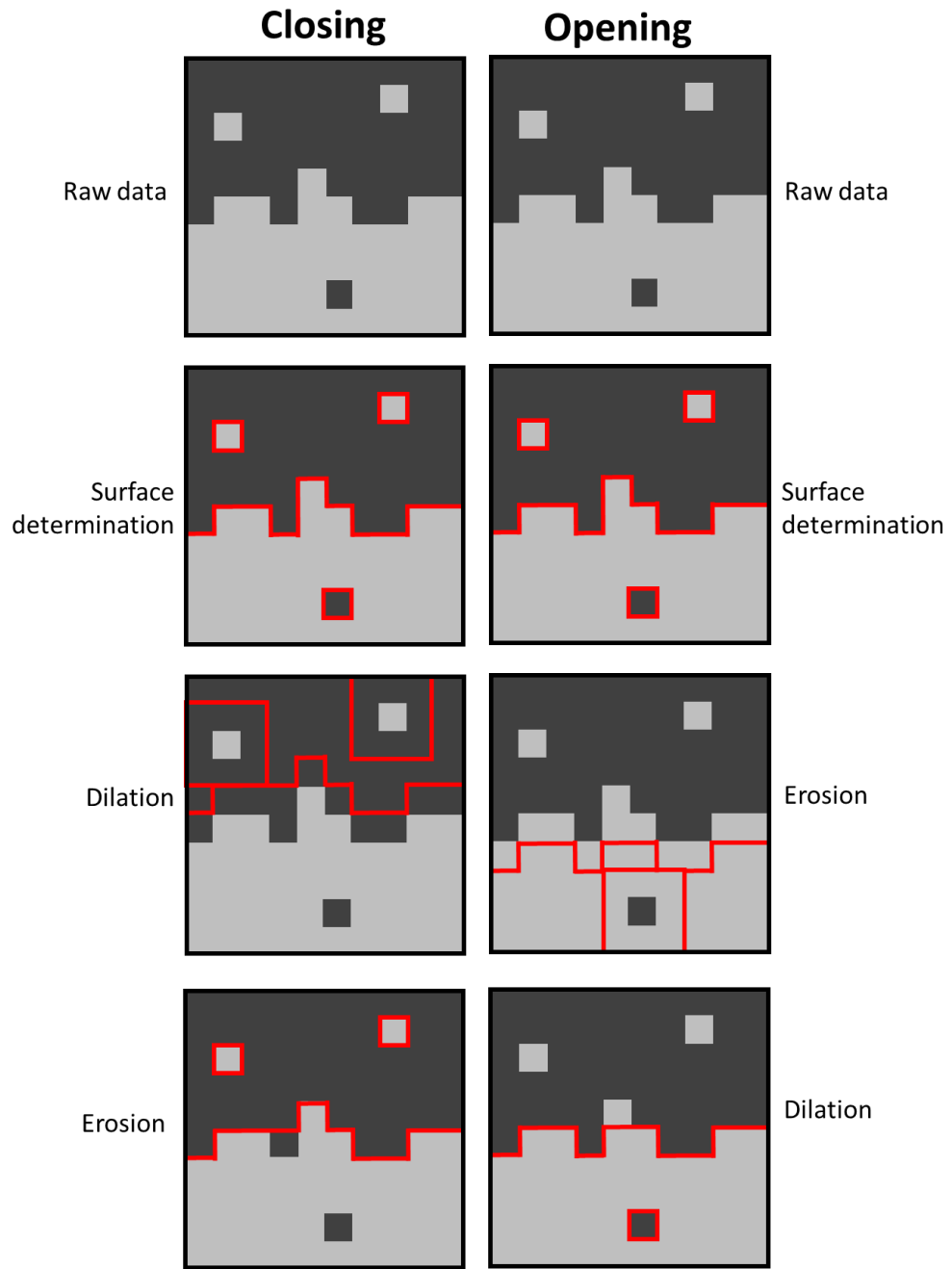
Figure 7.3. The opening and closing morphological operations. At each stage, the red line represents the determined surface after the respective operation has been performed. Lighter pixels represent material, while darker pixels represent the background.

The computed surfaces were exported as triangulated meshes in the STL format. Surfaces were then imported into MountainsMap [228], where they were automatically converted into 2.5D height maps to allow comparison to CSI data. As discussed in previous Chapters, height maps are representations of height points on a grid commonly used in surface measurement. Height map resolutions were automatically determined by MountainsMap to match the point

density of the triangulated meshes. The conversion removed any undercut features from the XCT data.

Height maps were imported into the in-house developed MATLAB [268] program outlined in Section 5.2.2.3 of Chapter 5, where they were converted into triangulated meshes for alignment in six degrees of freedom. Alignment was performed using the aforementioned two-step algorithmic procedure: coarse alignment by distance minimisation of matched landmarks [245], and fine alignment by application of the ICP method [252] using the sum of squared distances between paired points as the minimisation objective (global alignment). Topographies generated using the XCT 5×/50 % setup had insufficient topographic detail to allow alignment because of the low resolution, so were not considered in the analysis. A single CSI dataset was taken as the global alignment reference, and one XCT dataset for every combination of magnification and resolution was aligned to it. Other replicates in each XCT setup were then aligned to the first one of each set. As the alignment took place in six degrees of freedom, all the aligned datasets were finally reconverted into height maps by application of the method described in Section 5.2.2.3 of Chapter 5. The xy raster scanning grid was set at 5 μm spacing. Although greater than the point spacing in some of the original CSI and XCT datasets, this 5 μm spacing was chosen as a compromise between the need to minimise information loss and the need to prevent excessive computation time in higher resolution data. ISO 25178-2 [51] texture parameters were calculated in MountainsMap, while statistical modelling of topographies was performed in MATLAB. For calculation of texture parameters, a levelling F-operator (removal of a least-squares mean plane) was applied. No L- or S-filters were applied so as to maximise the measurement bandwidth, as data are intrinsically bandwidth matched [238] during the alignment, cropping (matching of larger wavelengths) and raster scanning (matching of smaller wavelengths) process. This bandwidth matching process homogenises the range of spatial frequencies across all datasets, preventing differences in calculated parameters as a result of spatial frequencies present in some datasets and not others (i.e. accounting also for partial volume effects, typically causing the loss of higher spatial frequencies in lower magnification data [56]).

7.3 Chapter results

7.3.1   Projections and orthoslices

Example projections at each magnification are shown in figure 7.4 (top). An initial analysis of the reconstructed volumetric datasets, performed via inspection of digital slices extracted from the datasets (orthoslices), showed an increasing, irregular dispersion of intensity values at higher magnifications, as observable in the middle and lower parts of figure 7.4. The bottom images of figure 7.4 also show the dependency of image sharpness on magnification. The image sharpness will in turn affect the determined surface, so these images provide an initial idea as to the eventual quality of the determined surfaces.
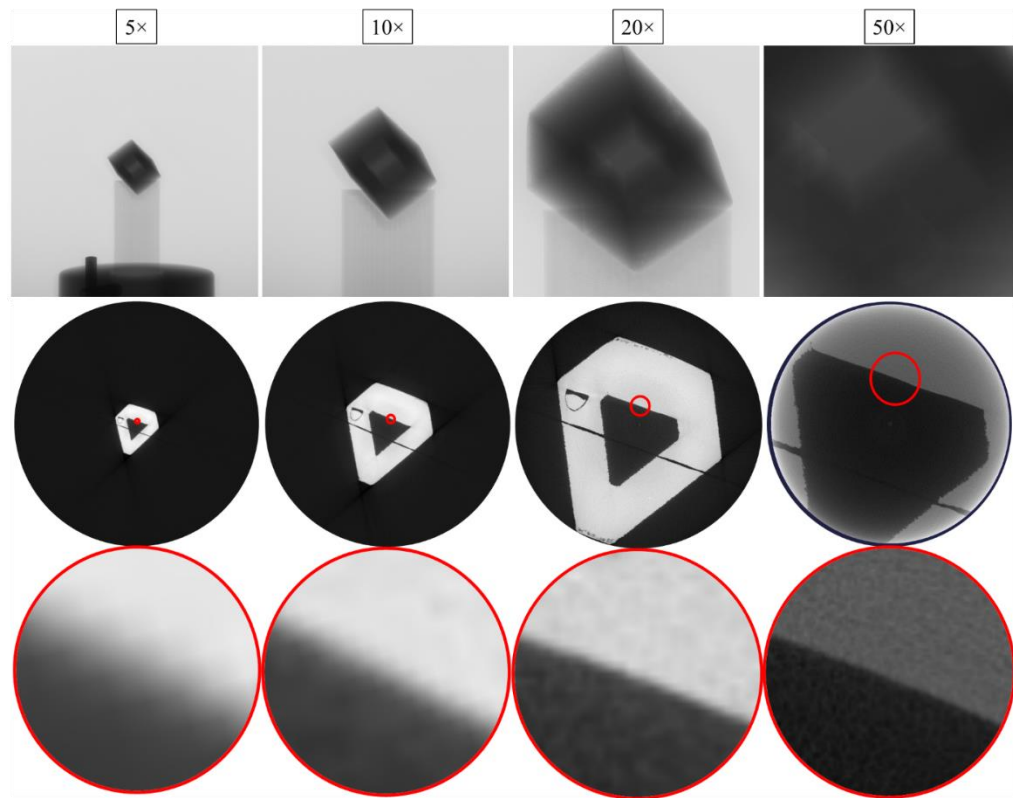
Figure 7.4. Magnification and its effects on projections and volumetric reconstruction; top: example individual projections obtained at increasing magnifications; middle: orthoslices (i.e. perpendicular to the rotation axis) extracted from the final volumes obtained at the same geometric magnifications, using 100 % resolution in the volumetric reconstruction step; bottom: magnified portions of orthoslices highlighted with red rings in middle images. Figure published in [261].

7.3.2 *Extracted surface data*

Figures 7.5a-l show all the individual CSI and all XCT topographies obtained using the various different setups. Figure captions contain details of each measurement setup, with XCT setups described in the format [Magnification]×/[resolution] %.

All the datasets are shown as they appear after the alignment procedure described in Section 5.2.2.3 of Chapter 5, but prior to additional levelling required for the calculation of ISO 25178-2 parameters (as described in Section 7.2.3). The surface topographies are rendered with height-based, artificial colouring, using a shared colour scale (i.e. mapped to the same range of heights). The colour scale was made uniform across datasets to facilitate visual comparison.

The CSI dataset that was removed (as discussed in Section 7.2.2) is highlighted in figure 7.5a by a red box. This dataset was eliminated because of a region with high data dropout, identified in the figure by the red ellipse. This region was initially filled with interpolated values in order for the analysis to be carried out (as described in Section 5.2.2.3 of Chapter 5), but ultimately resulted in outlier texture parameters with respect to the other datasets, hence the removal from the study.
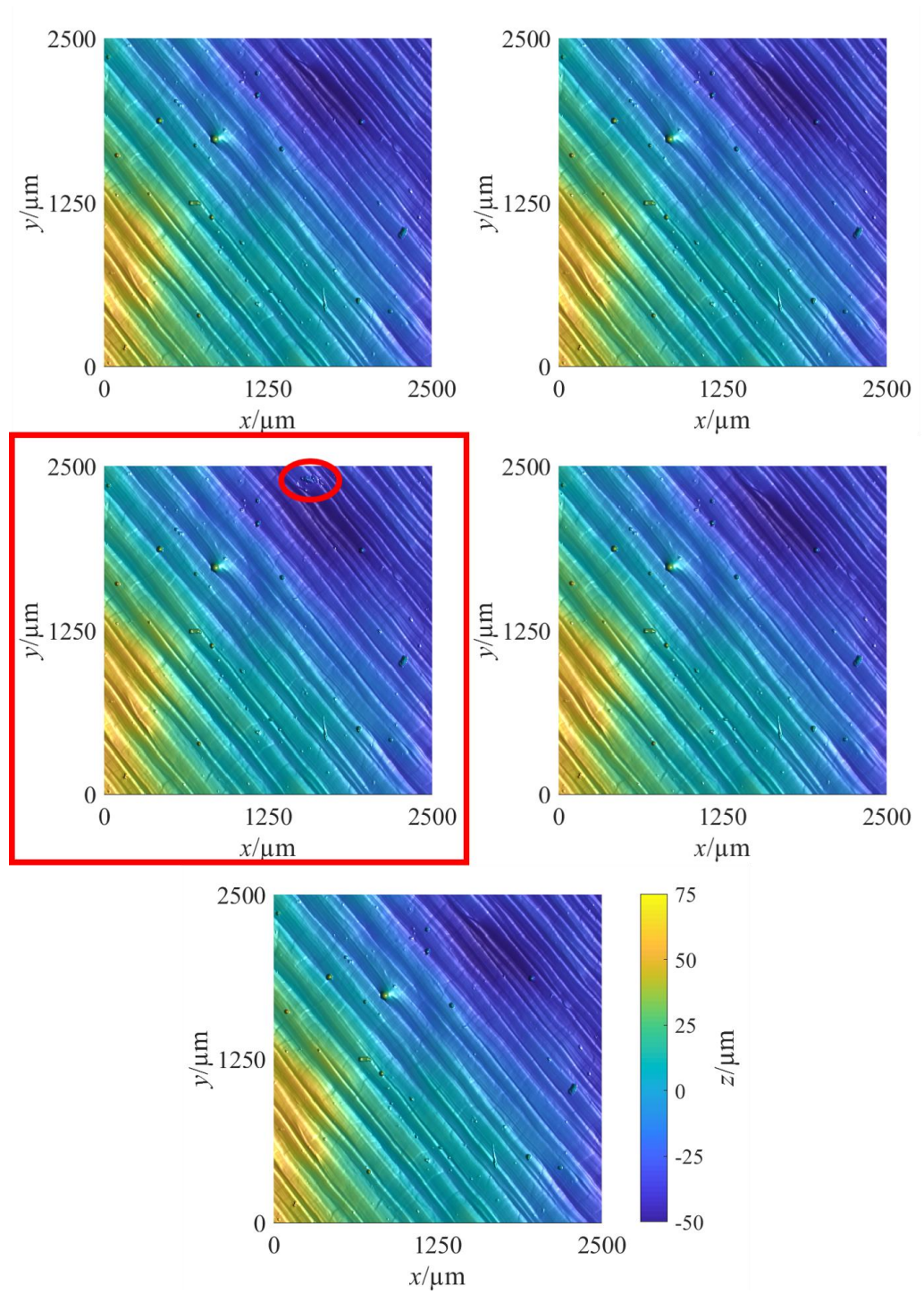
Figure 7.5a. CSI datasets. Red box indicates removed dataset, ellipse indicates area of high data dropout. Figure published in supplementary information to [261].
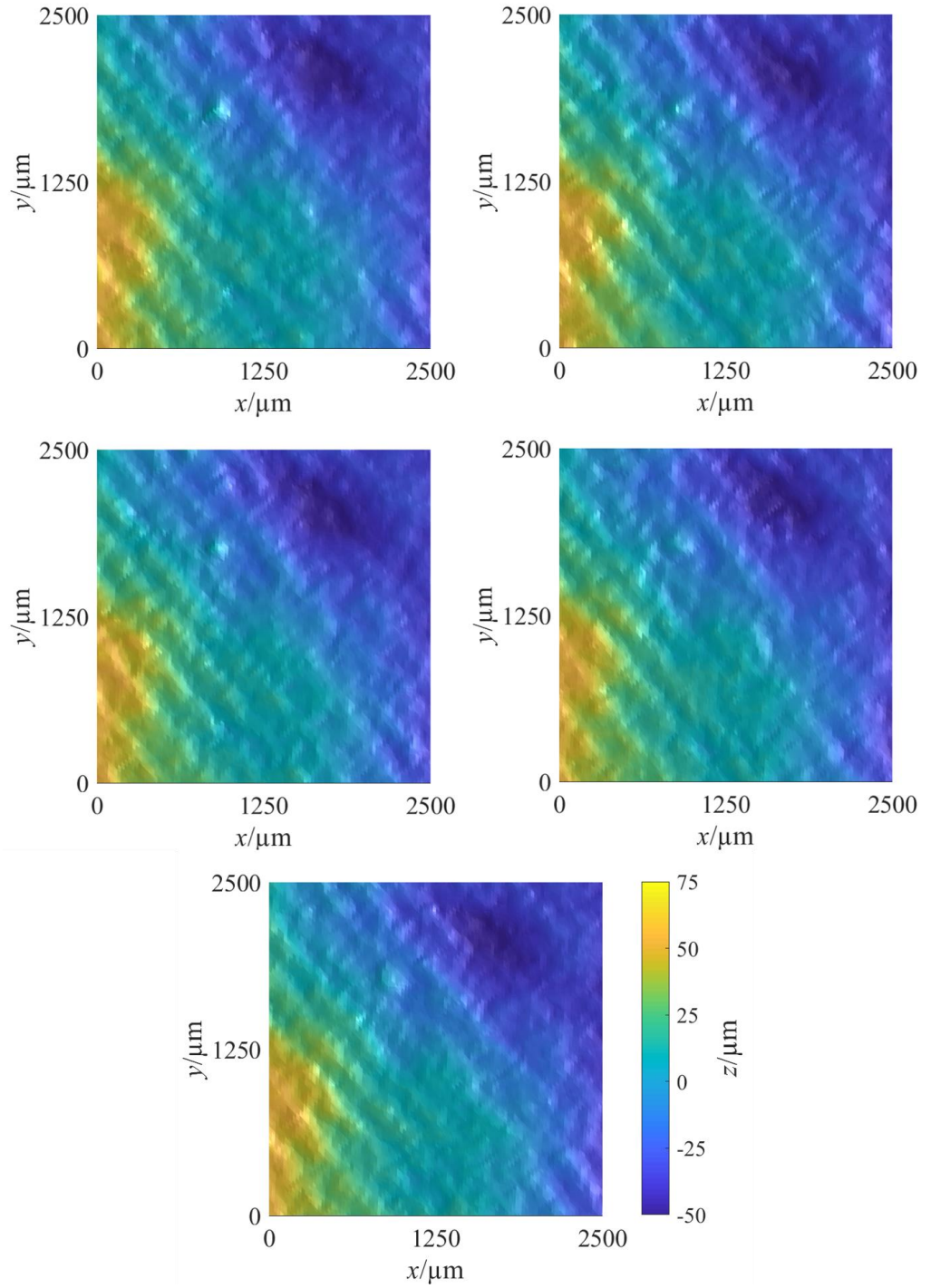
Figure 7.5b. 5×/100 % XCT datasets. Figure published in supplementary information to [261].
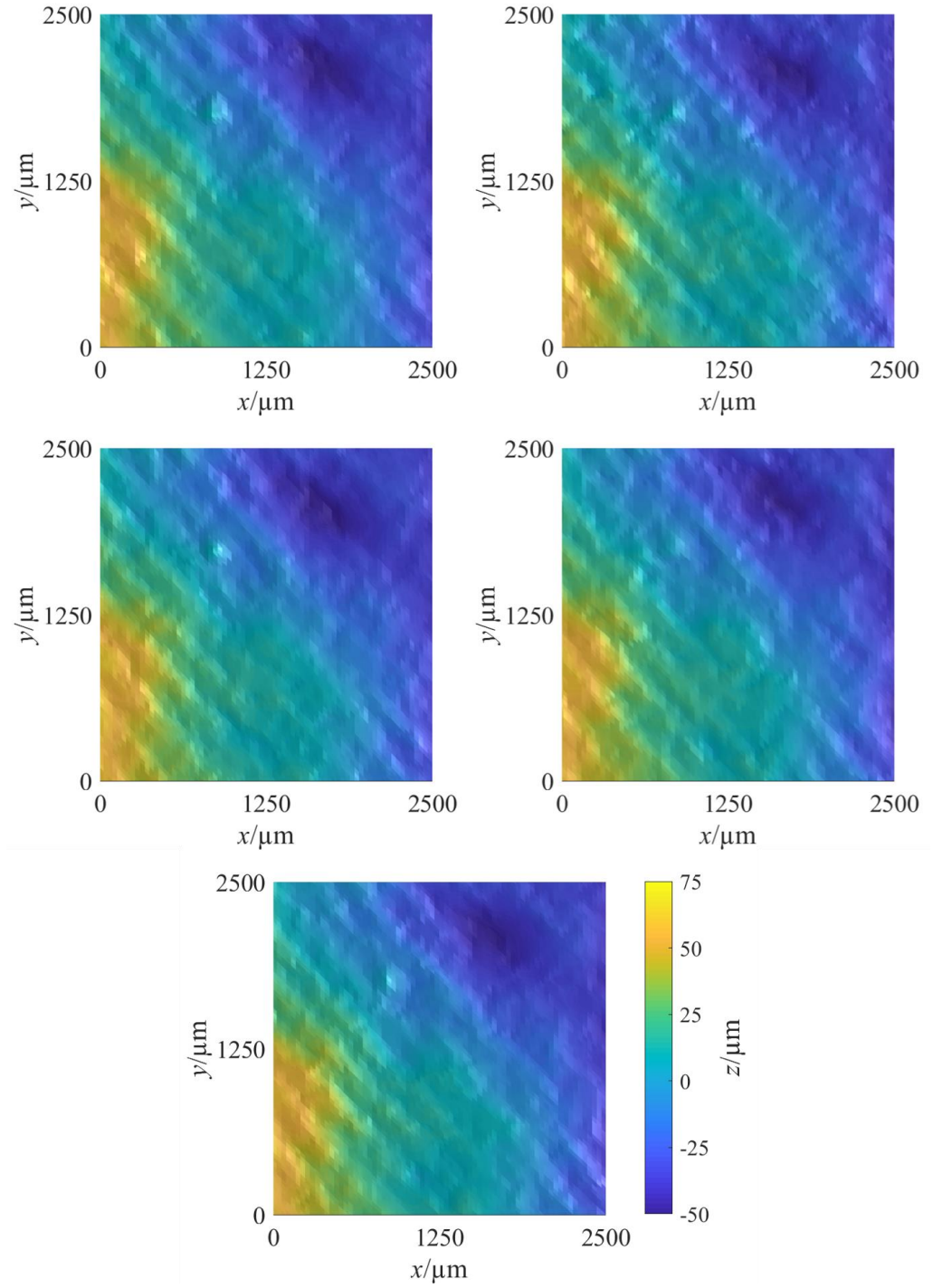
Figure 7.5c. 5×/150 % XCT datasets. Figure published in supplementary information to [261].
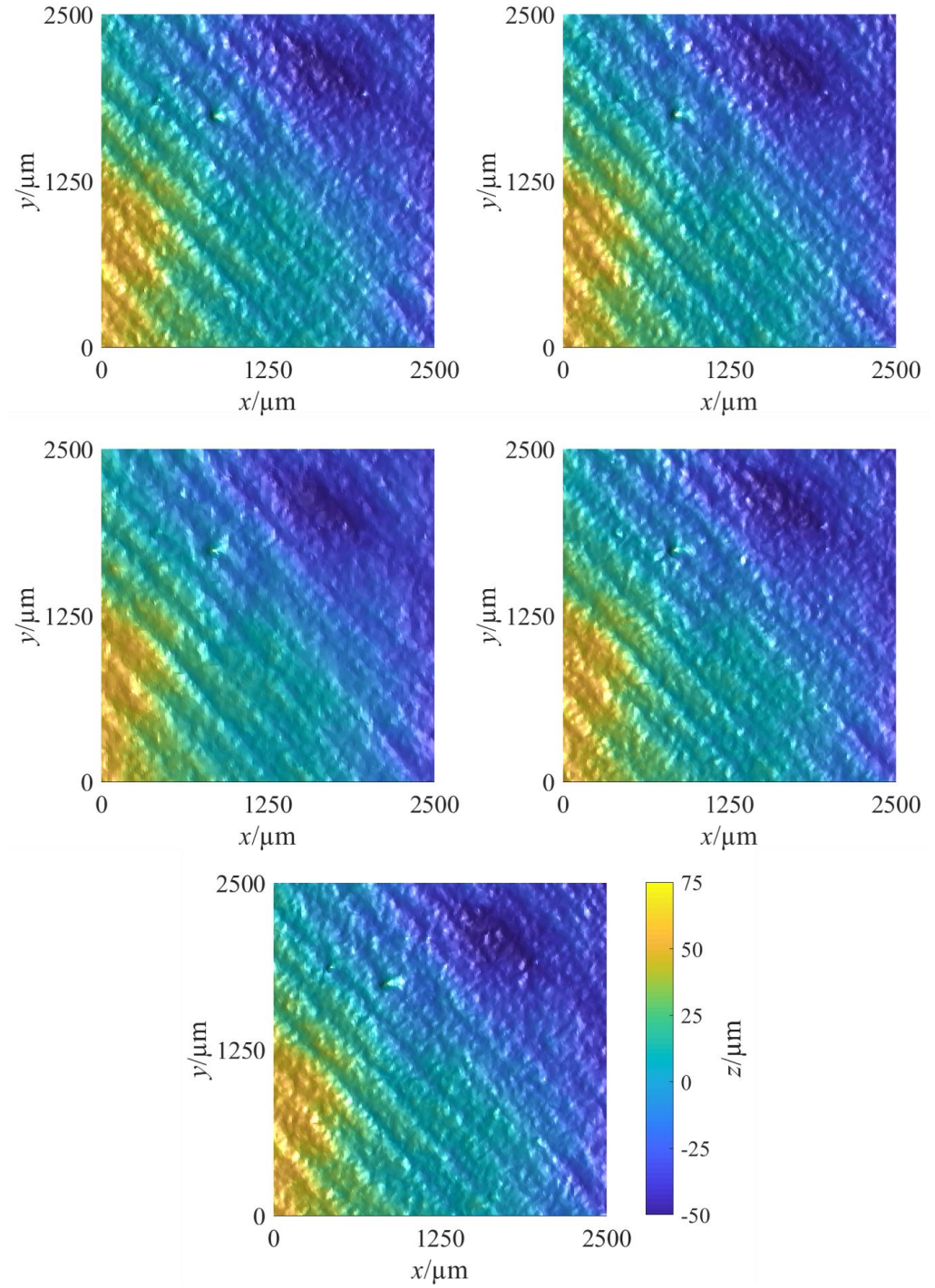
Figure 7.5d. 10×/50 % XCT datasets. Figure published in supplementary information to [261].
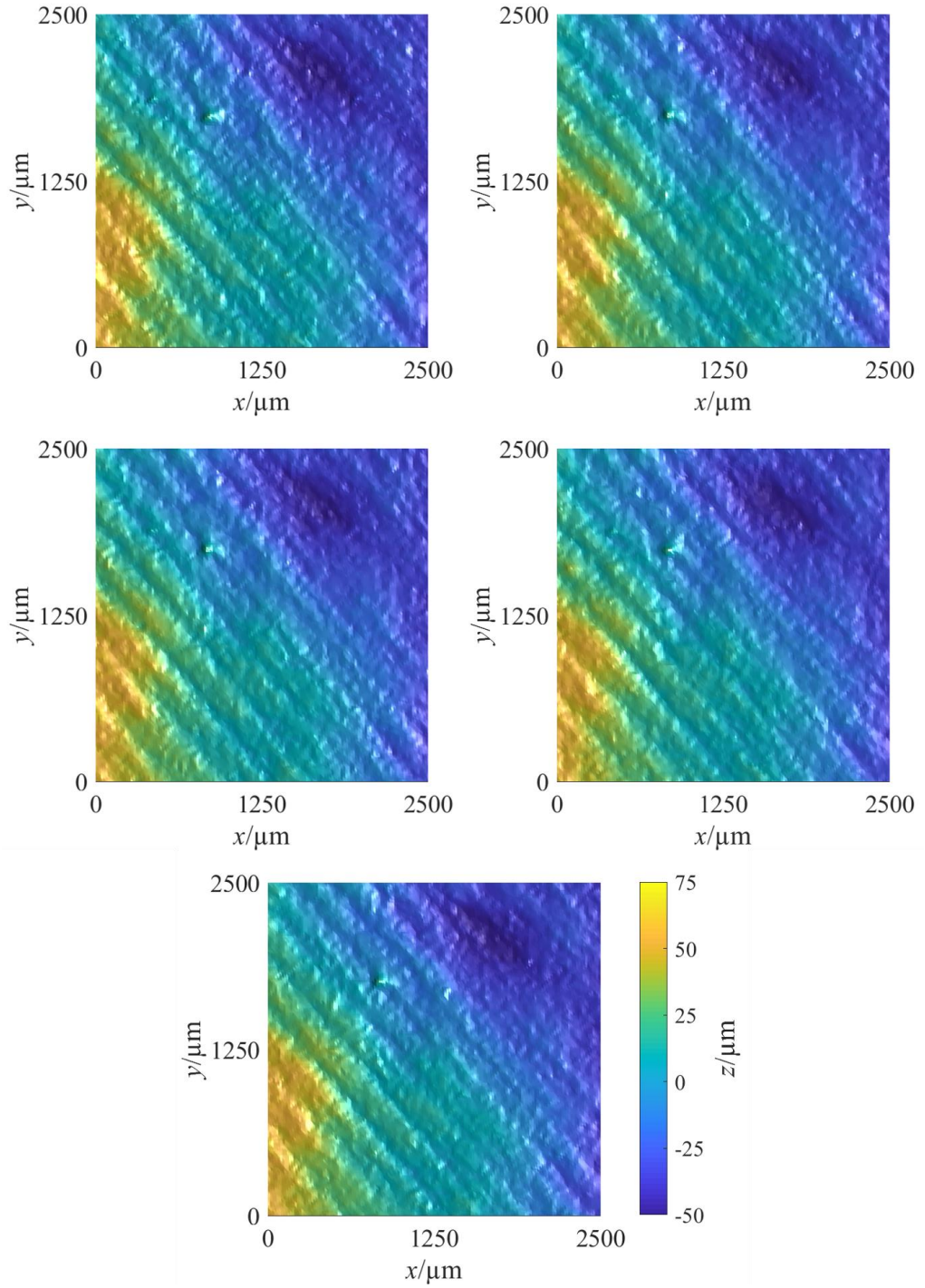
Figure 7.5e. 10×/100 % XCT datasets. Figure published in supplementary information to [261].
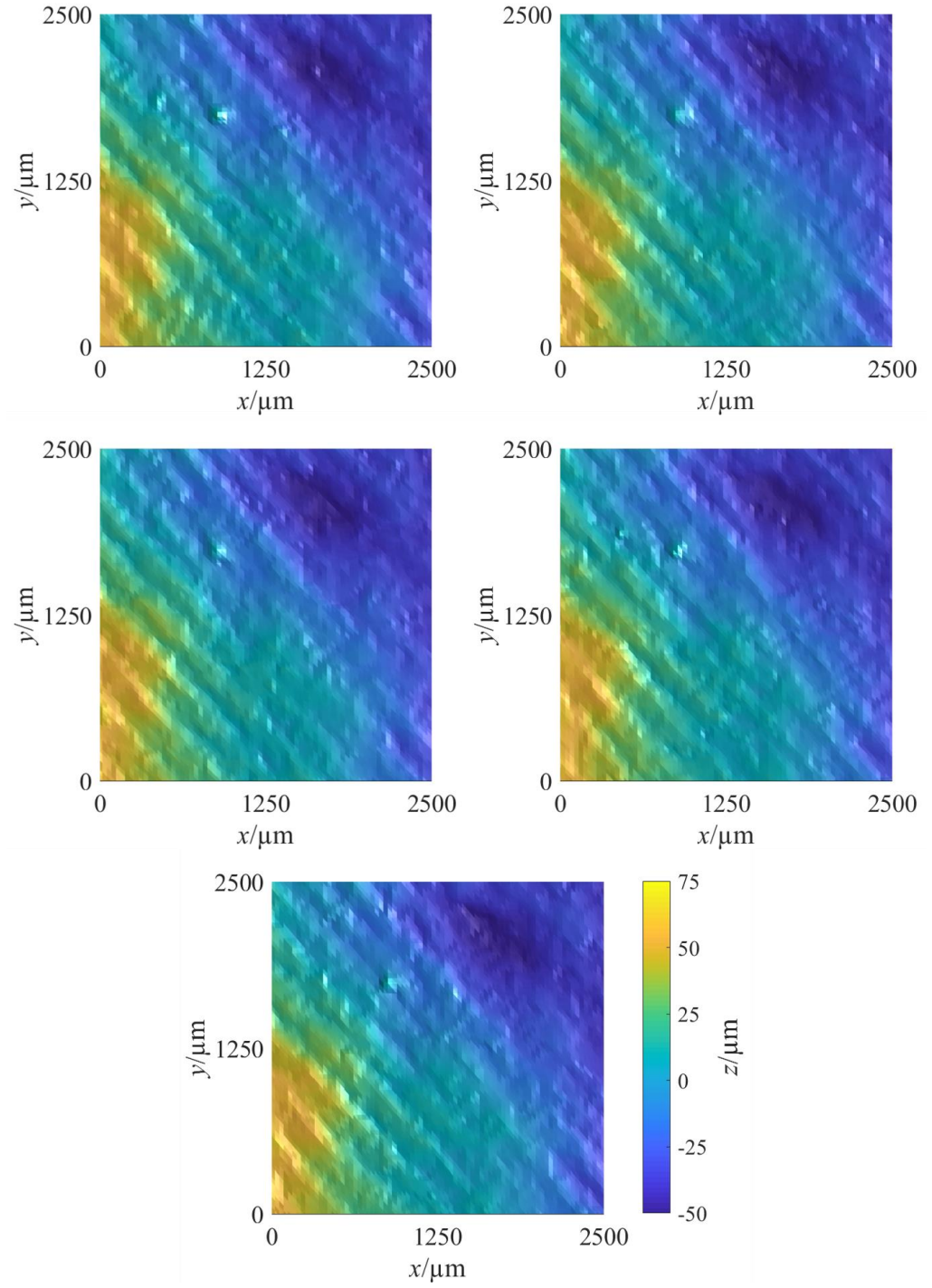
Figure 7.5f. 10×/150 % XCT datasets. Figure published in supplementary information to [261].
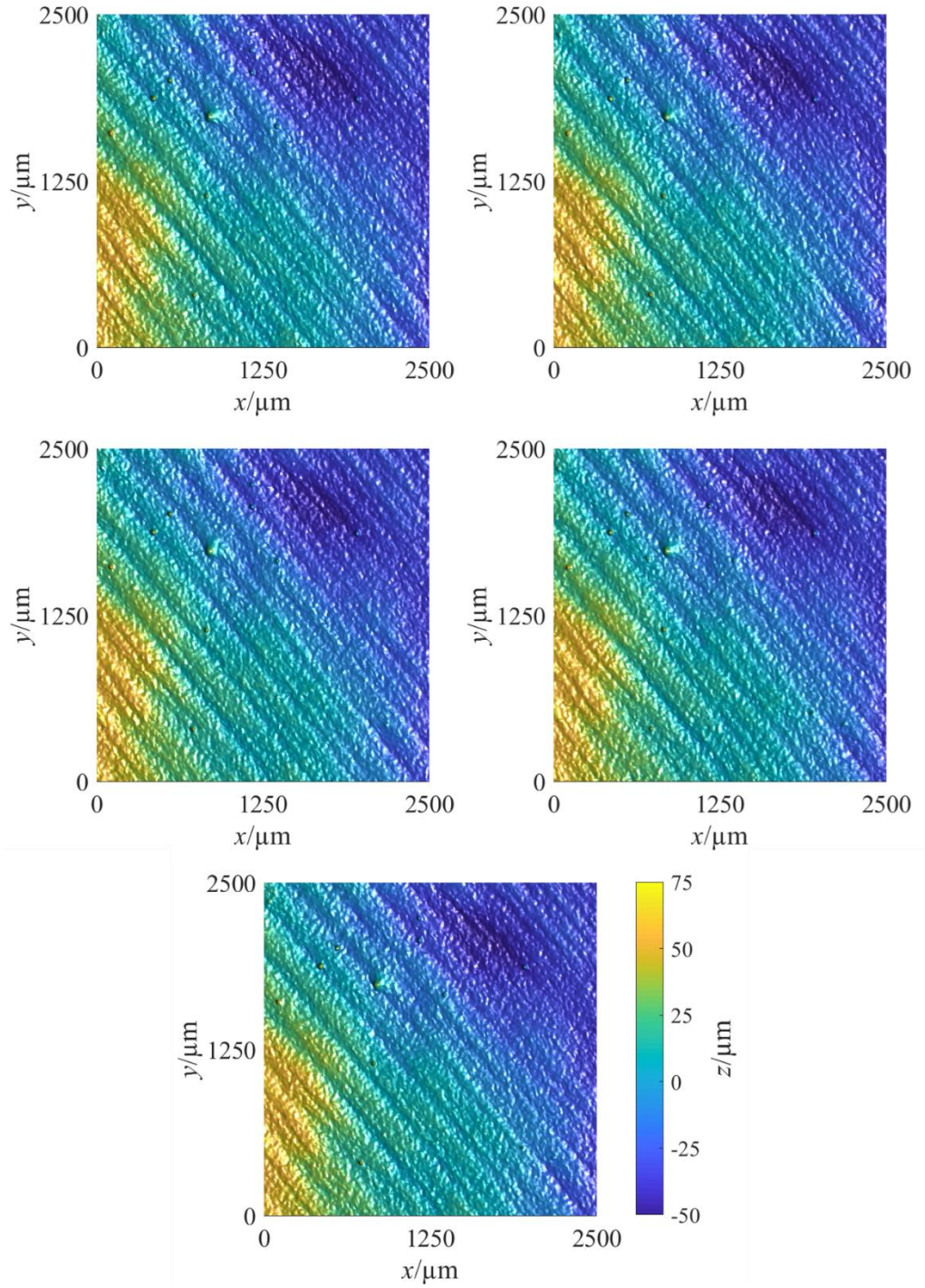
Figure 7.5g. 20×/50 % XCT datasets. Figure published in supplementary information to [261].
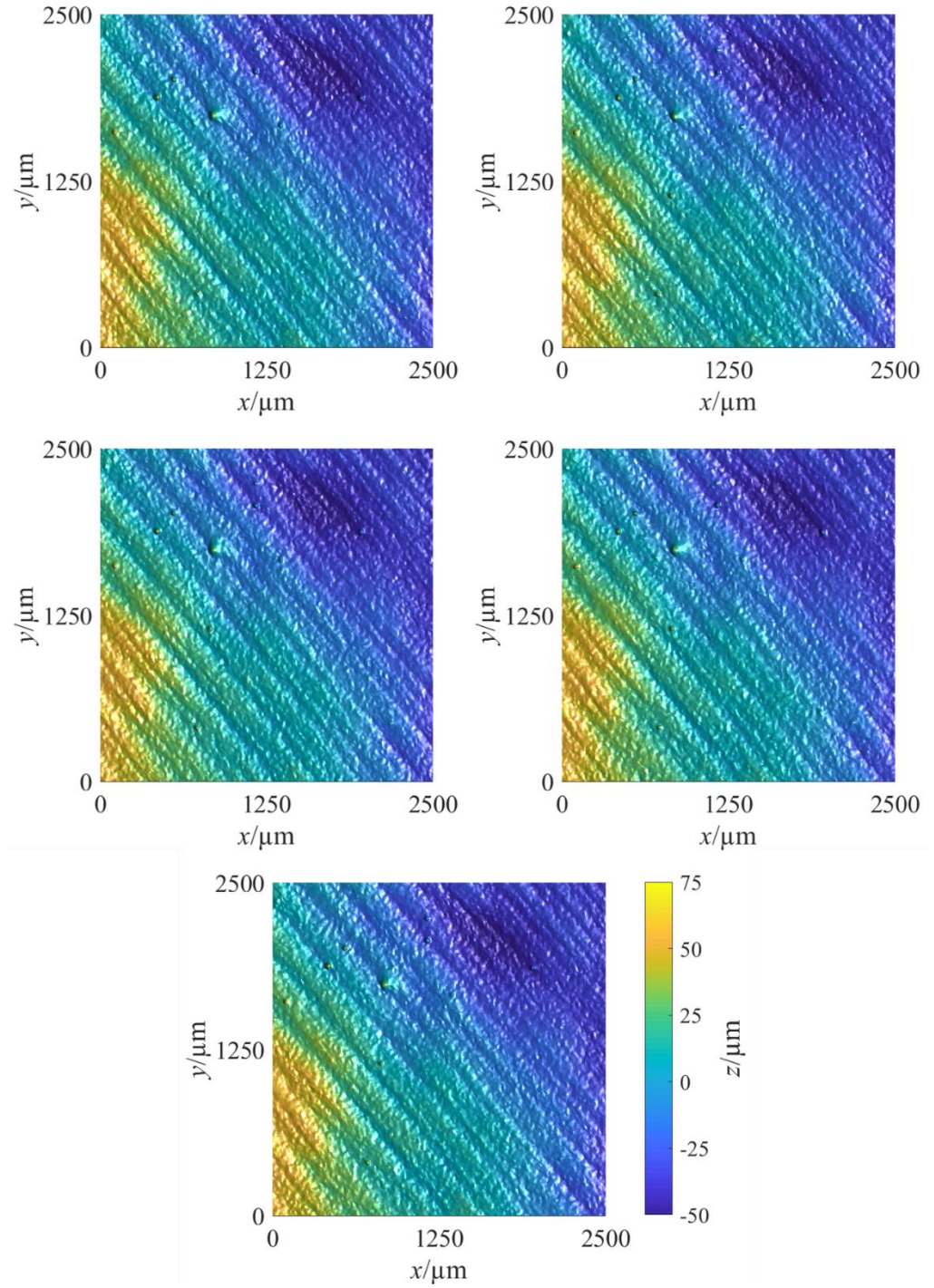
Figure 7.5h. 20×/100 % XCT datasets. Figure published in supplementary information to [261].
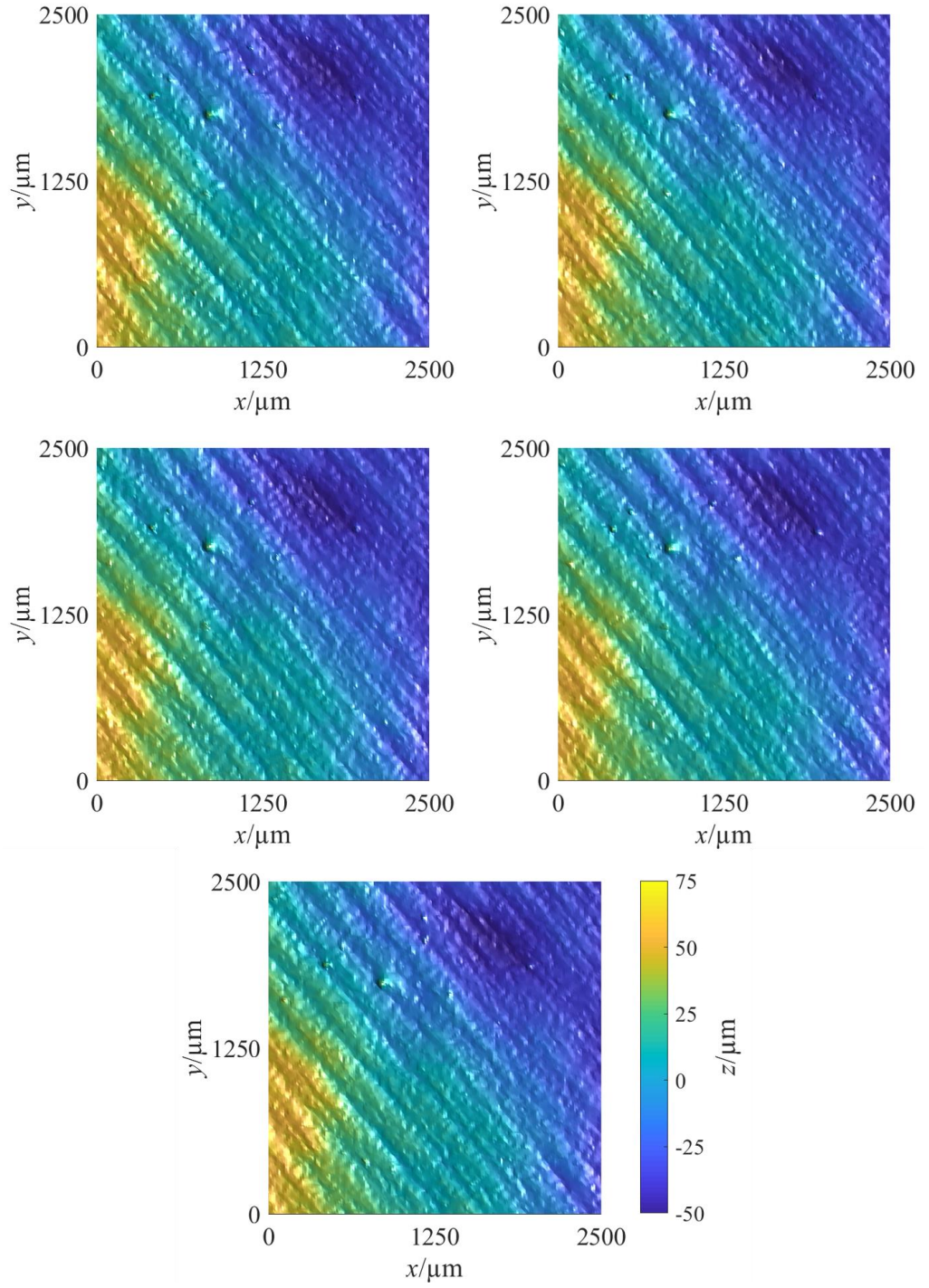
Figure 7.5i. 20×/150 % XCT datasets. Figure published in supplementary information to [261].
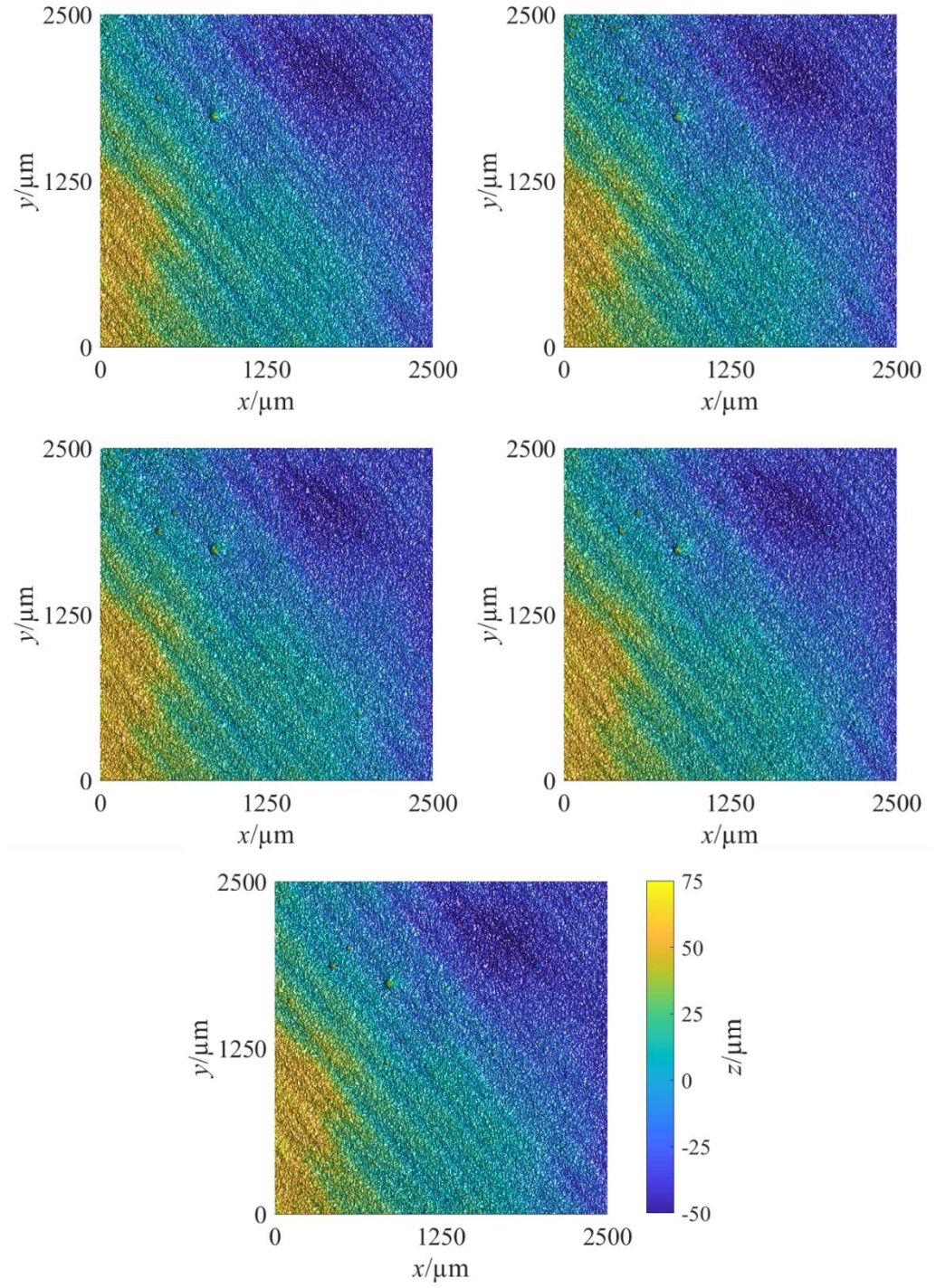
Figure 7.5j. 50×/50 % XCT datasets. Figure published in supplementary information to [261].
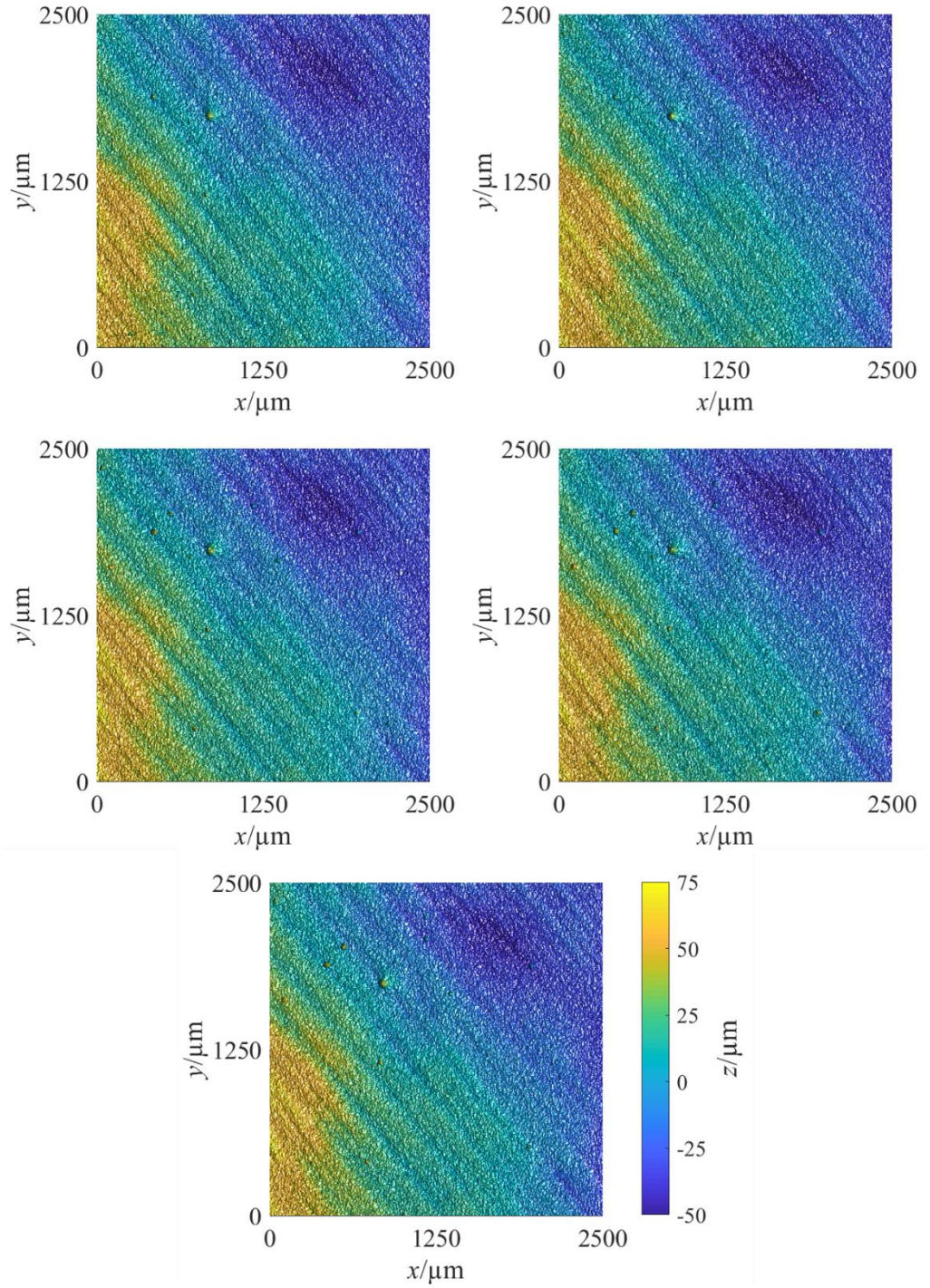
Figure 7.5k. 50×/100 % XCT datasets. Figure published in supplementary information to [261].
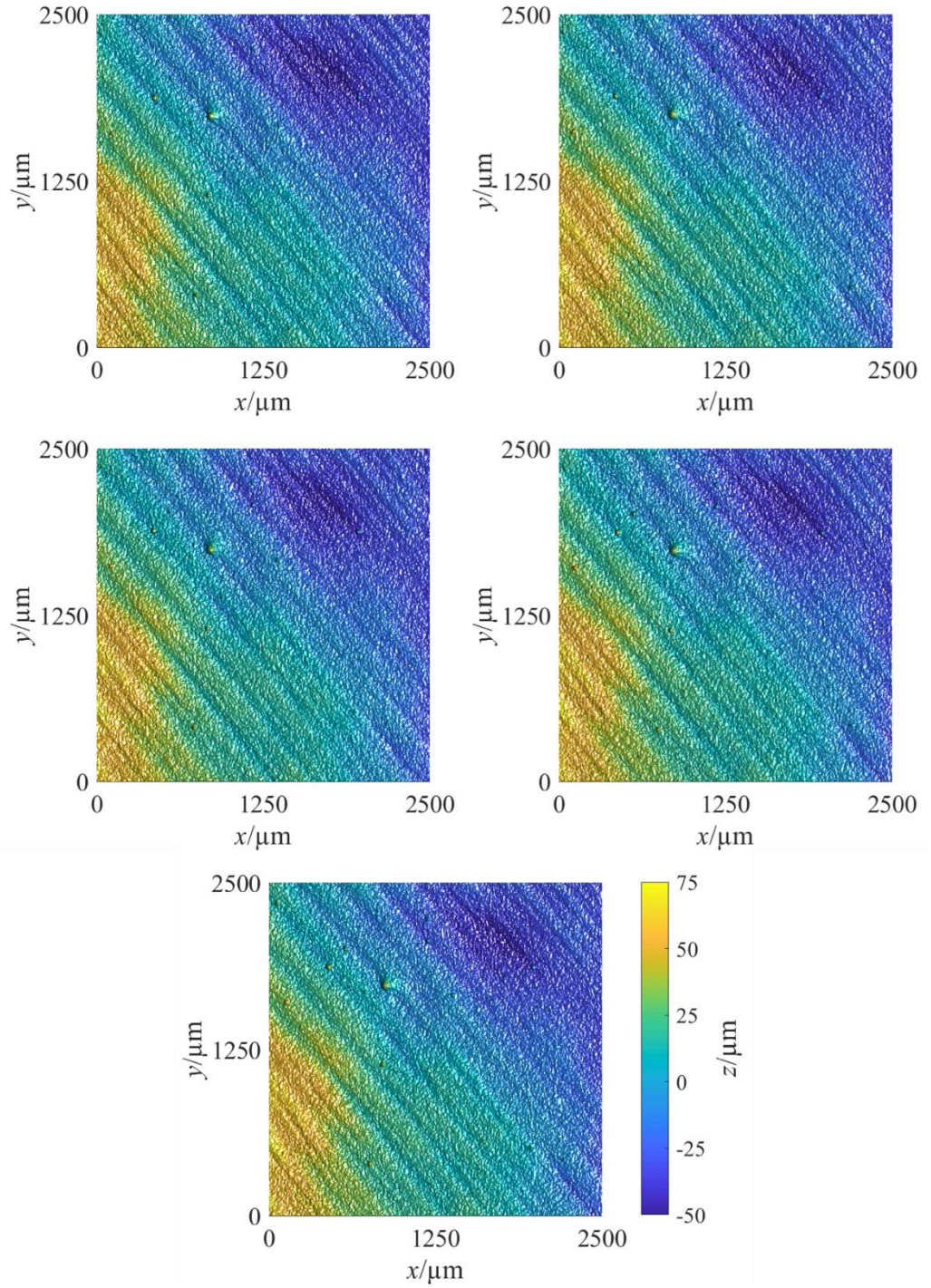
Figure 7.5l. 50×/150 % XCT datasets. Figure published in supplementary information to [261].

7.3.3   Topography preparation and comparison via texture parameters

XCT surface topographies were obtained by extracting surfaces from the volumetric datasets generated by all the combinations of magnification and resolution, repeating the measurement process on the same volume in each setup five times. Repeat measurements were taken under repeatability conditions; in that the same operator performed the measurement in sequence on the same instrument, without removing the sample. Further topography datasets were obtained using repeat CSI measurement of the same surface region. Topography datasets were aligned in space using the method presented in Section 5.2.2.3 of Chapter 5, using an arbitrary dataset from each measurement setup as the sub-masters. Data were again cropped to the same (2.5 × 2.5) mm region of interest to prevent discrepancies caused by topographic features present only in some datasets (e.g. peaks or pits that would fall outside the field of view in some measurements). Several ISO 25178-2 areal texture field parameters [51] were computed to quantify topographic properties, commonly used in industry for such characterisations (see Chapter 2 and the recent review by Townsend et al. [9]). Specifically the parameters used were: *Sa*, *Sq*, *Ssk*, *Sku*, *Sdr*, *Sal* and *Sdq* (see Chapter 1 for parameter definitions). These parameters were used as they were identified as common parameters for use in such evaluations in industry (see Chapter 2 and the recent review by Townsend at al. [9]). As in Chapter 5, confidence intervals (CIs) were calculated at 95 % confidence on the means of these parameters and used to investigate differences between measurement setups. Confidence intervals were generated in the same manner as described in Section 5.2.2.3 of Chapter 5. The results of this analysis are displayed in figures 7.6a-c.
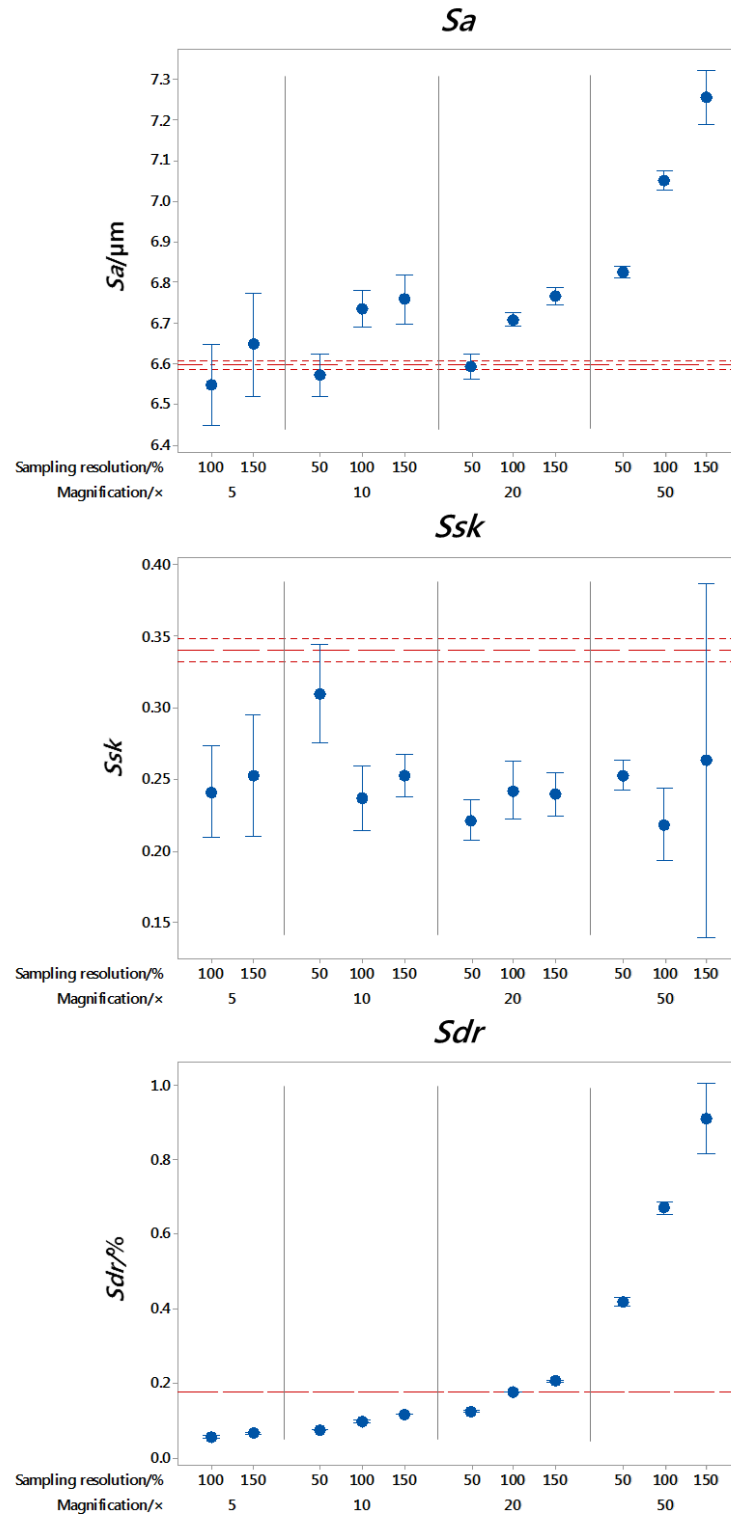
Figure 7.6a. ISO 25178-2 [51] areal texture field parameters computed for each XCT measurement setup (magnification and sampling resolution) and compared to the results for the CSI datasets (represented as reference lines, where the coarse dashed lines are means and fine dashed lines are the upper and lower CI bounds). The 5×/50 % setup is omitted as the topography of the reconstructed XCT surface was too deprived of detail to allow accurate alignment to CSI data. Confidence intervals computed at 95 % confidence on the repeat measurements. Figure published in [261].

194
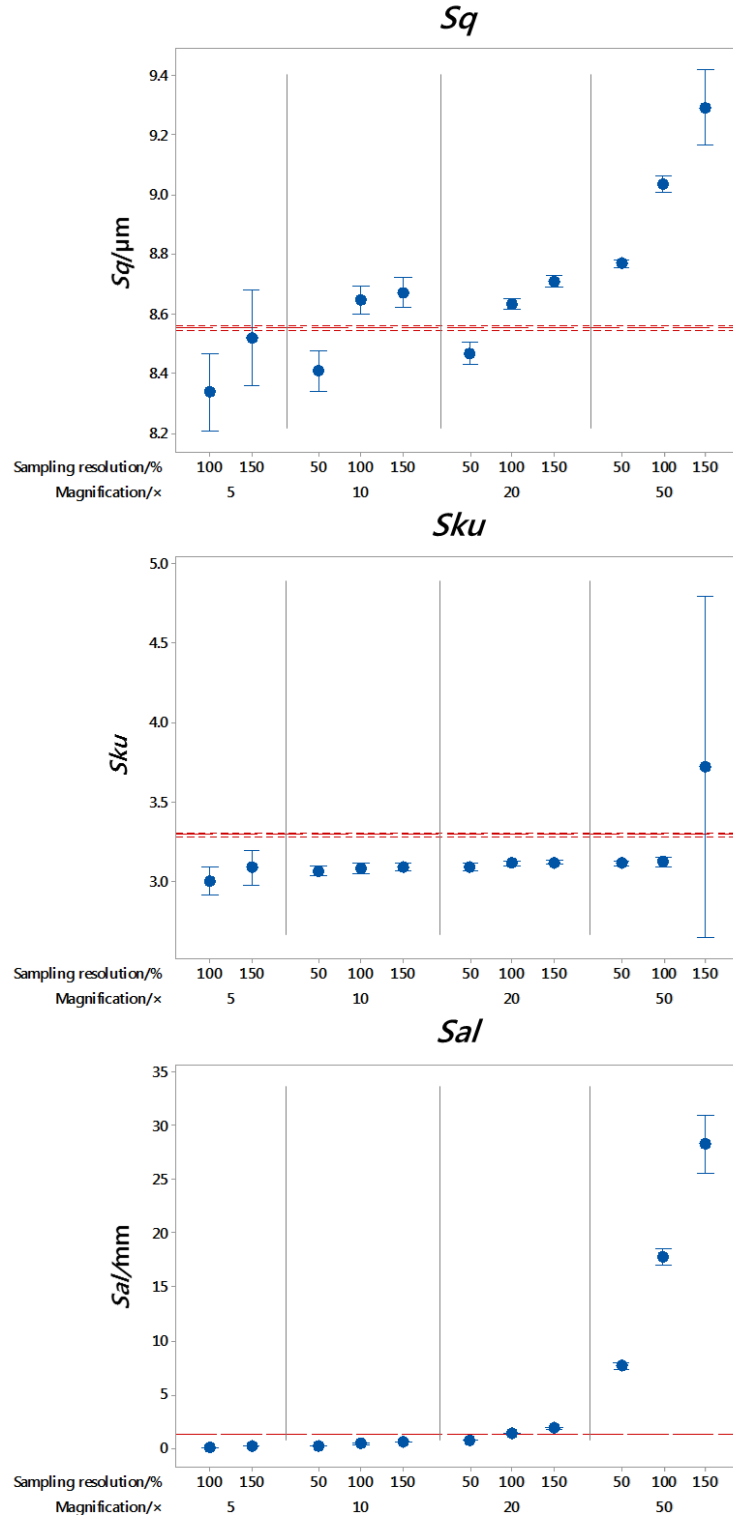
Figure 7.6b. ISO 25178-2 [51] areal texture field parameters computed for each XCT measurement setup (magnification and sampling resolution) and compared to the results for the CSI datasets (represented as reference lines, where the coarse dashed lines are means and fine dashed lines are the upper and lower CI bounds). The 5×/50 % setup is omitted as the topography of the reconstructed XCT surface was too deprived of detail to allow accurate alignment to CSI data. Confidence intervals computed at 95 % confidence on the repeat measurements. Figure published in [261].

195
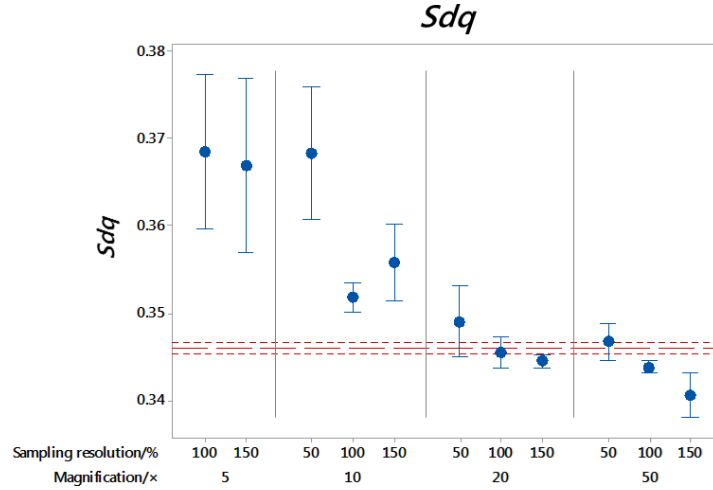
Figure 7.6c. ISO 25178-2 [51] areal texture field parameters computed for each XCT measurement setup (magnification and sampling resolution) and compared to the results for the CSI datasets (represented as reference lines, where the coarse dashed lines are means and fine dashed lines are the upper and lower CI bounds). The 5×/50 % setup is omitted as the topography of the reconstructed XCT surface was too deprived of detail to allow accurate alignment to CSI data. Confidence intervals computed at 95 % confidence on the repeat measurements. Figure published in [261].

7.3.4 Comparison via statistical topography models

Areal texture field parameters are essentially statistical descriptors, i.e. they are designed to summarise complex topographical properties pertaining to an entire surface region using scalar values. In figures 7.6a-c, discrepancies can be seen between XCT and CSI parameters, for example, *Ssk* and *Sku* parameters are routinely underestimated by XCT setups compared to CSI, and the 50×/150 % setup has here resulted in much larger CIs for these parameters than other setups. Discrepancies between texture parameter values imply the existence of topographical differences, but can provide only limited information on their exact nature, shape and spatial distribution. Essentially, the use of parameters alone does not provide particularly useful information about the differences between measurements. Therefore, to investigate topographical differences resulting from different XCT magnifications and resolutions, I adopted the method discussed in previous Chapters. This method involves the generation of statistical topographic models based on the same repeat measurements used for computing areal texture parameters. With reference to figure 7.7, each statistical

model referring to a specific XCT setup (magnification and sampling resolution) is comprised of a mean surface and CIs on the local mean height. These CIs – interpolated over the surface – create an upper and lower confidence boundary which identifies the estimated location of the mean height at a given confidence level (95 % in this test case). As in previous Chapters, here, CIs were obtained by treating the heights collected at each (x,y) location as independent random variables (i.e. without modelling spatial correlation between surface points) and by using t-distributions to estimate the CIs. Statistical topography models built for each XCT setup were used to assess local repeatability error (identified by the local width of the CIs) as a consequence of the setup choice. Statistical models were compared in pairs and used to assess disagreements between local mean height values. Upper and lower surfaces obtained by interpolation of the extreme points of the local CIs are displayed in figures 7.8a-c (for all combinations of magnification and resolution). In each case shown in figures 7.8a-c, upper and lower bounds for the reference CSI dataset are also rendered.

Figures 7.8a-c show that as magnification and sampling resolution increase, the topographic detail in the reconstructed surface improves. However, as magnification increases, the variance of height values across replicate measurements also increases (i.e. the CI widths get larger and more irregular), indicating larger repeatability error. At 50×, the variance of height values across replicate measurements essentially compromises the beneficial effects achieved in terms of better topographic detail.

Statistical models were also used to assess local discrepancy between mean height values estimated by each measurement setup. In these models, regions where CIs do not overlap can be considered as regions where the difference between heights is statistically significant. Using this information, I then defined a measure of overall discrepancy between measurement setups, computed as the ratio between the total area of the regions where height differences are statistically significant, over the total measured area (See figure 7.8). By pairing datasets acquired using each XCT setup to the CSI dataset, I can interpret any region where height difference is statistically significant as a

region where local bias in the XCT measurement can be detected with 95 % confidence; thus obtaining an indication of the measurement accuracy of each XCT setup.
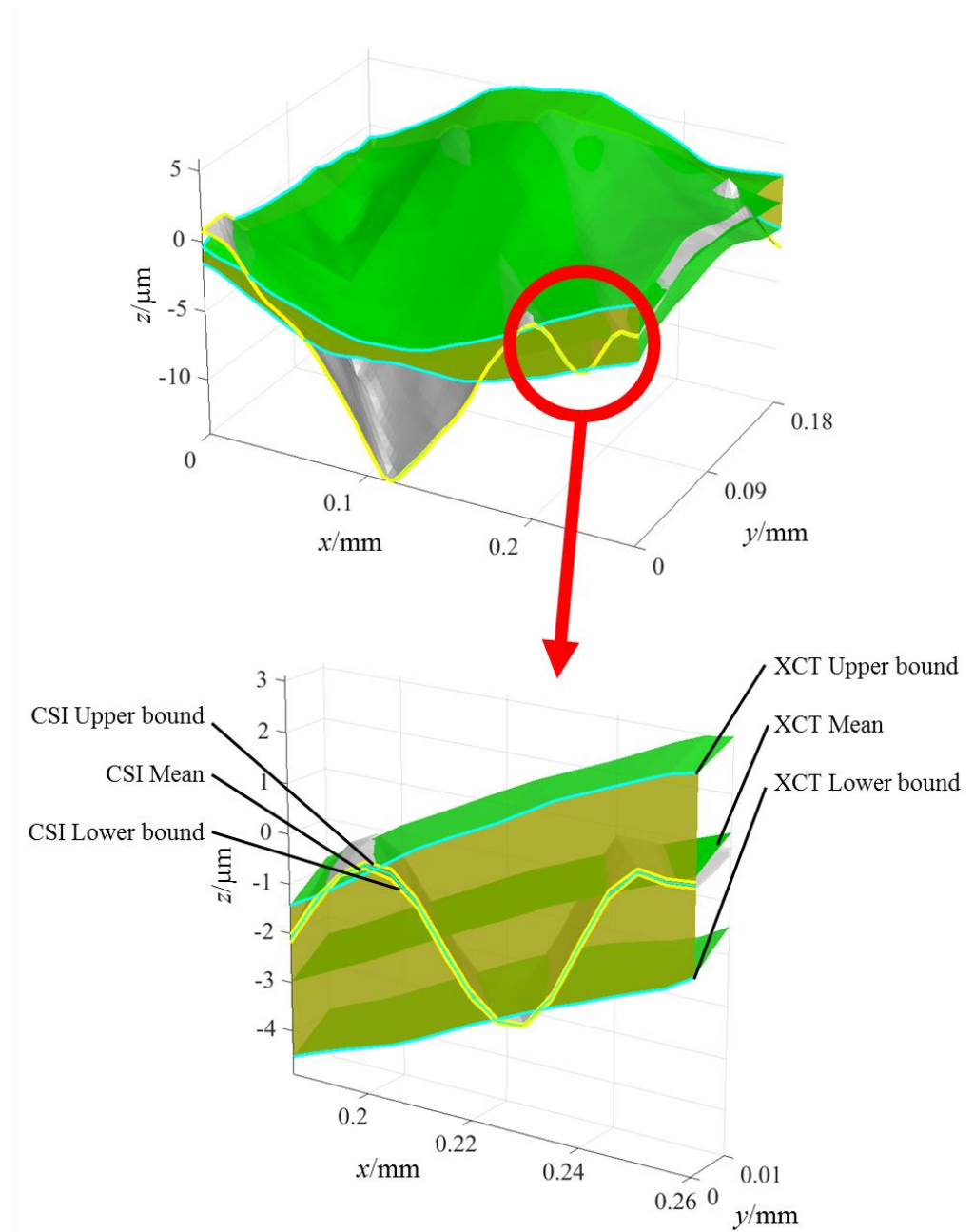
Figure 7.7. Statistical topography models, showing XCT and CSI mean surfaces and upper and lower bounds (extreme points of local CIs). Figure published in [261].
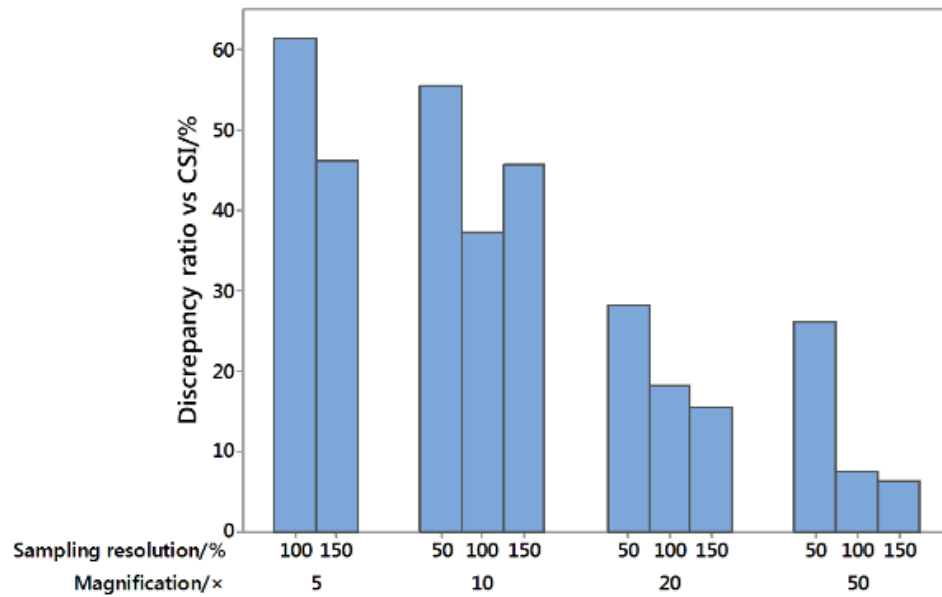
Figure 7.8. Discrepancy ratios between XCT and CSI data.

Local bias of the XCT measurements, with respect to the CSI reference is also shown in figures 7.9a-c. For XCT setups where repeatability error is lower (i.e. narrower CIs), discrepant regions are visible across the field of view. However, for XCT setups where the repeatability error is larger, discrepant regions are less common. This decrease in discrepancy does not necessarily mean that the agreement between measurements has improved, but rather that a higher number of repeat measurements is needed to better assess the statistical significance of the discrepancies. As such, the use of the discrepancy ratios to assess the difference between measurement setups alone can be misleading, so further metrics can be generated to provide better understanding of the discrepancies between setups.

In figure 7.10, the previous results are reorganised to provide another perspective to these findings. Particularly, the mean width of CIs computed over the sample region is shown as a function of magnification and resolution as a surface function, obtained by bilinear interpolation between experimental data points. The mean width of the CIs should be interpreted as a mean repeatability error for a given setup. Results show that the mean repeatability error is at minimum in the 20× data, but increases at lower or higher magnifications.

Modification of the sampling resolution also has an effect, with repeatability error increasing with sampling resolution.
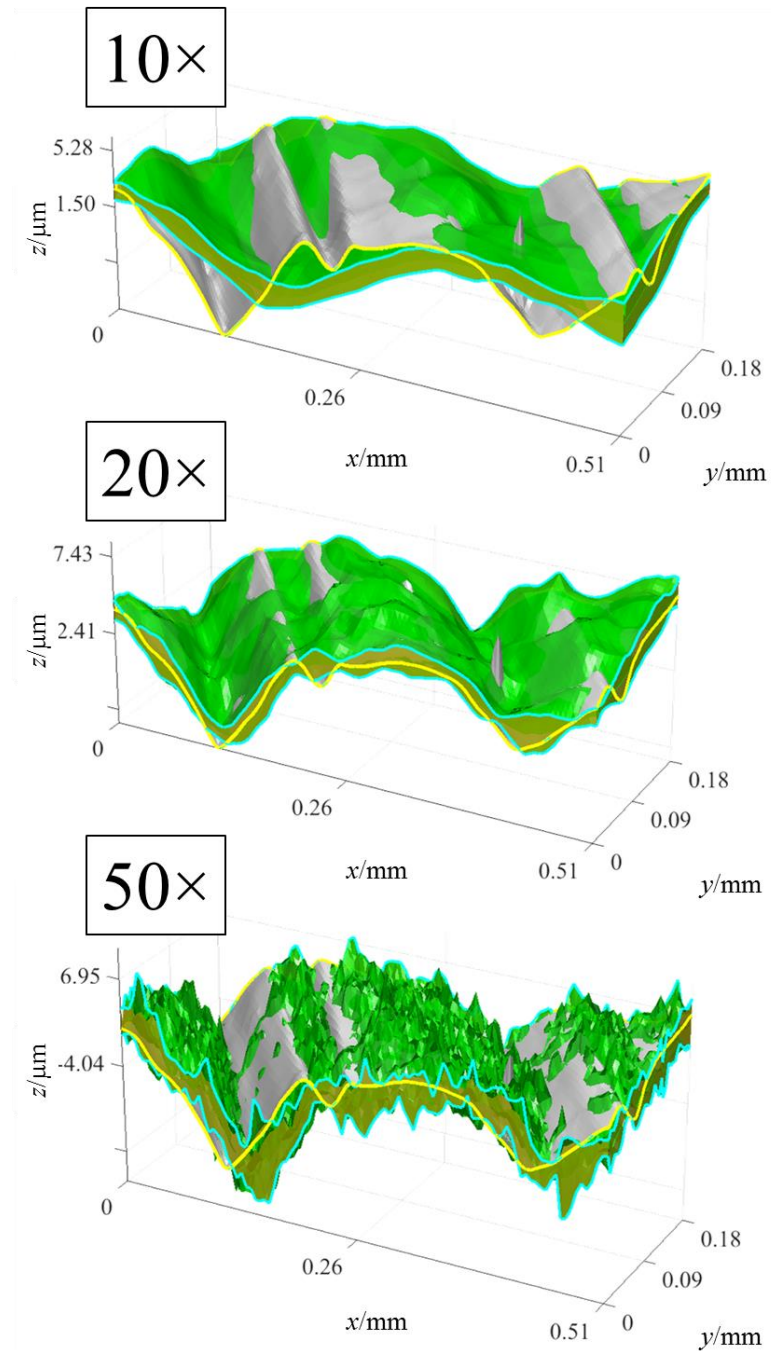
Figure 7.9a. Statistical topography models for 50 % resolution XCT setups, compared to the CSI setup. The 5×/50 % setup is omitted as the topographical detail of the reconstructed XCT surface was too deprived of topographical detail to allow accurate alignment to CSI data. Figure published in [261].
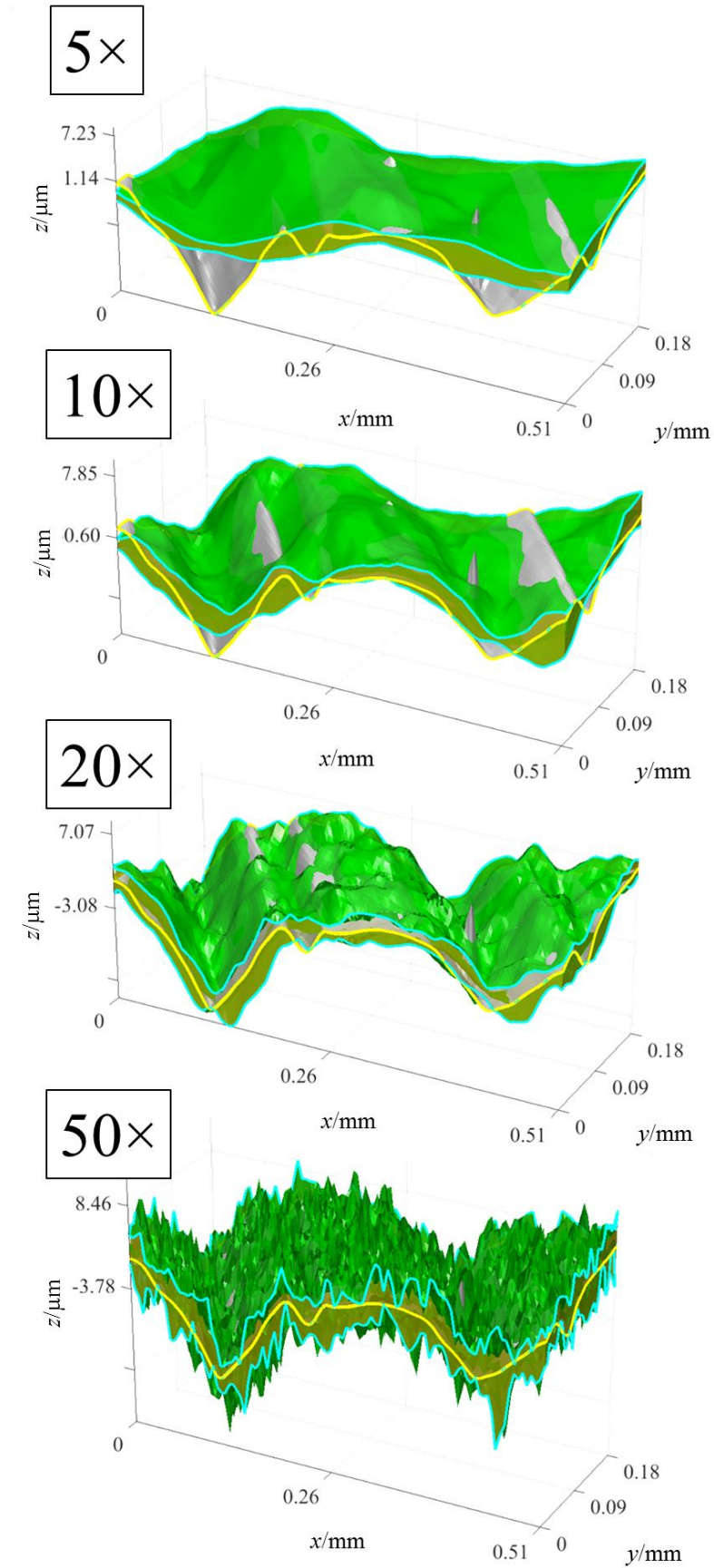
Figure 7.9b. Statistical topography models for 100 % resolution XCT setups, compared to the CSI setup. Figure published in [261].
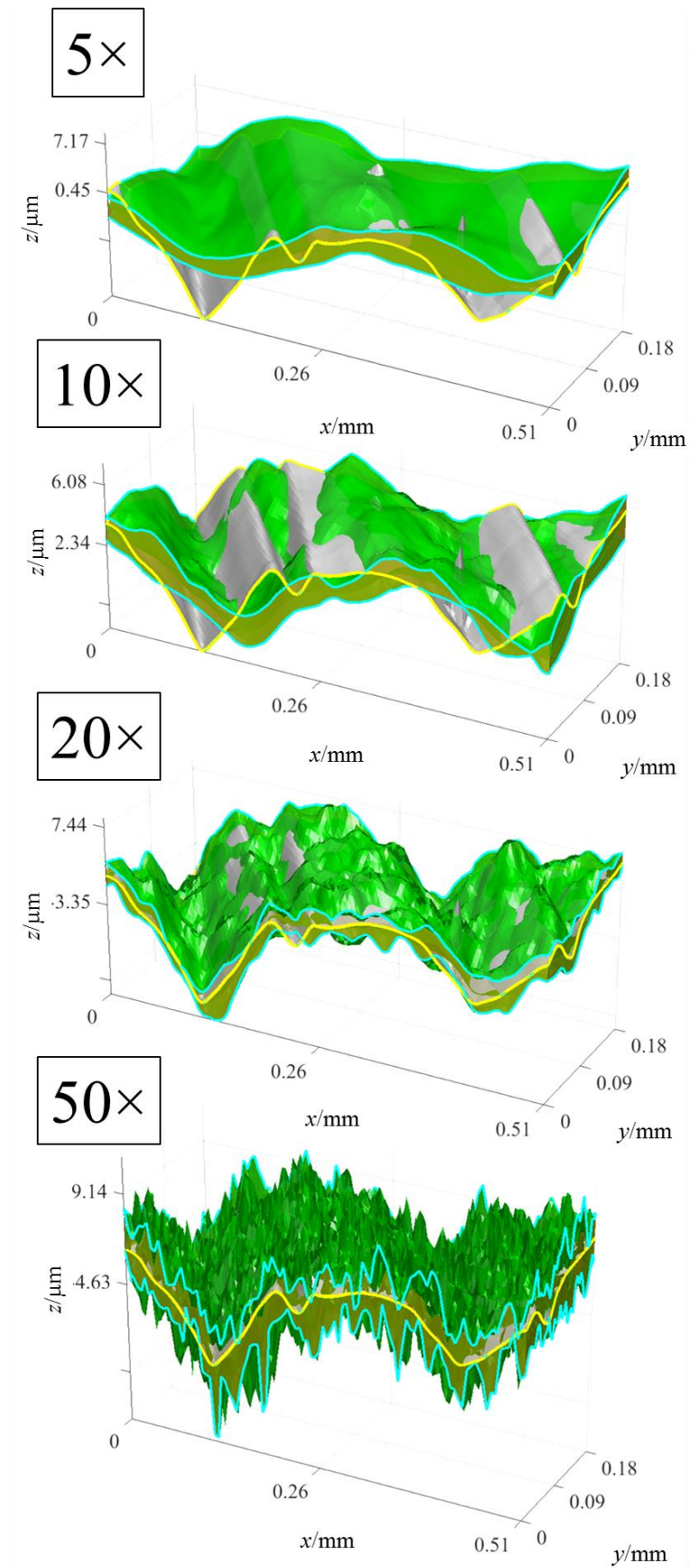
Figure 7.9c. Statistical topography models for 150 % resolution XCT setups, compared to the CSI setup. Figure published in [261].
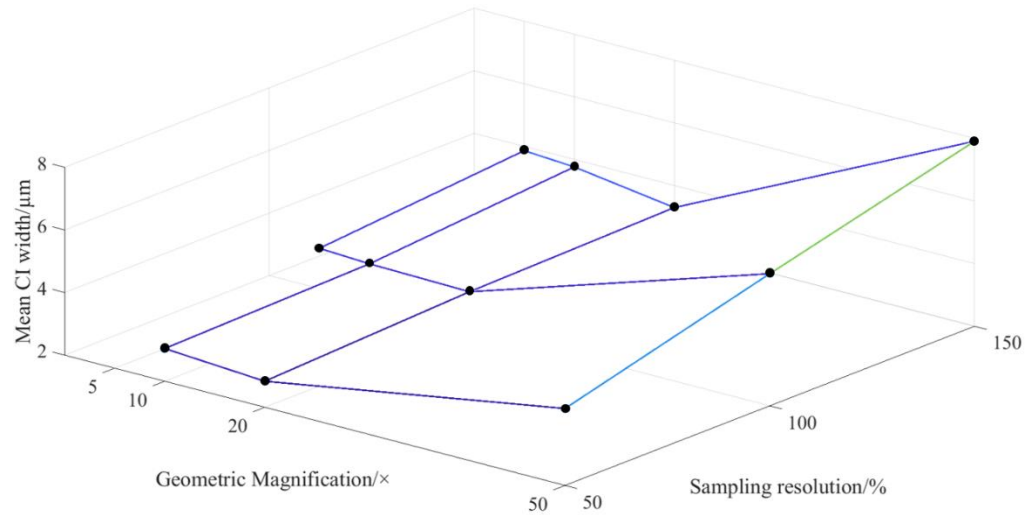
Figure 7.10. Mean repeatability error of XCT measurement corresponding to each setup, shown as an interpolated surface function. The mean repeatability error is computed as the arithmetic average of the CI widths over the sample region. The 5×/50 % setup is omitted as the topographical detail of the reconstructed XCT surface was too deprived of topographical detail to allow accurate alignment to CSI data. Figure published in [261].
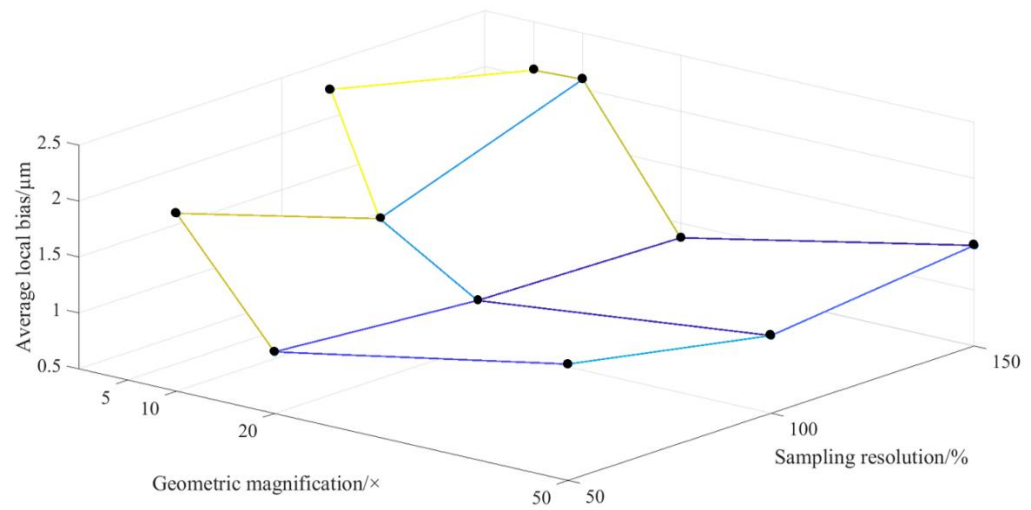
Figure 7.11 Arithmetic average of local bias in height determination when comparing each XCT measurement setup to CSI shown as an interpolated surface function. The 5×/50 % setup is omitted as the topographical detail of the reconstructed XCT surface was too deprived of topographical detail to allow accurate alignment to CSI data. Figure published in [261].

In figure 7.11, the mean surface obtained for each XCT setup is compared to the mean CSI surface, corresponding to the same (x,y) positions. The arithmetic average of the local unsigned difference between means was elected as a measure of mean bias (accuracy) of the XCT measurement with respect to the

CSI reference. In figure 7.11, the results are shown as a surface function (constructed using linear interpolation between experimental data points). The relationship between magnification, sampling resolution and the resulting accuracy shows the existence of a local minimum, corresponding to the 20×/150 % sampling resolution setup (i.e. least mean bias with respect to the CSI reference).

7.3.5   Comparison between paired, single surface datasets

In addition to comparing mean surfaces and the upper/lower bounds of statistical topography models, it is also possible to gain useful information by comparing paired, individual observations (i.e. individual topography datasets); as explained diagrammatically in figure 7.12, whilst all the combinations of paired comparisons are reported in figures 7.13a-c. Each plot represents a specific XCT surface (green) aligned to the same CSI dataset (grey). Local distances are coloured proportionally to signed differences between height values. The increase of local topographic detail in the XCT datasets as magnification and resolution increases is even more evident in this figure than in figures 7.9a-c, because of the absence of the smoothing effect introduced in the upper, mean and lower surfaces by the statistical model. An increase in high-spatial frequency, random, topographic content (i.e. noise) is also visible, most notably relating to magnification. This is the topographic component primarily responsible for the irregular behaviour of the local mean and corresponding upper/lower bounds observed in the statistical models corresponding to higher magnification presented in figures 7.9a-c.

Further inspection of figures 7.9a-c and 7.13a-c indicates that, in any XCT setup, both local bias and repeatability error seem to be related to local topographic properties. This relation implies that it is likely that specific topographic features may trigger variations in measurement behaviour, sometimes mostly influencing bias, other times mostly influencing repeatability error. As such, the process of performing an uncertainty analysis for XCT surface measurement would be complex and difficult to apply generally, and a requirement for a task specific analysis is likely. Significant further

investigation is therefore required into the significance of this problem and how it may be potentially minimised.
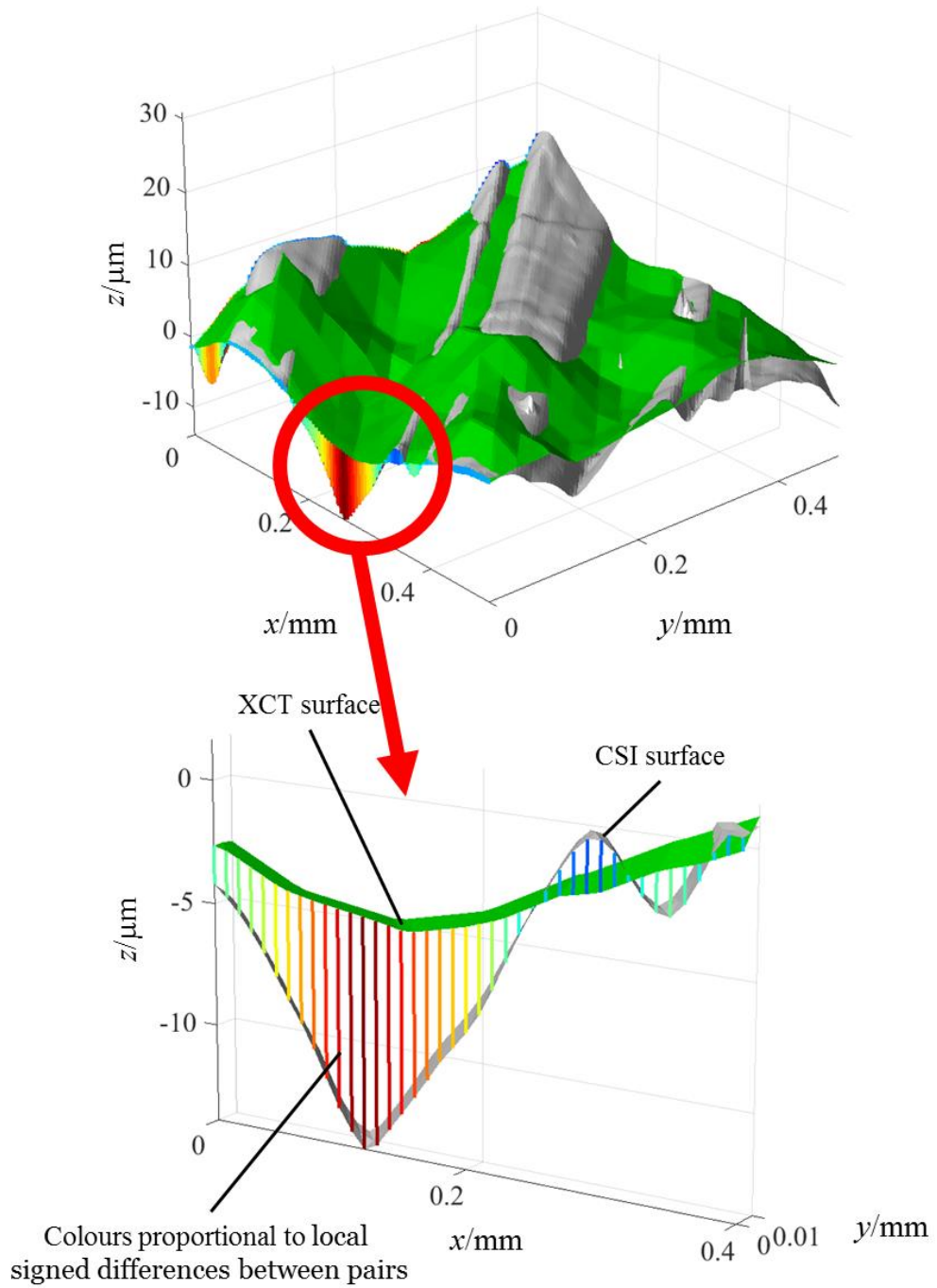
Figure 7.12. Local height differences (signed) computed between paired datasets. Figure published in [261].
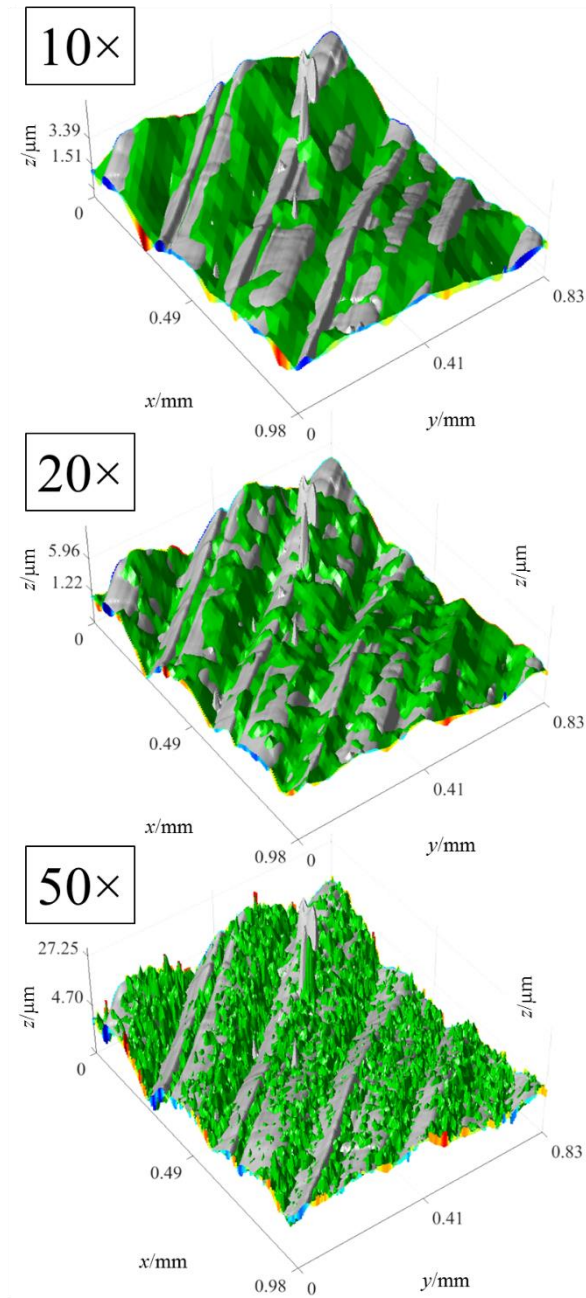
Figure 7.13a. Local height differences (signed) computed between paired datasets, each pair comprised of one dataset for each 50 % resolution XCT setup and a common CSI dataset. The 5×/50 % setup is omitted as the topographical detail of the reconstructed XCT surface was too deprived of topographical detail to allow accurate alignment to CSI data. Figure published in [261].
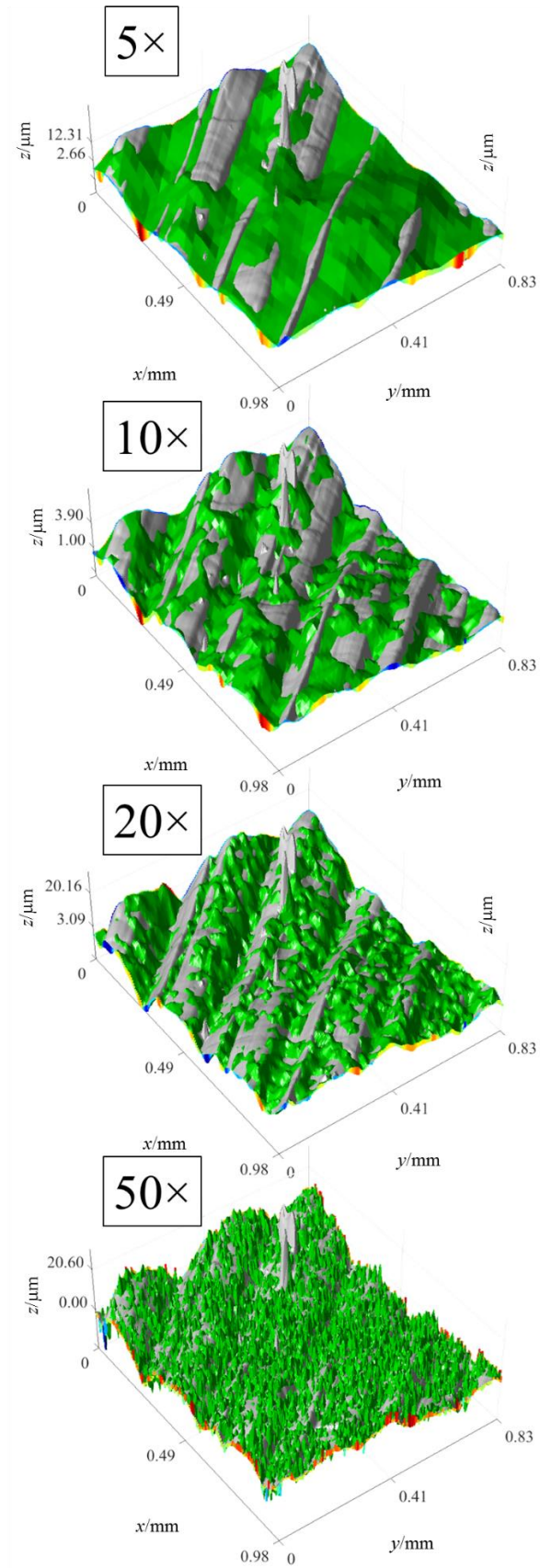
Figure 7.13b. Local height differences (signed) computed between paired datasets, each pair comprised of one dataset for each 100 % resolution XCT setup and a common CSI dataset. Figure published in [261].
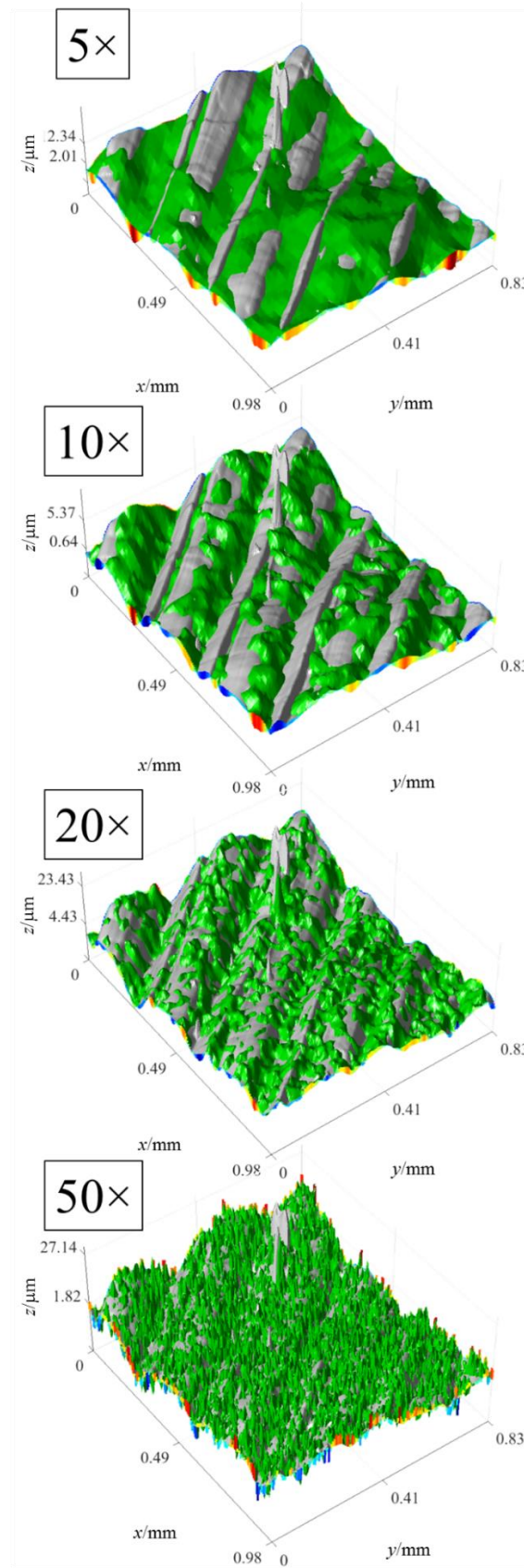
Figure 7.13c. Local height differences (signed) computed between paired datasets, each pair comprised of one dataset for each 150 % resolution XCT setup and a common CSI dataset. Figure published in [261].

7.4 Chapter discussion

7.4.1   XCT topography measurement

There are a large number of input parameters that affect XCT topography measurement, and two that are considered to be of greatest significance [56] have been examined in this Chapter. Results show a general improvement in measurement quality when magnification is increased from 5× to 20×, i.e. reduced bias with respect to the CSI reference dataset and reduced repeatability error, but a significant decrease from 20× to 50×. This quality decrease is likely to be a result of an increase in the noise present in volumetric reconstructions, as shown in figure 7.4. Out-of-field-of-view artefacts (e.g. streaking and shading in the reconstructed images [65,269,270]) will contribute towards the increase in noise present in the 50× case, though noise also increased between the 5× and 20× setups. This noise increase is most likely as a result of a slight decrease in contrast with an increase in magnification, as the X-ray flux per unit volume through the sample increases with magnification [56]. Further noise increases may also result from the effects of X-ray scatter, that are known to increase with magnification [271].

For the purposes of this work, it was necessary to treat the XCT measurement system as a 'black-box', and examined the effects of how altering certain input parameters to such a system affects the outcome of a surface measurement. This decision was made as, while models of noise transmission have been well studied in the literature [272–274], the means by which the noise present in raw XCT image data is transmitted to the noise present in the surface data extracted from that raw data is not yet understood, and represents a significant future effort. There are of course many influencing factors on the measurement beyond the two variables examined here, including the X-ray source settings, focal spot size, detector characteristics and other reconstruction parameters, but these have been held constant for the purposes of this experiment. Investigation of these influence factors, all of which may have some influence on the image sharpness (and therefore the eventual extracted topography), represent significant avenues of future research.

209

My results also provide insight into good practice in XCT surface measurement when considering the use of super- and sub-sampling of the reconstruction grid. Sub-sampling allows for small time savings in computation (a few minutes per sample), but as shown here, significantly reduces the quality of the data when compared to reference measurements. Sub-sampling leads to distortions in determined surfaces and increases in CI width (see figures 7.9a-c). Conversely, super-sampling of the reconstruction grid greatly increases processing time, while offering little to no improvement in the quality of the reconstructed topography. Although discrepancy ratios (figure 7.8) between statistical topography models of XCT and CSI measurements apparently decrease when the reconstruction grid is super-sampled, the decrease is clearly due to the widening of the CIs, which implies that there is not enough experimental evidence to determine whether or not datasets are discrepant. A simple observation of paired mean surfaces, and the associated mean unsigned distance between them, also clearly show that agreement has indeed decreased.

The data presented throughout this work help us to provide guidelines for good practice in surface measurement using XCT. For example, using a magnification of 5× clearly provides poor quality data by the metrics presented in this Chapter (see figures 7.10 and 7.11), and is likely insufficient for successful measurement of surfaces. Similarly, super- and sub-sampling of the reconstruction grid provides little benefit to the user. Improvements in data quality are generally provided by increasing magnification, but issues experienced at high magnification can also apparently cause issues that reduce the quality of the data. These issues, likely caused by the aforementioned out-of-field-of-view artefacts, decrease quality to the point where use of lower magnification may be beneficial to the user, despite the decrease in resolution. A case-specific trade-off in magnification settings therefore exists, balancing the desire for the highest possible magnification with the drawbacks with which high magnification scans come (i.e. increased noise). Because of this, I cannot recommend specific settings for successful surface measurement by XCT, but these findings should provide a basis by which XCT users may successfully conduct investigations of surfaces.

It is clear that many factors requiring investigation remain before XCT can become established as a common method of surface measurement in industry. Particularly, more work is required to understand the uncertainty in such a measurement, and establishment of traceability for measurements of complex AM surfaces (by XCT or otherwise) is a difficult, open research question. Experiments should also be extended in future work to examine material and multi-material specific effects on XCT surface measurements; as material choice (and particularly the use of multi-material samples) has been previously shown to have significant effects on measurements [56]. However, the need for this understanding is strong, in particular from the AM community, given the complex geometries commonly manufactured by AM processes and the likely presence of inaccessible or otherwise hard-to-reach surfaces.

In addition to the work presented in this Chapter, further assessment of how measurements are affected by the many unstudied variables factoring into XCT measurement is still required (e.g. X-ray voltage and current, angular sampling, sample material). Such assessments will feed into good practice in industry, thereby facilitating increased adoption of AM technologies.

7.4.2 Comparison methodology

Very few of the results highlighted in this Chapter could be captured by a simple comparison of ISO 25178-2 areal texture field parameters, which is the most common method in industry for performing comparative assessment of surface topographies. The application of the statistical topography modelling and comparison method (as discussed in previous Chapters and further developed here), clearly shows that it is possible to investigate measurement differences, in terms of what causes them, how they appear on the surface, and where they are located.

Additional scientific merit of this study is, therefore, found in the proposition of a method to support reliable assessment of XCT sensitivity to control parameters, and as a tool for measurement process optimisation. The method does suffer some limitations, in that the quality of the statistical model is

affected by alignment errors in the datasets. In this work, I have assumed the presence of minimal misalignment. However algorithmic global alignment is performed by applying the iterative closest point (ICP) method [252] in six degrees of freedom. The adopted approach is referred to as 'global alignment' as the optimisation takes into account the entirety of the datasets. However, one may wonder if, in the presence of significant differences between topographies, only the 'less varying' regions should be considered as valid references for alignment. In addition, the current alignment method does not take into account the lesser reliability of points associated to higher repeatability error. Development of more advanced alignment solutions that account for both topographic differences and associated measurement errors is part of ongoing work. Additionally, as discussed in Chapter 5, the method of statistical modelling used can still be refined by improving methods for computing local confidence intervals (e.g. by taking into account local spatial correlation between neighbouring surface points). Additional corrections to the statistical procedure for assessing local discrepancies may be adopted by introducing a correction factor for multiple comparisons (e.g. Bonferroni [275]).

7.5 Chapter summary

XCT measurement of areal surface topography is complex, and open to a wide array of influencing factors that affect the eventual measurement results. However, XCT's importance and potential in the domain of AM part quality inspection is undeniable. These findings complement and improve upon the conclusions of previous work examining the use of XCT for areal topography measurement [99,196]. Specifically, in addition to showing that areal texture parameters vary significantly across setups, I have illustrated the details of how the reconstructed topography (from which the texture parameters are calculated) varies across setups. Geometric magnification has a stronger effect than sampling resolution in determining the quality and appearance of the topographic reconstruction. In particular, the magnification setup providing the best accuracy (compared to the CSI reference) was at 20× for the test case, while bias (again with respect to the CSI reference) decreased at smaller and larger magnifications (see figure 7.11). Precision, indicated through the local

repeatability error, consistently decreased with magnification. Modifying the sampling resolution (either by sub-sampling or super-sampling) has less pronounced effects; although generally, decreasing sampling resolution worsens metrological performance, while increasing it may lead to slight improvements. However, such improvements are unlikely to be justified in an industrial setting, as the time required to reconstruct, extract and process super-sampled surface topographies increases significantly with respect to the super-sampling ratio (e.g. half an hour to many hours). At present, it is unclear as to what part of the presented results can be safely assumed as case-independent. What is clear, however, is that in XCT surface measurement, the optimal setup may not necessarily correspond to the highest magnification or highest reconstruction resolution, thus making the identification of an optimal measurement setup a non-trivial problem. Finally, I have demonstrated the importance and advantages of comparing measurement setups by means of statistical analysis of surface topographies reconstructed from measurement (as opposed to, or in addition to, the analysis of changes in texture parameter values). The amount of additional information that can be retrieved from the inspection of the actual topographic formations and how they vary as a consequence of measurement setup is invaluable when investigating the performance and behaviour of novel and partially unproven measurement technologies.

As discussed, however, XCT for surface measurement is very much in its infancy as a robust technique for validation of metal AM parts, and various avenues of further research exist. In addition to examination of the unstudied variables discussed in this Chapter, there exists an opportunity to examine an industrial case study in which measurement of an internal surface is required to understand how this technology may be directly applied to industry. I will, therefore, present such a case study in Chapter 8.

8. X-ray computed tomography surface measurement in industry

In Chapter 7, I highlighted how a case study of an industrial part has yet to be performed using the metrology techniques developed during my PhD. I therefore present such a case study here, as a means to rounding off the methods presented in this Thesis. Specifically, I present here a study of a part developed to be representative of a common industrial case; designed in conjunction with my sponsor company, 3TRPD, who are an additive manufacturing bureau that supply industrial AM parts to various industries. The part was intended to be representative of common parts containing cooling channels, with inaccessible surfaces of interest present in these channels. Surface verification is important for cooling channels, as the surface texture of such channels is well known to have a significant effect on the flow of fluids passing through them [276]; thereby affecting the functional properties of the channels. This work shows how such an industrial case can be conducted and meaning measurements obtained, and was presented as a poster at a conference in 2018 [277], where it won an award for best poster.

8.1 The application of XCT surface measurement to an industrial case

As discussed throughout this Thesis, AM processes have been lauded for their ability to produce highly complex geometries that are otherwise not manufacturable, including structures such as lattices and internal cooling channels. Such structures may have a significant impact on the aerospace, automotive and medical sectors because of their associated functional properties; for example, significant savings in mass, impact energy absorption, vibration isolation and thermal management. However, such structures present issues in verification, as crucial surface features are often difficult to access or entirely separated from the outside, and so cannot be measured by optical or contact methods. Work presented throughout this Thesis has demonstrated the feasibility of XCT for the measurement of internal and difficult-to-access surfaces. Using designed-for-purpose separable assemblies, pseudo-internal

surfaces have been investigated by comparison of XCT data with that acquired using established measurement technologies (see Chapters 6 and 7). In this Chapter, I present an XCT surface measurement case study, using an industrially representative part comprising a metal powder bed fusion AM Ti6Al4V cube of (20 × 20 × 20) mm, containing internal channels nominally of 1 mm in diameter (see figure 8.1). This part was developed in collaboration with 3TRPD, with design and production of the part being performed by 3TRPD at their site in Newbury, UK. The case study was set up in such a way as to maximise industrial input, so that the study is representative of a production part. However, due to confidentiality agreements between 3TRPD and various third parties, the use of an actual production part was deemed unfeasible. Hence, the use of a representative part was deemed the most appropriate option for the case study (see figure 8.1 and Section 3.1). The cube was measured by XCT at two different magnification settings and assessments of internal surfaces made based on this data. The cube was then sectioned in order to perform measurements by optical methods, and this data was compared to the XCT data. Comparisons were performed using direct topographies, as well as generated ISO 25178-2 surface texture parameters.
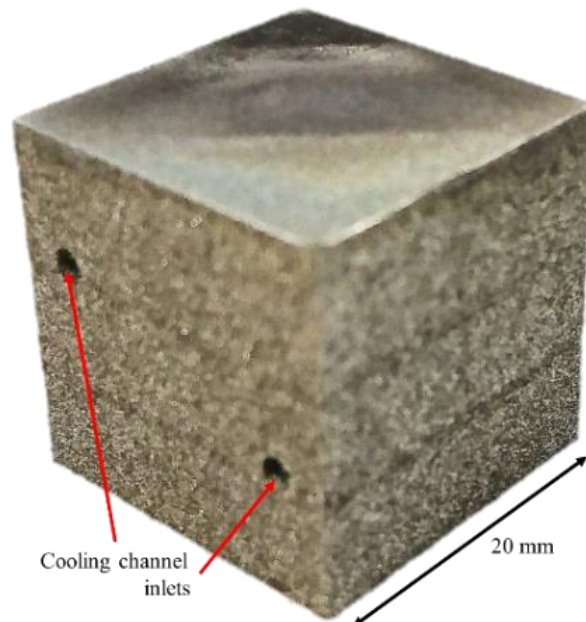
Figure 8.1. Industrially representative part, comprising a Ti6Al4V cube of (20 × 20 × 20) mm containing internal channels.

8.2 Chapter methodology

During the work that constitutes this Chapter, I employed the methods developed throughout my PhD to the case study, performing scans in line with the work presented in Chapters 6 and 7 and comparisons as discussed in Chapters 5 to 7. I will, therefore, not elaborate on these methods at length here, but will summarise the process in a concise format. All instrument names are once again redacted to prevent undue comparison of commercial instruments. For each measurement setup, five measurements were taken in repeatability conditions (i.e. without disturbing the sample between measurements).

8.2.1   Measurement setups

Data were acquired using two XCT setups, one where the whole part was contained in the field of view, and another at a higher magnification where sections of the part were outside of the field of view (similar to the 50× setup presented in Chapter 7). In an attempt to compensate for noise issues relating to out-of-field-of-view artefacts presented in that 50× setup, an increased number of projections was used in the higher magnification scan. As the size of the part when magnified and projected onto the detector was approximately double the size of the field of view, twice the default number of projections was used to compensate for discontinuities between projections induced by the object being partially outside of the field of view [65,269,270], where the default number is 3142. This default number is defined by the system geometry as the minimum number of projections where no discontinuities are present for a workpiece entirely inside the field of view. The specific setups and instruments used were as follows:

- XCT setup 1: measurements were performed at a geometric magnification of 11×, providing a voxel size of 18.1 μm. The following parameters were used: 3142 X-ray projections formed by averaging two frames per projection, each lasting 2 s, a detector gain 24 dB; X-ray tube voltage 225 kV and current 52 μA; a 0.75 mm copper X-ray pre-filter was used and a warmup scan of approximately one hour was performed prior to the scan. A

detector shading correction was applied by averaging 256 reference frames (128 bright and 128 dark), and flux normalisation was applied during the scan.

- XCT setup 2: measurements were performed at a geometric magnification of 20×, leading to voxel size of 10.0 μm. The following parameters were used: 6284 X-ray projections formed from a single frame, each lasting 2 s with a detector gain 24 dB; X-ray tube voltage 225 kV and current 44 μA; a 0.75 mm copper X-ray pre-filter was used and a warmup scan of approximately one hour was performed prior to the scan. A detector shading correction was applied by averaging 256 reference frames (128 bright and 128 dark), and flux normalisation was applied during the scan.

Following XCT measurement, the part was sectioned by face milling, in order to compare XCT data to data acquired using optical methods (see figure 8.2). A region of interest (ROI) representative of the wider surface was selected on the part (highlighted in figure 8.2).
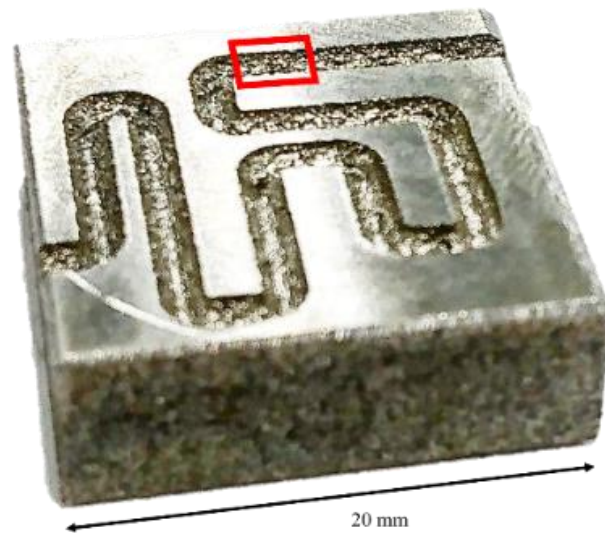
Figure 8.2. Industrially representative Ti6Al4V part after sectioning by face milling to reveal internal channels. Red box shows the region of interest used in this case study. Dimensions after sectioning were (20 × 20 × 10) mm

Data were acquired using coherence scanning interferometry (CSI) and focus variation (FV) instruments. Setups for each of these instruments are described

217

below. As in Chapters 4 to 7, FoV is the field of view, LR is lateral resolution and NA is numerical aperture. LR-pixel refers to the pixel spacing of the detector used by each instrument, LR-optical refers the calculated Sparrow optical limit [34] of each instrument and LR-contrast refers specifically to the distance from the centre of each pixel used by the FV instrument to compute local contrast; selected during the measurement. The Sparrow optical limit was calculated using a wavelength of 580 nm for both systems. The setups used for measurements acquired using these systems were as follows:

- CSI: 20× objective lens at 1× zoom (NA 0.40, FoV 0.42 mm × 0.42 mm, LR-pixel 0.41 μm, LR-optical 0.68 μm), stitching of multiple images performed in the manufacturer's software. Vertical stitching was also applied, to merge multiple measurement z intervals.
- FV: 20× objective lens (NA 0.40, FoV 0.81 mm × 0.81 mm, LR-pixel 0.44 μm, LR-optical 0.68 μm, LR-contrast 3 μm), ring light illumination, stitching of multiple images performed in the manufacturer's software.

8.2.2 Data analysis

X-ray imaging and volumetric reconstruction were performed for both XCT setups using the manufacturer's software, using the FDK algorithm [61] using a third-order beam hardening correction and a Hanning noise filter, with cut-off at the maximum spatial frequency. This filter was chosen to reduce image noise present when alternatively using an edge-preserving ramp filter, without substantially degrading the quality of the edges present in the data. Noise was an issue in the 20× XCT measurement setup, in that this setup necessitated the application of an opening/closing operation on the determined surfaces to remove noise during the determination process (as in the 50× magnification setups in Chapter 7, see Chapter 7 for details). Modification of these measurement setups to alleviate this requirement was considered, but discarded because of the excessive time increases incurred by such changes. A filter with a greater effect on noise reduction was also considered to alleviate this requirement, but the literature suggests that the application of a stronger noise

filter would have caused unacceptable degradation of edges, likely having significant effect on the outputted surfaces (see Bartscher et al. [70]).

Following reconstruction, XCT data were again imported into Volume Graphics VGStudioMAX 3.0 [73] and surfaces were determined using the iterative local maximum gradient algorithm over a search distance of four voxels, using the ISO 50 % isosurface [139] as the start point. For the 20× setup, an additional opening/closing morphological operator was applied to remove noise artefacts both above and below the determined surface (as per the method presented in Section 7.2.3 of Chapter 7). In this case, a second surface determination using the local maximum gradient algorithm was performed after the opening/closing operation, using the post-operation surface as the start point. Computed surfaces were exported as triangulated meshes in the STL format with no mesh simplification. Surfaces were then imported into MountainsMap [228], where they were automatically converted into 2.5D height maps to allow comparison to CSI and FV data. Height map resolutions were automatically determined by MountainsMap to match the point density of the triangulated meshes. The conversion removed any undercut features from the XCT data.

Height maps were converted into triangulated models and imported into the in-house developed MATLAB [268] program outlined in Section 5.2.2.3 of Chapter 5 and aligned to a single CSI dataset as described previously. Aligned datasets were converted back into height maps using raster scanning onto an *xy* grid set at 0.5 µm spacing. Statistical modelling of topographies was performed in MATLAB as per the methods outlined in Chapter 7.

ISO 25178-2 [51] texture parameters were calculated in MountainsMap. For calculation of texture parameters, a levelling F-operator (removal of a least-squares mean plane) was applied. Data are intrinsically bandwidth matched [238] during the alignment, cropping (matching of larger wavelengths) and raster scanning (matching of smaller wavelengths) process. However, an S-filter and an L-filter were applied to all datasets, respectively, to remove small scale features and to remove the cylindrical form of the channel and any underlying waviness. Surfaces were filtered first using a Gaussian convolution S-filter with

a 2.5 μm cut-off. A Gaussian convolution L-filter with a 0.2 mm cut-off was then applied, chosen as approximately equal to the width of weld tracks in the data.

8.3 Chapter results

8.3.1 Visual comparison of reconstructed topographies

The first comparison made during this case study was to perform a qualitative visual examination of unfiltered surface topographies, as reconstructed using each measuring instrument and setup (see figure 8.3). Consistent with results presented in Chapters 4 to 7, large features in particular are clearly similarly represented across the datasets. Smaller features (e.g. attached particles, weld ripples) recognisable in CSI data are less visible in both FV and XCT data. Comparing XCT setups, resolution visibly improves between the 11× and 20× cases, but there also appears to be a substantial increase in randomly distributed high spatial frequency features; as seen in the results presented in Chapter 7.
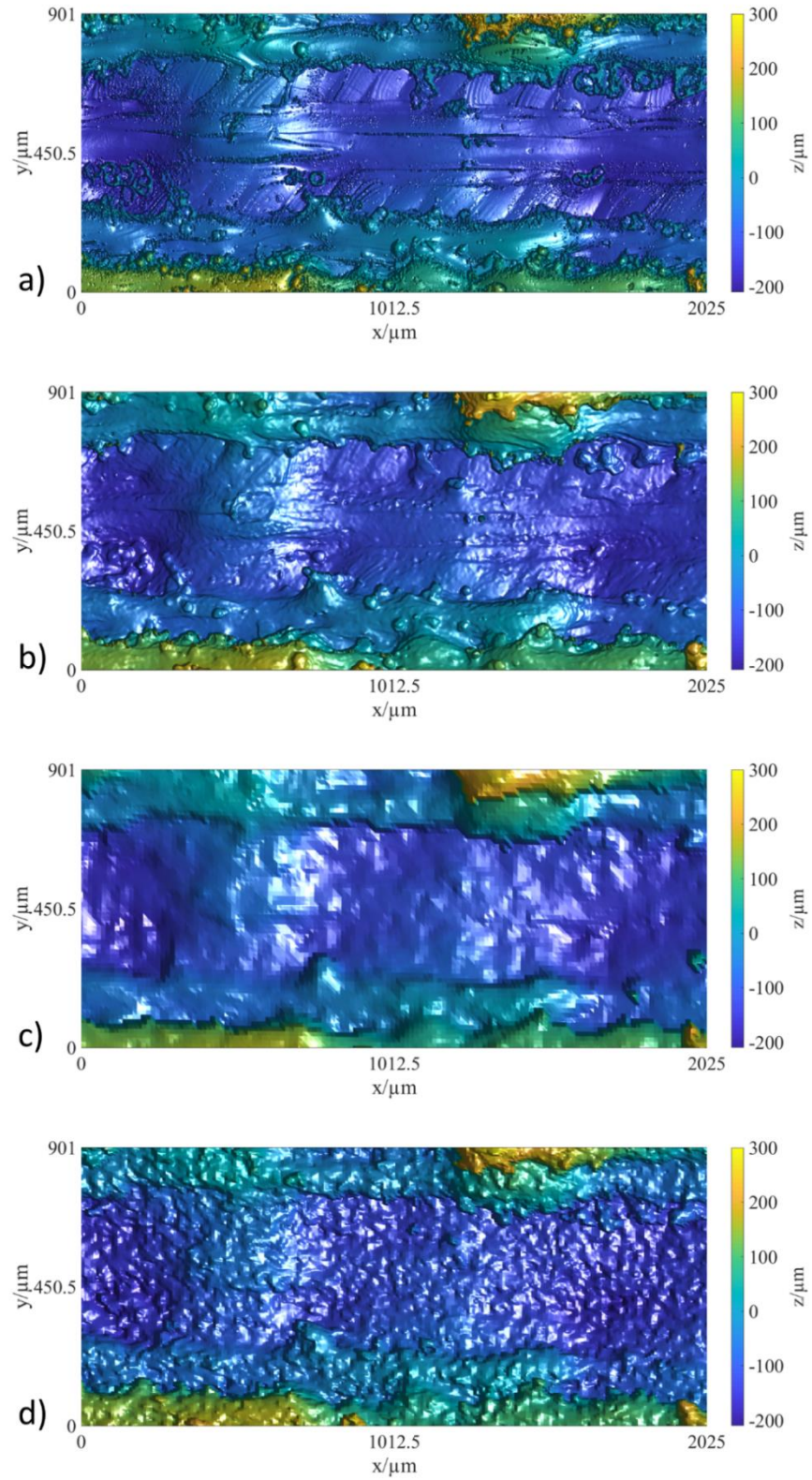
Figure 8.3. Example individual datasets from each measurement setup; (a) CSI; (b) FV; (c) XCT (11×); (d) XCT (20×).

8.3.2 Comparison of ISO 25178-2 parameters

The second comparison performed during this case study was of common ISO 25178-2 [51] field parameters. Following the findings of previous Chapters, parameters generated from data acquired using different instruments were generally in disagreement with each other. These parameters, and the discrepancies between them, are shown in figure 8.4.
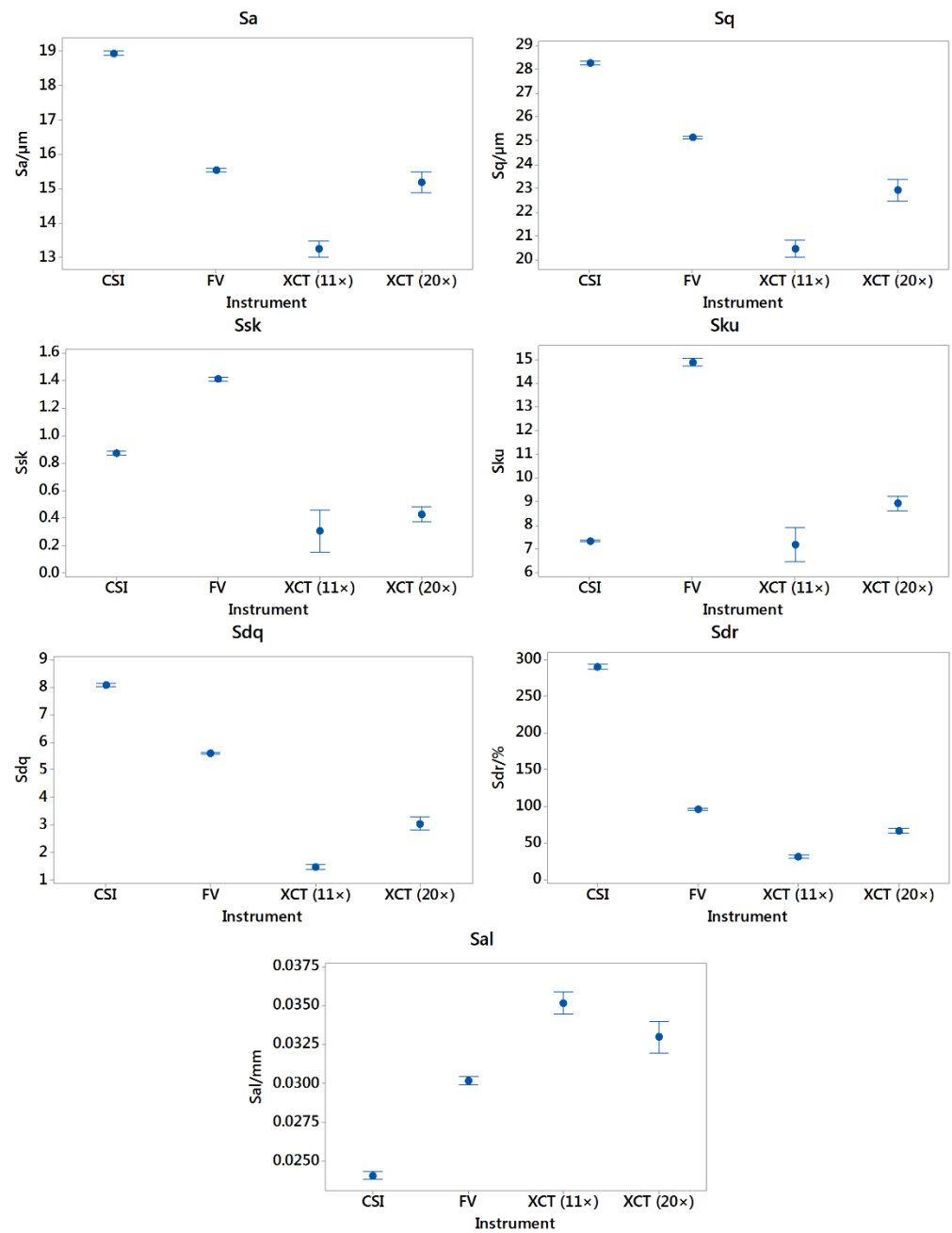
Figure 8.4. ISO 25178-2 [51] areal texture field parameters computed for each dataset. Confidence intervals computed at 95 % confidence on five repeat measurements.

8.3.3 Comparison via statistical topography models

The third comparison performed during this case study was of statistical models of topography, presented in figure 8.5; similar to those shown in Chapter 7 in figure 7.8a-c. Unlike those in figure 7.8a-c, however, in these visualisations, confidence interval (CI) plots for individual instruments are shown, as opposed to overlapping data from two separate measurement setups (as shown previously). In these visualisations, green surfaces represent the upper and lower bounds of CIs, with the yellow lines representing the same in cross-section. Purple lines in this case represent mean surfaces.

As in Chapter 5, visualisations of data acquired using optical methods show notable spikes surrounding areas containing high slopes, while XCT datasets do not suffer from such spikes. The CI width for the higher magnification XCT setup is greater than for the lower magnification setup, but comparison to data from optical methods shows the higher magnification setup captures more of the high spatial frequency information on the surface.

Also, it is possible to quantify discrepancies between setups using the mean CI width for each plot (i.e. repeatability error), as well as using the mean local bias between two plots. Figure 8.6 shows the former of these two metrics for each instrument. To construct the latter metric, FV and XCT data have been compared to CSI data (figure 8.7). In this case CSI was used as a reference, as, of the four datasets, the mean CI width was lowest for the CSI data.

What is notable from figure 8.6 is that while XCT measurement setups provide greater mean CI widths than the two optical setups, CI widths (i.e. repeatability errors) are of broadly comparable sizes (particularly in the $11\times$ magnification case). Figure 8.7 tells a similar story, in that although there are discrepancies between all measurement setups (as expected, given previous results presented throughout this Thesis), the mean local bias between the two optical systems is of comparable magnitude to the mean local bias between one of these setups and the XCT setups.
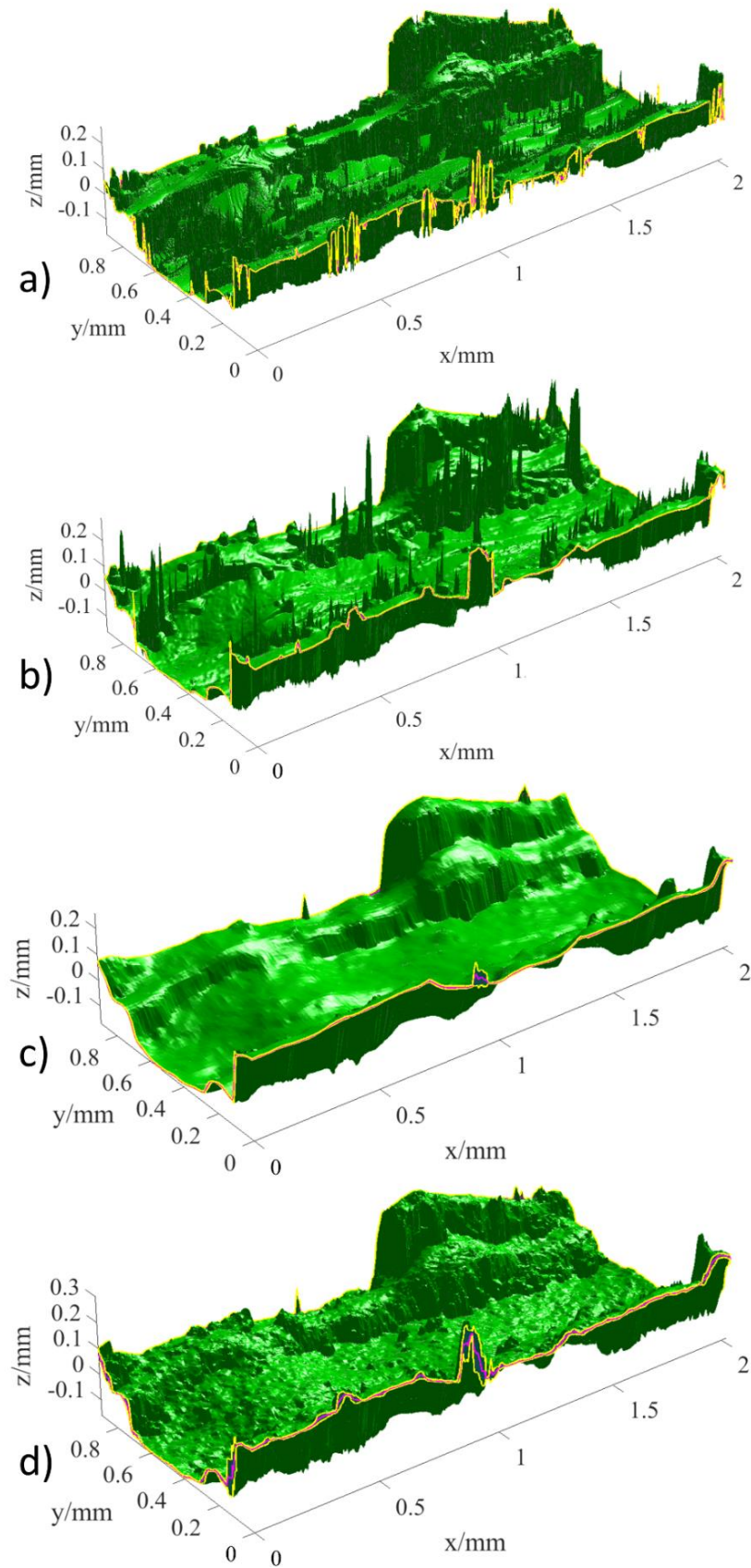
Figure 8.5. Statistical models of surface topography from each measurement setup; (a) CSI; (b) FV; (c) XCT (11×); (d) XCT (20×). Green surfaces and yellow lines represent the upper and lower bounds of CIs. Purple lines represent mean surfaces.
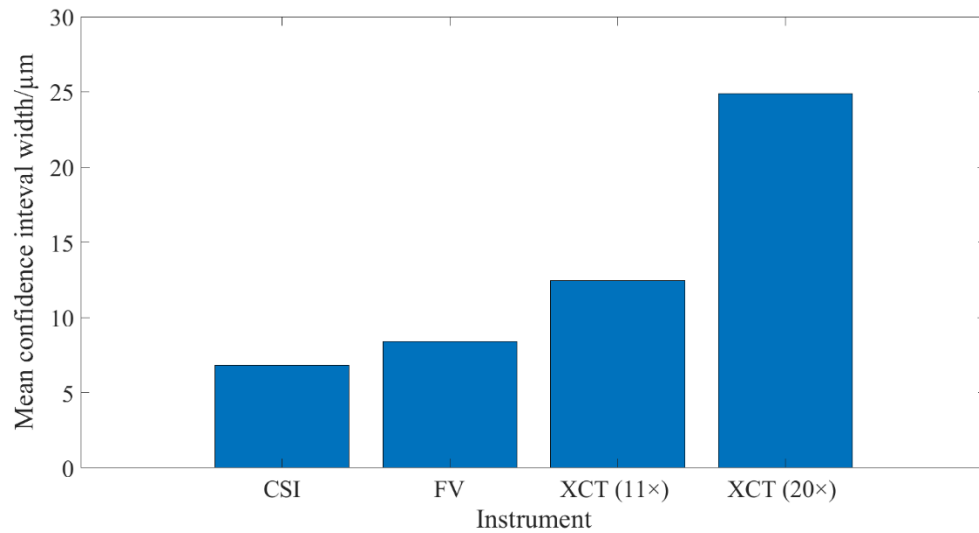
Figure 8.6. Mean CI width (i.e. repeatability error) of XCT measurement corresponding to each setup computed as the arithmetic average of the CI widths over the sample ROI.
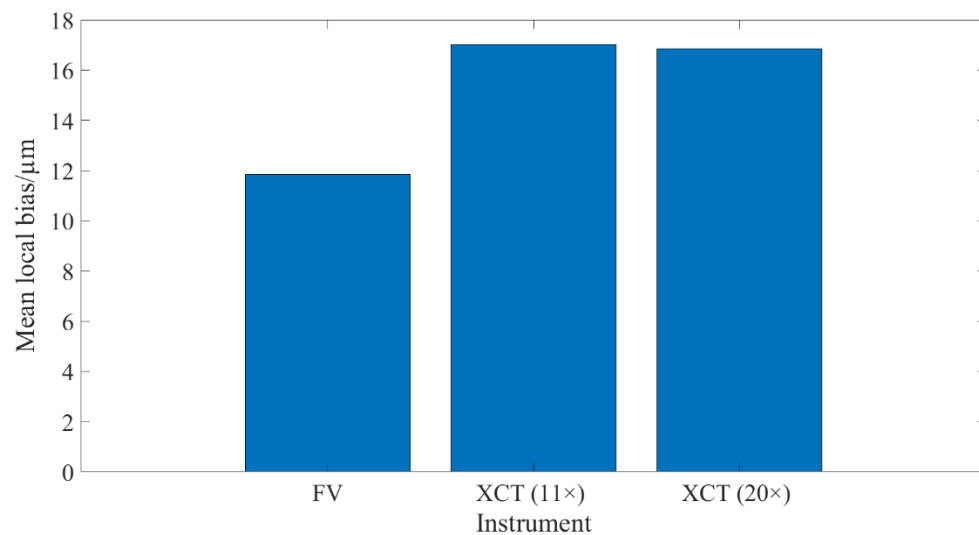
Figure 8.7. Arithmetic average of local bias in height determination when comparing FV and XCT measurement setups to the CSI setup.

8.4 Chapter discussion

It is clearly the case that for surfaces such as those present in this case study, computation of ISO 25178-2 [51] surface texture parameters for the purpose of data comparison is of minimal value in isolation. Parameters alone are capable of showing very little other than that they are often in general disagreement with one another; the reason for which is rarely apparent from examining only the parameters themselves. Additionally, in this particular case, the cylindrical

geometry of the internal cooling channels makes the generation of meaningful field parameters difficult. Parameter generation is difficult because the cylindrical geometry present in these channels makes a complex form removal process necessary, as ISO 25178-2 [51] parameter-based characterisation methods require data to be filtered so that the analysed surface represents a grid of deviations from a flat plane. Furthermore, the nominal channel diameter of 1 mm is problematic when generating parameters, as previous literature (see [106]), as well as the work performed throughout my PhD, suggests that an evaluation area of (2.5×2.5) mm is required to generate such parameters, and acquisition of an evaluation area this size is not possible for a channel only 1 mm in diameter. As such, when this knowledge is coupled with the complex cylindrical geometry and the associated potential difficulties in form removal, parameter results displayed in figure 8.4 clearly represent an inappropriate method of surface characterisation; at least when presented in isolation of other characterisation techniques. However, such an analysis remains common in both industry and academia, and so guidelines are clearly required to improve good practice across the board.

Following the results presented in Chapter 7, efforts were made during this case study to compensate for increases in CI width when XCT magnification is set at or above the point where part of the object being scanned lies outside of the measured field of view. These CI width increases were identified previously as resulting from out-of-field-of-view artefacts in the XCT data (e.g. streaking and shading in the reconstructed images [65,269,270]). Compensation was performed here by doubling the number of acquired projections, but as shown in figures 8.5 and 8.6, notable increases in CI width were still seen. However, there was a slightly lower mean local bias compared to the CSI reference in the higher magnification XCT setup than in the lower magnification setup. This result represents an improvement when compared to the results presented in Chapter 7, where mean local bias increased greatly when out-of-field–of-view artefacts were introduced. This improvement was most likely as a result of doubling the number of projections to compensate for the discontinuities between projections (see Section 8.1). Significant further work is clearly required to investigate the phenomena that occur when measuring the surfaces

226

of objects only partially inside the field of view, as methods for successfully avoiding the induced repeatability decrease reported, in this and the previous Chapter, are not yet clear. This investigation is of particular use in the measurement of metal AM surfaces, as high resolution XCT measurement of internal and otherwise difficult-to-access surfaces of parts significantly larger than the surface of interest is likely of particular interest to the AM community [59].

XCT data presented in this Chapter can be considered broadly comparable to data from optical methods, with each comparison method providing similar results for each measurement setup. Data were visually similar, and, despite the noted issues with parameter based comparisons, the magnitude of discrepancies between data acquired using the two optical methods and between these methods and the XCT measurement setups were comparable. XCT repeatability in parameter generation was generally poorer than in the established technology cases, but not by a large amount. Examination of CI plots and their associated metrics provides similar information, with repeatability for each measurement setup (i.e. mean CI widths) taking similar values for each instrument. The average discrepancies (i.e. mean local biases) also take similar values between two established techniques as between CSI and the two XCT setups.

The implication of these results is that, while discrepancies are present, it is possible to use XCT to measure the internal and difficult-to-access surfaces of an industrial part. If this method is to be employed in industry, however, there are a number of caveats and avenues for future research that should be considered. Particularly, until it is possible to establish a traceable reference for the acquired data, broad comparisons between measurement setups (such as these) must be used to draw conclusions about the viability of such measurements. However, the need for traceability in these industrial measurements is yet to be addressed, and the development of statistical methods for establishing traceability for any non-contact surface measurement technology remains an open question. The development of point-wise traceability (e.g. by using extensions of the statistical methods discussed throughout this Thesis) is of particular interest, as having uncertainties ascribed

to each *xyz* point in a surface dataset will allow the propagation of uncertainty into any metric derived from that dataset.

Until traceability is established, however, manufacturers wishing to use XCT for surface measurement must consider the metrics used for their specific cases and how these compare between datasets acquired using different systems. Without the understanding of measurement uncertainty provided by establishing traceability, comparisons between metrics may differ from those employed during the production of this Chapter (and indeed, this Thesis), and so similar comparisons must be made to understand how XCT systems used for specific measurement cases react to the production of such metrics. Through the work presented in this Chapter, however, I have demonstrated that results comparable to those generated by optical methods are achievable using XCT in an industrial case.

8.5 Chapter summary

In this Chapter, I applied methods developed throughout my PhD to an industrial test case, examining the applicability of the techniques used to the measurement of an industrially relevant part. This being a test case, sectioning of the part was possible, so XCT data could be compared to data acquired using optical methods. Results showed discrepancies between each measurement setup employed, but also that the average discrepancy between the two optical methods used was of similar magnitude to the discrepancy between two example XCT setups and the established methods.

I have also opened up a number of additional questions for avenues of future research, but these generally exist outside of the scope of this PhD. As such, in Chapter 9, I will summarise the conclusions and avenues of future work identified throughout this Thesis.

9. Summary, conclusions and future work

In this Chapter, I will summarise the findings of my PhD, in reference to the aims set out at the beginning of this Thesis. Primarily, the work performed during this PhD was to develop the use of X-ray computed tomography (XCT) for the measurement of surface topography, based on the outcomes of the literature review performed during the production of Chapter 2. During the review process, it became clear that there was a need for the verification of internal and difficult-to-access surfaces, and that XCT was a potential solution to this need. However, existing research into XCT surface measurement was preliminary, and scope existed for significant work in developing XCT surface measurement techniques. This aim was achieved by meeting the objectives discussed in Chapter 1, with the following contributions to science:

- Contribution 1: A review of the current state of the art in the combined use of XCT and AM
- Contribution 2: Development of a deep understanding of the features on a metal surface through the creation of an 'atlas' of metal AM surfaces.
- Contribution 3: Application of novel methods of data comparison for the investigation of surface topographies.
- Contribution 4: Development of novel procedures for the extraction of surfaces from XCT data;
- Contribution 5: Evaluation of the sensitivity of XCT systems to surface topography measurement.
- Contribution 6: Application of the methods developed during this work to an industrial case.

9.1.1 Contribution 1: state-of-the-art review

I began this Thesis with a review of the state of the art in the use of XCT for AM, and found a number of open research avenues. Particularly, I identified a requirement for new research regarding the texture present on AM surface, and in gaining a deeper understanding of the features present on the surfaces, as well

as how measurement instruments react to these features. Additionally, there also existed a lack of research regarding the use of XCT for the measurement of AM surfaces, though recent preliminary studies involving profile measurement using XCT implied that such measurement was likely to be possible. This work represents a contribution to the field, in the form of a summary review.

9.1.2   Contribution 2: a metal additive surface measurement atlas

The experimental work presented in this Thesis began with an examination of metal AM surfaces using various measuring instruments, with the objective of building an understanding of the features present on metal AM surfaces (see Chapter 4). Differences were noted in the way that surface measuring instruments reacted to these features, but at that stage of the research it was not clear how to quantify these discrepancies, and so further work was required to understand these features. The novelty of this preliminary experimental work lies in the development of an understanding of the features present on metal AM surfaces from a surface measurement perspective, with respect to different measurement technologies. While observations of these features had been made previously in other works, a comparative assessment of how different instruments react to these features had not previously been performed.

9.1.3   Contribution 3: direct comparison of surface topographies

In Chapter 5, I presented new methods of comparing surfaces, the first of which involved the computation of confidence intervals for profile datasets acquired using a number of different instruments. This quantitative comparison allowed for the visualisation of point-by-point repeatability for the analysed datasets and allowed the percentage global agreement and discrepancy between these datasets to be computed. In the latter part of Chapter 5, I presented work on how different measuring instruments react to a variety of specific features present on metal AM surfaces. During this work, it was particularly noted that discrepancies between measured points acquired using different instruments are often on the same order of magnitude as the size of the features themselves. Aside from the contribution to science represented by the quantification of

discrepancies between measurement instruments when measuring metal AM surfaces, this work was also the first application of these novel methods of surface data comparison.

9.1.4   Contribution 4: X-ray computed topography surface measurement in depth

In Chapter 6, I provided a more in-depth assessment of the capability of XCT for surface measurement, presenting data from two XCT systems and two optical surface measurement systems. I showed similarities between data acquired using these measurement systems using a number of common surface characterisation methodologies and highlighted some of the issues in XCT surface measurements. This in-depth capability assessment represents a novel contribution to science, in that the method presented for extracting and characterising surface data acquired using XCT is one of the first presentations of such a method.

9.1.5   Contribution 5: X-ray computed tomography surface measurement sensitivity

In Chapter 7, I elaborated on the findings presented in Chapter 6, by assessing some the effects of varying measurement setup parameters on the resulting surface datasets. The comparison techniques used in Chapter 7 also represented a development of those presented earlier in Chapter 5, extending the confidence interval model from 1.5D profile datasets to 2.5D surface datasets. In this work, the confidence interval comparison method was also reduced to two metrics that represented the data beyond the simple percentage discrepancy metric presented previously. Particularly, I generated a mean confidence interval width and mean local bias for each of the investigated measurement setups, respectively representing measurement repeatability and average discrepancy between two datasets. In terms of the contribution to science, the cases presented as part of this work represent examples of a new method of surface data comparison, which previously had generally involved only the comparison of ISO 25178-2 [51] parameters. These parameters were shown in this work to be insufficient

for the comparison of such data, and so these methods represent a novel tool for performing similar work in the future. This work also represents the first development of an understanding of how the two key measurement parameters (magnification and resolution) affect surface measurements made using XCT.

9.1.6   Contribution 6: X-ray computed tomography surface measurement in industry

Finally, in Chapter 8, I presented an industrial case study tying together the various aspects of this Thesis, employing XCT for the measurement of internal channel surfaces present in an industrially representative part. XCT was, for the first time, successfully used to measure internal surfaces by comparison of XCT data to optical methods, using the techniques discussed throughout this Thesis. This case study was performed in collaboration with my sponsor company, 3TRPD, who are a major UK-based additive manufacturer.

9.2 Overarching conclusions

A number of conclusions can be drawn from the work performed during my PhD. Primarily, I have demonstrated that is possible to acquire data using XCT for the purpose of performing assessments of surfaces. 'Surface assessments' here may take many different forms, the most common of which involves the generation of areal field and feature parameters (ISO 25178-2 [51] or otherwise). However, in an increasing number of applications further assessments are performed, such as customised characterisation techniques employed for functional surface assessments [209].

Furthermore, as part of my PhD, a series of comparison techniques have been developed to assess the ability of XCT to measure surfaces. These techniques allow for a more in-depth comparison than previously possible using existing characterisation methods. While these methods were developed for the comparison of data acquired relating specifically to complex metal AM surfaces, the methodology is by no means tied to these surfaces, and allows for the comparison of surface data acquired using any system or systems. These

methods will be of particular use during the development of novel surface measuring instruments, and are now available to instrument manufacturers (such as 3TRPD) and users for that purpose.

A rigorous assessment of the measurement parameters that affect XCT surface measurements has begun. Of particular note is the fact that increasing the scan magnification is not always a guaranteed method of achieving better data. On the contrary, increasing magnification can actually result in less repeatable results, that, when quantified, deviate further from similar results provided by established methods than lower magnification setups; a clear need for which was identified in Chapter 2. In addition, a second and highly valuable outcome of the work is a more thorough understanding of the future requirements for XCT surface measurement, and how these might be achieved. The characterisation of the sensitivity of XCT systems to surface measurements is an area of open research, which has hardly had its proverbial surface scratched during the course of this PhD.

9.3 Outline of future work

There are a number of broad areas of future research that result from the work presented in this Thesis, the most significant of which I will cover in this Section. These areas relate, respectively, to the development of data comparison methods used throughout this Thesis, the need for calibration of XCT systems, and the use of XCT for surface measurement, and how this technology may experience increased adoption for this purpose.

9.3.1   Development of data comparison methods

Firstly, I will address the existing research needs of the comparison methods presented here. At present, through the comparison of statistical models obtained from multiple instruments and/or setups, it is possible to capture local discrepancy and agreement, as well as to generate some of the other metrics used throughout this Thesis. However, at present, these statistical models cannot incorporate spatial correlation of height points, nor have they yet been used to

demonstrate point-by-point measurement uncertainty by comparison to a traceable reference. Future work is, therefore, required in order to develop such capability, as incorporation of uncertainties into the existing models will greatly broaden the scope and usefulness of these methods, allowing traceable measurements of complex surfaces using methods such as XCT. This work may entail using statistical topography models to estimate bias on low accuracy datasets with respect to higher accuracy references measurements. In the case where higher accuracy measurements are performed using a traceable instrument, it should be possible to establish traceability via this method. Specifically, it should be feasible to establish the confidence interval model for reference data acquired using traceable instruments (such as those based at national measurement institutes), which should in turn allow traceability to be extended to data acquired using non-traceable instruments.

9.3.2 Establishing traceability

On the topic of establishing traceability, it has become clear to me during this PhD that the primary barrier preventing the adoption of XCT as an established measurement technology is the lack of knowledge regarding calibration of the technology. The currently-under-development ISO 10360-11 [257] performance verification standard represents a strong intermediary step towards this outcome and should homogenise the structure of claims made by instrument manufacturers; thereby allowing users to make better informed choices regarding the appropriateness of an XCT system to their specific application. However, while, as a community, we are beginning to understand some of the measurement influence factors that will eventually allow calibration of an XCT system [278], the point where we will be able to perform such a calibration is not yet within reach. Much work is, therefore, required in understanding the XCT measurement influence factors and how they propagate through XCT measurement models.

9.3.3 Development of XCT surface measurement

Regarding the measurement of XCT surfaces, specifically, the development of the two areas outlined already will greatly contribute to the increased adoption of XCT as an established surface measurement technology. Eventually, it is likely that an XCT part of ISO 25178 [47] may be developed, in line with the other entries in the ISO 25178-60X series. As discussed throughout the latter half of this Thesis and elsewhere in this Chapter, the XCT influence factors should be investigated specifically in regards to the measurement of surfaces, as there are likely specific effects related to resolving ever-smaller features that may not have as significant an impact on form measurement using XCT. The other issue most specifically relating to XCT surface measurement that has not yet been addressed is the 3D nature of XCT data. Throughout the comparisons performed in this Thesis, 3D XCT data have been converted to 2.5D height maps by removal of undercuts in order to perform comparisons between XCT data and data acquired using intrinsically 2.5D measurement systems. While this action is required in order to facilitate such comparisons, it essentially amounts to throwing away a likely significant portion of useful information about the surface of interest, which can be generally considered counter-productive when one wishes to maximise the knowledge generated by performing a measurement. At present, because the standards were developed for 2.5D datasets, the mathematics used to generate parameters, such as those described by ISO 25178-2 [51], are not capable of handling the undercuts and re-entrant features common in XCT data (i.e. where there is more than one z point for some of the xy points). As such, a full redesign of these parameters is required in order to utilise this lost information. Such work has begun [197], but again, is far from standardisation.

9.3.4 Development of transparent software

Arguably the most significant issue regarding XCT surface measurement to arise from the work presented in this Thesis is the constant problem of 'black-box' instruments and software, currently employed throughout the measurement process. While these black boxes are a current necessity in the

absence of well-understood, open-source methods, work must be performed in developing such open-source techniques for the extraction and characterisation of surface data acquired using XCT. While characterisation methods for data alignment and conversion between 3D and 2.5D datasets have been developed and used throughout this Thesis, there still exist some notable black-boxes during the measurement process, particularly relating to the determination of surfaces on reconstructed XCT data. The VGStudio MAX [73] gradient-based algorithm is currently accepted by the XCT community as the most appropriate surface determination algorithm for performing metrological XCT [58], but a lack of understanding of how this algorithm operates is a fundamental flaw in the surface measurement process. While this algorithm may well provide reliable results in distance measurement of macro-scale features, when performing surface measurement of micro-scale features we do not yet fully understand how this algorithm (and the inevitable errors in surface determination it causes) impact the surfaces being measured. As such, a fully rigorous study into surface determination techniques is required, with respect to how AM surfaces (and indeed surfaces in general) are affected by different surface determination algorithms.

9.4 Industrial impact

There are a number of notable outcomes for industry that stem from the work presented in this Thesis. Primarily, through the methods presented in Chapters 4 to 8, I have shown that measurement of surfaces using XCT is possible for the types of surfaces used as test cases here; particularly metal AM surfaces where $Sa > 1$ μm, present on samples that can be penetrated using X-rays generated by state-of-the-art commercial systems (e.g. a cube of Ti6Al4V < 20 mm $\times$ 20 mm $\times$ 20 mm in size). Measurement of smoother samples is yet to be investigated, and successful measurement of larger samples or less X-ray penetrable materials has not yet been performed. Because of the levels of noise present in XCT surface measurements (as seen in the work presented here), such measurements are likely to be impossible until the state of the art in XCT measurement improves. Measurement of samples is possible at a range of X-

ray magnifications, though magnifications > 10× are likely to provide results that are most closely comparable to measurements made using optical systems.

Additionally, novel methods of data comparison have been presented here that will be of use in industrial cases, for determination of appropriate measurement technologies for specific applications, or for validation of new measurement instruments. These techniques have been demonstrated in the case of complex metal AM surface measurement by established and new systems, but methods are surface and scale independent. As such, these methods can be applied to a large variety of industrial cases in metrology, but also extending, for example, to measurement of topography in a geographical context.

9.5 Final remarks

In this Chapter, I have summarised the general findings of my PhD, and presented the resulting requirements for future work within the metrology for AM community. The results presented throughout this Thesis imply that XCT presents a potentially useful method for assessment of internal and difficult-to-access surfaces, which until recently was not considered possible. As long as it remains the case that these assessments are considered by industry to be impossible, a constraint is imposed on the design community, preventing the use of functional internal and difficult-to-access surfaces in parts. Establishing the methods presented here in industry will help to lift this constraint, and so expand the design freedom afforded to AM technologies in high value manufacture.

References

[1] Thompson A, Maskery I and Leach R K 2016 X-ray computed tomography for additive manufacturing: a review *Meas. Sci. Technol.* **27** 072001

[2] Thompson A and Leach R K 2017 Introduction to industrial X-ray computed tomography *Industrial X-ray computed tomography* ed Carmignato S, Dewulf W and Leach R K (New York, USA: Springer) pp 1–23

[3] ISO/ASTM 52900:2015 Additive manufacturing -- General principles – terminology (International Organisation for Standardisation)

[4] Gibson I, Rosen D W and Stucker B 2010 *Additive manufacturing technologies: 3D printing, rapid prototyping, and direct digital manufacturing* (New York, USA: Springer)

[5] Baumers M 2012 *Economic aspects of additive manufacturing: benefits, costs and energy consumption* (Loughborough, UK: University of Loughborough)

[6] ASTM F2792-12a:2012 Standard terminology for additive manufacturing technologies (ASTM International)

[7] Sachs E, Wylonis E, Allen S, Cima M, Gu H and Guo H 2000 Production of injection molding tooling with conformal cooling channels using the three dimensional printing process *Polym. Eng. Sci.* **40** 1232–1247

[8] Parry L, Ashcroft I A and Wildman R D 2016 Understanding the effect of laser scan strategy on residual stress in selective laser melting through thermo-mechanical simulation *Addit. Manuf.* **12** 1–15

[9] Townsend A, Senin N, Blunt L, Leach R K and Taylor J S 2016 Surface texture metrology for metal additive manufacturing: a review *Precis. Eng.* **46** 34–47

[10] Zhang S J, To S, Wang S J and Zhu Z W 2015 A review of surface roughness generation in ultra-precision machining *Int. J. Mach. Tools Manuf.* **91** 76–95

[11] Vaezi M, Seitz H and Yang S 2013 A review on 3D micro-additive manufacturing technologies *Int. J. Adv. Manuf. Technol.* **67** 1721–1754

[12]   Wijshoff H 2010 The dynamics of the piezo inkjet printhead operation *Phys. Rep.* **491** 77–177

[13]   Ameta G, Lipman R, Moylan S and Witherell P 2015 Investigating the Role of Geometric Dimensioning and Tolerancing in Additive Manufacturing *J. Mech. Des.* **137** 111401

[14]   Leach R K 2016 Metrology for additive manufacturing *Meas. + Control* **49** 132–135

[15]   Stavroulakis P I and Leach R K 2016 Review of post-process optical form metrology for industrial-grade metal additive manufactured parts *Rev. Sci. Instrum.* **87** 041101

[16]   Campbell I, Bourell D and Gibson I 2012 Additive manufacturing: rapid prototyping comes of age *Rapid Prototyp. J.* **18** 255–258

[17]   Frazier W E 2014 Metal additive manufacturing: a review *J. Mater. Eng. Perform.* **23** 1917–1928

[18]   Gibson I, Rosen D W and Stucker B 2010 Powder bed fusion processes In: *Additive manufacturing technologies: 3D printing, rapid prototyping, and direct digital manufacturing* (New York, USA: Springer) pp 103–142

[19]   BIPM 2012 *International Vocabulary of Metrology – Basic and General Concepts and Associated Terms (VIM 3rd edition)* (Paris, France: Bureau International des Poids et Mesures)

[20]   BIPM 2006 *Le Système International d'Unités* (Paris, France: Bureau International des Poids et Mesures)

[21]   Leach R K 2014 *Fundamental principles of engineering nanometrology* (Oxford, UK: Elsevier)

[22]   BIPM 2008 Evaluation of measurement data — Guide to the expression of uncertainty in measurement (Paris, France: Bureau International des Poids et Mesures)

[23]   Leach R K and Smith S T 2018 *Basics of precision engineering* (Boca Raton, USA: CRC Press)

[24]   Ferrucci M, Haitjema H and Leach R K 2018 Dimensional metrology In *Basics of precision engineering* (Boca Raton, USA: CRC Press) pp 151–204

[25]   Everton S K, Hirsch M, Stavroulakis P, Leach R K and Clare A T 2016

Review of in-situ process monitoring and in-situ metrology for metal additive manufacturing *Mater. Des.* **95** 431–445

[26] Grasso M and Colosimo B M 2017 Process defects and in situ monitoring methods in metal powder bed fusion: A review *Meas. Sci. Technol.* **28** 044005

[27] Flack D, Claverly J and Leach R K 2014 Coordinate Metrology *Fundamental principles of engineering nanometrology* (Oxford, UK: Elsevier) pp 295–325

[28] ISO 10360–X:2000 Geometrical product specifications (GPS) -- Acceptance and reverification tests for coordinate measuring systems (CMS) (International Organisation for Standardisation)

[29] Leach R K 2014 Surface topography measurement instrumentation In: *Fundamental principles of engineering nanometrology* (Oxford, UK: Elsevier) pp 115–175

[30] Leach R K 2013 *Characterisation of areal surface texture* (Berlin, Germany: Springer)

[31] ISO 25178–601:2010 Geometrical product specifications (GPS) -- Surface texture: areal -- Part 601: nominal characteristics of contact (stylus) instruments (International Organisation for Standardisation)

[32] Leach R K 2011 *Optical measurement of surface topography* (Berlin, Germany: Springer)

[33] Rayleigh, Lord 1879 Investigations in optics, with special reference to the spectroscope *Philos. Mag.* **8** 261–274

[34] Sparrow C M 1916 On spectroscopic resolving power *Astrophys. J.* **44** 76–86

[35] ISO 25178–607 Geometrical product specifications (GPS) -- Surface texture: areal -- Part 607: nominal characteristics of non-contact (confocal microscopy) instruments (International Organisation for Standardisation)

[36] Artigas R 2011 Imaging confocal microscopy In: *Optical measurement of surface topography* ed Leach R K (Berlin, Germany: Springer) pp 237–286

[37] ISO 2010 25178–602:Under development Geometrical product specifications (GPS) -- Surface texture: areal -- Part 602: nominal

characteristics of non-contact (confocal chromatic probe) instruments (International Organisation for Standardisation)

[38]   Blateyron F 2011 Chromatic confocal microscopy, In: *Optical measurement of surface topography* ed Leach R K (Berlin, Germany: Springer) pp 171–106

[39]   ISO 25178–605:2014 Geometrical product specifications (GPS) -- Surface texture: areal -- Part 605: nominal characteristics of non-contact (point autofocus probe) instruments instruments (International Organisation for Standardisation)

[40]   Miura K and Nose A 2011 Point autofocus instruments, In: *Optical measurement of surface topography* ed Leach R K (Berlin, Germany: Springer) pp 107–130

[41]   ISO 25178–604:2013 Geometrical product specifications (GPS) -- Surface texture: areal -- Part 604: nominal characteristics of non-contact (coherence scanning interferometry) instruments (International Organisation for Standardisation)

[42]   de Groot P 2011 Coherence scanning interferometry In: *Optical measurement of surface topography* ed Leach R K (Berlin, Germany: Springer) pp 187–208

[43]   ISO 25178–603:2013 Geometrical product specifications (GPS) -- Surface texture: areal -- Part 603: nominal characteristics of non-contact (phase-shifting interferometric microscopy) instruments (International Organisation for Standardisation)

[44]   de Groot P 2011 Phase shifting interferometry In: *Optical measurement of surface topography* ed Leach R K (Berlin, Germany: Springer) pp 167–186

[45]   ISO 25178–606:2015 Geometrical product specifications (GPS) -- Surface texture: areal -- Part 606: nominal characteristics of non-contact (focus variation) instruments (International Organisation for Standardisation)

[46]   Helmli F 2011 Focus variation instruments In: *Optical measurement of surface topography* ed Leach R K (Berlin, Germany: Springer) pp 131–166

[47]   ISO 25178:2017 Geometrical product specifications (GPS) -- Surface

texture: areal (International Organisation for Standardisation)

[48] Leach R, Leigh Brown X J, Blunt R and Mike Conroy D M 2008 Good practice guide no. 108 Guide for the Measurement of Smooth Surface Topography using Coherence Scanning Interferometry (London, UK: National Physical Laboratory)

[49] Gomez C, Su R, Thompson A, DiSciacca J, Lawes S and Leach R K 2017 Optimisation of surface measurement for metal additive manufacturing using coherence scanning interferometry *Opt. Eng.* **56** 111714

[50] ISO 4287:1997 Geometrical product specifications (GPS) -- Surface texture: profile method -- Terms, definitions and surface texture parameters (International Organisation for Standardisation)

[51] ISO 25178–2:2012 Geometrical product specifications (GPS) -- Surface texture: areal -- Part 2: terms, definitions and surface texture parameters (International Organisation for Standardisation)

[52] Leach R K 2014 Surface topography characterisation In: *Fundamental principles of engineering nanometrology* ed Leach R K (Oxford, UK: Elsevier) pp 241–291

[53] Leach R K 2001 Good practice guide no. 37 The measurement of surface texture using stylus instruments (London, UK: National Physical Laboratory)

[54] Auld B A and Moulder J C 1999 Review of advances in eddy current nondestructive evaluation *J. Nondestruct. Eval.* **18** 3–36

[55] Drinkwater B W and Wilcox P D 2006 Ultrasonic arrays for non-destructive evaluation: A review *NDT&E Int.* **39** 525–41

[56] Carmignato S, Dewulf W and Leach R K 2017 *Industrial X-ray computed tomography* (New York, USA: Springer)

[57] Kruth J-P P, Bartscher M, Carmignato S, Schmitt R, De Chiffre L and Weckenmann A 2011 Computed tomography for dimensional metrology *Ann. CIRP* **60** 821–842

[58] De Chiffre L, Carmignato S, Kruth J-P P J-P, Schmitt R and Weckenmann A 2014 Industrial applications of computed tomography *Ann. CIRP* **63** 655–677

[59] du Plessis A, Yadroitsev I, Yadroitsava I and le Roux S 2018 X-ray

micro computed tomography in additive manufacturing: a review of the current technology and applications *3D Print. Addit. Manuf.* **5** 227–246

[60] Scott A E, Mavrogordato M, Wright P, Sinclair I and Spearing S M 2011 In situ fibre fracture measurement in carbon-epoxy laminates using high resolution computed tomography *Compos. Sci. Technol.* **71** 1471–1477

[61] Hermanek P, Sing J, Rathore, Aloisi V and Carmignato S 2017 Principles of X-ray computed tomography In: *Industrial X-ray computed tomography* ed Carmignato S, Dewulf W and Leach R K (New York, USA: Springer) pp 25–68

[62] Hsieh J 2009 *Computed tomography: principles, design, artifacts, and recent advances* (Bellingham, USA: SPIE Press)

[63] Flay N 2016 *An investigation of the factors associated with the x-ray tube and their influence on dimensional measurement in micro-focus cone-beam industrial x-ray computed tomography systems* (Southampton, UK: University of Southampton)

[64] Dewulf W, Tan Y and Kiekens K 2012 Sense and non-sense of beam hardening correction in CT metrology *Ann. CIRP* **61** 495–498

[65] Tofts P S and Gore J C 1980 Some sources of artefact in computed tomography *Phys. Med. Biol.* **25** 117–127

[66] Feldkamp L A, Davis L C and Kress J W 1984 Practical cone-beam algorithm *J. Opt. Soc. Am. A* **1** 612–619

[67] Hsieh J 2009 Image reconstruction In: *Computed tomography: principles, design, artifacts, and recent advances* (Bellingham, USA: SPIE Press) pp 55–118

[68] Radon J 1986 On the determination of functions from their integral values along certain manifolds *IEEE Trans. Med. Imaging* **5** 170–6

[69] Lifton J J 2015 *The influence of scatter and beam hardening in X-ray computed tomography for dimensional metrology* (Southampton, UK: University of Southampton)

[70] Bartscher M, Staude A, Ehrig K and Ramsey A 2012 The influence of data filtering on dimensional measurements with CT *18th world conference on nondestructive testing* pp 16–20

[71] Lifton J J, Malcolm A A and McBride J W 2015 On the uncertainty of surface determination in x-ray computed tomography for dimensional

metrology *Meas. Sci. Technol.* **26** 35003

[72]   Ding L and Goshtasby A 2001 On the canny edge detector *Pattern Recognit.* **34** 721–725

[73]   Volume Graphics 2018 VGStudio MAX (Available at https://www.volumegraphics.com/en/products/vgstudio-max.html) Accessed: 19th September 2018

[74]   Lewandowski J J and Seifi M 2016 Metal additive manufacturing: a review of mechanical properties *Annu. Rev. Mater. Res* **46** 151–186

[75]   Sing S L, An J, Yeong W Y and Wiria F E 2016 Laser and electron-beam powder-bed additive manufacturing of metallic implants: a review on processes, materials and designs *J. Orthop. Res.* **34** 369–385

[76]   Bikas H, Stavropoulos P and Chryssolouris G 2016 Additive manufacturing methods and modelling approaches: a critical review *Int. J. Adv. Manuf. Technol.* **83** 389–405

[77]   Gao W, Zhang Y, Ramanujan D, Ramani K, Chen Y, Williams C B, Wang C C L, Shin Y C, Zhang S and Zavattieri P D 2015 The status, challenges, and future of additive manufacturing in engineering *Comput. Des.* **69** 65–89

[78]   ISO/TC 213:1996 Dimensional and geometrical product specifications and verification (International Organisation for Standardisation)

[79]   ISO 3534–2:1993 Statistics - vocabulary and symbols - part 2: statistical quality control (International Organisation for Standardisation)

[80]   Sun W, Brown S B and Leach R K 2012 *An overview of industrial x-ray computed tomography* (London, UK: National Physical Laboratory)

[81]   Mankovich N J, Cheeseman A M and Stoker N G 1990 The display of three-dimensional anatomy with stereolithographic models *J. Digit. Imaging* **3** 200–203

[82]   Marro A, Bandukwala T and Mak W 2016 Three-dimensional printing and medical imaging: a review of the methods and Applications *Curr. Probl. Diagn. Radiol.* **45** 2–9

[83]   Ashley S 1993 Rapid prototyping for artificial body parts *Mech. Eng.* **115** 50–53

[84]   Berry E, Brown J M, Connell M, Craven C M, Efford N D, Radjenovic A and Smith M A 1997 Preliminary experience with medical

applications of rapid prototyping by selective laser sintering *Med. Eng. Phys.* **19** 90–6

[85]   Jamieson R and Hacker H 1995 Direct slicing of CAD models for rapid prototyping *Rapid Prototyp. J.* **1** 4–12

[86]   Losano F, Marinsek G, Merlo A A M and Ricci M 1999 Computed tomography in the automotive field. Development of a new engine head case study *Computerized tomography for industrial applications and image processing in radiology* (Berlin, Germany) pp 65–73

[87]   Taud H, Martinez-Angeles R, Parrot J F and Hernandez-Escobedo L 2005 Porosity estimation method by X-ray computed tomography *J. Pet. Sci. Eng.* **47** 209–217

[88]   Hildebrand T and Rüegsegger P 1997 A new method for the model-independent assessment of thickness in three-dimensional images *J. Microsc.* **185** 67–75

[89]   Heinl P, Müller L, Körner C, Singer R F and Müller F A 2008 Cellular Ti–6Al–4V structures with interconnected macro porosity for bone implants fabricated by selective electron beam melting *Acta Biomater.* **4** 1536–1544

[90]   Heinl P, Korner C and Singer R F 2008 Selective electron beam melting of cellular titanium: mechanical properties *Adv. Eng. Mater.* **10** 882–888

[91]   Kerckhofs G, Schrooten J, Elicegui L, Van Bael S, Moesen M, Lomov S V and Wevers M 2008 Mechanical characterization of porous structures by the combined use of micro-CT and in-situ loading *17th World conference on non-destructive testing (WCNDT)* (Shanghai, China)

[92]   Lopez-Heredia M A, Sohier J, Gaillard C, Quillard S, Dorget M and Layrolle P 2008 Rapid prototyped porous titanium coated with calcium phosphate as a scaffold for bone tissue engineering *Biomaterials* **29** 2608–2615

[93]   Ryan G E, Pandit A S and Apatsidis D P 2008 Porous titanium scaffolds fabricated using a rapid prototyping and powder metallurgy technique *Biomaterials* **29** 3625–3635

[94]   Ibrahim D, Broilo T L, Heitz C, de Oliveira M G, de Oliveira H W, Nobre S M W, dos Santos Filho J H G and Silva D N 2009 Dimensional

error of selective laser sintering, three-dimensional printing and PolyJet™ models in the reproduction of mandibular anatomy *J. Cranio-Maxillo-Facial Surg.* **37** 167–173

[95] Ryan G, McGarry P, Pandit A and Apatsidis D 2009 Analysis of the mechanical behavior of a titanium scaffold with a repeating unit-cell substructure *J. Biomed. Mater. Res. Part B Appl. Biomater.* **90** 894–906

[96] Eshraghi S and Das S 2010 Mechanical and microstructural properties of polycaprolactone scaffolds with one-dimensional, two-dimensional, and three-dimensional orthogonally oriented porous architectures produced by selective laser sintering *Acta Biomater.* **6** 2467–2476

[97] Kerckhofs G, Pyka G, Loeckx D, Van Bael S, Schrooten J and Wevers M 2010 The combined use of micro-CT imaging, in-situ loading and non-rigid image registration for 3D experimental local strain mapping on porous bone tissue engineering scaffolds under compressive loading *Proc. European conference for non-destructive testing (ECNDT)* (Moscow, Russia)

[98] UK Additive Manufacturing Steering Group 2016 *Additive Manufacturing UK September 2016 strategy update* (London, UK: UK Additive Manufacturing Steering Group)

[99] Townsend A, Pagani L, Scott P and Blunt L A 2017 Areal surface texture data extraction from x-ray computed tomography reconstructions of metal additively manufactured parts *Precis. Eng.* **48** 254–264

[100] Spierings A B, Starr T L and Wegener K 2013 Fatigue performance of additive manufactured metallic parts *Rapid Prototyp. J.* **19** 88–94

[101] Xu Z, Hyde C J, Thompson A, Leach R K, Maskery I, Tuck C and Clare A T 2017 Staged thermomechanical testing of nickel superalloys produced by selective laser melting *Mater. Des.* **133** 520–527

[102] Thompson A, Senin N, Maskery I, Körner L, Lawes S and Leach R K 2018 Internal surface measurement of metal powder bed fusion parts *Addit. Manuf.* **20** 126–133

[103] Matthews M J, Guss G, Khairallah S A, Rubenchik A M, Depond P J and King W E 2016 Denudation of metal powder layers in laser powder bed fusion processes *Acta Mater.* **114** 33–42

[104] Tuck C and Blunt L 2016 Special issue collection on additive manufacturing (AM) *Surf. Topogr.: Metrol. Prop.* **4** 020201

[105] Hong M-H, Min B and Kwon T-Y 2016 The influence of process parameters on the surface roughness of a 3D-printed Co–Cr dental alloy produced via selective laser melting *Appl. Sci.* **6** 401

[106] Triantaphyllou A, Giusca C L, Macaulay G D, Roerig F, Hoebel M, Leach R K, Tomita B and Milne K A 2015 Surface texture measurement for additive manufacturing *Surf. Topogr.: Metrol. Prop.* **3** 24002

[107] Grimm T, Wiora G and Witt G 2015 Characterization of typical surface effects in additive manufacturing with confocal microscopy *Surf. Topogr.: Metrol. Prop.* **3** 014001

[108] Safdar A, He H Z, Wei L-Y, Snis A and Chavez de Paz L E 2012 Effect of process parameters settings and thickness on surface roughness of EBM produced Ti-6Al-4V *Rapid Prototyp. J.* **18** 401–408

[109] Thompson A, McNally D, Maskery I and Leach R K 2017 X-ray computed tomography and additive manufacturing in medicine: a review *Int. J. Metrol. Qual. Eng.* **8** 17

[110] Duan B, Wang M, Zhou W Y, Cheung W L, Li Z Y and Lu W W 2010 Three-dimensional nanocomposite scaffolds fabricated via selective laser sintering for bone tissue engineering *Acta Biomater.* **6** 4495–44505

[111] Rüsenberg S, Schmidt L and Schmid H-J 2011 Mechanical and physical properties – a way to assess quality of laser sintered parts *Solid freeform fabrication symposium* (Austin, USA: University of Texas Austin) pp 239–51

[112] Leuders S, Thöne M, Riemer A, Niendorf T, Tröster T, Richard H A and Maier H J 2013 On the mechanical behaviour of titanium alloy TiAl6V4 manufactured by selective laser melting: fatigue resistance and crack growth performance *Int. J. Fatigue* **48** 300–307

[113] Van Bael S, Desmet T, Chai Y C, Pyka G, Dubruel P, Kruth J-P P and Schrooten J 2013 In vitro cell-biological performance and structural characterization of selective laser sintered and plasma surface functionalized polycaprolactone scaffolds for bone regeneration *Mater. Sci. Eng. C* **33** 3404–3412

[114] Ghita O R, James E, Trimble R and Evans K E 2014 Physico-chemical

behaviour of poly (ether ketone)(PEK) in high temperature laser sintering (HT-LS) *J. Mater. Process. Technol.* **214** 969–978

[115] Rouholamin D and Hopkinson N 2014 An investigation on the suitability of micro-computed tomography as a non-destructive technique to assess the morphology of laser sintered nylon 12 parts *Proc. Inst. Mech. Eng. Part B J. Eng. Manuf.* **228** 1529–1542

[116] Ziółkowski G, Chlebus E, Szymczyk P and Kurzac J 2014 Application of x-ray CT method for discontinuity and porosity detection in 316L stainless steel parts produced with SLM technology *Arch. Civ. Mech. Eng.* **14** 608–614

[117] Spierings A B, Schneider M and Eggenberger R 2011 Comparison of density measurement techniques for additive manufactured metallic parts *Rapid Prototyp. J.* **17** 380–386

[118] Van Bael S, Kerckhofs G, Moesen M, Pyka G, Schrooten J, Kruth. J-P and Kruth J P 2011 Micro-CT-based improvement of geometrical and mechanical controllability of selective laser melted Ti6Al4V porous structures *Mater. Sci. Eng. A* **528** 7423–7431

[119] Dadbakhsh S and Hao L 2012 Effect of Al alloys on selective laser melting behaviour and microstructure of in situ formed particle reinforced composites *J. Alloys Compd.* **541** 328–334

[120] Dupin S, Lame O, Barrès C and Charmeau J-Y 2012 Microstructural origin of physical and mechanical properties of polyamide 12 processed by laser sintering *Eur. Polym. J.* **48** 1611–1621

[121] Pyka G, Burakowski A, Kerckhofs G, Moesen M, Van Bael S, Schrooten J and Wevers M 2012 Surface modification of Ti6Al4V open porous structures produced by additive manufacturing *Adv. Eng. Mater.* **14** 363–370

[122] Truscello S, Kerckhofs G, Van Bael S, Pyka G, Schrooten J and Van Oosterwyck H 2012 Prediction of permeability of regular scaffolds for skeletal tissue engineering: a combined computational and experimental study *Acta Biomater.* **8** 1648–1658

[123] Van Bael S, Chai Y C, Truscello S, Moesen M, Kerckhofs G, Van Oosterwyck H, Kruth J-P P and Schrooten J 2012 The effect of pore geometry on the in vitro biological behavior of human periosteum-

derived cells seeded on selective laser-melted Ti6Al4V bone scaffolds *Acta Biomater.* **8** 2824–2834

[124] Yavari S A, Wauthlé R, van der Stok J, Riemslag A C, Janssen M, Mulier M, Kruth J-P, Schrooten J, Weinans H and Zadpoor A A 2013 Fatigue behavior of porous biomaterials manufactured using selective laser melting *Mater. Sci. Eng. C* **33** 4849–4858

[125] Hrabe N W, Heinl P, Flinn B, Körner C and Bordia R K 2011 Compression-compression fatigue of selective electron beam melted cellular titanium (Ti-6Al-4V) *J. Biomed. Mater. Res. Part B.* **99** 313–320

[126] Attar H, Calin M, Zhang L C, Scudino S and Eckert J 2014 Manufacture by selective laser melting and mechanical behavior of commercially pure titanium *Mater. Sci. Eng. A* **593** 170–177

[127] Zarringhalam H, Hopkinson N, Kamperman N F and De Vlieger J J 2006 Effects of processing on microstructure and properties of SLS nylon 12 *Mater. Sci. Eng. A* **435** 172–180

[128] Gogolewski S, Czerntawska K and Gastorek M 1980 Effect of annealing on thermal properties and crystalline structure of polyamides. Nylon 12 (polylaurolactam) *Colloid Polym. Sci.* **258** 1130–1136

[129] Léonard F, Tammas-Wiliams S, Prangnell P B, Todd I and Withers P J 2012 Assessment by x-ray CT of the effects of geometry and build direction on defects in titanium ALM parts *Conference on industrial computed tomography (iCT)* (Wels, Austria) pp 85–93

[130] Yan C, Hao L, Hussein A and Raymont D 2012 Evaluations of cellular lattice structures manufactured using selective laser melting *Int. J. Mach. Tools Manuf.* **62** 32–38

[131] Xia Y, Zhou P Y, Cheng X S, Xie Y, Liang C, Li C and Xu S G 2013 Selective laser sintering fabrication of nano-hydroxyapatite/poly-ε-caprolactone scaffolds for bone tissue engineering applications *Int. J. Nanomedicine* **8** 4197–4273

[132] Fukuda A, Takemoto M, Saito T, Fujibayashi S, Neo M, Pattanayak D K, Matsushita T, Sasaki K, Nishida N and Kokubo T 2011 Osteoinduction of porous Ti implants with a channel structure fabricated by selective laser melting *Acta Biomater.* **7** 2327–2336

[133] Van der Stok J, Van der Jagt O P, Amin Yavari S, De Haas M F P, Waarsing J H, Jahr H, Van Lieshout E M M, Patka P, Verhaar J A N, Zadpoor A A and Weinans H 2013 Selective laser melting-produced porous titanium scaffolds regenerate bone in critical size cortical bone defects *J. Orthop. Res.* **31** 792–799

[134] Pyka G, Kerckhofs G, Braem A, Mattheys T, Schrooten J and Wevers M 2010 Novel micro-ct based characterization tool for surface roughness measurements of porous structures *SkyScan User Meeting* (Mechelen, Belgium) pp 1–5

[135] Kerckhofs G, Pyka G, Moesen M, Van Bael S, Schrooten J and Wevers M 2013 High-resolution microfocus x-ray computed tomography for 3D surface roughness measurements of additive manufactured porous materials *Adv. Eng. Mater.* **15** 153–158

[136] Pyka G, Kerckhofs G, Papantoniou I, Speirs M, Schrooten J and Wevers M 2013 Surface roughness and morphology customization of additive manufactured open porous Ti6Al4V structures *Materials* **6** 4737–4757

[137] Carmignato S, Pierobon A, Rampazzo P, Parisatto M and Savio E 2012 CT for industrial metrology-accuracy and structural resolution of CT dimensional measurements *Conference on industrial computed tomography (iCT)* (Wels, Austria) pp 161–172

[138] Carmignato S 2012 Accuracy of industrial computed tomography measurements: experimental results from an international comparison *Ann. CIRP* **61** 491–494

[139] Kiekens K, Welkenhuyzen F, Tan Y, Bleys P, Voet A, Kruth J-P and Dewulf W 2011 A test object with parallel grooves for calibration and accuracy assessment of industrial computed tomography (CT) metrology *Meas. Sci. Technol.* **22** 115502

[140] Moylan S, Slotwinski J, Cooke A, Jurrens K, Donmez M A and Donmez A 2012 Proposal for a standardized test artifact for additive manufacturing machines and processes *Solid freeform fabrication symposium* (Austin, USA) pp 6–8

[141] Laycock S D, Bell G D, Corps N, Mortimore D B, Cox G, May S and Finkel I 2015 Using a combination of micro-computed tomography, CAD and 3D printing techniques to reconstruct incomplete 19th-century

Cantonese chess pieces *J. Comput. Cult. Herit.* **7** 25

[142] Howe R, Shahbazmohamadi S, Bass R and Singh P 2014 Digital evaluation and replication of period wind instruments: the role of micro-computed tomography and additive manufacturing *Early Music* **42** 529–536

[143] Ishida N and Kishimoto N 2015 Three-dimensional imaging of the Jurassic radiolarian Protunuma? ochiensis Matsuoka: an experimental study using high-resolution x-ray micro-computed tomography *Vol. Jurassica* **13** 77–82

[144] Henson K D 2015 *Stories in bone still told: digitization and replication of the clover Site, fort ancient human remains* (Huntington, USA: Marshall University)

[145] Appleby J, Mitchell P D, Robinson C, Brough A, Rutty G, Harris R A, Thompson D and Morgan B 2014 The scoliosis of Richard III, last Plantagenet King of England: diagnosis and clinical significance *Lancet* **383** 1944

[146] Cox S C, Thornby J A, Gibbons G J, Williams M A and Mallick K K 2015 3D printing of porous hydroxyapatite scaffolds intended for use in bone tissue engineering applications *Mater. Sci. Eng. C* **47** 237–247

[147] Ziegelmeier S, Christou P, Wöllecke F, Tuck C, Goodridge R, Hague R, Krampe E and Wintermantel E 2015 An experimental study into the effects of bulk and flow behaviour of laser sintering polymer powders on resulting part properties *J. Mater. Process. Technol.* **215** 239–250

[148] Carlton H D, Haboub A, Gallegos G F, Parkinson D Y and MacDowell A A 2015 Damage evolution and failure mechanisms in additively manufactured stainless steel *Mater. Sci. Eng. A* **651** 406–414

[149] Leuders S, Vollmer M, Brenne F, Tröster T and Niendorf T 2015 Fatigue strength prediction for titanium alloy TiAl6V4 manufactured by selective laser melting *Metall. Mater. Trans. A Phys. Metall. Mater. Sci.* **46** 1–8

[150] Kasperovich G and Hausmann J 2015 Improvement of fatigue resistance and ductility of TiAl6V4 processed by selective laser melting *J. Mater. Process. Technol.* **220** 202–214

[151] Attar H, Löber L, Funk A, Calin M, Zhang L C, Prashanth K G, Scudino

S, Zhang Y S and Eckert J 2015 Mechanical behavior of porous commercially pure Ti and Ti–TiB composite materials manufactured by selective laser melting *Mater. Sci. Eng. A* **625** 350–356

[152] Maskery I, Aboulkhair N T, Corfield M R, Tuck C, Clare A T, Leach R K, Wildman R D, Ashcroft I A and Hague R J M 2015 Quantification and characterisation of porosity in selectively laser melted Al–Si10–Mg using x-ray computed tomography *Mater. Charact.* **111** 193–204

[153] Chlebus E, Ku??nicka B, Dziedzic R, Kurzynowski T, Kuźnicka B, Dziedzic R and Kurzynowski T 2015 Titanium alloyed with rhenium by selective laser melting *Mater. Sci. Eng. A* **620** 155–163

[154] Castilho M, Gouveia B, Pires I, Rodrigues J and Pereira M 2015 The role of shell/core saturation level on the accuracy and mechanical characteristics of porous calcium phosphate models produced by 3Dprinting *Rapid Prototyp. J.* **21** 43–55

[155] Rezayat H, Zhou W, Siriruk A, Penumadu D and Babu S S 2015 Structure-mechanical property relationship in fused deposition modelling *Mater. Sci. Technol.* **31** 895–903

[156] Tammas-Williams S, Zhao H, Léonard F, Derguti F, Todd I and Prangnell P B 2015 XCT analysis of the influence of melt strategies on defect population in Ti–6Al–4V components manufactured by selective electron beam melting *Mater. Charact.* **102** 47–61

[157] Berretta S, Evans K E and Ghita O 2015 Processability of PEEK, a new polymer for high temperature laser sintering (HT-LS) *Eur. Polym. J.* **68** 243–266

[158] Grünberger T and Domröse R 2014 Optical in-process monitoring of direct metal laser sintering (DMLS) *Laser Tech. J.* **11** 40–42

[159] Slotwinski J A, Garboczi E J and Hebenstreit K M 2014 Porosity measurements and analysis for metal additive manufacturing process control *J. Res. Natl. Inst. Stand. Technol.* **119** 494–528

[160] Nassar A R, Spurgeon T J and Reutzel E W E 2014 Sensing defects during directed-energy additive manufacturing of metal parts using optical emissions spectroscopy *Solid freeform fabrication symposium* (Austin, TX, USA) pp 278–287

[161] van Uden S, Silva-Correia J, Correlo V M, Oliveira J M and Reis R L

2015 Custom-tailored tissue engineered polycaprolactone scaffolds for total disc replacement *Biofabrication* **7** 15008

[162] Raguvarun K, Balasubramaniam K, Rajagopal P, Palanisamy S, Nagarajah R, Hoye N, Curiri D and Kapoor A 2015 A study of internal structure in components made by additive manufacturing process using 3D X-ray tomography *AIP Conference on Proc. vol 1650: 41st Annual review of progress in quantitative nondestructive evaluation (QNDE)* (Boise, USA) pp 146–155

[163] Chou R, Milligan J, Paliwal M and Brochu M 2015 Additive manufacturing of Al-12Si alloy via pulsed selective laser melting *J. Miner. Met. Mater. Soc.* **67** 590–596

[164] Mireles J, Ridwan S, Morton P A, Hinojos A and Wicker R B 2015 Analysis and correction of defects within parts fabricated using powder bed fusion technology *Surf. Topogr.: Metrol. Prop.* **3** 34002

[165] Siddique S, Imran M, Rauer M, Kaloudis M, Wycisk E, Emmelmann C and Walther F 2015 Computed tomography for characterization of fatigue performance of selective laser melted parts *Mater. Des.* **83** 661–669

[166] Slotwinski J A, Garboczi E J, Stutzman P E, Ferraris C F, Watson S S and Peltz M A 2014 Characterization of metal powders used for additive manufacturing *J. Res. Natl. Inst. Stand. Technol.* **119** 460–493

[167] Slotwinski J A and Garboczi E J 2015 Metrology needs for metal additive manufacturing powders *J. Miner. Met. Mater. Soc.* **67** 538–543

[168] Rivas Santos V M, Maskery I, Sims-waterhouse D, Thompson A, Leach R, Ellis A and Woolliams P 2018 Benchmarking of an additive manufacturing process *ASPE/euspen conference: advancing precision in additive manufacturing* (Berkeley, USA)

[169] Turner N and MTC 2015 *A10998 - Technology review of x-ray CT for inspection and dimensional metrology: deliverable 1: review of x-ray computed tomography for non-destructive testing applications* (Coventry, UK: Manufacturing Technology Centre)

[170] Brierley N, Akhtar S and MTC 2015 *A11108 - Simulation enhanced inspection: deliverable 1: background review report* (Coventry, UK: Manufacturing Technology Centre)

[171] Möhring H-C C, Kersting P, Carmignato S, Yagüe-Fabra J A, Maestro M, Jiménez R, Ferraris E, Tunc L T, Bleicher F, Wits W W, Walczak K and Hedlind M 2015 A testpart for interdisciplinary analyses in micro production engineering *Procedia CIRP* **28** 106–112

[172] Xiong J, Mines R, Ghosh R, Vaziri A, Ma L, Ohrndorf A, Christ H and Wu L 2015 Advanced micro-lattice materials *Adv. Eng. Mater.* **17** 1253–1264

[173] Villarraga H, Lee C, Corbett T, Tarbutton J A and Smith S T 2015 Assessing additive manufacturing processes with X-ray CT metrology *ASPE spring topical meeting: achieving precision tolerances in additive manufacturing* (Raleigh, USA: ASPE) pp 116–121

[174] Lee C and Tarbutton J A 2015 Compliance and control characteristics of an additive manufactured-flexure stage *Rev. Sci. Instrum.* **86** 45107

[175] Cooper D, Thornby J, Blundell N, Henrys R, Williams M A and Gibbons G 2015 Design and manufacture of high performance hollow engine valves by additive layer manufacturing *Mater. Des.* **69** 44–55

[176] Seol S K, Kim D, Lee S, Kim J H, Chang W S and Kim J T 2015 Electrodeposition-based 3D printing of metallic microarchitectures with controlled internal structures *Small* **11** 3896–3902

[177] Sercombe T B, Xu X, Challis V J, Green R, Yue S, Zhang Z and Lee P D 2015 Failure modes in high strength and stiffness to weight scaffolds produced by selective laser melting *Mater. Des.* **67** 501–508

[178] Teeter M G, Kopacz A J, Nikolov H N and Holdsworth D W 2015 Metrology test object for dimensional verification in additive manufacturing of metals for biomedical applications *Proc. Inst. Mech. Eng. Part H: J. Eng. Med.* **229** 20–27

[179] Wüst S, Müller R and Hofmann S 2014 3D Bioprinting of complex channels—effects of material, orientation, geometry, and cell embedding *J. Biomed. Mater. Res. Part A* **103** 2558–2570

[180] Abele E, Stoffregen H a., Klimkeit K, Hoche H and Oechsner M 2015 Optimisation of process parameters for lattice structures *Rapid Prototyp. J.* **21** 117–127

[181] Lin M W, Morgan B W, Jovanovic I, Hsieh C Y, Liu Y L and Chen S H 2015 Progress on the study of direct laser electron acceleration in

density-modulated plasma waveguides *Proc. 6th international particle accelerator conference (IPAC)* (Richmond, USA) pp 2723–2725

[182] Todorov E, Spencer R, Gleeson S, Jamshidinia M and Kelly S M 2014 *America makes: national additive manufacturing innovation institute (NAMII) project 1: nondestructive evaluation (NDE) of complex metallic additive manufactured (AM) structures* (Columbus, USA: Edison Welding Inst. Inc.)

[183] Moylan S, Slotwinski J, Cooke A, Jurrens K and Donmez M A 2014 An additive manufacturing test artifact *J. Res. Natl. Inst. Stand. Technol.* **119** 429–459

[184] van Grunsven W, Hernandez-Nava E, Reilly G C and Goodall R 2014 Fabrication and mechanical characterisation of titanium lattices with graded porosity *Metals* **4** 401–409

[185] Huang H, Hsieh M-F, Zhang G, Ouyang H, Zeng C, Yan B, Xu J, Yang Y, Wu Z and Huang W 2015 Improved accuracy of 3D-printed navigational template during complicated tibial plateau fracture surgery *Australas. Phys. Eng. Sci. Med.* **38** 109–117

[186] Li Y, Yang W, Li X X, Zhang X, Wang C C, Meng X, Pei Y, Fan X, Lan P, Wang C C, Li X X and Guo Z 2015 Improving osteointegration and osteogenesis of three-dimensional porous Ti6Al4V scaffolds by polydopamine-assisted biomimetic hydroxyapatite coating *ACS Appl. Mater. Interfaces* **7** 5715–5724

[187] Mroz W, Budner B B, Syroka R, Niedzielski K, Golanski G, Slosarczyk A, Schwarze D, Douglas T E L, Golański G, Słósarczyk A, Schwarze D and Douglas T E L 2015 In vivo implantation of porous titanium alloy implants coated with magnesium-doped octacalcium phosphate and hydroxyapatite thin films using pulsed laser depostion *J. Biomed. Mater. Res. Part B Appl. Biomater.* **103** 151–158

[188] Narra N, Blanquer S B, Haimi S P, Grijpma D W and Hyttinen J 2015 μCT based assessment of mechanical deformation of designed PTMC scaffolds *Clin. Hemorheol. Microcirc.* **60** 99–108

[189] Evans A G, Hutchinson J W, Fleck N A, Ashby M F and Wadley H N G 2001 The topological design of multifunctional cellular metals *Prog. Mater. Sci.* **46** 309–327

[190] Williams J M, Adewunmi A, Schek R M, Flanagan C L, Krebsbach P H, Feinberg S E, Hollister S J and Das S 2005 Bone tissue engineering using polycaprolactone scaffolds fabricated via selective laser sintering *Biomaterials* **26** 4817–4827

[191] Rivas Santos V M, Sims-waterhouse D, Piano S, Maskery I, Leach R K, Ellis A and Woolliams P 2017 Metrological design of calibration and benchmarking artefacts for an additive manufacturing system *euspen/ASPE conference: dimensional accuracy and surface finish in additive manufacturing* (Leuven, Belgium) pp 24–27

[192] Rebaioli L and Fassi I 2017 A review on benchmark artifacts for evaluating the geometrical performance of additive manufacturing processes *Int. J. Adv. Manuf. Technol.* **93** 2571–2598

[193] Townsend A, Blunt L and Bills P 2016 Investigating the capability of microfocus x-ray computed tomography for areal surface analysis of additively manufactured parts *ASPE/euspen conference: dimensional accuracy and surface finish in additive manufacturing* (Raleigh, USA)

[194] Townsend A, Racasan R, Bills P, Blunt L, Leach R K and Bate D 2017 Development of an interlaboratory comparison investigating the generation of areal surface texture data per ISO 25178 from XCT *Conference on industrial computed tomography (iCT)* (Leuven, Belgium)

[195] Townsend A, Racasan R, Bills P, Thompson A, Senin N, Leach R K and Blunt L 2017 Results from an interlaboratory comparison of areal surface texture parameter extraction from X-ray computed tomography of additively manufactured parts *euspen's 17th international conference & exhibition* (Hannover, Germany)

[196] Townsend A, Pagani L, Blunt L, Scott P J and Jiang X 2017 Factors affecting the accuracy of areal surface texture data extraction from X-ray CT *Ann. CIRP* **66** 547–550

[197] Townsend A, Pagani L, Scott P J and Blunt L 2017 Measurement and characterisation of additively manufactured re-entrant surfaces *euspen/ASPE conference: dimensional accuracy and surface finish in additive manufacturing* (Leuven, Belgium) pp 140–144

[198] Townsend A, Racasan R, Leach R, Senin N, Thompson A, Ramsey A,

Bate D, Woolliams P, Brown S and Blunt L 2018 An interlaboratory comparison of X-ray computed tomography measurement for texture and dimensional characterisation of additively manufactured parts *Addit. Manuf.* **23** 422–432

[199] Fox J C, Kim F, Reese Z, Evans C and Taylor J S 2017 Investigation of complementary use of optical metrology and x-ray computed tomography for surface finish in laser powder bed fusion additive manufacturing *euspen/ASPE conference: dimensional accuracy and surface finish in additive manufacturing* (Leuven, Belgium) pp 132–136

[200] Stimpson C K, Snyder J C, Thole K A and Mongillo D 2016 Scaling roughness effects on pressure loss and heat transfer of additively manufactured channels *J. Turbomach.* **139** 021003

[201] Maszybrocka J, Stwora A, Gapiński B, Skrabalak G and Karolus M 2017 Morphology and surface topography of Ti6Al4V lattice structure fabricated by selective laser sintering *Bull. Polish Acad. Sci. Tech. Sci.* **65** 85–92

[202] Zanini F, Sorgato M and Carmignato S 2017 Experimental investigation on the accuracy of surface topography measurements of additively manufacturedmetal parts scanned by X-ray micro computed tomography *euspen/ASPE conference: dimensional accuracy and surface finish in additive manufacturing* (Leuven, Belgium) pp 137–9

[203] Jansson A, Hermanek P, Pejryd L and Carmignato S 2018 Multi-material gap measurements using dual-energy computed tomography *Precis. Eng.* **In Press**

[204] Travitzky N, Bonet A, Dermeik B, Fey T, Filbert-Demut I, Schlier L, Schlordt T and Greil P 2014 Additive manufacturing of ceramic-based materials *Adv. Eng. Mater.* **16** 729–754

[205] Pagani L, Qi Q, Jiang X and Scott P J 2017 Towards a new definition of areal surface texture parameters on freeform surface *Measurement* **109** 281–291

[206] Lou S, Abdul-rahman H, Zeng W, Jiang X and Scott P J 2017 A Preliminary investigation on surface roughness assessment of complex additive manufactured parts scanned by X-ray computed tomography *Conference on industrial computed tomography (iCT)* (Leuven,

Belgium)

[207] Lou S, Townsend A, Jiang X, Blunt L, Zeng W and Scott P J 2016 On characterising surface topography of metal powder bed fusion additive manufactured parts *euspen's 16th international conference & exhibition* (Nottingham, UK)

[208] Senin N, Thompson A and Leach R K 2017 Feature-based characterisation of laser powder bed fusion surfaces *euspen/ASPE conference: dimensional accuracy and surface finish in additive manufacturing* (Leuven, Belgium) pp 121–123

[209] Senin N, Thompson A and Leach R K 2017 Feature-based characterisation of signature topography in laser powder bed fusion of metals *Meas. Sci. Technol.* **29** 045009

[210] Disciacca J, Gomez C, Thompson A, Lawes S, Leach R, Lega X C De and Groot P De 2017 True-color 3D surface metrology for additive manufacturing using interference microscopy *euspen/ASPE conference: dimensional accuracy and surface finish in additive manufacturing* (Leuven, Belgium) pp 145–8

[211] Gómez C A, Su R, Thompson A, Disciacca J, Lawes S and Leach R K 2017 Optimisation of surface topography characterisation for metal additive manufacturing using coherence scanning interferometry *euspen/ASPE conference: dimensional accuracy and surface finish in additive manufacturing* (Leuven, Belgium) pp 162–6

[212] Newton L, Senin N and Leach R K 2018 Focus variation measurement of metal additively manufactured surfaces *ASPE/euspen conference: advancing precision in additive manufacturing* (Berkeley, USA) pp 232–237

[213] Koutiri I, Pessard E, Peyre P, Amlou O and De Terris T 2017 Influence of SLM process parameters on the surface finish, porosity rate and fatigue behavior of as-built Inconel 625 parts *J. Mater. Process. Technol.* **255** 536–546

[214] Sidambe A T 2017 Three dimensional surface topography characterization of the electron beam melted Ti6Al4V *Met. Powder Rep.* **72** 200–205

[215] Cabanettes F, Joubert A, Chardon G, Dumas V, Rech J, Grosjean C and

Dimkovski Z 2018 Topography of as built surfaces generated in metal additive manufacturing: a multi scale analysis from form to roughness *Precis. Eng.* **52** 249–265

[216] Thompson A, Senin N and Leach R K 2016 Towards an additive surface atlas A *SPE/euspen conference: dimensional accuracy and surface finish in additive manufacturing* (Raleigh, USA)

[217] Clark D and Brown B 2015 A rapid image acquisition method for focus stacking in microscopy *Micros. Today* **23** 18–25

[218] Haugstad G 2012 *Atomic force microscopy: understanding basic modes and advanced applications* (Hoboken, USA: Wiley)

[219] MacAulay G D, Senin N, Giusca C L and Leach R K 2016 Study of manufacturing and measurement reproducibility on a laser textured structured surface *Measurement* **94** 942–948

[220] Scott P J 2009 Feature parameters *Wear* **266** 548–51

[221] Senin N and Blunt L 2013 Characterisation of individual areal features In: *Characterisation of areal surface texture* ed Leach R K (Berlin, Germany: Springer) pp 179–216

[222] Mazumder J 1991 Overview of melt dynamics in laser processing *Opt. Eng.* **30** 1208–1219

[223] Read N, Wang W, Essa K and Attallah M M 2015 Selective laser melting of AlSi10Mg alloy: Process optimisation and mechanical properties development *Mater. Des.* **65** 417–424

[224] Simonelli M, Tuck C, Aboulkhair N T, Maskery I, Ashcroft I, Wildman R D and Hague R 2015 A study on the laser spatter and the oxidation reactions during selective laser melting of 316L stainless steel, Al-Si10-Mg, and Ti-6Al-4V *Metall. Mater. Trans. A Phys. Metall. Mater. Sci.* **46** 3842–3851

[225] Tolochko N K, Mozzharov S E, Yadroitsev I A, Laoui T, Froyen L, Titov V I and Ignatiev M B 2004 Balling processes during selective laser treatment of powders *Rapid Prototyp. J.* **10** 78–87

[226] Gong H, Gu H, Zeng K, Dilip J J S, Pal D, Stucker B, Christiansen D, Beuth J and Lewandowski J J 2014 Melt pool characterization for selective laser melting of Ti-6Al-4V pre-alloyed powder *Solid freeform fabrication symposium* (Austin, USA) pp 256–67

[227] Khairallah S A, Anderson A T, Rubenchik A and King W E 2016 Laser powder-bed fusion additive manufacturing: physics of complex melt flow and formation mechanisms of pores, spatter, and denudation zones *Acta Mater.* **108** 36–45

[228] Digital Surf 2018 Mountains® surface imaging & metrology software (Available at https://www.digitalsurf.com/software-solutions/multi-purpose/) Accessed: 19th September 2018

[229] Senin N, Thompson A and Leach R K 2017 Characterisation of the topography of metal additive surface features with different measurement technologies *Meas. Sci. Technol.* **28** 095003

[230] Török P 2003 *Optical imaging and microscopy: techniques and advanced systems* (Berlin: Springer)

[231] Postek M T 1994 Critical issues in scanning electron microscope metrology *J. Res. Natl. Inst. Stand. Technol.* **99** 641–671

[232] Aguilar J F, Lera M and Sheppard C J R 2000 Imaging of spheres and surface profiling by confocal microscopy *Appl. Opt.* **39** 4621–4628

[233] Weise W, Zinin P, Wilson T, Briggs A, Boseck S, Briggs G A D and Boseck S 1996 Imaging of spheres with the confocal scanning optical microscope *Opt. Lett.* **21** 1800–1802

[234] Gao F, Leach R K, Petzing J and Coupland J M 2007 Surface measurement errors using commercial scanning white light interferometers *Meas. Sci. Technol.* **19** 015303

[235] Groot P de 2015 Principles of interference microscopy for the measurement of surface topography *Adv. Opt. Photonics* **7** 1–65

[236] Fay M F and Badami V 2014 Characterizing additive manufacturing parts using coherence scanning interferometry *ASPE/euspen conference: dimensional accuracy and surface finish in additive manufacturing* (Berkeley, USA) pp 135–138

[237] Nikolaev N, Petzing J and Coupland J 2016 Focus variation microscope: linear theory and surface tilt sensitivity *Appl. Opt.* **55** 3555–3565

[238] Leach R K and Haitjema H 2010 Bandwidth characteristics and comparisons of surface texture measuring instruments *Meas. Sci. Technol.* **21** 32001

[239] CloudCompare 2018 CloudCompare 3D point cloud and mesh

processing software open source project (Available at https://www.danielgm.net/cc/) Accessed: 19th September 2018

[240] Thompson A, Senin N, Giusca C and Leach R K 2017 Topography of selectively laser melted surfaces: A comparison of different measurement methods *Ann. CIRP* **66** 543–546

[241] Leach R K 2011 Introduction to surface texture measurement In: *Optical measurement of surface topography* ed Leach R K (Berlin, Germany: Springer) pp 1–11

[242] Haitjema H 2015 Uncertainty in measurement of surface topography *Surf. Topogr.: Metrol. Prop.* **3** 035004

[243] Tosello G, Haitjema H, Leach R K, Quagliotti D, Gasparin S and Hansen H N 2016 An international comparison of surface texture parameters quantification on polymer artefacts using optical instruments *Ann. CIRP* **65** 529–532

[244] Visual Computing Lab - ISTI - CNR 2018 MeshLab (Available at http://www.meshlab.net/) Accessed: 19th September 2018

[245] Gower J C 1975 Generalized procrustes analysis *Psychometrika* **40** 33–51

[246] Condeço J, Christensen L H and Rosén B G 2001 Software relocation of 3D surface topography measurements *Int. J. Mach. Tools Manuf.* **41** 2095–2101

[247] Morrison S J 2009 *Statistics for engineers an introduction* (Chichester, UK: Wiley)

[248] ISO 4288:1996 Geometrical product specifications (GPS) -- Surface texture: profile method -- Rules and procedures for the assessment of surface texture (International Organisation for Standardisation)

[249] [Bonferroni C E 1935 Il calcolo delle assicurazioni su gruppi di teste In: *Studi in onore del Professore Salvatore Ortu Carboni* (Rome, Italy: Bardi) pp 13–60

[250] George P-L and Borouchaki H 1998 *Delaunay triangulation and meshing: application to finite elements* (Oxford, UK: Butterworth-Heinemann)

[251] Horn B K P 1987 Closed-form solution of absolute orientation using unit quaternions *J. Opt. Soc. Am. A* **4** 629–642

[252] Besl P J and McKay N D 1992 A Method for Registration of 3D-Shapes *IEEE Trans. Pattern Anal. Mach. Intel.* **14** 239–256

[253] Zanini F, Pagani L, Scott P J, Savio E and Carmignato S 2018 Measurement of additively manufactured surfaces with re-entrant features by X-ray computed tomography *ASPE/euspen conference: advancing precision in additive manufacturing* (Berkeley, USA)

[254] Giusca C L and Leach R K 2013 Calibration of the scales of areal surface topography measuring instruments: part 3. resolution *Meas. Sci. Technol.* **24** 105010

[255] Thompson A, Körner L, Senin N, Lawes S, Maskery I and Leach R K 2017 X-ray computed tomography for the measurement of internal surface texture of additively manufactured hollow parts *CIRP winter meeting* (Paris, France)

[256] Thompson A, Körner L, Senin N, Leach R, Lawes S and Maskery I 2017 Measurement of the internal surface texture of additively manufactured parts by X-ray computed tomography *Conference on industrial computed tomography (iCT)* (Leuven, Belgium)

[257] ISO 10360-11:Under development Geometrical product specification (GPS) -- Acceptance and reverification tests for coordinate measuring machines (CMM) -- Part 11: computed tomography (International Organisation for Standardisation)

[258] Petzing J, Coupland J and Leach R K 2010 Good practice guide no. 116 The measurement of rough surface topography using coherence scanning interferometry (London, UK: National Physical Laboratory)

[259] Jacobs T D B, Junge T and Pastewka L 2017 Quantitative characterization of surface topography using spectral analysis *Surf. Topogr.: Metrol. Prop.* **5** 013001

[260] Jiang X, Scott P and Whitehouse D 2007 Freeform Surface Characterisation - A Fresh Strategy *Ann. CIRP* **56** 553–556

[261] Thompson A, Senin N, Maskery I and Leach R K 2018 Effects of magnification and sampling resolution in X-ray computed tomography for the measurement of additively manufactured metal *Precis. Eng.* **53** 54–64

[262] Thompson A, Körner L, Senin N, Lawes S and Leach R K 2017 X-ray

computed tomography of additively manufactured metal parts: the effect of magnification and reconstruction sampling on surface topography measurement *16th international conference on metrology and properties of engineering surfaces* (Gothenburg, Sweden)

[263] Thompson A, Körner L, Senin N, Lawes S and Leach R K 2017 A sensitivity analysis for the measurement of internal additively manufactured surfaces by X-ray computed tomography *Dimensional X-ray computed tomography* (Coventry, UK)

[264] VDI/VDE 2630:2014 Part 1.1 Draft Computed tomography in dimensional measurement Fundamentals and definitions (VDI/VDE)

[265] Zygo 2014 NewView ™ 8300 Specifications (Available at http://www.lambdaphoto.co.uk/pdfs/Zygo/Lambda_NewView8300_Specs_SS0100_3_14.pdf) Accessed: 19th September 2018

[266] Su R, Wang Y, Coupland J and Leach R K 2017 On tilt and curvature dependent errors and the calibration of coherence scanning interferometry *Opt. Express* **25** 3297–3310

[267] Soille P 1999 Opening and closing In: *Morphological image analysis: principles and applications* (New York, USA: Springer) pp 105–37

[268] MathWorks 2018 MATLAB 2018b (Available at https://uk.mathworks.com/products/matlab.html) Accessed: 19th September 2018

[269] Hsieh J 2009 Image artifacts: appearances, causes and correction In: *Computed tomography: principles, design, artifacts, and recent advances* (Bellingham, USA: SPIE Press) pp 207–300

[270] Barrett J F and Keat N 2004 Artifacts in CT: recognition and avoidance *RadioGraphics* **24** 1679–1691

[271] Lifton J and Carmignato S 2017 Simulating the influence of scatter and beam hardening in dimensional computed tomography *Meas. Sci. Technol.* **28** 104001

[272] Hiller J and Hornberger P 2016 Measurement accuracy in X-ray computed tomography metrology: Toward a systematic analysis of interference effects in tomographic imaging *Precis. Eng.* **45** 18–32

[273] Illemann J, Bartscher M, Jusko O, Härtig F, Neuschaefer-Rube U and Wendt K 2014 Procedure and reference standard to determine the

structural resolution in coordinate metrology *Meas. Sci. Technol.* **25** 064015

[274] Buzug T M 2008 *Computed tomography: from photon statistics to modern cone-beam CT* (Berlin, Germany: Springer)

[275] Shaffer J P 1995 Multiple hypothesis testing *Annu. Rev. Psychol.* **46** 561–584

[276] Taylor J B, Carrano A L and Kandlikar S G 2006 Characterization of the effect of surface roughness and texture on fluid flow—past, present, and future *Int. J. Therm. Sci.* **45** 962–968

[277] Thompson A, Maskery I and Leach R K 2018 Internal surface measurement by X-ray computed tomography: an additive manufacturing industrial case study *Dimensional X-ray computed tomography* (Nottingham, UK)

[278] Ferrucci M, Leach R K, Giusca C L, Dewulf W and Carmignato S 2015 Towards geometrical calibration of X-ray computed tomography systems – a review *Meas. Sci. Technol.* **26** 9200